Magnetic Fields and Non-Local Transport in Laser Plasmas

Christopher Paul Ridgers

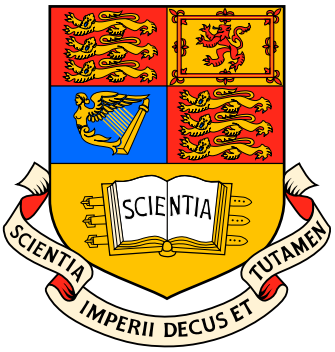

Submitted in partial fulfillment of the requirements for the degree of Doctor of Philosophy of Imperial College London.

Department of Physics
The Blackett Laboratory
Imperial College
London SW7 2BZ

June 2008

I dedicate this thesis to the memory of my father, Norman and to my mother and brother, Andrea and Stephen. Without their support this work would never have been possible.

"Failure is instructive. The person who really thinks learns quite as much from his failures as from his successes."

– John Dewey

The role of the author

The theorist, whose efforts are generally not as collaborative as the experimentalist, does not work in isolation. As such some clarification of the author's role in the work contained within this thesis is required. The kinetic code IMPACT which was used to perform the simulations yielding the bulk of the results presented was originally written by Dr. Robert Kingham in 2002. The augmentation of this code to include hydrodynamic ion motion was entirely done by the author.

When a figure's data is taken directly from external sources the source is clearly cited. Figures produced by others are acknowledged; permission has been obtained from the authors of these figures to reproduce them here.

Declaration

I hereby certify that the material in this thesis, which I submit for the degree of Doctor of Philosophy, is entirely original unless otherwise cited or acknowledged in the text.

Christopher Paul Ridgers
25/6/2008

Acknowledgments

A meticulous approach is the key to good science and I must first thank my supervisor Robert Kingham, whose guidance has provided an excellent example of this. I must also thank all of my colleagues at Imperial College past and present. Particularly Alex Robinson and Mark Sherlock who, as my immediate predecessors, helped me get to grips with the basics. Also thanks to Alec Thomas for the contribution he has already made as the latest addition to the VFP team at Imperial. Discussions with experimentalists can sometimes be useful too, thank you Peter Norreys, Philip Nilson and Stuart Mangles for letting me know what can realistically be done and helping me avoid pure conjecture. I would also like to thank Matthew Lilley and Minas Bacharis for prompting me to question the basics from time to time.

Finally and most importantly, a very special thank you is in order for my wife, Eleanor. Thank you for giving me the sense of perspective to realise that there are much more important things in life than ones PhD.

Abstract

The first Vlasov-Fokker-Planck simulations of nanosecond laser-plasma interactions – including the effects of self-consistent magnetic fields and hydrodynamic plasma expansion – will be presented. The coupling between non-locality and magnetic field advection is elucidated. For the largest (initially uniform) magnetic fields externally imposed in recent long-pulse laser gas-jet plasma experiments (12T) a significant degree of cavitation of the B-field will be shown to occur ($> 40\%$) in under 500ps. This is due to the Nernst effect and leads to the re-emergence of non-locality even if the initial value of the magnetic field strength is sufficient to localize transport.

Classical transport theory may also break down in such interactions as a result of inverse bremsstrahlung heating. Although non-locality may be suppressed by a large B-field, inverse bremsstrahlung still leads to a highly distorted distribution. Indeed the best fit for a 12T applied field (after 440ps of laser heating) is found to be a super-Gaussian distribution – $f_0 \propto e^{-v^m}$ – with $m = 3.4$. The effects of such a distribution on the transport properties under the influence of magnetic fields are elucidated in the context of laser-plasmas for the first time.

In long pulse laser-plasma interactions magnetic fields generated by the thermo-electric ('$\nabla n_e \times \nabla T_e$') mechanism are generally considered dominant. The strength of B-fields generated by this mechanism are affected, and new generation mechanisms are expected, when non-locality is important. Non-local B-field generation is found to be dominant in the interaction of an elliptical laser spot with a nitrogen gas-jet.

Symbol	Definition
$\underline{\underline{\alpha}}$	Resistivity tensor.
$\alpha_\perp$	Resistivity perpendicular to the magnetic field and parallel to $\mathbf{j}_\perp$
$\alpha_\parallel$	Resistivity parallel to the magnetic field
$\underline{\underline{\beta}}$	Thermoelectric tensor.
$\beta_\perp$	Thermoelectric coefficient perpendicular to the B-field and parallel to $\nabla_\perp T_e$.
$\beta_\wedge$	Thermoelectric coefficient perpendicular to the B-field and $\nabla_\perp T_e$.
Δx_i	Grid cell size at x_i in finite difference equations.
Δt	Time-step size in finite difference equations.
ϵ_e	Internal energy per unit mass of the electrons.
ϵ_0	Permittivity of free space, $8.85\times10^{-12}\,\mathrm{Fm}^{-1}$ in S.I. units.
γ	Ratio of specific heat capacity at constant pressure to specific heat capacity at constant volume, taken to be 5/3.
$\underline{\underline{\kappa}}$	Thermal conductivity tensor.
$\kappa_\perp$	Thermal conductivity perpendicular to the B-field and parallel to $\nabla_\perp T_e$.
$\kappa_\wedge$	Thermal conductivity perpendicular to the magnetic field and $\nabla_\perp T_e$.
$\kappa_\parallel$	Thermal conductivity parallel to the magnetic field.
λ_L	Laser wavelength
$\lambda_{\alpha\beta}$	Mean free path for collisions of particles of species α with those of species β.
λ_D	Debye length.
λ_{ed}	Delocalisation length $\lambda_{ed} = (\lambda_{ei}\lambda_{ee})^{1/2}$.
μ_0	Permeability of free space, $(4\pi)\mathrm{x}10^{-7}\,\mathrm{Hm}^{-1}$ in S.I. units.
$\nu_{\alpha\beta}$	Collision frequency of species α due to species β.
$\underline{\underline{\pi}}$	Stress tensor.
ρ	Mass density.
ρ_α	Mass density of species α.
σ	Electrical conductivity.
$\tau_{\alpha\beta}$	Collision time between particle α and particle β.
$\tau^E_{\alpha\beta}$	Energy exchange time between particle α and particle β.
τ_B	Braginskii's electron-ion collision time ($= 3\sqrt{\pi}\tau_{ei}/4$).
$\underline{\omega}$	Electron gyro-frequency ($= e\mathbf{B}/m_e$).
ω_L	Laser frequency.
ω_{pe}	Electron plasma frequency.
$\omega\tau$	Hall parameter (or magnetisation).
$\nabla_\perp$	Gradient perpendicular to the magnetic field, parallel to the driving force.
$\nabla_\parallel$	Gradient parallel to the magnetic field.
$\nabla_\mathbf{r}$	Gradient in configuration space.
$\nabla_\mathbf{v}$	Gradient in velocity space.
$\nabla_\mathbf{w}$	Gradient in velocity space where the velocity is in the ion's rest frame.

Symbol	Definition
$\mathbf{a}$	Electron's acceleration due to the electric field ($= e\mathbf{E}/m_e$).
$\mathbf{B}$	Magnetic field.
$\mathbf{b}$	Unit vector in the direction of the magnetic field.
c	Speed of light, $2.99\times10^8\mathrm{ms}^{-1}$ in S.I. units.
$\mathbf{C}$	Average ion velocity.
c_a	Alfven speed, given by $(B^2/\mu_0\rho)^{\frac{1}{2}}$.
$\mathbf{C}_e$	Average electron velocity in the ion rest-frame.
$\mathbf{C}'_e$	Average electron velocity in the laboratory frame.
c_s	Sound speed, given by $(\gamma P/\rho)^{\frac{1}{2}}$.
$\mathsf{d}\Omega$	An infinitesimal element of solid angle in velocity space.
e	Electron charge.
$\mathbf{E}$	Electric field.
$f_\beta(\mathbf{v},\mathbf{r},t)$	Distribution function for species β.
f_0	Isotropic part of the electron's distribution function.
$(\partial f_0/\partial t)_{coll(isional)}$	The rate of change of f_0 due to collisions.
f_m	The Maxwellian distribution.
$\mathbf{f}_1$	Anisotropic part of the electron's distribution function.
I	Laser intensity
$\mathbf{j}$	Electrical current, magnitude is j.
$\mathbf{j}_\perp$	Current perpendicular to the magnetic field.
$\mathbf{j}_\parallel$	Current parallel to the magnetic field.
k_b	Boltzmann's constant, $1.38\times10^{-23}\,\mathrm{JK}^{-1}$ in S.I. units.
$\mathsf{ln}\Lambda_{ei}$	Coulomb logarithm.
m_β	Mass of a particle of species β.
n_α	Number density of species α.
p_β	Scalar pressure due to species β.
q	Artificial viscosity.
$\mathbf{q}_e$	Electron heat flow.
$\mathbf{r}$	position coordinate in phase space, modulus represented by r.
r_L	The Larmor radius.
t	Time coordinate.
T_β	Temperature of species β.
$\mathbf{v}$	Velocity coordinate in phase space, modulus represented by v.
$\mathbf{v}_N$	Nernst velocity.
v_{osc}	Quiver velocity of the electrons in the laser's $\mathbf{E}$-field.
v_T	Thermal velocity, defined as $(2k_bT_e/m_e)^{1/2}$.
$\mathbf{w}$	Electron's velocity in the ion's rest frame, modulus is w.
$\mathbf{w}'$	Random part of the electron's velocity, modulus is w'.
w_T	Thermal velocity in $(\mathbf{w},\mathbf{r},t)$ coordinate system ($w_T = v_T$)
w_0	Laser beam waist.
Z	Ionic charge.

Contents

List of Figures

List of Tables

Chapter 1

Introduction

1.1 The need for fusion

The dramatic rise in the world's energy consumption over the last 150 years – as shown in figure 1.1 [1] – is of concern as fuel sources are depleted and the output of pollutants rises. It is difficult to estimate the world's remaining fossil fuel reserves accurately. Recent estimates are of the order of 80-100 years. Nuclear fission and renewable sources provide viable alternatives to fossil fuels. However, fission leads to very long-lived radioactive byproducts and although renewables are useful on the small scale it is difficult to imagine how such sources could provide high power density facilities. Nuclear fusion on the other hand could potentially provide such facilities with relatively low levels of pollution and virtually limitless resources (of the order of 10^9 years of power from sea water alone).

The fusion reaction which has the most promise for use in a power plant is that between a nucleus of deuterium and one of tritium, i.e.:

$$\mathrm{D}_1^2 + \mathrm{T}_1^3 \rightarrow \mathrm{He}_2^4 + \mathrm{n}_0^1 \quad (\Delta E = 17.6\mathrm{MeV},\ \sigma_{max} = 5.0\mathrm{barn}) \tag{1.1}$$

Here ΔE represents the quantity of energy released in the reaction and σ_{max} is the maximum reaction cross-section. Other reactions are also candidates for controlled fusion, for example:

$$\begin{aligned} \mathrm{T}_1^3 + \mathrm{p}_1^1 &\quad (\Delta E = 4.04\mathrm{MeV},\ \sigma_{max} = 0.096\mathrm{barn}) \\ \mathrm{D}_1^2 + \mathrm{D}_1^2 \rightarrow \mathrm{He}_2^3 + \mathrm{n}_0^1 &\quad (\Delta E = 3.27\mathrm{MeV},\ \sigma_{max} = 0.11\mathrm{barn}) \\ \mathrm{He}_2^4 + \gamma &\quad (\Delta E = 23.9\mathrm{MeV},\ \sigma_{max} = 0.16\mathrm{barn}) \end{aligned} \tag{1.2}$$

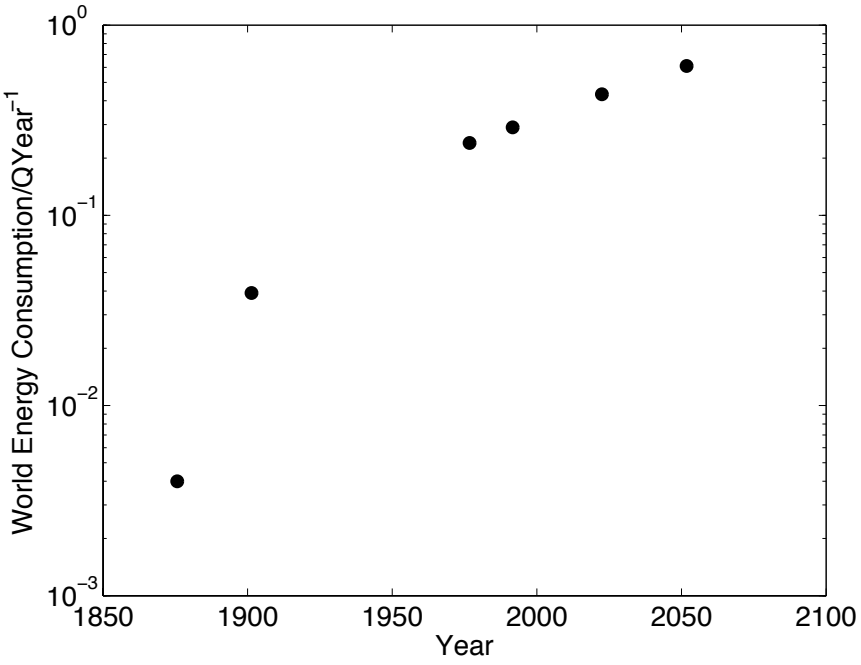

Figure 1.1: World energy consumption over the last 150 years (and projected into the future if current trends continue). NB: 1Q is 10^{21}J. This data has been taken from the World Energy Council.

Despite the fact that tritium is radioactive and rare, the reaction between deuterium and tritium has several advantages over those between two deuterium nuclei. The D-T reaction releases a reasonable amount of energy. More importantly, its maximum cross-section is the largest. Furthermore, its cross-section is much larger at the typical temperatures considered in controlled inertial fusion (10keV). This is shown in figure 1.2.

The tritium for the fusion reactions can be bred from lithium and fusion-produced neutrons in the following reactions:

$$\mathrm{Li}_3^6 + \mathrm{n}_0^1 \rightarrow \mathrm{T}_1^3 + \mathrm{He}_2^4 \quad (\Delta E = -4.86\mathrm{MeV}) \tag{1.3}$$

$$\mathrm{Li}_3^7 + \mathrm{n}_0^1 \rightarrow \mathrm{T}_1^3 + \mathrm{He}_2^4 + \mathrm{n}_0^1 \quad (\Delta E = 2.87\mathrm{MeV}) \tag{1.4}$$

The central relationship when determining the viability of a fusion power plant scheme is the Lawson criterion [3]:

$$n_e \tau = \frac{3 k_b T}{\frac{\eta}{4(1-\eta)} \langle \sigma v \rangle \Delta E - \alpha T^{1/2}} \tag{1.5}$$

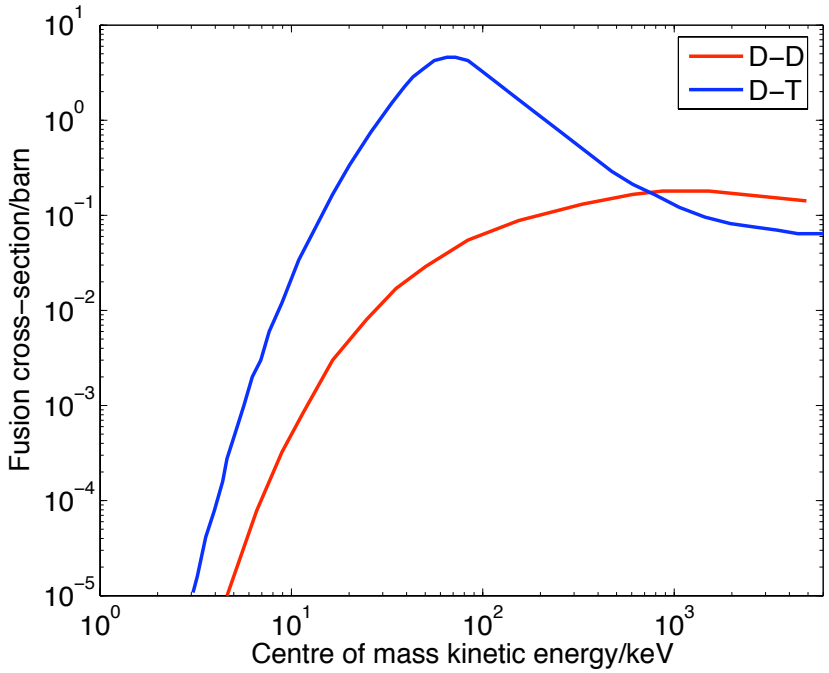

Figure 1.2: Fusion cross-sections for deuterium-deuterium (D-D) reactions – i.e. the reactions in equation (1.2) – and the deuterium-tritium reaction (D-T) in equation (1.1). Data taken from Atzeni & Meyer-Ter-Vehn [2].

Here τ is the confinement time – the internal energy of the plasma must be confined so that the temperature is high enough for fusion to occur. n_e is the electron's number density, k_b is Boltzmann's constant, T is the plasma temperature, σ represents the reaction cross section; when combined with the velocity v and averaged over velocity this yields the reactivity $\langle \sigma v \rangle$. The energy liberated by the fusion reaction is ΔE. The constant α is $5.34 \times 10^{-24}\text{ergs}^{-1}\text{cm}^{-3}$ and represents the energy lost by bremsstrahlung. This equation is valid when the power gain from the fusion reactions is equal to that lost – $n_e\tau$ must be greater than the quantity on the right-hand side if the fusion scheme is viable for power production. η is the efficiency of the fusion scheme. Choosing $\eta = 0.2$, and a temperature of 20keV, on enumeration this criterion gives $n_e\tau > 10^{20}\text{m}^{-3}\text{s}$. Two mainstream fusion schemes have been proposed: inertial confinement fusion (ICF) and magnetic confinement fusion (MCF). These approach the problem of confining the plasma in very different ways. MCF devices use relatively tenuous plasmas confined by a magnetic field for time-scales of the order of seconds. This presents problems as such a plasma is prone to many instabilities. ICF proposes to do away with the need for long confinement times, meaning one must deal with high density plasmas.

1.1.1 Inertial confinement fusion

The simplest version of the ICF scheme is for a D-T pellet to be compressed by many laser beams to 1000 times solid density with a central 'hot-spot' which is heated to tens of keV, allowing fusion to occur. The plasma is only 'confined' by its inertia and so the confinement time is very short. This method is known as direct drive ICF. The uniformity of the lasers is of paramount importance – small non-uniformities (on the order of 1%) can cause growth of the Rayleigh-Taylor instability and thwart attempts to compress the pellet [4, 5]. A more uniform drive is possible using the indirect-drive method [6,7], as illustrated in figure 1.3. Here a uniform bath of x-rays is used to implode the capsule. These x-rays are either generated by shining lasers into a hohlraum (effectively an empty cylindrical chamber made of a high Z material – usually gold) with the D-T target at the centre, or by using a wire-array z-pinch (the x-rays from which are made uniform using a hohlraum) [8, 9]. The laser-driven version of this method is in general less efficient than direct drive as the hohlraum intermediary causes some energy loss.

The Lawson criterion for inertial fusion is usually expressed in terms of a criterion on ρR where ρ is the density and R is the radius of the capsule. This can be seen to be equivalent to $n_e\tau$ by noting that the density of the capsule is $\rho = n_i m_i$ where n_i and m_i are the number density and mass of the ions and $n_e = ZN_i$, the plasma is quasi-neutral; the time taken for disassembly is approximately $\tau = R/c_s$ (c_s is the ion sound speed). In order to satisfy Lawson's criterion for hot-spot ignition ρR should be from 0.2gcm^{-2} to 0.5gcm^{-2}. In inertial fusion a common figure of merit for the reaction is the energy gain. The gain is the ratio of the energy released by fusion in the implosion of a single ICF capsule to the driver energy delivered to that capsule. A gain of 30-100 is required for power production.

Currently two large scale facilities are under development to achieve ignition (satisfy the Lawson criterion and so create a self-sustained fusion burn) using the indirect-drive ICF scheme. These are the culmination of a long series of incremental improvements to the laser energy available to such a scheme – this is shown in figure 1.4 [10]. These facilities are the National Ignition Facility (NIF) at Lawrence Livermore National Laboratory (Livermore, California), and Laser Megajoule (LMJ) at CEA (Bordeaux, France); the development of these has created a vigorous interest in the relevant laser-plasma interactions. Note that the energy gain for the NIF is expected to be on the order of 10. When the lasers interact with the hohlraum walls they ionize and ablate the wall material to create a plasma. An understanding of how the deposited heat flows in this plasma is essential if the drive uniformity is to

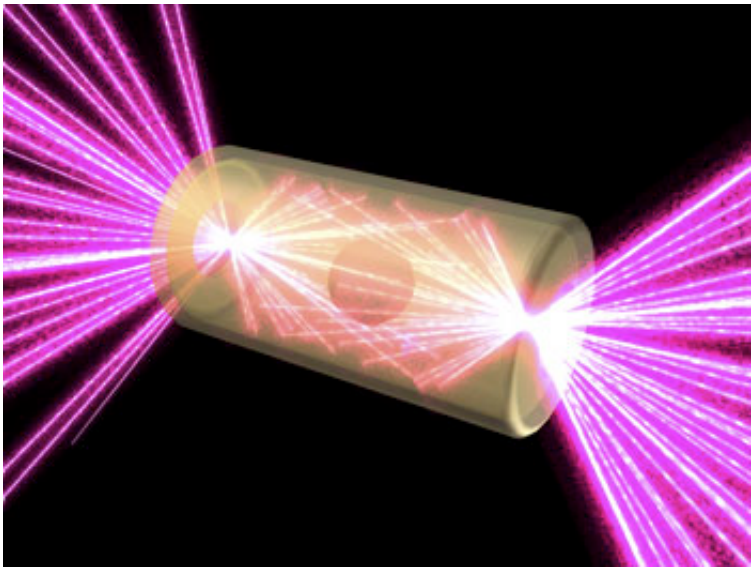

Figure 1.3: An artist's impression of a NIF hohlraum, taken from the National Ignition Facility's website (www.llnl.gov/nif).

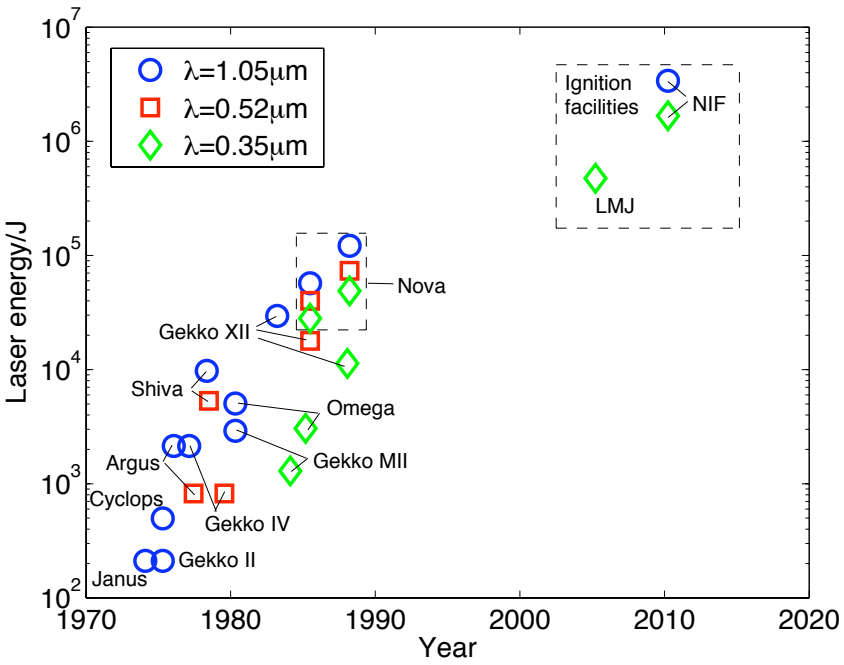

Figure 1.4: The recent increase in laser power for ICF – facilities designed to achieve ignition are now possible. Data taken from Nakai [10].

be predicted with confidence. Most simulations to address this solve the equations of magnetohydrodynamics (MHD), with the inherent assumptions about transport coefficients (discussed in section 2.3). Codes which directly solve the kinetic Vlasov-Fokker-Planck (VFP) equation elegantly solve for the transport of heat, current and other macroscopic quantities without these assumptions.

It will be shown, by discussing several important experiments, that a VFP treatment is necessary to determine the heat flow correctly. The key consideration will involve the importance of non-local transport. The concept of non-local transport is described in section 2.4. Furthermore, it has been shown that large (mega-gauss strength) magnetic fields can be generated in laser-solid interactions – thus these must be included in the model as must their effect on non-locality. The need to develop kinetic codes has been justified here in a hohlraum-centred way. These codes provide theoretical tools for other problems too. An understanding of the heat flow in laser-plasmas has implications for direct-drive ICF, indeed in many situations where MHD is not valid Vlasov-Fokker-Planck simulations may be of use.

1.1.2 Typical hohlraum conditions

Long-pulse laser plasma interactions will form the subject matter of this thesis. Long-pulse lasers are those used to drive the compression of the fusion target in direct-drive ICF and to heat the hohlraum walls in indirect-drive. The typical plasma parameters in the simulations – whose results are presented in chapters 5, 6 and 7 – are within an order of magnitude of those in a hohlraum. Figure 1.5 shows a schematic cut-through of a hohlraum. At the NIF the lasers will come in through the entrance hole in two cones – the 'inner' and 'outer' cones. The number of beams will be very large, 192 in total; these are expected to deliver at least 1MJ of energy to the hohlraum. These lasers are expected to give rise to a radiation temperature in the hohlraum of 270-300eV. Hohlraums are generally made of a high atomic number solid (gold was the example given in the previous section) and are filled with a low Z gas-fill, such as neon or methane, to slow the ablation of the walls [7]. The electron number density (n_e) and temperature (T_e) along the 'outer' beams, from MHD simulations, are shown in figure 1.6 [7]. The number densities are normalised to $n_{crit} = 10^{22}\text{cm}^{-3}$ (the critical density for light with a wavelength of 0.3μm – the significance of the critical density is described in the next chapter).

The typical conditions simulated in chapters 5, 6 and 7 are most similar to those in the gas-fill, towards the entrance hole. The electron number density considered

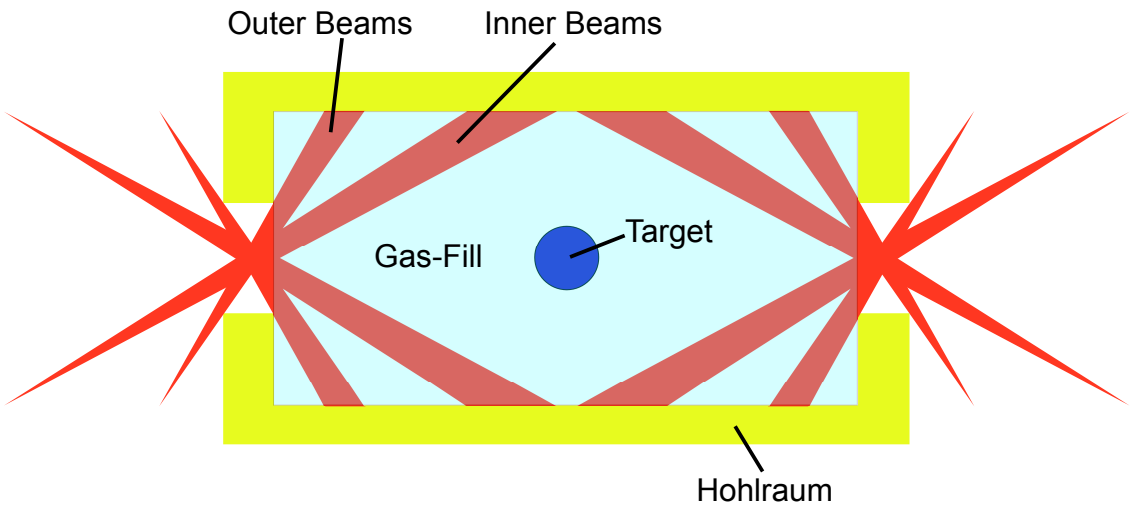

Figure 1.5: A schematic of a hohlraum.

will be $1.5\times10^{19}\text{cm}^{-3}$ – this is a factor of ten less than the lowest density in the NIF gas-fill. The maximum temperature obtained will be 600eV under the influence of a 12T B-field. The temperature is thus about half that expected near the entrance hole; the magnetic fields are as expected in the gas-fill [7, 11]. The lasers modelled later will be Neodymium-Glass and so have a wavelength of 1.054μm. These lasers deliver 100J in 1ns in the simulations – figure 1.4 shows that this is low compared to the energy required for ignition. In ICF shorter wavelength radiation is generally used – at the second ($\lambda = 0.52\mu$m) or third ($\lambda = 0.35\mu$m) harmonic frequencies of a Neodymium-Glass laser – such radiation better penetrates an ablating plasma (the critical density is higher) and so couples its energy better to this plasma. As the laser intensity in the simulations is relatively low relativistic effects may be ignored (the importance of the laser intensity in determining the physics relevant to a given laser-plasma interaction will be discussed in the next section). Nitrogen plasmas will be modelled and will be assumed to be fully ionised from the outset ($Z = 7$).

These conditions are chosen to correspond to the recent experiment of Froula *et al* [12]. This experiment provided a demonstration of the effect of B-fields on transport under conditions relevant to hohlraums. It showed the suppression of non-locality by an externally applied magnetic field in conditions relevant to the gas-fill unambiguously for the first time. The simulations presented in their paper used a VFP model for the situation when no B-field was present and an MHD one when the

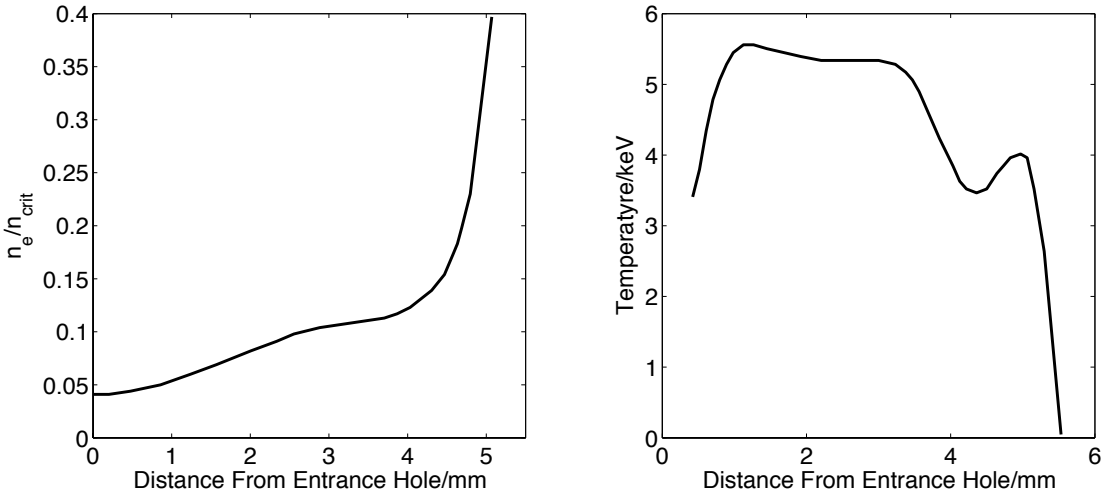

Figure 1.6: The electron number density (left) and temperature (right) along the line of one of the outer beams.

largest (12T) field was present. The intermediate regime will be studied here using a VFP treatment which includes magnetic fields. Froula's experiment is described in more detail in sections 2.4.1 and 5.1. The effects which are deemed important in the experiment (non-locality, the Nernst effect – see later) should be considered in ICF plasmas.

1.2 Thesis outline

The main subject matter of this thesis is the addition of hydrodynamic flow to the VFP code IMPACT. The procedure by which this is done will be outlined in chapters 3 and 4. The remaining chapters detail the use of this new code to investigate kinetic effects and magnetic fields in long-pulse laser-plasma interactions.

Chapter 2 – Background: Basic laser-plasma physics will briefly be discussed, followed by a description of the various theoretical models typically used in long-pulse laser-plasma physics. This leads into a discussion of the VFP equation and its relationship to the classical theory of transport in plasmas (including B-fields). Situations in which this breaks down are discussed – the mechanisms which cause this to happen will be given. Previous attempts to deal with the invalidity of classical transport in laser-plasmas will be outlined.

Chapter 3 – Ion hydrodynamics in the VFP equation: The motivation for the inclusion of hydrodynamics into the VFP code IMPACT will be given. Imple-

menting this gives the first such code in 2D, with self-consistent magnetic fields and the ability to simulate nanosecond time-scale interactions. Ion-motion will be included by transforming the VFP equation into the average ion rest frame.

Chapter 4 – Numerical solution of the new model: The inclusion of ion-motion into IMPACT creates new terms in the VFP equation. The numerical scheme by which these are included in the code will be outlined here. Testing will also be described – to do this magnetosonic waves will be simulated.

Chapter 5 – Non-local transport in a magnetic field: In current long-pulse laser-plasma experiments the magnetic field is thought to advect with the hydrodynamic plasma flow. This will be tested in one such experimental situation (that of Froula *et al*) and found not to be the case. The B-field dynamics will be shown to be dominated by the Nernst effect; leading to strong coupling between magnetic field dynamics and non-locality. This work has also been published in Physical Review Letters [13].

Chapter 6 – Transport theory for a super-Gaussian distribution: Inverse bremsstrahlung heating may also distort the distribution function in long-pulse laser-plasma interactions. The effects of this on transport theory are derived, the resulting new theory of transport is found to agree well with simulations of Froula's experimental conditions in some situations. This work is under review for publication in Physics of Plasmas.

Chapter 7 – Non-classical magnetic field generation: The generation of magnetic fields will be shown to be strongly dependent on non-locality. The magnetic field from an elliptical laser spot will be seen to be due to a purely non-local mechanism.

Chapter 2

Background

2.1 Laser-plasma interactions

Laser-plasma interactions (LPI) are not only of great importance to ICF but to understanding fundamental plasma physics. The physical processes which are relevant to a given experiment depend on the intensity of the laser. This can be seen by considering the equation which gives the maximum quiver velocity of the electron (v_{osc}) – the velocity which the electron acquires through acceleration by the laser's electric field.

$$\gamma_{osc}\frac{v_{osc}}{c} = \left(\frac{I\lambda^2}{1.4\times10^{18}\mathrm{Wcm^{-2}}\mu\mathrm{m}^2}\right)^{1/2} \qquad \gamma_{osc} = \frac{1}{\sqrt{1-v_{osc}^2/c^2}} \tag{2.1}$$

The intensity of the laser is represented by I and its wavelength by λ, c is the speed of light. Consider the energy the electrons acquire as a result of this quiver motion (in the non-relativistic, low-intensity regime):

$$\frac{m_e v_{osc}^2}{2k_b T_e} = \frac{1.6I\lambda^2}{1\times10^{18}\mathrm{Wcm^{-2}}\mu\mathrm{m}^2}\left(\frac{T_e}{\mathrm{eV}}\right)^{-1} \tag{2.2}$$

m_e is the electron mass and k_b is Boltzmann's constant. Therefore $I\lambda^2$ determines the velocity and energy the electrons have as a result of the laser field – it is the most important parameter when determining the physical processes excited by the absorption of the laser. In figure 2.1 a description of the important physics at some landmark values of this parameter is given.

With $I\lambda^2$ between $10^{11}\mathrm{Wcm^{-2}}$ and $10^{22}\mathrm{Wcm^{-2}}$ the interaction of a laser with matter produces a plasma. Today experiments investigating such laser-plasma interactions (LPI) usually fall into one of two categories: short-pulse (or ultra-short pulse)

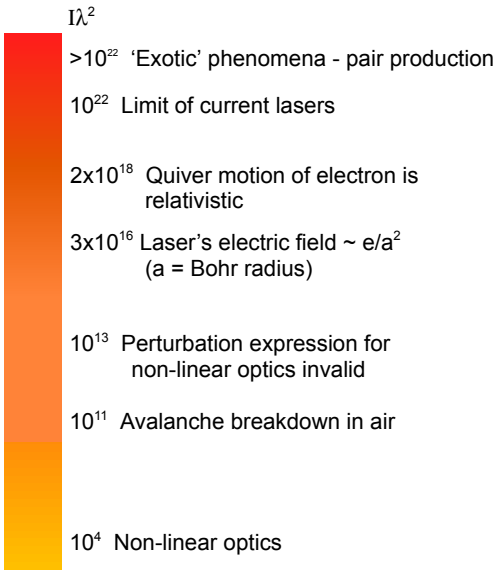

Figure 2.1: Important landmarks in $I\lambda^2$ space.

interactions which occur over the order of one picosecond (one femtosecond), and have $I\lambda^2$ between $10^{18}\mathrm{Wcm}^{-2}$ and $10^{22}\mathrm{Wcm}^{-2}$; and long-pulse, which are over several hundred picoseconds to several nanoseconds and have $I\lambda^2$ at about $10^{15}\mathrm{Wcm}^{-2}$. In ICF relevant experiments long-pulse lasers are generally used. From figure 2.1 it is clear that such LPI do not have sufficient intensity to cause the electron's quiver motion to be relativistic – the interactions considered here are non-relativistic.

2.1.1 Absorption mechanisms

There are various ways in which laser light may be absorbed by a plasma. The dominant mechanism depends on the intensity of the laser. The two most important mechanisms in long-pulse laser-plasma interactions will be discussed here; i.e. inverse bremsstrahlung and resonance absorption. First it is important to note that electromagnetic propagation is not possible beyond the critical density n_c in an ablating plasma. This is the density at which the wave frequency is equal to the plasma frequency (ω_{pe}).

$$\omega_{pe} = \left(\frac{n_e e^2}{\epsilon_0 m_e}\right)^{1/2} \tag{2.3}$$

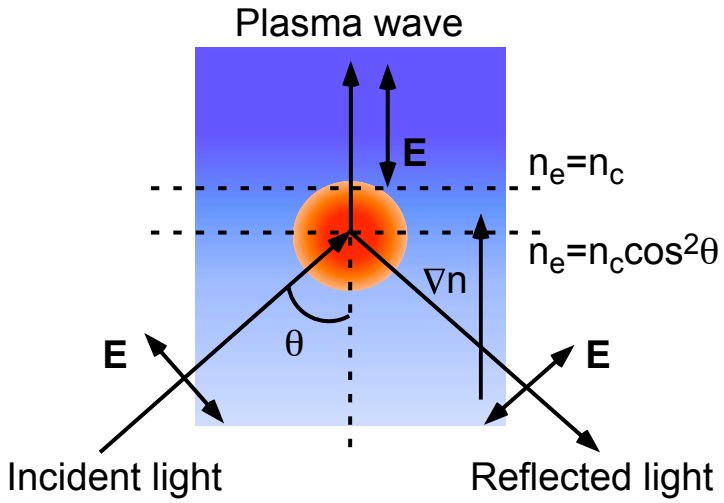

Figure 2.2: A schematic explaining resonance absorption.

In the above formula e represents the charge of the electron and ϵ_0 is the permittivity of free-space, the electron's number density is represented by n_e. The plasma frequency is the typical response frequency of the electrons to a perturbation in the electric field and so waves with frequencies below this threshold may be screened-out by the plasma. The plasma frequency is also the frequency of electrostatic wave modes in the plasma known as Langmuir waves. When the plasma's density is less than the critical density the plasma is said to be under-dense, when it is greater than n_c it is over-dense.

Resonance absorption

A laser propagating into a region of plasma with a density close to the critical density may excite plasma waves and thus deposit some of it's energy in the plasma. The standard configuration considered when discussing this type of absorption is shown in figure 2.2. The laser must be polarised in such a way that a component of its electric field is in the direction of the density gradient, this component may then give rise to electrostatic plasma modes (Langmuir waves) These waves may then generate hot electrons with a temperature which may be estimated by the formula below [14, 15].

$$\frac{T_{hot}}{\text{keV}} \approx 6 \left(\frac{T_e}{\text{keV}} \frac{I\lambda^2}{1 \times 10^{15} \text{Wcm}^{-2} \mu\text{m}^2} \right)^{1/3} \tag{2.4}$$

Where T_{hot} is the temperature the hot electrons acquire by absorption. For a typical long-pulse laser with a wavelength of one micron heating a plasma with tempera-

ture 100eV the heated temperature is of the order of about 1keV – this is significant. However, in the interactions considered here, resonance absorption may be neglected. Only under-dense plasmas will be considered. It should be noted that there is no absorption if the laser strikes the target at normal incidence ($\theta = 0$); in this case there is no component of the laser's E-field in the ∇n_e direction. The absorption decreases to zero as $\theta \to \pi/2$. The laser is reflected when the density is $n_c \cos^2\theta$, the electric field must evanescently tunnel through to n_c where it may excite Langmuir waves. As $\theta \to \pi/2$ the distance between these two densities increases, less E-field tunnels through and so less absorption occurs.

Inverse bremsstrahlung (IB)

As the laser passes through an under-dense plasma the electrons begin to quiver in it's electric field. If some of these electrons then collide with ions a proportion of this quiver energy is transformed to thermal energy and the plasma heats up. This mechanism is illustrated in figure 2.3. The rate of energy absorption into the plasma by IB can be estimated as follows. Assuming that all of the quiver energy is thermalised in one electron-ion collision time (τ_{ei}), the power input per unit volume (P/V) is:

$$\frac{P}{V} \approx \frac{1/2 n_e m_e v_{osc}^2}{\tau_{ei}} \tag{2.5}$$

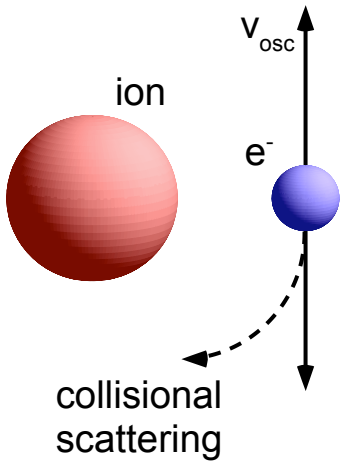

Figure 2.3: The IB heating mechanism.

Using equation (2.2) this can be estimated for the typical laser and plasma parameters considered later. Heating region of 50 cubic microns with an electron density of 10^{19}cm^3, an ionic charge of 7 and an initial temperature of 100eV; and assuming a constant rate of input of power (100J in 1ns); this mechanism should heat the plasma by 125eV in one nanosecond. This mechanism is the most important in the interactions studied here and so is the only one included.

2.2 Kinetic modelling of plasmas

A plasma is a collection of charged particles. Further, under the conditions considered in this thesis these particles behave classically (and non-relativistically). Therefore, the most complete way in which to describe the plasma is to specify the positions

and velocities of all the particles. This can be done using the N-particle distribution function (f_N) [3]:

$$f_N(\mathbf{r}_1, \mathbf{v}_1, \mathbf{r}_2, \mathbf{v}_2, \ldots, \mathbf{r}_N, \mathbf{v}_N) = \prod_{i=1}^{N} \delta[\mathbf{r}_i - \mathbf{R}_i(t)]\delta[\mathbf{v}_i - \dot{\mathbf{R}}_i(t)] \tag{2.6}$$

This distribution function is defined in 6-N dimensional phase space, i.e. there are three position and velocity coordinates for each particle. f_N is only non-zero when all the position coordinates $\mathbf{r}_i$ and the velocity coordinates $\mathbf{v}_i$ are equal to the position and velocity of the respective particle i (i.e. $\mathbf{R}_i$ and $\dot{\mathbf{R}}_i$). Taking the time derivative of equation (2.6) gives the Liouville equation:

$$\frac{\partial f_N}{\partial t} = \sum_{i=1}^{N} \left(\dot{\mathbf{R}}_i \cdot \frac{\partial f_N}{\partial \mathbf{R}_i} + \ddot{\mathbf{R}}_i \cdot \frac{\partial f_N}{\partial \dot{\mathbf{R}}_i} \right) \tag{2.7}$$

This is only non-zero when $\mathbf{r}_i = \mathbf{R}_i$ and $\mathbf{v}_i = \dot{\mathbf{R}}_i$. The acceleration of a particle is $\ddot{\mathbf{R}}_i = \mathbf{F}_i/m_i$ (m_i is the mass of particle i and $\mathbf{F}_i$ is the force on it). Assuming that the only forces on the particle are electromagnetic, $\mathbf{F}_i$ is given by the Lorentz force.

$$\frac{\partial f_N}{\partial t} + \sum_{i=1}^{N} \left[\mathbf{v}_i \cdot \nabla_{\mathbf{r}_i} f_N + \frac{q_i}{m_i}(\mathbf{E}_N + \mathbf{v}_i \times \mathbf{B}_N) \cdot \nabla_{\mathbf{v}_i} f_N \right] = 0 \tag{2.8}$$

The symbols $\nabla_{\mathbf{r_i}}$ and $\nabla_{\mathbf{v_i}}$ refer to differentiation by the coordinates $\mathbf{r}_i$ and $\mathbf{v}_i$ respectively. The fields $\mathbf{E}_N$ and $\mathbf{B}_N$ are those felt by particle i as a result of the positions and velocities of all the other particles. Of course such a description as this is of no use when applied to a macroscopic plasma. The number of electrons in experimental laser-plasmas is larger than 10^{11}. Therefore, not only is an exact solution to equation (2.8) analytically intractable, but a numerical simulation of it would require N^2 operations and so is also impossible. This problem can be overcome in a variety of ways. The most ubiquitous numerical model is Particle-in-Cell (PIC). The PIC model conglomerates many particles to form a single macroparticle. The charge and current distributions from the distribution of these macroparticles are then used in Maxwell's equations to compute the electric and magnetic fields, which then go on to accelerate the macroparticles. In this way the number of calculations is reduced to N which makes numerical simulation a possibility.

Can progress be made analytically? The rigorous way to proceed from equation (2.8) is through a procedure known as the 'BBGKY hierarchy' [16]. This is very complicated and as such it will not be detailed here. The coordinates of all but one particle are 'integrated-out' from equation (2.8). This introduces the distribution

function f, in 6D phase space; in such a phase space the coordinates of a point are $(\mathbf{r}, \mathbf{v})$. This distribution function is the statistically-averaged density of particles in phase space. The time evolution of this is given by the VFP equation. The necessity of this approach is obvious when one notes that any solution of the Liouville equation as given would involve an exact knowledge of the initial positions and velocities of all the particles. Realistically, only the statistically averaged initial conditions can be known.

2.2.1 The Vlasov-Fokker-Planck equation

The Vlasov-Fokker-Planck (VFP) equation is given by [3]:

$$\frac{\partial f_\alpha}{\partial t} + \nabla_{\mathbf{r}} \cdot (f_\alpha \mathbf{v}) + \nabla_{\mathbf{v}} \cdot \left[\frac{Z_\alpha e}{m_e} (\mathbf{E} + \mathbf{v} \times \mathbf{B}) f_\alpha \right] = \left(\frac{\partial f_\alpha}{\partial t} \right)_{collisional} \tag{2.9}$$

In cartesian coordinates $\nabla_{\mathbf{r}} = (\partial/\partial x, \partial/\partial y, \partial/\partial z)$ and $\nabla_{\mathbf{v}} = (\partial/\partial v_x, \partial/\partial v_y, \partial/\partial v_z)$. A somewhat heuristic justification of this equation comes from applying arguments about the conservation of f_α in six-dimensional phase space; the VFP equation is a continuity equation in phase space. The right hand side gives the (yet to be elucidated) affect of collisions. The distribution function $f_\alpha(\mathbf{v}, \mathbf{r}, t)$ is for species α with charge Z_α. This distinction may be dropped as a VFP treatment is only used for the electrons. The collisional term may be expressed as a series expansion in the average deflection of a particle due to a collision. The electric and magnetic fields ($\mathbf{E}$ & $\mathbf{B}$) in equation (2.9) are the macroscopic fields, i.e. those arising large-scale collective phenomena. The distinction between these and the microscopic fields will be clarified shortly. Equation (2.9) can be simplified by noting that the variables $\mathbf{r}$ and $\mathbf{v}$ are independent as are $\mathbf{v}$ and the acceleration (the $\mathbf{v} \times \mathbf{B}$ term is dependent on the velocity, but its i^{th} component does not depend on v_i). The VFP equation may be written in gradient form.

$$\frac{\partial f}{\partial t} + \mathbf{v} \cdot \nabla_{\mathbf{r}} f - \frac{e}{m_e} (\mathbf{E} + \mathbf{v} \times \mathbf{B}) \cdot \nabla_{\mathbf{v}} f = -\nabla_{\mathbf{v}} \cdot \left[f \frac{\langle \mathbf{\Delta v} \rangle}{\Delta t} \right] + \frac{1}{2} \nabla_{\mathbf{v}} \nabla_{\mathbf{v}} : \left[f \frac{\langle \mathbf{\Delta v} \mathbf{\Delta v} \rangle}{\Delta t} \right] \tag{2.10}$$

The terms on the left-hand side of this equation are the Vlasov terms. They describe the advection of particles in phase space. Note that the acceleration term (the third term) involves macroscopic forces. The terms on the right-hand side are

the collisional terms – these describe the change in the distribution function due to collisional effects, i.e. microscopic forces. The quantities $\langle \mathbf{\Delta v} \rangle$ and $\langle \mathbf{\Delta v \Delta v} \rangle$ are the averages over velocity of combinations of the change in the particles velocity due to a collision ($\mathbf{\Delta v}$). The reason why collisional effects can be split from macroscopic forces can be understood through the concept of Debye shielding. The idea that plasmas can shield out charge imbalances if they have a frequency below the plasma frequency has already been mentioned; there is an analogous condition which states that a plasma may also shield charge imbalances occurring on spatial scales smaller than the Debye length (λ_D). This is given by:

$$\lambda_D = \left(\frac{\epsilon_0 k_b T_e}{n_e e^2} \right)^{1/2} \tag{2.11}$$

A charge imbalance created at a point in the plasma will create a microscopic electric field which cannot penetrate beyond a sphere with radius λ_D (the Debye sphere). This leads to the concept of quasi-neutrality ($Zn_i = n_e$, where n_i is the ion density) – charge imbalances in plasmas are very small as Debye shielding is so effective, so the plasma is almost neutral on length scales larger than the Debye length and time scales longer than the inverse of the plasma frequency. The responses of electrons to microscopic charge perturbations within the Debye sphere are known as collisions, fields coming from outside this sphere result in the macroscopic forces just described. This separation of effects is only valid for weakly coupled plasmas. These are plasmas in which the average thermal energy of the electrons is much larger than the average electrostatic potential energy between electrons a distance of λ_D apart.

$$\frac{e^2}{\epsilon_0 \lambda_D k_b T_e} = \frac{1}{n_e \lambda_D^3} << 1 \tag{2.12}$$

This is equivalent to demanding that there are many electrons in the Debye sphere. Obviously, if there were few then Debye shielding would not work.

Consider the force term in the Liouville equation (2.8). This is due to the fields $\mathbf{E}_N$ and $\mathbf{B}_N$ – the electric and magnetic fields resulting from the positions and velocities of all the N particles. The difference between these fields and the macroscopic and collisional terms in the VFP equation shows the second important difference between the VFP and Liouville equations – the first being that the VFP treatment deals with the statistically averaged distribution function instead of the exact N-particle distribution. The fields $\mathbf{E}$ and $\mathbf{B}$ are the average macroscopic fields, these are the fields that act over scales larger than the Debye length and are generated by collective phenomena. Contrastingly, microscopic fields are generated within the Debye sphere

and so are only significant between a limited number of particles. $\mathbf{E}_N$ and $\mathbf{B}_N$, by contrast, are the micro-fields from all the particles. In this way the VFP equation requires significantly less computation to solve numerically.

As an aside, note that the PIC model is collisionless. The macroparticles only respond to the macroscopic fields. It is possible to include collisions in PIC via random Monte-Carlo interactions between macroparticles [17]. The difficulty here lies in doing enough collisions to get accurate statistics and this model has yet to be adequately tested against classical transport theory. The VFP equation includes a good model for the collisions and so is the preferred method for kinetic simulations of long-pulse experiments where collisions are important.

2.2.2 Collisions – the Rosenbluth potentials

The quantities $\langle \mathbf{\Delta v} \rangle$ and $\langle \mathbf{\Delta v \Delta v} \rangle$ are defined by [3]:

$$\langle \mathbf{\Delta v} \rangle = \frac{1}{\Delta t} \int \psi(\mathbf{v}, \mathbf{\Delta v}) \mathbf{\Delta v} \mathrm{d}(\mathbf{\Delta v}) \tag{2.13}$$

$$\langle \mathbf{\Delta v \Delta v} \rangle = \frac{1}{\Delta t} \int \psi(\mathbf{v}, \mathbf{\Delta v}) \mathbf{\Delta v \Delta v} \mathrm{d}(\mathbf{\Delta v}) \tag{2.14}$$

$\psi(\mathbf{v}, \mathbf{\Delta v})$ is the probability that in a time Δt an electron travelling with velocity $\mathbf{v}$ will get deflected by an amount $\mathbf{\Delta v}$. The quantities in the angled brackets give the averages of the deflection $\mathbf{\Delta v}$ and the dyadic product $\mathbf{\Delta v \Delta v}$. To evaluate these quantities consider the interaction, via the Coulomb force, between a particle of mass m_α with initial velocity $\mathbf{v}_\alpha$ and a 'scatterer' with mass m_β and initial velocity $\mathbf{v}_\beta$. This situation is shown in figure 2.4. A small difference in initial impact parameter δb gives rise to the particle scattering by $\delta\theta$ less – i.e. it scatters into a different solid angle $\delta\Omega$.

On integrating over solid angle of the scattered particle, and assuming that small angle collisions dominate the scattering – this is valid for a weakly coupled plasma – the following expressions for $\langle \Delta \mathbf{v} \rangle$ and $\langle \Delta \mathbf{v} \Delta \mathbf{v} \rangle$ are arrived at [18]:

$$\frac{\langle \Delta \mathbf{v} \rangle}{\Delta t} = \Gamma \frac{\partial H}{\partial \mathbf{v}} \qquad \frac{\langle \Delta v_i \Delta v_j \rangle}{\Delta t} = \Gamma \frac{\partial^2 G}{\partial v_i \partial v_j} \qquad \Gamma = \frac{Z_\alpha^2 e^4}{4\pi\epsilon_0^2 m_\alpha^2} \mathsf{ln}\Lambda_{\alpha\beta} \tag{2.15}$$

The Coulomb logarithm ($\mathsf{ln}\Lambda_{\alpha\beta}$) is given by the logarithm of the Debye length divided by the impact parameter for ninety degree scattering for collisions between particles of species α and β (or the de Broglie wavelength of particle α if this is larger).

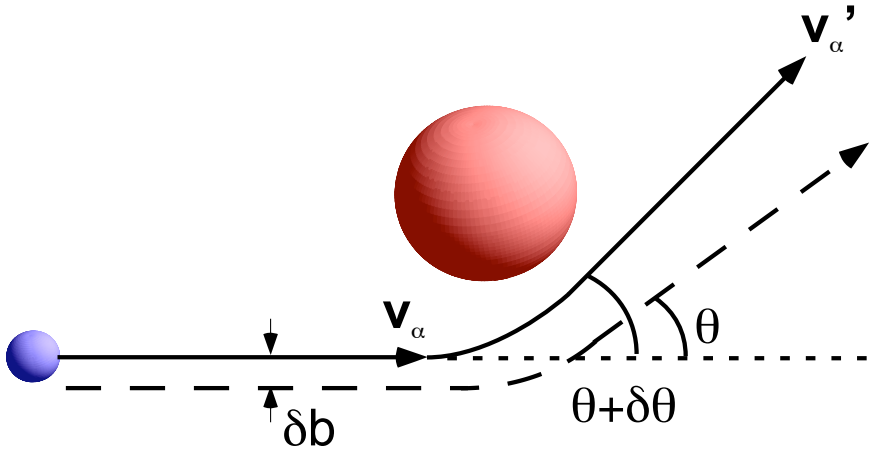

Figure 2.4: A sketch of the collision between the ‘scattered’ particle (blue) and the ‘scattering’ particle (red).

The ‘scattered’ particle has been denoted by α and the ‘scatterer’ by β. Therefore, Z_α refers to the charge of the scattered particles. The functions $H(\mathbf{v})$ and $G(\mathbf{v})$ are known as the Rosenbluth potentials and are given by [18]:

$$H(\mathbf{v}_\alpha) = \sum_\beta Z_\beta^2 \left(\frac{m_\alpha + m_\beta}{m_\beta}\right) \int \frac{f_\beta(\mathbf{v}_\beta)}{|\mathbf{v}_\alpha - \mathbf{v}_\beta|} \mathrm{d}\mathbf{v}_\beta \tag{2.16}$$

$$G(\mathbf{v}_\alpha) = \sum_\beta Z_\beta^2 \int |\mathbf{v}_\alpha - \mathbf{v}_\beta| f_\beta(\mathbf{v}_\beta) \mathrm{d}\mathbf{v}_\beta \tag{2.17}$$

These functions depend on the distribution function of the scatterers f_β. Substitution into the VFP equation yields:

$$\frac{\partial f_\alpha}{\partial t} + \mathbf{v} \cdot \nabla_\mathbf{r} f_\alpha - \frac{e}{m_e} (\mathbf{E} + \mathbf{v} \times \mathbf{B}) \cdot \nabla_\mathbf{v} f_\alpha = -\Gamma \nabla_\mathbf{v} \cdot (f_\alpha \nabla_\mathbf{v} H) + \frac{\Gamma}{2} \nabla_\mathbf{v} \nabla_\mathbf{v} : (f_\alpha \nabla_\mathbf{v} \nabla_\mathbf{v} G) \tag{2.18}$$

For simplicity it will be assumed that the scattered particles are electrons and the scatterers are either other electrons or a single species of ion with charge Z. The subscript α will be dropped. The dominance of small angle collisions in deriving these forms for the Rosenbluth potentials can be seen clearly by considering the impact parameter for a binary Coulomb collision (between a stationary ion and an electron moving with speed v) [19]:

$$b = \frac{Ze^2}{4\pi\epsilon_0 m_e v^2} \mathsf{cot}\left(\frac{\theta}{2}\right) \approx \frac{Ze^2}{2\pi\epsilon_0 m_e v^2 \theta} \tag{2.19}$$

The second equality has been achieved by making the small angle approximation. In this case the smaller the angle of deflection in the collision (θ), the larger the impact parameter. Therefore, small angle collisions are much more likely.

2.2.3 The cartesian tensor expansion

To make progress in solving equation (2.18), the electron distribution function is expanded in the cartesian tensors. An n^{th} order cartesian tensor is of rank n and is given by the direct product of n velocity unit vectors ($\hat{\mathbf{v}}$). The distribution function is then expanded as follows [20, 21]:

$$f(\mathbf{v}, \mathbf{r}, t) = \sum_{l=0}^{\infty} f_l(v, \mathbf{r}, t)\ (\cdot)^l\ \hat{\mathbf{v}}^l \tag{2.20}$$

Here f_l is a rank l tensor and is a function of the magnitude of the velocity only (v). The symbol $(\cdot)^l$ represents contraction over l indices. The result of the contraction in equation (2.20) is always a scalar. Terms where l is greater than unity are neglected [22]. Thus the form of the expansion is:

$$f(\mathbf{v}, \mathbf{r}, t) = f_0(v, \mathbf{r}, t) + \mathbf{f}_1(v, \mathbf{r}, t) \cdot \hat{\mathbf{v}} \tag{2.21}$$

The isotropic part of the distribution function (in velocity space) is described by f_0, this part of the distribution function describes the number density and temperature of the plasma at a point. $\mathbf{f}_1$ describes the anisotropy which leads to heat flow and electric current. Half of what is known as the diffusive approximation has been made. The full diffusive approximation involves not only neglecting all terms involving $\underline{\underline{f}}_2$ and higher, but also neglecting electron inertia terms ($\partial \mathbf{f}_1 / \partial t$ – the correspondence of which to the electron inertia will be shown in section 3.4.2). This term is retained. Velocity space is described in spherical polar coordinates (v, θ, ϕ). The f_0 term in equation (2.21) is angularly isotropic in velocity space. The $\mathbf{f}_1$ term is anisotropic. To describe finer scale angular variation than this would require retaining more terms in the expansion.

Substitution of the expanded distribution function, in equation (2.21), into the VFP equation (2.10), yields the following two equations [20, 22]:

$$\frac{\partial f_0}{\partial t} + \frac{v}{3}\nabla_{\mathbf{r}} \cdot \mathbf{f}_1 - \frac{(e/m_e)}{3v^2}\frac{\partial}{\partial v}\left(v^2 \mathbf{E} \cdot \mathbf{f}_1\right) = \frac{\nu'_{ee}}{v^2}\frac{\partial}{\partial v}\left[C(f_0)f_0 + D(f_0)\frac{\partial f_0}{\partial v}\right] \tag{2.22}$$

$$\frac{\partial \mathbf{f}_1}{\partial t} + v\nabla f_0 - \frac{e\mathbf{E}}{m_e}\frac{\partial f_0}{\partial v} - \frac{e}{m_e}(\mathbf{B} \times \mathbf{f}_1) = -\nu_{ei}\mathbf{f}_1 \tag{2.23}$$

Equation (2.22) is known as the f_0 equation and equation (2.23) as the $\mathbf{f}_1$ equation. As discussed previously, the right-hand sides have been obtained by considering the velocity deflection of an electron due to many small angle Coulomb collisions, a two particle collision mediated by Coulomb forces, to obtain $\langle \mathbf{\Delta v} \rangle$ and $\langle \mathbf{\Delta v \Delta v} \rangle$. In equation (2.22) only the effects of electron-electron collisions have been considered. The evolution of f_0 here describes electron energy equilibration, which primarily depends on energy exchange between electrons. Electrons may exchange energy much more easily with each other than with the ions due to the ions much larger mass. The constant ν'_{ee} and the operators C and D acting on f_0 account for the effect of electron-electron collisions. Conversely, the magnitude and direction of $\mathbf{f}_1$, which describes anisotropies in the electron's velocities, depends on angular scattering rates. Such scattering is strongly increased when the charge of the scatterer is large; therefore the ions are much more effective at angular scattering than the electrons in the limit of high ionic charge (Z). Neglecting electron-electron collisions in the $\mathbf{f}_1$ equation is known as the Lorentz approximation.

The following relations define the symbols in the f_0 and $\mathbf{f}_1$ equations:

$$\nu_{ei} = \frac{YZ^2 n_i \mathsf{ln}\Lambda_{ei}}{v^3} \qquad \nu'_{ee} = Y\mathsf{ln}\Lambda_{ee} \qquad Y = 4\pi\left(\frac{e^2}{4\pi\epsilon_0 m_e}\right)^2$$

$$C(f_0) = 4\pi\int_0^v f_0(u, \mathbf{r}, t)u^2 \mathrm{d}u \qquad D(f_0) = \frac{4\pi}{v}\int_0^v u^2\left[\int_u^\infty f_0(v', \mathbf{r}, t)v' \mathrm{d}v'\right]\mathrm{d}u$$

2.2.4 Fluid models

The models described so far have been kinetic models; they have retained the position and velocity information about the particles (albeit in a statistically averaged form). The commonly used magnetohydrodynamic model is a fluid model – it does away with the velocity-space information of the particle distribution. In fact in fluid models the velocity distribution is prescribed to be Maxwellian. The equations solved by MHD are simply the conservation equations for mass, momentum and energy of an

indivisible fluid (in conjunction with Maxwell's equations). Often the model includes other effects such as radiation or ionisation dynamics, in fact part of its utility is in the fact that including such effects is relatively straightforward. The fluid equations can be derived from the VFP equation by taking various velocity averages (velocity moments) – this is discussed in more detail in section 3.4.1. However, the mass, momentum and energy equations derived in this way do not form a closed system. Specifically an equation is required for the heat flow. This can be derived analytically if the distribution function is close to a Maxwellian. The result is the classical heat flow equation. This and the classical Ohm's law (similarly derived) form classical transport theory.

If the particles are highly collisional, i.e. they collide many times over the length and time scales of interest, classical theory works well. However, the most interesting laser-plasma interactions often take place in the partially collisional regime: i.e. where collisions are not important for some particles. This can be seen by considering the expression for the mean free path in a plasma (for electron-ion collisions) [19].

$$\lambda_{ei} = \frac{v^4}{YZ^2 n_i \mathsf{ln}\Lambda_{ei}} \qquad Y = 4\pi \left(\frac{e^2}{4\pi\epsilon_0 m_e}\right)^2 \tag{2.24}$$

The dependence of this on the fourth power of the particles speed means that hot (fast) particles are much less collisional than cold (slow) ones. Thus in long pulse LPI there is usually always some population of electrons which are not very collisional.

2.2.5 The definition of λ, τ, ω and r_L

The mean free path given in equation (2.24) is the distance over which an electron moves before being scattered by ninety degrees by many small-angle collisions with ions. The corresponding collision time is given by:

$$\tau_{ei} = \frac{v^3}{YZ^2 n_i \mathsf{ln}\Lambda_{ei}} \tag{2.25}$$

τ_{ei} depends on the velocity of the particle, it will be beneficial to define an average collision time. The convention which is used in most of this thesis is to define this average to be the collision time for electrons moving with the thermal speed ($v_T^2 = 2k_b T_e/m_e$). Unless otherwise stated this is the collision time (and corresponding mean free path) represented by τ_{ei}. Braginskii used a different convention, where the mean averaged velocity was used (averaged over the the distribution, which was assumed to be Maxwellian). This will be denoted as τ_B. The two are related by:

$$\tau_B = \frac{3\sqrt{\pi}}{4}\tau_{ei} \tag{2.26}$$

The gyro-frequency of an electron (ω) is given by:

$$\omega = \frac{eB}{m_e} \tag{2.27}$$

The radius of this gyration is given by the Larmor radius (r_L):

$$r_L = \frac{m_e v_\perp}{eB} \tag{2.28}$$

The speed $v_\perp$ is that of the gyrating electron perpendicular to the field line. Again, an average value is often required. The Larmor radii calculated in this thesis are those for electrons gyrating with the thermal speed. The quantity $\omega\tau$ is known as the Hall parameter (or the magnetisation); this quantity tells us how many times an electron moving with the thermal speed collides with an ion in one gyration. It is therefore a measure of the relative importance of the magnetic field and collisions.

2.3 Classical transport theory

The transport relations used to close the MHD equations are given by the classical transport theory first derived by Braginskii [23]. The classical Ohm's law and heat flow equation are given by [24, 25]:

$$\frac{e}{m_e}\mathbf{E} = -\frac{\nabla P_e}{m_e n_e} - \frac{e}{m_e}\mathbf{j}\times\mathbf{B} + \underline{\underline{\alpha}}^c \cdot \frac{\mathbf{j}}{n_e e} - \underline{\underline{\beta}}^c \cdot \frac{\nabla T_e}{m_e} \tag{2.29}$$

$$\mathbf{q}_e = -\frac{n_e k_b T_e \tau_B}{m_e}\underline{\underline{\kappa}}^c \cdot \nabla T_e - \underline{\underline{\beta}}^c \cdot \frac{\mathbf{j} T_e}{e} \tag{2.30}$$

Here $\underline{\underline{\alpha}}^c$, $\underline{\underline{\beta}}^c$ and $\underline{\underline{\kappa}}^c$ are the classical transport coefficients. The electron pressure is given by P_e, the current by $\mathbf{j}$ and the heat flow by $\mathbf{q}_e$. The most important terms in these equations (at least for the results presented later) are those proportional to $\underline{\underline{\beta}}^c \cdot \nabla T_e$ (in Ohm's law) and $\underline{\underline{\kappa}}^c \cdot \nabla T_e$ (in the heat flow equation). The components of these terms perpendicular to the B-field and the temperature gradient are responsible for the Nernst effect and the Righi-Leduc heat flow respectively. When discussing Froula's experiment in chapter 5 it will be shown that the Nernst term dominates magnetic field advection for all imposed fields. The Righi-Leduc heat flow will become very large as the imposed magnetic field increases – up to ten times the size of the

heat flow parallel to ∇T_e. Equations (2.29) and (2.30) are derived by taking moments of the f_0 and $\mathbf{f}_1$ equations (neglecting electron inertia). The isotropic part of the distribution function f_0 is assumed to be a Maxwellian. The break down of this assumption is what leads to classical transport theory not being valid. The variation of the transport coefficients with the Hall parameter ($\omega\tau$) are shown in figure 2.5 – the reason why $\omega\tau$ is crucial to transport is explained in section 2.3.1. The transport coefficients also vary with Z. The red curves are for $Z = 1$, the pink for $Z = 7$ and the blue are valid as Z approaches infinity (the Lorentz approximation).

The transport coefficients in equations (2.29) and (2.30) – i.e. $\underline{\underline{\alpha}}^c$, $\underline{\underline{\beta}}^c$ and $\underline{\underline{\kappa}}^c$ – are in dimensionless form and as such are only functions of the Hall parameter. These are related to the dimensional coefficients by:

$$\underline{\underline{\alpha}} = \frac{m n_e \underline{\underline{\alpha}}^c}{\tau_B} \qquad \underline{\underline{\beta}} = \underline{\underline{\beta}}^c \qquad \underline{\underline{\kappa}} = \frac{n_e k_b T_e \tau_B \underline{\underline{\kappa}}^c}{m_e} \tag{2.31}$$

In a magnetized plasma the B-field provides a unique axis whereby transport is different parallel to this axis as compared to perpendicular to it. Thus the components of the transport coefficients are described with reference to the magnetic field and the driving force behind the transport. Therefore:

$$\underline{\underline{\phi}} \cdot \mathbf{s} = \phi_\parallel \mathbf{b}(\mathbf{b} \cdot \mathbf{s}) + \phi_\perp \mathbf{b} \times (\mathbf{s} \times \mathbf{b}) \pm \phi_\wedge \mathbf{b} \times \mathbf{s} \tag{2.32}$$

$\underline{\underline{\phi}}$ is a general transport coefficient, $\mathbf{s}$ is the driving force and $\mathbf{b}$ is the unit vector in the direction of the B-field. In the case of the resistivity $\underline{\underline{\alpha}}$ the sign of the last term is negative and the driving force is the current $\mathbf{j}$. For the thermoelectric tensor $\underline{\underline{\beta}}$ and thermal conductivity $\underline{\underline{\kappa}}$ the sign is positive and the driving force is the electron temperature gradient ∇T_e.

It should be noted that there is an alternative way in which to express the transport equations. This is the formulation used by Shkarofsky, Bernstein and Robinson [26]. In this case equations are provided for the current ($\mathbf{j}$) and total heat flow ($\mathbf{q}_T$).

$$\mathbf{j} = \underline{\underline{\sigma}} \cdot \left(\mathbf{E} + T_e \frac{\nabla n_e}{n_e e} \right) + \underline{\underline{\tau}} \cdot \nabla T_e \tag{2.33}$$

$$\mathbf{q}_T = -\underline{\underline{\mu}} \cdot \left(\mathbf{E} + T_e \frac{\nabla n_e}{n_e e} \right) + \underline{\underline{\mathsf{K}}} \cdot \nabla T_e \tag{2.34}$$

The transport coefficients here are: the electrical conductivity tensor $\underline{\underline{\sigma}}$, the ther-

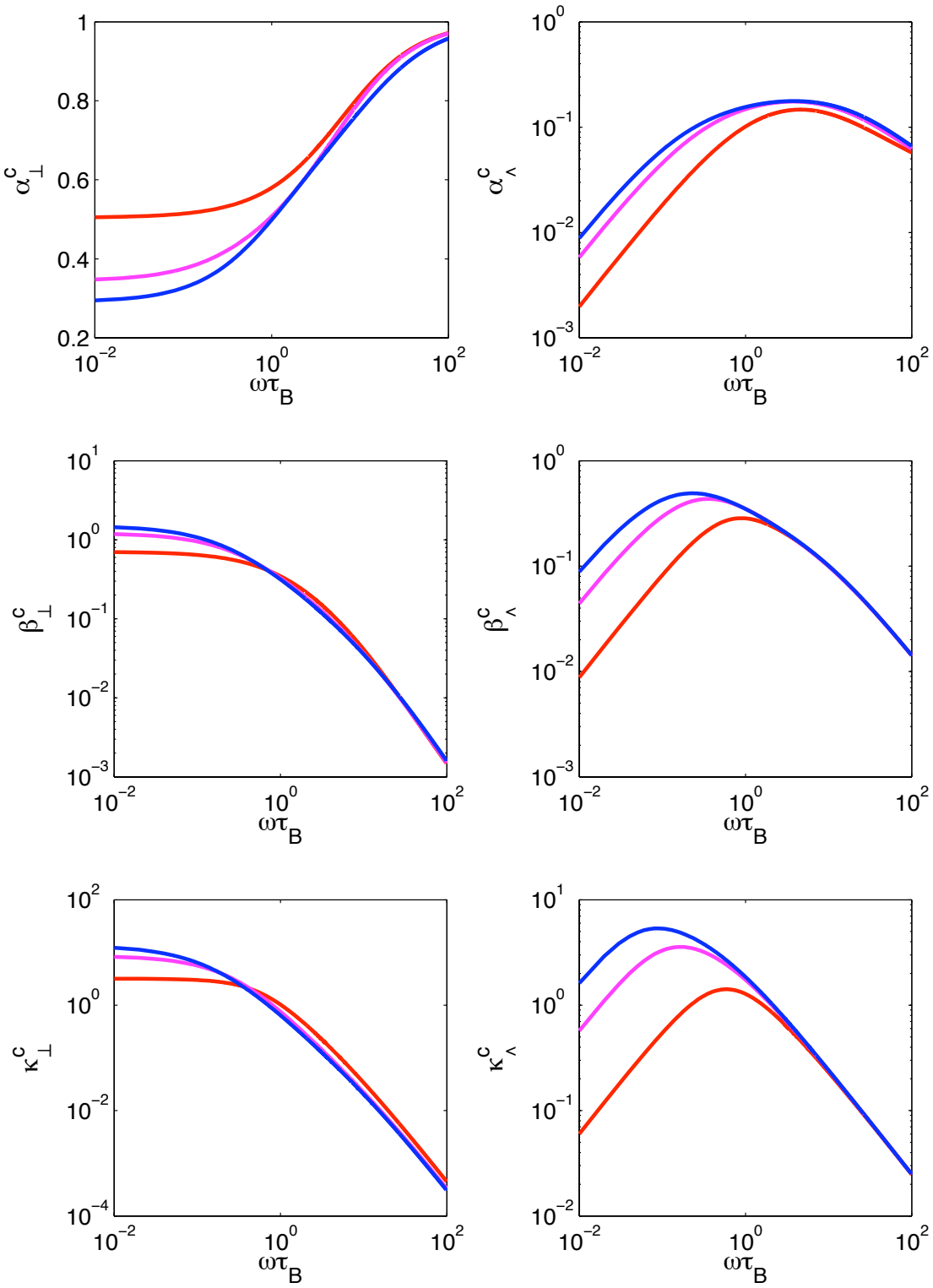

Figure 2.5: The variation of the dimensionless transport coefficients with Hall parameter. The red curves are for $Z = 1$, the pink for $Z = 7$ and the blue is valid as Z approaches infinity.

moelectric tensor $\underline{\tau}$, the energy conductivity tensor $\underline{\underline{\mu}}$ and the thermal diffusion tensor $\underline{\underline{\mathsf{K}}}$. Note that the total heat flow is that including the electron's average velocity – the thermal heat flow is given by the random velocity only. The relationship between these is [25]:

$$\mathbf{q}_T = \mathbf{q} - \mathbf{j}\left(\frac{5/2P_e}{n_e e} + \frac{1/2 m_e n_e C_e'^2}{n_e e}\right) \tag{2.35}$$

Where C_e' is the average electron velocity. The formulation of Epperlein & Haines will be employed here almost always. This is because it gives the thermal heat flow, which is usually required in MHD to close the equations, and $\mathbf{E}$, which gives $\partial\mathbf{B}/\partial t$ (using Faraday's law) and so determines the B-field dynamics.

2.3.1 The effect of magnetic fields on (classical) transport

The equation for the evolution of the electron's internal energy per unit mass ϵ_e as a result of thermal conduction perpendicular to the B-field (but parallel to the cross-field temperature gradient) is:

$$\frac{\partial \epsilon_e}{\partial t} = -\nabla \cdot (\kappa_\perp \nabla T_e) \tag{2.36}$$

This can be rearranged (assuming quasi-neutrality):

$$\frac{\partial T_e}{\partial t} = -\frac{(\gamma-1)m_i}{Z k_b}\nabla \cdot \left(\frac{n_e k_b T_e \tau_B}{m_e}\kappa_\perp^c \nabla T_e\right) = \nabla \cdot (D_\perp \nabla T_e) \tag{2.37}$$

This is a diffusion equation with diffusion constant $D_\perp$. In this equation γ is the ideal gas constant ($\gamma = 5/3$) and m_i is the ion mass. In the limits of weak and strong magnetic field:

$$\kappa_\perp^c \approx \kappa_\parallel^c \qquad \omega\tau << 1 \tag{2.38}$$

$$\kappa_\perp^c \approx \frac{\gamma_1'}{(\omega\tau_B)^2} \qquad \omega\tau >> 1 \tag{2.39}$$

γ_1' is a constant whose value is given in appendix A (for $Z = 7$). Substituting the results from equations (2.38) and (2.39) into (2.37) yields expressions for the diffusion constant in the strong and weak field limits:

$$D_\perp \propto \frac{\lambda_{ei}^2}{\tau_{ei}} \qquad \omega\tau << 1 \tag{2.40}$$

$$D_\perp \propto \frac{r_L^2}{\tau_{ei}} \qquad \omega\tau >> 1 \tag{2.41}$$

In general, the diffusion constant is given by the ratio of the square of the characteristic diffusion length to the characteristic diffusion time. In the weak B-field limit this length is the mean-free path. If the Hall parameter is large, i.e. in the case of strong magnetic fields, then the particles gyrate around the magnetic field lines many times before colliding. In this case the gyro-radius and not the collisional mean free path becomes the step-length that controls the thermal transport perpendicular to the field – the transport parallel to the field is unaffected. In this case $r_L << \lambda_{ei}$ and so transport is suppressed. In fact, if r_L controls the transport the mobility of the hot electrons is more strongly curtailed than the colder ones. This can be seen from the fact that the Larmor radius scales with velocity much more gently than the mean free path: $r_L \propto v$ and $\lambda \propto v^4$. This is the reason why magnetic fields suppress non-locality as discussed later.

Magnetic fields do not just affect thermal transport. Figure 2.5 shows that all the transport coefficients are dependent on the Hall parameter and so on the magnetic field. This dependence can be expressed using the approximate polynomial fits derived by Epperlein & Haines [25]. These polynomials are given in appendix A. They are only in error by a maximum of 15% and so give the most convenient way to calculate the classical transport coefficients; in fact the transport coefficients in figure 2.5 have been calculated in this way. Two of these will be important to later discussions and so should be considered in more detail.

$$\beta_\wedge^c = \frac{\omega\tau_B(\beta_1''\omega\tau_B + \beta_0'')}{(\omega\tau_B)^3 + b_2''(\omega\tau_B)^2 + b_1''\omega\tau_B + b_0''} \tag{2.42}$$

$$\kappa_\perp^c = \frac{\gamma_1'\omega\tau_B + \gamma_0'}{(\omega\tau_B)^3 + c_2'(\omega\tau_B)^2 + c_1'\omega\tau_B + c_0'} \tag{2.43}$$

The values of constants $\beta_0'', \beta_1'', b_0'', b_1'', b_2'', \gamma_0', \gamma_1', c_0', c_1'$ and c_2' (for $Z = 7$) are given in appendix A along with the fits to the rest of the components of the transport coefficients. The limiting cases of the conductivity component $\kappa_\perp$ have been discussed. The regime of intermediate $\omega\tau$ will be of the most interest; in this case equation (2.43) can be used. Equation (2.42) is useful as the Nernst effect is crucially dependent on

this transport coefficient and will be shown to play an important role in magnetic field advection in long-pulse LPI in chapter 5.

2.3.2 Classical magnetic field generation

Large (mega-gauss strength) magnetic fields have been observed in laser-solid target interactions. These are believed to be generated by the '$\nabla n_e \times \nabla T_e$' (or thermoelectric) mechanism. This mechanism can be understood simply by considering part of the classical Ohm's law already discussed (the term proportional to ∇P_e) and Faraday's law:

$$\frac{\partial \mathbf{B}}{\partial t} = -\frac{k_b}{e n_e} \nabla n_e \times \nabla T_e \tag{2.44}$$

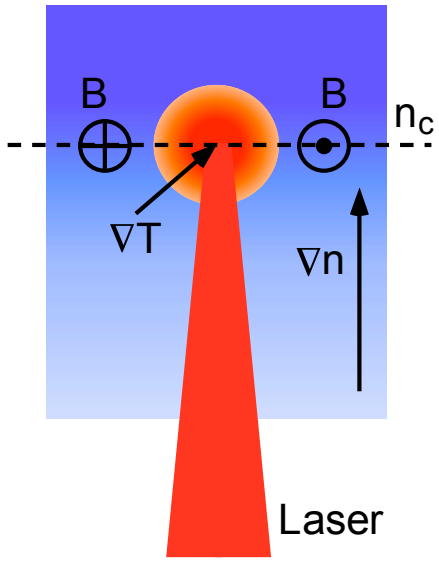

Figure 2.6: The generation of magnetic fields by the thermoelectric mechanism in laser-plasmas.

Figure 2.6 illustrates how this mechanism typically operates in laser-plasma interactions. When a laser is shone into a plasma ablating from a solid target it encounters a density gradient as shown. The laser deposits its energy around the critical density – by exciting plasma waves in the process of resonance absorption – and generates temperature gradients towards the laser-heated region. Such a plasma then has temperature and density gradients which are not parallel; these generate azimuthal B-fields as shown.

The first high-strength B-fields generated by this mechanism in laser-plasmas were measured by Stamper *et al* in 1971 [27]. Field strengths of several kilogauss were measured in the interaction between a neodymium-glass laser – delivering 60J in 1ns. Larger fields were later observed closer to the laser focal region in such interactions, with field strengths reaching 1MG [28, 29]. Experimental and numerical data found that these fields could only be generated by the thermoelectric method [30, 31]. Megagauss fields have also been observed in short-pulse laser-solid interactions [32]; thus high-strength magnetic fields are ubiquitous in solid density LPI. Such interactions are of obvious relevance to ICF – particularly indirect drive – thus B-fields should be included in ICF modelling. Glenzer *et al* demonstrated, through the comparison

between experiments and fluid simulations, that large B-fields are generated at the hohlraum wall and advected into the gas-fill [11].

It is possible to use a reduced model of collisions in the plasma to derive a simple equation for the rate of change of the magnetic field. Haines has shown that under certain conditions the electron-ion collision frequency may be modelled as $\nu_{ei} \propto v^{-2}$ instead of the realistic $\nu_{ei} \propto v^{-3}$ [33]. In this case the following simplified equation for $\partial\mathbf{B}/\partial t$ may be derived:

$$\begin{aligned}\frac{\partial \mathbf{B}}{\partial t} =& \nabla \times \left(\mathbf{C} \times \mathbf{B} - \frac{\mathbf{j} \times \mathbf{B}}{n_e e} \right. \\ & \left. + \frac{\nabla P_e}{n_e e} + \frac{\nabla T_e}{e} + \frac{2\mathbf{q}_e \times \mathbf{B}}{5P_e} - \eta \mathbf{j} \right)\end{aligned} \tag{2.45}$$

η is the resistivity. The important terms for the work presented later in the thesis are as follows. The second term, describes frozen-in flow – i.e. advection of the B-field with the bulk flow velocity $\mathbf{C}$. The thermoelectric term ($\nabla P_e/n_e e$) is responsible for the '$\nabla n_e \times \nabla T_e$' magnetic field generation. The term $\eta\mathbf{j}$ describes diffusion of magnetic field as a result of the plasma not being a perfect conductor – known as resistive diffusion. Finally, the Nernst term ($\propto \mathbf{q}_e \times \mathbf{b}$) acts to advect the B-field with the heat flow – as will be described in more detail in section 5.4. It has been shown that equation (2.45) is accurate to approximately 5% for plasmas with moderate Z – in the range from 3-8 – and for any Hall parameter [33]. Note the plasmas later investigated fall into this range, with $Z = 7$.

The equation for $\partial\mathbf{B}/\partial t$ using the correct collision model may be derived using Ohm's law as given in equation (2.29). Expressing the transport coefficients in their components, for example ($\alpha^c_{\parallel}$,$\alpha^c_{\perp}$,$\alpha^c_{\wedge}$), yields Ohm's law in the form [33, 34]:

$$\begin{aligned}\mathbf{E} + \mathbf{C} \times \mathbf{B} = & -\frac{\nabla P_e}{n_e e} + \frac{\alpha_{\parallel}}{n_e^2 e^2}\mathbf{b}(\mathbf{b} \cdot \mathbf{j}) + \frac{\alpha_{\perp}}{n_e^2 e^2}\mathbf{b} \times (\mathbf{j} \times \mathbf{b}) - \frac{\alpha_{\wedge}}{n_e^2 e^2}(\mathbf{b} \times \mathbf{j}) \\ & - \frac{\beta_{\parallel}}{e}\mathbf{b}(\mathbf{b} \cdot \nabla T_e) - \frac{\beta_{\perp}}{e}\mathbf{b} \times (\nabla T_e \times \mathbf{b}) - \frac{\beta_{\wedge}}{e}(\mathbf{b} \times \nabla T_e)\end{aligned} \tag{2.46}$$

Similarly the heat flow equation (2.30) can be broken down:

$$\mathbf{q}_e = -\kappa_\parallel \mathbf{b}(\mathbf{b}\cdot\nabla T_e) - \kappa_\perp \mathbf{b}\times(\nabla T_e \times \mathbf{b}) - \kappa_\wedge(\mathbf{B}\times\nabla T_e) - \frac{\beta_\parallel T_e}{e}\mathbf{b}(\mathbf{b}\cdot\mathbf{j}) - \frac{\beta_\perp T_e}{e}\mathbf{b}\times(\mathbf{j}\times\mathbf{b}) - \frac{\beta_\wedge T_e}{e}(\mathbf{b}\times\mathbf{j}) \quad (2.47)$$

Taking the vector product of the heat flow equation (2.47) with the unit vector in the direction of the magnetic field ($\mathbf{b}$); making $\nabla T_e \times \mathbf{b}$ the subject of this equation and then eliminating it from equation (2.46); yields the rate of change of the magnetic field as [33]:

$$\frac{\partial \mathbf{B}}{\partial t} = \nabla\times\left\{(\mathbf{C}\times\mathbf{B}) - \frac{\mathbf{j}\times\mathbf{B}}{n_e e}\left[1+\frac{1}{\omega_e\tau_e}\left(\alpha_\wedge^c - \frac{\beta_\wedge\beta_\perp}{\kappa_\perp^c}\right)\right] + \frac{\nabla P_e}{n_e e} + \frac{\beta_\parallel}{e}\nabla_\parallel T_e + \left(\beta_\perp + \frac{\beta_\wedge\kappa_\wedge}{\kappa_\perp}\right)\frac{\nabla_\perp T_e}{e} + \frac{\beta_\wedge}{e\kappa_\perp}\mathbf{q}_e\times\mathbf{b} - \frac{\alpha_\parallel}{n_e^2e^2}\mathbf{j}_\parallel - \left(\frac{\alpha_\perp}{n_e^2e^2} - \frac{\beta_\wedge^2 T_e}{e^2\kappa_\perp}\right)\mathbf{j}_\perp\right\} \quad (2.48)$$

The important terms already mentioned take on a very similar form in this more complicated equation.

2.3.3 B-field generation by other mechanisms

The equation for $\partial\mathbf{B}/\partial t$, i.e. equation (2.48), was derived neglecting several effects. Firstly, it was assumed that high frequency effects from the laser fields, as discussed by Haines [33], could be ignored. This is justified by the fact that the laser period is of the order of 1fs – this is much shorter than the time-periods which will be simulated and can thus be ignored. Additionally, the time-averaged effects of the high frequency field, such as the ponderomotive force, may be neglected as the laser intensities considered are low.

The derivation outlined in section 2.3.2 used the assumption that the distribution function was close to a Maxwellian. If this is not true, i.e. if $|\mathbf{f}_1|$ is not small compared to f_0, then more terms must be retained in the Cartesian tensor expansion. This makes the derivation of an analytical solution for $\partial\mathbf{B}/\partial t$, such as that outlined in the last section, impossible. However, if the electron distribution can be approximated by a beam of 'fast' particles and a Maxwellian background of 'slow' ones then the following approximation may be used [35]:

$$\frac{\partial \mathbf{B}}{\partial t} = \nabla \times (\eta \mathbf{j}_f) \tag{2.49}$$

The fast electron current is $\mathbf{j}_f$. The plasmas considered in this thesis will be close to isotropic (not close to Maxewellian as f_0 may take any form) and so this effect need not be considered.

Magnetic fields may be generated in the process of resonant absorption of laser light [36]. However, it has already been shown that such absorption is not important in the simulations considered here; additionally, this process only generates large B-fields (of the order of 1MG) when the laser intensity is greater than $10^{16}\mathrm{Wcm}^{-2}$ – this is a factor of 100 larger than the intensities simulated here. Magnetic fields may also be generated by anisotropic radiation pressure [37] or anisotropic pressure [38]. By neglecting terms in $\underline{\underline{f}}_2$ the pressure is forced to be isotropic in the model used here.

Finally, if the laser light is circularly polarised then laser photons may deposit their angular momentum directly into the plasma, this may then generate a magnetic field [39]. In which case:

$$\frac{\partial \mathbf{B}}{\partial t} = \frac{1}{r}\frac{\partial}{\partial r}\left(\frac{\beta r}{n_e e \omega_L L}\frac{\partial I}{\partial r}\right) \tag{2.50}$$

The distance r is from the centre of the laser spot, β is the fraction of laser energy absorbed over a distance L. For a Gaussian intensity profile this is maximised on the laser axis. A field of only 10^{-12}T would be produced in one nanosecond by a laser with maximum intensity of $10^{15}\mathrm{Wcm}^{-2}$ (e-folding distance of 75μm), and a frequency of $10^{15}\mathrm{s}^{-1}$, in a plasma with an electron density of $10^{19}\mathrm{cm}^{-3}$. This mechanism is much more important for high intensity lasers. Another (more well established) mechanism by which a laser may directly induce a magnetic field in the plasma is by the inverse Faraday effect. The B-field comes directly from the curl of the lasers electric field. Magnetic fields of several mega-gauss have been measured from the mechanism [40]. The laser intensity required to do this was of the order of $10^{19}\mathrm{Wcm}^{-2}$ – much higher than dealt with here. This mechanism can safely be ignored.

2.4 The break-down of classical transport

Classical transport theory ceases to be valid when the distribution function is strongly non-Maxwellian. There are many processes which can cause this to happen, some of which will be briefly described here. Following this the most important of these processes in the LPI considered in this thesis will be discussed in more detail.

Non-local transport

When the scale-length of a macroscopic physical quantity (examples – temperature, density) is not much greater than the mean free path of the particles which transport the quantity most effectively, then non-local transport becomes important. As an example, the temperature scale-length L_T, in the x-direction, is given by:

$$L_T = \left(\frac{1}{T} \frac{\partial T}{\partial x} \right)^{-1} \tag{2.51}$$

Consider non-local heat flow: when the temperature scale-length becomes less than 100 times the mean free path of electrons moving with the thermal speed, non-locality is important [41]. In this case electrons with speeds 2-3 times the thermal velocity will have a mean free path comparable to the scale-length (mean free path scales with speed to the fourth power). Electrons moving at such speeds are of particular interest as they carry most of the heat. From equation (2.24) it can be seen that the mean-free path increases strongly with speed; but the number of particles at this speed generally decreases more rapidly. Two or three times the thermal speed represents the optimum speed below which the collisional mean free path is too small and above which there are too few particles to effectively transport heat. Strongly non-local heat flow causes the distribution function to become non-Maxwellian. The faster (hotter) electrons have longer mean free paths than the slower (colder) ones; thus non-locality can lead to a depletion of hot electrons in one region and an excess in another region.

The criterion imposed on the scale-length is actually only applicable to non-linear transport. This is a sub-set of non-local transport – the transport becomes non-linear when the gradients of the physical variables become very steep (This is equivalent to the scale-length getting small). Steep gradients are not a requisite for non-locality to be important. It has been shown that in the case of a small temperature perturbation, which can have a long scale-length, that the wavelength determines whether the transport is non-local [42]. Additionally, this discussion has not included the effects of magnetic fields.

Inverse bremsstrahlung

It has already been discussed that inverse bremsstrahlung is the process by which laser energy is absorbed by under-dense plasmas at low intensities ($\approx 10^{14}\mathrm{Wcm}^{-2}$) – as opposed to resonance absorption in over-dense plasmas. This mechanism preferentially heats the slower electrons and so leads to the distribution function tending

towards a Langdon distribution, i.e.: $f_0 \propto e^{-v^5}$ [43].

Collisions with neutral molecules in an electric field

A similar distribution is obtained when the collision of electrons with neutral molecules under the influence of an electric field are considered – for example in a plasma discharge. In this case it can be shown that the distribution function is described by the Druyvestyn distribution ($f_0 \propto e^{-v^4}$) [20].

Ionization

Various ionization processes operate in plasmas, which do not necessarily result in a Maxwellian distribution of electrons. Mechanisms which can be important at high intensities are multi-photon ionization – where several photons are absorbed by a neutral particle; and direct field ionization – the electric field of the laser is strong enough to rip electrons from the neutrals directly. At the lower intensities considered here collisional ionization is the dominant process, a free electron collides with an ion and increases its ionization state (or ionizes a neutral particle). Whether ionization occurs depends on whether the incident, ionizing, electron has energy greater than the ionization energy. The newly liberated electrons are initially 'cold'; the injection of these low-velocity particles distorts the distribution (as does the opposite process of recombination). The distortion depends on the ionization energy; this is a material dependent property which complicates matters [44].

2.4.1 Non-local transport

Two of the processes described will be discussed in this thesis – namely non-local transport and inverse bremsstrahlung. In fully ionised long-pulse laser plasma interactions these two are the dominant causes of the break down of classical transport. Non-locality is important in laser-plasmas when the effective delocalisation length ($\sqrt{\lambda_{ei}\lambda_{ee}}$ – λ_{ee} is the mean free path for electron-electron collisions) becomes equal to 0.01 times the laser spot radius. This limitation on the validity of classical theory was predicted by several independent numerical solutions to the VFP equation [45–48]. The fact that such a combination of mean-free paths determines the importance of non-locality [49, 50] may be understood by considering the following factors: it was shown in section 2.3.1 that classical transport is controlled by λ_{ei} (in the absence of B-fields) and so one might expect this to affect the degree of distortion of the distribution functions also; electron-electron collisions will act to return the distribution

function to Maxwellian so the shorter λ_{ee} the less important non-locality should be.

In the situation where nonlocal effects are dominant classical transport theory can predict un-physically large heat flows – i.e. greater than the heat flow if all the electrons are streaming directly down the temperature gradient (the free-streaming limit). This free-streaming heat flow ($\mathbf{q}_F$) is given by:

$$\mathbf{q}_F = \frac{1}{2} n_e m_e v_T^3 \frac{\nabla T_e}{|\nabla T_e|} \tag{2.52}$$

Attempts have been made to overcome this problem by arbitrarily limiting the heat flux to some fraction of the free-streaming limit, by using a flux-limiter (f) when classical theory predicts it to be un-physically large [51]. This can be done a variety of ways, the most common is to blend the classical heat flow $\mathbf{q}_B$ and the flux-limiter multiplied by the free-streaming heat flow $\mathbf{q}_F$ in the following manner [19] (in the absence of a magnetic field):

$$\mathbf{q} = -\left[\left(\frac{1}{|\mathbf{q}_B|}\right)^n + \left(\frac{1}{f|\mathbf{q}_F|}\right)^n\right]^{-1/n} \frac{\nabla T_e}{|\nabla T_e|} \tag{2.53}$$

Alternatively some degree of non-locality can be included in fluid models by using a convolution method to calculate the heat flux [48]. This represents the heat flux, in one dimension, as:

$$q(x) = \int_{-\infty}^{\infty} W(x, x') q_B(x') dx' \tag{2.54}$$

Where q_B is the Braginskii heat flow. The problem with using a flux-limiter or convolution function to circumvent non-locality is that the choice of f or W is somewhat arbitrary – if they are to be useful these methods must be calibrated against experimental data or a fully kinetic (i.e. VFP) theory. This has been done in a limited number of situations [52–59]; however, there is no simple way of including the full effect of non-locality in classical MHD.

The effect of non-locality on the thermal conductivity (in the absence of magnetic fields) is shown in figure 2.7. The analytical expression for the non-local thermal conductivity plotted in this figure was derived by Bell [42]. In order to do this the VFP equation was linearised. The distribution function was written as:

$$f = f_m + \sum_{n=0}^{\infty} f_n P_n e^{i(kx - \omega t)} \tag{2.55}$$

Where P_n are the Legendre polynomials – this is the equivalent expansion to the

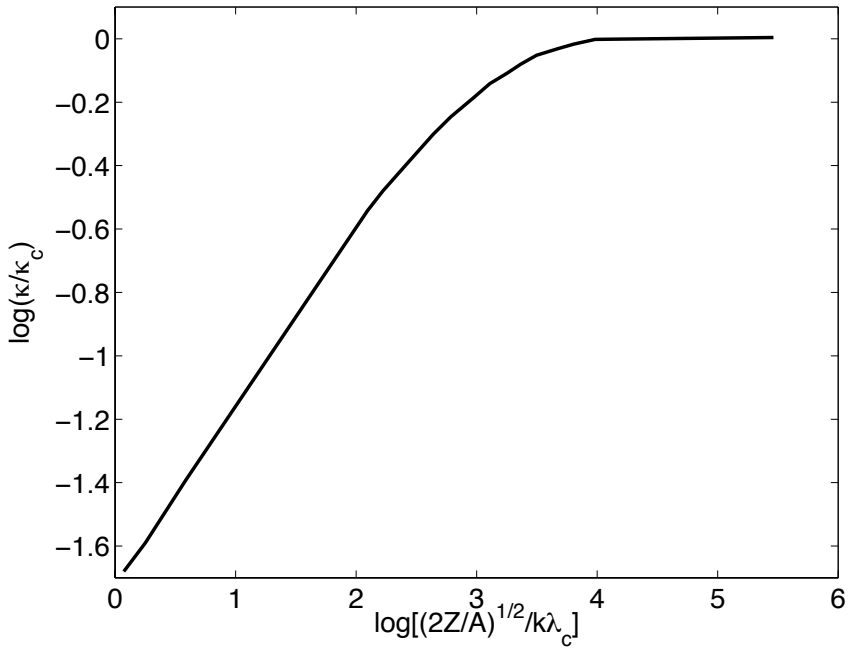

Figure 2.7: The ratio of the thermal conductivity from the linearised non-local theory to the classical thermal conductivity. Note that for classical conductivity $\log(\kappa/\kappa_c) = 0$.

spherical harmonics in the absence of B-fields and when the spatial gradients are in one direction only. Linearised theories rely on the fact that any perturbations from equilibrium are small; terms second-order in perturbed quantities can then be ignored. In the this case the anisotropy is small, but the deviation from Maxwellian is not. The spatial variation of the distribution function is set to be that for a wave (an ion-wave), i.e. $e^{i(kx-\omega t)}$. Therefore, this is a linear theory for wave motion in the plasma. Figure 2.7 shows the ratio of the thermal conductivity to the classical conductivity against the ratio of λ/λ_c (λ is the wavelength of the ion wave. k is its wavevector, λ_c is the collisional mean free path and is proportional to λ_{ei}). This shows that as λ/λ_c gets smaller non-local effects become more important and the conductivity decreases below the classical value (κ_c). The reason for this decrease is that non-locality leads to strong flow of the 'hot', i.e. less collisional, electrons away from any hot regions and into colder ones ahead of the classically predicted heat front [42,45,46,49,60,61]. The thermal conductivity is suppressed in regions where the temperature is high due to the depletion of the tail of the distribution and high in colder regions due to it's enhancement. The non-local dispersion relation was also derived for these waves. It shows a significant divergence from the classically derived dispersion relation. This implies that hydrodynamic ion-motion and non-locality can affect one another – this

is an important motivation for developing the improved code described in chapter 4.

2.4.2 The effect of magnetic fields on non-locality

So far the concept of non-locality has been discussed in the absence of magnetic fields. Not only can large magnetic fields reduce transport, they can also act to re-localise it. The important parameter for the suppression of non-locality is again the Hall parameter. If the Larmor radius is much smaller than the thermal mean free path and any scale-lengths of interest then non-locality is not important. If the Hall parameter is sufficiently large transport is localised no matter how large λ_{ed}. The intermediate regime where magnetic fields and non-locality are important is still poorly understood.

The effects of magnetic fields on non-local transport have been considered in several situations. Kho & Haines discussed the effect of non-locality on magnetic field advection (due to the Nernst effect) using 1D VFP simulations [62]. Luciani, Mora & Bendib also investigated this analytically and numerically using a convolution method [52]. This work was extended recently to show that simulations of recent laser-solid target experiments agreed best when both B-fields and non-locality were included in the model [55,59]. An entirely non-local mechanism for the self-generation of magnetic fields has been proposed analytically and corroborated with 2D VFP simulations (using IMPACT) [63] – this will be described in more detail in section 2.4.4 and its relevance to B-field generation by elliptical laser-spots in chapter 7. Linearised theories of non-local transport in the presence of magnetic fields have been expounded by Brantov *et al* [64]. Alternatively, noting that the fluid equations solve for the first three velocity moments of the distribution function, non-classical effects may be included by solving for higher moments [65]. As the number of moments (n) retained gets larger then the distribution function is more accurately represented; as n tends to infinity then the full distribution is retained. This can be understood by noting that the most important limitation of fluid theory – as discussed in section 2.2.4 – is that to close the set of equations the classical heat flow equation is used, this assumes that the distribution function is close to a Maxwellian. If this hypothetical infinite number of moment equations were used there would be no need for closure and such a fluid theory would work as well as VFP [66]. A fully kinetic VFP treatment of long-pulse LPI including the effects of self-generated fields and plasma motion is clearly missing from the previous work and forms the subject of this thesis.

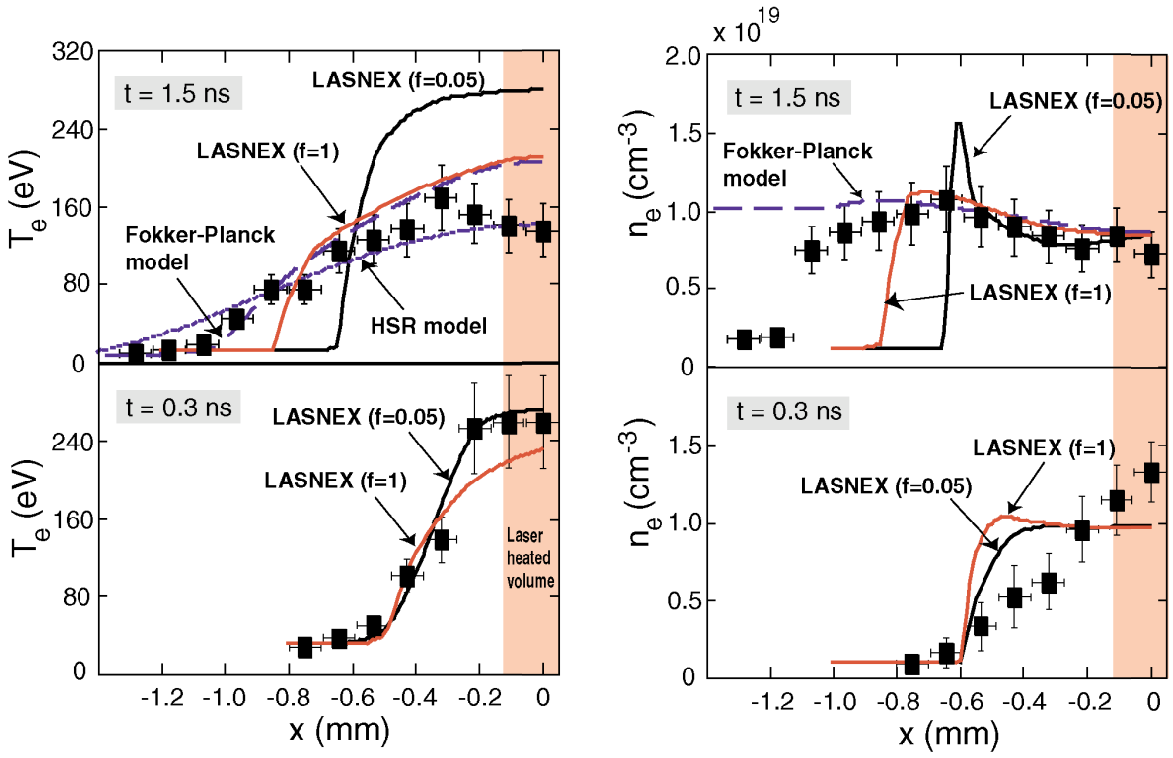

Figure 2.8: Electron temperature profiles at two times (reproduced with the author's permission). The variable x refers to distance from the centre of the gas jet backwards relative to the direction of the laser propagation. The value of f is the flux-limiter. Note the time dependence of the flux-limiter.

2.4.3 Experimental measurements of the importance of non-locality

Non-local transport is not merely a theoretical curiosity, it has been observed to be important in many experimental long pulse laser-plasma interactions. The first experimental observations to definitively show the importance of non-locality in nanosecond laser-plasma interactions were made in 1975 [67]. These experiments involved the interaction of a CO_2 laser ($\lambda_L = 10.6\mu$m, $I = 3 \times 10^{10}$Wcm^{-2}) with a z-pinch produced plasma. This, along with several follow-up experiments [41, 68, 69] showed that the thermal conductivity was significantly reduced due to non-local effects. Although the plasma was approximately 100 times more tenuous compared to those considered here ($n_e = 8 \times 10^{16}$cm^{-3}).

Gregori *et al* measured the electron temperature and number density profiles in the interaction between a nitrogen gas-jet (initial density $n_e = 1.5 \times 10^{19}$cm^{-3}) and a nanosecond neodymium-glass laser beam (with an intensity of 1.5×10^{14}Wcm^{-2} and

wavelength $\lambda = 1.054\mu$m). To determine the importance of non-locality the profiles for n_e and T_e (taken after 0.3ns and 1.5ns) were compared to fluid simulations (using LASNEX which has a flux-limited heat flow model), Fokker-Planck simulations and hot spot relaxation (HSR) simulations. These results are shown in figure 2.8. HSR refers to a fluid model which captures some of the non-local transport effects by using a convolution formula for the heat flux, as in equation (2.54). Gregori *et al* observed that using a Fokker-Planck model or the HSR model gave better agreement than the fluid LASNEX model at later times. At early times LASNEX gave good agreement, so the other models were not shown in the early time plots. The fully Fokker-Planck simulation gave the best agreement; the conclusion drawn from this by Gregori *et al* was that non-locality was dominating the transport of heat. Furthermore the flux-limiter required by LASNEX was found to be strongly time-dependent.

A similar comparison between Fokker-Planck, fluid theory and experiment was made by Hawreliak *et al*. This was done for the interaction between six neodymium-glass lasers and a solid aluminium foil [70]. The combined focal spot intensity of all the lasers was $3 \times 10^{14}\text{Wcm}^{-2}$. the experimental temperature profiles agreed best with those from the Fokker-Planck code IMPACT rather than the fluid code. Taken together, these experiments show that non-locality is important in a wide range of long-pulse LPI.

Recently the nitrogen-gas jet experiment described previously has been repeated with the introduction of an externally applied magnetic field (and an intensity of 10^{15}Wcm^{-2}); the intention being to measure its suppression of non-locality [12]. The external magnet could provide a field of up to 12T. Such a B-field strength was deemed enough to re-localise transport through kinetic simulations with no magnetic field and using LASNEX including B-fields. The experiment just described will be simulated using the new kinetic code developed here – the results of which are presented and discussed in chapter 5 – particular interest will be taken in the intermediate B-field regime which has not been well characterised. These simulations will lead into the first comprehensive discussion of the temporal evolution of the coupling between non-locality and magnetic field dynamics in these types of laser-plasma interactions.

2.4.4 Non-local magnetic field generation

The equation for the evolution of the magnetic field (2.48) is only valid if the distribution function is close to Maxwellian. This is not the case in many important laser-plasma experiments. Kingham & Bell have formulated a non-classical theory of

magnetic field generation [63,71]. This was a perturbative theory valid for a magnetic field initially growing up from zero. Therefore, they considered a simpler form of the $\mathbf{f}_1$ equation than used in the classical analysis, i.e.:

$$\tilde{v}\tilde{\nabla}\tilde{f}_0 + \tilde{\mathbf{E}}\frac{\partial \tilde{f}_0}{\partial \tilde{v}} = -\frac{\hat{Z}^2\tilde{n}_i}{\tilde{v}^3}\tilde{\mathbf{f}}_1 \tag{2.56}$$

Note the variables in the above equation are normalised. The exact normalisations are unimportant here but will be given in chapter 4 – normalised variables will be denoted by the tilde, for example as $\tilde{X}$. Electron inertia has been ignored (the $\partial\mathbf{f}_1/\partial t$ term) and it is assumed there is no initial magnetic field. By taking the current moment – i.e. $\int_0^\infty ...v^3\mathsf{d}v$ – and setting $\mathbf{j} = 0$ Ohm's law was derived as in equation (2.57). Setting the current to zero in this way is valid if the plasma remains quasi-neutral because initially there is no magnetic field.

$$\tilde{\mathbf{E}} = -\frac{\nabla(\tilde{n}_e\langle\tilde{v}^5\rangle)}{6\tilde{n}_e\langle\tilde{v}^3\rangle} \tag{2.57}$$

Where:

$$\langle\tilde{v}^m\rangle = \frac{4\pi}{\tilde{n}_e}\int_0^\infty \tilde{f}_0\tilde{v}^{m+2}\mathsf{d}\tilde{v} \tag{2.58}$$

Ohm's law is left in terms of moments of the distribution function; i.e. its integral in velocity space. The fact that these correspond to familiar physical variables such as number density, bulk flow velocity and temperature will be discussed in section 3.4.1. Usually such an identification is made when the distribution function has some specified form, in order to clarify that that the distortion of the distribution is arbitrary in our case the description remains one explicitly in terms of moments. From this Ohm's law, Faraday's law gives the rate of change of the magnetic field ($\underline{\tilde{\omega}}$) as:

$$\frac{\partial\underline{\tilde{\omega}}}{\partial\tilde{t}} = \frac{\nabla\left(\tilde{n}_e\langle\tilde{v}^5\rangle\right)\times\nabla\left(\tilde{n}_e\langle\tilde{v}^3\rangle\right)}{6\left(\tilde{n}_e\langle\tilde{v}^3\rangle\right)^2} \tag{2.59}$$

Equation (2.59) is the generalised expression for the thermoelectric magnetic field generation term already discussed several times so far. Further progress can be made with this formulation by calculating the moment in equation (2.58) for a Maxwellian distribution.

$$\langle\tilde{v}^m\rangle_M = \Gamma\left(\frac{m+3}{2}\right)\frac{2^{m/2+1}}{\sqrt{\pi}}\tilde{T}_e^{m/2} \tag{2.60}$$

Where $\Gamma(n)$ is the gamma function whose properties are briefly discussed in appendix F. On substitution of this result into equation (2.59) the standard '$\nabla n_e \times \nabla T_e$' mechanism is recovered. If f_0 is not Maxwellian a whole host of new generation mechanisms are introduced, one such mechanism will now be described. On enforcing that $\langle v^m \rangle = \langle v^m \rangle_M$ *but* $\partial \langle v^m \rangle / \partial t \neq \partial \langle v^m \rangle_M / \partial t$ an early time model is derived for the non-local magnetic field generation rate [63,71]. Note that the previous assumption makes physical sense – the plasma is initially in equilibrium with a Maxwellian distribution, the model describes the small deviation from this at early times. This model predicts magnetic field generation in a plasma with no density gradients. This early-time seed magnetic field is given by:

$$\underline{\tilde{\omega}}\bar{\tau} = -\frac{1}{2}\left(\frac{\tilde{t}}{\bar{\tau}_{ei}}\right)^2 \frac{\tilde{\nabla}\tilde{T}_e}{\tilde{T}_e} \times \left[154\frac{\tilde{\nabla}(\tilde{\nabla}^2\tilde{T}_e)}{\tilde{T}_e} + 620\frac{|\nabla\tilde{T}_e|^2}{\tilde{T}_e{}^2}\right]\frac{\bar{\lambda}_{ei}^4}{6\pi\sqrt{2}} \tag{2.61}$$

Note that this expression is derived by assuming that the temperature profile is constant and as such is only valid for the first few collision times. The barred variables are those for the local plasma conditions instead of the global 'normalising' conditions. In section 7.1.3 this formula will be useful for predicting the early-time seed to non-locally generated magnetic fields by an elliptical laser spot.

2.4.5 Inverse bremsstrahlung

The second important effect leading to distortion of the distribution function is inverse bremsstrahlung. The fact that IB heating tends to cause the distribution function to become a Langdon distribution can be shown by a consideration of reduced forms of the f_0 and $\mathbf{f}_1$ equations [43]). Considering the 1D form of the $\mathbf{f}_1$ equation, neglecting magnetic fields and electron-electron collisions yields:

$$\frac{\partial f_0}{\partial t} = \frac{eE}{m_e}\frac{1}{3v^2}\frac{\partial}{\partial v}\left(v^2 f_1\right) \tag{2.62}$$

$$\frac{\partial f_1}{\partial t} = \frac{eE}{m_e}\frac{\partial f_0}{\partial v} - \frac{\nu'_{ei}}{v^3} f_1 \tag{2.63}$$

If the electric field driving the anisotropy in the distribution function is harmonically varying with the laser frequency ω_L, i.e. $\mathbf{E} = \mathbf{E}_0 e^{-i\omega_L t}$ then the anisotropy itself must vary in this manner. In this case it is possible to express f_1 as:

$$f_1(v) = \frac{ieE_0}{m_e\omega}\left(1 + \frac{i\nu'_{ei}}{\omega_L v^3}\right)^{-1}\frac{\partial f_0}{\partial v} \tag{2.64}$$

Here: $\nu'_{ei} = \nu_{ei} v^3$. After assuming that the collisional term in the above equation is small – i.e. $\nu_{ei}/\omega_L << 1$ – this is substituted into the f_0 equation. This then gives the solution (where time is represented by t):

$$f_0 = \left(\frac{6}{5\nu'_{ei} v_{osc}^2 t}\right)^{3/5} \exp\left[-\frac{1}{5}\left(\frac{6}{5\nu'_{ei} v_{osc}^2 t}\right) v^5\right] \tag{2.65}$$

However, if the effects of electron-electron collisions are included than the distribution function will lie somewhere between a Langdon and a Maxwellian. In this case the distribution function is given by the more general super-Gaussian [72–74], i.e.:

$$f_0^{SG} = C(m)\frac{n_e}{v_T^3} e^{-(v/\alpha_e v_T)^m} \tag{2.66}$$

Here $\alpha_e = [3\Gamma(3/m)/2\Gamma(5/m)]^{1/2}$ and $C(m) = m/4\pi\alpha_e^3\Gamma(3/m)$. m varies between 2 and 5. Note that 'super-Gaussian' is the term used to describe any distribution that goes as e^{-v^m} with $m > 2$. How closely the value of m gets to five is quantified by the following formula (derived by fitting numerical results from VFP simulations, in the absence of B-fields and transport, by Matte *et al* [74]):

$$m = 2 + \frac{3}{1 + \frac{1.66}{\alpha^{0.724}}} \qquad \alpha = Z\frac{v_{osc}}{v_T} \tag{2.67}$$

Here α is the Langdon parameter, as this tends to infinity then m tends to five. It is clear that as v_{osc} increases, i.e. as the laser becomes more intense, m increases from two to five. Increasing Z has the same effect. For larger Z the electron-ion scattering rate increases and more of the laser's quiver energy is thermalised and so the rate of collisional heating is greater.

To date no direct experimental measurement of the importance of the super-Gaussian distribution has been made. However, simulations have shown that the distortion of the distribution function can affect X-ray emission in LPI [74] and non-local transport [75–77]. It has also been shown that although the super-Gaussian distribution gives the best fit to the bulk of the electron distribution, when electron-electron collisions are considered it does not work well in the tail [78] – a Maxwellian often gives a better fit here. The electrons in the tail of the distribution can seriously affect transport properties, which could be an important effect. Non-locality will only exacerbate this problem – in some regions the tail will be enhanced, in others depleted. An investigation of the simultaneous action of inverse bremsstrahlung and non-locality on the distribution function will be presented in chapter 5, and the transport theory for a super-Gaussian in chapter 6.

Chapter 3

Ion hydrodynamics in the VFP equation

3.1 The importance of ion hydrodynamics

Previous IMPACT simulations treated the ions as a stationary neutralizing background. However, ion motion is expected to be very important in nanosecond LPI. An estimate of the importance of ion-motion and examples of experiments where it is crucial will be discussed here. The task of including such motion in a VFP treatment will be simplified by justifying a fluid treatment of the ions.

3.1.1 A simple estimate of hydrodynamics' importance

A first justification of the inclusion of ion motion may be made by showing that a significant degree of hydrodynamic plasma flow is expected in a typical NIF hohlraum. As a simple first estimate the ablation velocity can be approximated to the ion acoustic speed (c_s), so that the ablation distance x_a in the time t_a is given by:

$$x_a = c_s t_a = \left(\frac{\gamma k_b T_e}{m_i}\right)^{1/2} t_a \tag{3.1}$$

Here, γ is the ideal gas constant ($\gamma = 5/3$). A conservative estimate for the electron temperature achievable near the wall in a NIF hohlraum is 1keV. Considering a pulse duration of five nanoseconds, the ablation distance is estimated to be 2mm. The hot-spot size on the wall of a NIF hohlraum is of the order of one millimetre [7]. Ion fluid effects are therefore expected to travel a significant distance over the pulse

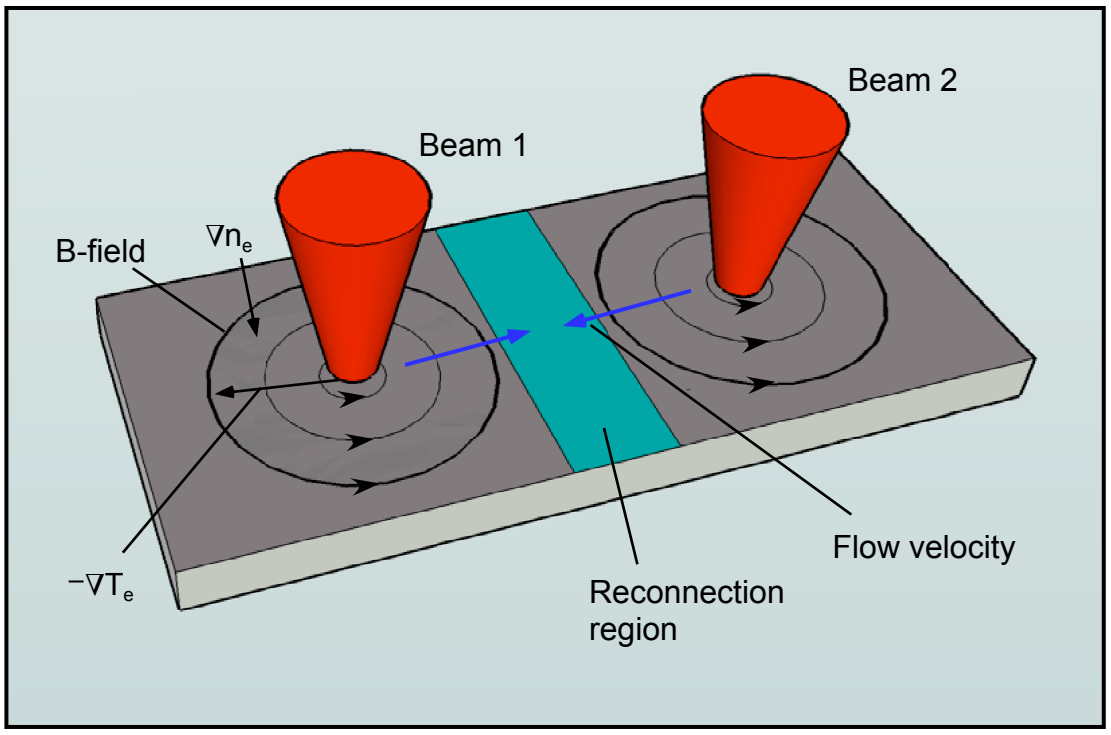

Figure 3.1: A schematic of the two-beam experiment.

duration, and therefore ion hydrodynamics should play an important role.

3.1.2 Ion motion is crucial in long-pulse laser-plasma interactions

Perhaps a more important consideration than the amount of hydrodynamic flow that will occur is the effect of this flow. Ion flow is thought to be important in hohlraums; such flow is predicted to advect magnetic fields produced at the hohlraum wall into the gas-fill plasma [7, 11]. Indeed this effect, as well as non-uniform plasma flows, could modify the x-ray symmetry of the hohlraum. In order to model a direct-drive ICF implosion one must clearly include ion-motion, a full VFP treatment of this including magnetic fields has yet to be done. The inclusion of hydrodynamics is crucial to understanding the interplay of magnetic field dynamics and non-local transport in these situations.

The recent experiment by Froula *et al* (which was discussed in section 2.4.1) was designed to investigate the effect of an externally applied B-field on non-locality in long-pulse LPI. The coupling between the importance of non-locality and magnetic

field dynamics (controlled by hydrodynamic flow in Froula's analysis) in the presence of moderate B-fields is poorly understood. These two effects are also of interest to laser-solid target experiments where the intention is to characterise the B-field profile [79, 80], or measure such effects as reconnection in the high energy density regime [81, 82]. Figure 3.1 shows a schematic of the first experiment where such reconnection was inferred [81]. Two long-pulse laser beams illuminated a solid target (either aluminium or gold) the resulting temperature and density gradients in the plasma then generated a magnetic field by the '$\nabla n_e \times \nabla T_e$' mechanism. These fields were orientated azimuthally around each laser spot as shown in figure 3.1. The fields were then advected away from the laser spots leading to compressed fields with opposite orientations close together – a situation in which magnetic reconnection might be expected. Indeed this was postulated to be responsible for anomalous heating in the marked 'reconnection region'. The B-field was assumed to be frozen into the plasma and as such hydrodynamic plasma expansion was thought crucial in getting the B-field from where it was generated to the reconnection region – later the possibility that the Nernst effect may be responsible for the advection of the B-field will be explored. The plasma was also observed to form fast moving jets in the reconnection region – clearly the inclusion of bulk plasma motion is essential to conducting simulations pertinent to this experiment.

3.1.3 Justification for a hydrodynamic model

Having demonstrated the importance of ion motion the way in which it is to be modelled must now be considered. In long-pulse LPI a fluid treatment is justified. It has already been argued that fluid treatments break down when non-local transport becomes important. To show that this is not the case for the ions, consider the ratio of the ion-ion to the electron-ion collisional mean free paths (for electrons and ions moving with their thermal speeds [3]).

$$\frac{\lambda_{ii}}{\lambda_{ei}} = \frac{1}{Z^2}\left(\frac{T_i}{T_e}\right)^2 \frac{\mathsf{ln}\Lambda_{ei}}{\mathsf{ln}\Lambda_{ii}} \tag{3.2}$$

This ratio will usually be smaller than unity. For the plasmas considered here $Z = 7$ – recall that the Lorentz approximation requires it to be larger than unity. The factor $1/Z^2$ is then 0.02. The factor $(T_i/T_e)^2$ is expected to be less than one. This ratio depends on the fact that laser energy heats the electrons first which later come into thermal equilibrium with the ions due to their much higher inertia. The ion temperature is expected to be less than the electron temperature over relatively

long time-scales. The weak dependence on temperature in the Coulomb logarithms ($\ln\Lambda_{ei}/\ln\Lambda_{ii}$) has been ignored. The time-scale over which this temperature equilibration is expected to take place is dependent on the ratio of the electron-ion and electron-electron energy exchange times. The energy exchange time τ^E_{AB} is the time taken for the change in the kinetic energy of particle A to equal to its original kinetic energy by collisions with particles of species B. The ratio (τ^E_{ei}/τ^E_{ii}), for thermal particles, is proportional to the mass ratio ($m_i/m_e^{1/2}$). The ions take this factor longer to equilibrate with the electrons than they do to equilibrate with each other.

It then follows that the the ion-ion thermal mean free path should be less than the electron-ion thermal mean free path. For ion non-locality to be unimportant, λ_{ii} needs to be much smaller than the length scales of the macroscopic variables. In typical long-pulse LPI a regime where λ_{ii} is significantly smaller than λ_{ei} is studied, therefore electron non-locality is important but ion non-locality is not. Additionally, for a fluid treatment to be valid the ions must be in local thermodynamic equilibrium with each other. In this case the ion's distribution function is a Maxwellian at all points in space with a different temperature at each point. The rate at which energy is transferred from the electrons to the ions is very slow compared to the rate at which it is transferred amongst the ions. Recall that the ion-ion energy equilibration time (τ^E_{ii}) is a factor of $(m_i/m_e)^{\frac{1}{2}}$ faster than the electron-ion energy equilibration time. This means the ions can much more easily equilibrate with themselves than with the electrons maintaining local thermodynamic equilibrium.

3.1.4 Some caveats

Some important effects will be lost by assuming that the ions behave as a fluid (with a Maxwellian velocity distribution). Taking the specific example of the experiment performed by Nilson *et al* (discussed in section 3.1.2), there are several ion-kinetic effects that might be important. The ion flows coming into the reconnection region are expected to interpenetrate somewhat, influencing the magnetic field. This cannot be described by a single-fluid ion model. These separate flows, while being in equilibrium with themselves will not be with each other. This is illustrated by figure 3.2. The counter-propagating beams from the two laser spots are represented by the orange ion distributions. If the beams are moving at a high velocity then even if they are Maxwellian they will be shifted by a velocity u_x. Eventually the beams would be expected to equilibrate with each other – resulting in the red ion distribution. If this takes a significant fraction of the experimental time, i.e. if the beams are moving

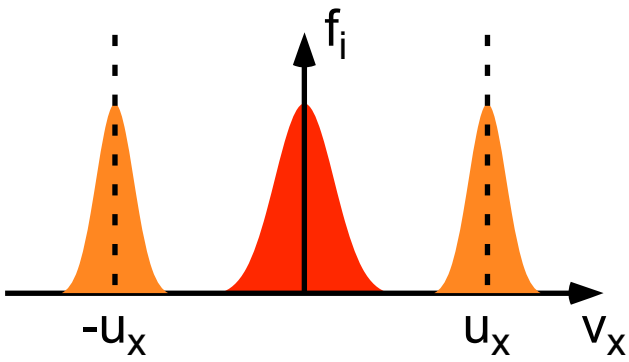

Figure 3.2: If two counter-propagating beams (moving in the x-direction) are present the ion distribution function f_i is given by two shifted Maxwellians (orange curves), instead of the single Maxwellian required for a fluid treatment to be valid (red curve).

sufficiently quickly, the fluid assumption that f_i is a single Maxwellian will break down.

Shocks were shown to occur in the reconnection region as the two plasmas met in Nilson's experiment. If one is interested in resolving the structure of such shocks then ion kinetics must be included. Shocks cannot be exactly described by a fluid treatment, although they can be approximately modelled – as discussed in appendix D.

3.2 The transformation

Now that a fluid-ion treatment has been justified, the effects of ion-motion can be included in the electron's VFP equation by transforming it into the ion's rest frame. First, recall the VFP equation:

$$\frac{\partial f}{\partial t} + \mathbf{v}\cdot\nabla_{\mathbf{r}} f + (\mathbf{a} + \mathbf{v}\times\underline{\omega})\cdot\nabla_{\mathbf{v}} f = \left(\frac{\partial f}{\partial t}\right)_{collisional} \tag{3.3}$$

$$\mathbf{a} = \frac{e\mathbf{E}}{m_e} \qquad \underline{\omega} = \frac{e\mathbf{B}}{m_e}$$

Let $\mathbf{v}$ be given by the sum of the electron velocity in the ion's rest frame $\mathbf{w}$ and the ion drift velocity $\mathbf{C}$ – this drift velocity is the average ion velocity, and is as such a function of position and time only [20]. As well as the velocity coordinate, the derivatives must be transformed. The important results are given below.

$$\mathbf{v} = \mathbf{w} + \mathbf{C}(\mathbf{r}, t) \tag{3.4}$$

$$f(\mathbf{r}, \mathbf{v}, t) = f'(\mathbf{r}, \mathbf{w}, t) \tag{3.5}$$

$$\frac{\partial f}{\partial t} = \frac{\partial f'}{\partial t} - \frac{\partial f'}{\partial w_j}\frac{\partial C_j}{\partial t} \tag{3.6}$$

$$\frac{\partial f}{\partial r_i} = \frac{\partial f'}{\partial r_i} - \frac{\partial f'}{\partial w_j}\frac{\partial C_j}{\partial r_i} \tag{3.7}$$

$$\frac{\partial f}{\partial v_i} = \frac{\partial f'}{\partial w_i} \tag{3.8}$$

Substituting these results into equation (3.3) yields equation (3.9). Note that the collisional part of the equation remains unchanged; the collision operators in the VFP equation are unaffected by the change of variables as collisions are naturally expressed in the ion's rest frame.

$$\begin{aligned}\frac{\partial f'}{\partial t} + w_i\frac{\partial f'}{\partial r_i} - (a_i + \epsilon_{kji}w_k\omega_j)\frac{\partial f'}{\partial w_i} - \frac{\partial f'}{\partial w_i}\frac{\partial C_i}{\partial t} - w_i\frac{\partial f'}{\partial w_j}\frac{\partial C_j}{\partial r_i} \\ + C_i\frac{\partial f'}{\partial r_i} - C_i\frac{\partial f'}{\partial w_j}\frac{\partial C_j}{\partial r_i} - \epsilon_{kji}C_k\omega_j\frac{\partial f'}{\partial w_i} = \left(\frac{\partial f'}{\partial t}\right)_{collisional}\end{aligned} \tag{3.9}$$

In the above equation the summation over components is implied by repeated indices. Terms involving C_i are the new ones resulting from the transformation. The relationship between the velocities $\mathbf{v}$ and $\mathbf{w}$ is shown in figure 3.3. It can be seen that in both the $(\mathbf{r}, \mathbf{v}, t)$ and $(\mathbf{r}, \mathbf{w}, t)$ coordinate systems the velocity coordinate is independent of the space and time coordinates. The diagram shows that if we know $\mathbf{r}$ and t in either frame we have no information about $\mathbf{v}$ or $\mathbf{w}$ (a velocity vector with a given magnitude can lie anywhere on a sphere in velocity space as shown).

Strictly speaking the transformation just made is not a coordinate transformation. Equation (3.9) is the VFP equation in the 'laboratory' frame. If a coordinate transformation were then made into the ion-rest frame all of the new terms would vanish, leaving the old VFP equation as solved by the previous version of IMPACT. The difficulty with solving the VFP equation in the moving frame is that such a treatment is Lagrangian (one where at every point we are following the ion-fluid). In two spatial dimensions this fluid can moving in very complicated ways – making re-mapping back

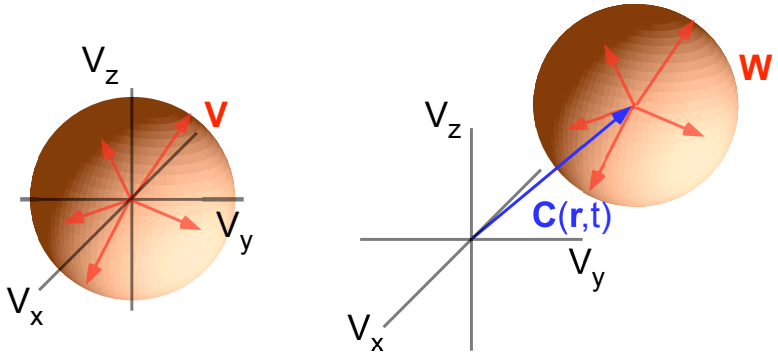

Figure 3.3: A diagrammatic representation of the transformation into the ion 'drift' frame.

onto the lab frame equally complicated. When the equation is solved numerically the spatial grid can become hopelessly tangled using such a treatment.

For these reasons an Eulerian (lab-frame based) treatment will be used here. This involves solving equation (3.9) in a fixed 2-D configuration space. The transformation made to obtain equation (3.9) is perhaps best described as a 'separation of effects transformation' where terms resulting from ion-motion have been separated from the 'standard' Vlasov terms. Not only is the Eulerian approach easier to solve numerically, but it transparently shows the effects that ion-motion has on the VFP equation. This will be important when the velocity moments of the transformed VFP equation are considered.

3.3 The cartesian tensor expansion

The distribution function must now be expanded in Cartesian tensors (described in section 2.2.3). This expansion is truncated after two terms.

$$f = f_0 + \mathbf{f}_1 \cdot \frac{\mathbf{w}}{w} \tag{3.10}$$

In the above equation the distribution function is expressed in the $(\mathbf{r}, \mathbf{w}, t)$ system but the primes have been dropped from f_0 and $\mathbf{f}_1$ for brevity. Substitution of this into equation (3.9) yields:

$$\frac{\partial f_0}{\partial t}+\frac{\partial \mathbf{f}_1}{\partial t}\cdot\frac{\mathbf{w}}{w}+\mathbf{w}\cdot\nabla_{\mathbf{r}}f_0+(w\nabla_{\mathbf{r}}\mathbf{f}_1):\frac{\mathbf{ww}}{w^2}+\frac{\mathbf{a}\cdot\mathbf{f}_1}{w}+\frac{\partial f_0}{\partial w}\mathbf{a}\cdot\frac{\mathbf{w}}{w}+\left[w\mathbf{a}\frac{\partial}{\partial w}\left(\frac{\mathbf{f}_1}{w}\right)\right]:\frac{\mathbf{ww}}{w^2}$$
$$+(\underline{\omega}\times\mathbf{f}_1)\cdot\frac{\mathbf{w}}{w}-\frac{\partial\mathbf{C}}{\partial t}\cdot\frac{\mathbf{f}_1}{w}-\frac{\partial f_0}{\partial w}\frac{\partial\mathbf{C}}{\partial t}\cdot\frac{\mathbf{w}}{w}-\left[w\frac{\partial\mathbf{C}}{\partial t}\frac{\partial}{\partial w}\left(\frac{\mathbf{f}_1}{w}\right)\right]:\frac{\mathbf{ww}}{w^2}-\left(\frac{\partial f_0}{\partial w}w\nabla_{\mathbf{r}}\mathbf{C}\right):\frac{\mathbf{ww}}{w^2}$$
$$+\left[\left(\frac{\mathbf{w}}{w}\cdot\nabla_{\mathbf{r}}\mathbf{C}\right)\right]\cdot\mathbf{f}_1-\left[w^2\nabla_{\mathbf{r}}\mathbf{C}\frac{\partial}{\partial w}\left(\frac{\mathbf{f}_1}{w}\right)\right]\vdots\frac{\mathbf{www}}{w^3}+\mathbf{C}\cdot\nabla_{\mathbf{r}}f_0+[(\mathbf{C}\cdot\nabla_{\mathbf{r}})\,\mathbf{f}_1]\cdot\frac{\mathbf{w}}{w}$$
$$-\left[(\mathbf{C}\cdot\nabla_{\mathbf{r}})\mathbf{C}\frac{\partial f_0}{\partial w}\right].\frac{\mathbf{w}}{w}-[(\mathbf{C}\cdot\nabla_{\mathbf{r}})\mathbf{C}].\frac{\mathbf{f}_1}{w}-\left\{w[(\mathbf{C}\cdot\nabla_{\mathbf{r}})\mathbf{C}]\frac{\partial}{\partial w}\left(\frac{\mathbf{f}_1}{w}\right)\right\}:\frac{\mathbf{ww}}{w^2}+\frac{(\mathbf{C}\times\omega)\cdot\mathbf{f}_1}{w}$$
$$+\left[(\mathbf{C}\times\underline{\omega})\frac{\partial f_0}{\partial w}\right]\cdot\frac{\mathbf{w}}{w}+\left[w(\mathbf{C}\times\underline{\omega})\frac{\partial}{\partial w}\left(\frac{\mathbf{f}_1}{w}\right)\right]:\frac{\mathbf{ww}}{w^2}=\left(\frac{\partial f}{\partial t}\right)_{collisional} \tag{3.11}$$

Next the above equation is multiplied by the direction cosines in velocity-space ($\mathsf{cos}\theta_j = v_j/v$) and integrated over solid angle in velocity space; this will be referred to as 'taking the angular moment'. This splits equation (3.11) into equations for the time evolution of f_0 and $\mathbf{f}_1$ (using the orthogonality of the direction cosines). To begin this procedure, consider taking angular moments of the several generic types of terms in equation 3.11. Note that summation is implied over repeated indices.

Scalar terms:

$$T_s = A(w) \tag{3.12}$$

Vector terms:

$$T_v = \mathbf{A}(w)\cdot\frac{\mathbf{w}}{w} = A_j(w)\mathsf{cos}\theta_j \tag{3.13}$$

Matrix terms:

$$T_m = \mathbf{A}(w)\mathbf{B}(w):\frac{\mathbf{ww}}{w^2} = A_i(w)B_j(w)\mathsf{cos}\theta_i\mathsf{cos}\theta_j \tag{3.14}$$

Not all terms in equation (3.11) fit into these categories. The two misfit terms below will henceforth be referred to as the 'other' terms.

$$\left[\left(\frac{\mathbf{w}}{w}\cdot\nabla_{\mathbf{r}}\mathbf{C}\right)\right]\cdot\mathbf{f}_1 \qquad \left[w^2\nabla_{\mathbf{r}}\mathbf{C}\frac{\partial}{\partial w}\left(\frac{\mathbf{f}_1}{w}\right)\right]\vdots\frac{\mathbf{www}}{w^3} \tag{3.15}$$

The following useful identity has been used to evaluate these integrals:

$$\int \mathsf{cos}^p\theta_x \mathsf{cos}^q\theta_y \mathsf{cos}^r\theta_z \mathrm{d}^2\Omega = 4\pi \frac{1.3.5...(p-1).1.3...(q-1).1.3...(r-1)}{1.3.5...(p+q+r+1)} \tag{3.16}$$

Note that this is only true if p, q and r are all even, otherwise the integral is zero.

3.3.1 The zeroth angular moment

The zeroth moment is taken by integrating equation 3.11 over solid angle. Consider the angular moments of the generic terms:

Scalar terms

$$\int T_s \mathrm{d}^2\Omega = A(w) \int \mathrm{d}^2\Omega = 4\pi A \tag{3.17}$$

Vector terms

$$\int T_v \mathrm{d}^2\Omega = A_j(w) \int \mathsf{cos}\theta_j \mathrm{d}^2\Omega = 0 \tag{3.18}$$

Matrix terms

$$\int T_m \mathrm{d}^2\Omega = A_i(w)B_j(w) \int \mathsf{cos}\theta_i \mathsf{cos}\theta_j \mathrm{d}^2\Omega = \frac{4\pi}{3}\mathbf{A}\cdot\mathbf{B} \tag{3.19}$$

Other terms

$$\int \left[\left(\frac{\mathbf{w}}{w}\cdot\nabla_{\mathbf{r}}\mathbf{C}\right)\right]\cdot\mathbf{f}_1 \mathrm{d}^2\Omega = f_{1k}\int \mathsf{cos}\theta_j \frac{\partial C_k}{\partial r_j}\mathrm{d}^2\Omega = 0 \tag{3.20}$$

$$\int \left[w^2\nabla_{\mathbf{r}}\mathbf{C}\frac{\partial}{\partial w}\left(\frac{\mathbf{f}_1}{w}\right)\right] \vdots \frac{\mathbf{www}}{w^3}\mathrm{d}^2\Omega = A_i(w)B_j(w)C_k(w)\int \mathsf{cos}\theta_i \mathsf{cos}\theta_j \mathsf{cos}\theta_k \mathrm{d}^2\Omega = 0 \tag{3.21}$$

Where:

$$\mathbf{A} = w^2\nabla_{\mathbf{r}} \qquad \mathbf{B} = \frac{\partial}{\partial w}\left(\frac{\mathbf{f}_1}{w}\right) \tag{3.22}$$

These results can then be used to determine the new f_0 equation:

$$\frac{\partial f_0}{\partial t} + \frac{w}{3}\nabla_{\mathbf{r}} \cdot \mathbf{f}_1 + \mathbf{C} \cdot \nabla_{\mathbf{r}} f_0 - \frac{w}{3}\frac{\partial f_0}{\partial w}\nabla_{\mathbf{r}} \cdot \mathbf{C} + \frac{1}{3w^2}\frac{\partial}{\partial w}\left\{w^2\left[\mathbf{a} + \mathbf{C} \times \underline{\omega} - \frac{\partial \mathbf{C}}{\partial t} - (\mathbf{C} \cdot \nabla_{\mathbf{r}})\mathbf{C})\right] \cdot \mathbf{f}_1\right\} = \text{collisional terms} \tag{3.23}$$

3.3.2 The first angular moments

To take these moments equation (3.11) is multiplied by $\cos\theta_j$ and integrated over solid angle.

Scalar terms

$$\int T_s \cos\theta_j \mathrm{d}^2\Omega = A(w) \int \cos\theta_j \mathrm{d}^2\Omega = 0 \tag{3.24}$$

Vector terms

$$\int T_v \cos\theta_j \mathrm{d}^2\Omega = A_i(w) \int \cos\theta_i \cos\theta_j \mathrm{d}^2\Omega = \frac{4\pi}{3} A_j \tag{3.25}$$

Matrix terms

$$\int T_m \cos\theta_j \mathrm{d}^2\Omega = A_i(w) B_k(w) \int \cos\theta_i \cos\theta_k \cos\theta_j \mathrm{d}^2\Omega = 0 \tag{3.26}$$

Other terms

$$\int \left[\left(\frac{\mathbf{w}}{w} \cdot \nabla_{\mathbf{r}} \mathbf{C}\right)\right] \cdot \mathbf{f}_1 \cos\theta_j \mathrm{d}^2\Omega = f_{1k} \int \cos\theta_i \frac{\partial C_k}{\partial r_i} \cos\theta_j \mathrm{d}^2\Omega = \frac{4\pi}{3} f_{1k} \frac{\partial C_k}{\partial r_j} \tag{3.27}$$

$$\int \left[w^2 \nabla_{\mathbf{r}} \mathbf{C} \frac{\partial}{\partial w}\left(\frac{\mathbf{f}_1}{w}\right)\right] \vdots \frac{\mathbf{www}}{w^3} \cos\theta_j \mathrm{d}^2\Omega = A_i(w) B_l(w) C_k(w) \int \cos\theta_i \cos\theta_l \cos\theta_k \cos\theta_j \mathrm{d}^2\Omega = \frac{4\pi}{15} w^2 \left[\frac{\partial C_i}{\partial r_j}\frac{\partial}{\partial w}\left(\frac{f_{1i}}{w}\right) + \frac{\partial C_j}{\partial r_i}\frac{\partial}{\partial w}\left(\frac{f_{1i}}{w}\right) + \frac{\partial C_i}{\partial r_i}\frac{\partial}{\partial w}\left(\frac{f_{1j}}{w}\right)\right] \tag{3.28}$$

These results then give the new $\mathbf{f}_1$ equation:

$$\frac{\partial f_{1j}}{\partial t} + w\frac{\partial f_0}{\partial r_j} + \frac{\partial f_0}{\partial w}a_j + [\underline{\omega} \times \mathbf{f}_1]_j + \frac{\partial f_0}{\partial w}[\mathbf{C} \times \underline{\omega}]_j - \frac{\partial f_0}{\partial w}\frac{\partial C_j}{\partial t} + C_k\frac{\partial f_{1j}}{\partial r_k} - f_{1k}\frac{\partial C_k}{\partial r_j}$$
$$-\frac{\partial f_0}{\partial w}C_k\frac{\partial C_j}{\partial r_k} - \frac{w^2}{3}\left[\frac{\partial C_k}{\partial r_j}\frac{\partial}{\partial w}\left(\frac{f_{1k}}{w}\right) + \frac{\partial C_j}{\partial r_k}\frac{\partial}{\partial w}\left(\frac{f_{1k}}{w}\right) + \frac{\partial C_k}{\partial r_k}\frac{\partial}{\partial w}\left(\frac{f_{1j}}{w}\right)\right] = \text{collisional terms} \tag{3.29}$$

3.4 Velocity moments

Physical insight into the meaning of the various new terms in the f_0 and $\mathbf{f}_1$ equations – i.e. equations (3.23) and (3.29) – may be gained by taking their zeroth, first and second velocity moments. Firstly, a brief description of velocity moments of the distribution function, particularly those leading to important physical variables, is required.

3.4.1 Notes concerning velocity moments

In section 2.2.4 the derivation of the fluid equations was said to be a result of taking velocity averages of the VFP equation. These are known as velocity moments, how they lead to the derivation of fluid quantities (such as the n_e and T_e) from the distribution function will now be briefly described. The velocity-averaged value of a velocity-dependent quantity (α), over a velocity-distribution of particles (f), is given by:

$$\langle\alpha\rangle(\mathbf{r}, t) = \frac{1}{n_e}\int \alpha(\mathbf{w}, \mathbf{r}, t) f \mathsf{d}^3\mathbf{w} \tag{3.30}$$

Note that the velocities considered are those in the ion's rest frame. This will become important later. For now note that when considering the VFP equation without ion-motion the ion rest-frame is stationary and the velocity coordinate $\mathbf{w}$ becomes the more usual $\mathbf{v}$. The integral is over the whole of velocity space. The resulting average $\langle\alpha\rangle$ is a function of position and time only. Velocity moments have in fact already been used; in the discussion of non-local magnetic field generation quantities such as that above appeared. Equation (3.30) applies to the components of a rank n tensor as well as to a scalar. The important fluid quantities are defined by the following moments:

$$n_e = \int f \mathsf{d}^3\mathbf{w} = n_e\langle 1\rangle \tag{3.31}$$

$$\mathbf{C}_e = \int \mathbf{w} f \mathsf{d}^3\mathbf{w} = n_e\langle \mathbf{w}\rangle \tag{3.32}$$

$$\underline{\underline{\mathsf{P_e}}} = m_e \int (\mathbf{w}-\mathbf{C}_e)(\mathbf{w}-\mathbf{C}_e) f \mathsf{d}^3\mathbf{w} = n_e m_e \langle (\mathbf{w}-\mathbf{C}_e)(\mathbf{w}-\mathbf{C}_e)\rangle \tag{3.33}$$

$$\underline{\underline{\underline{\mathsf{q_e}}}} = \frac{m_e}{2} \int (\mathbf{w}-\mathbf{C}_e)(\mathbf{w}-\mathbf{C}_e)(\mathbf{w}-\mathbf{C}_e) f \mathsf{d}^3\mathbf{w} = \frac{n_e m_e}{2} \langle (\mathbf{w}-\mathbf{C}_e)(\mathbf{w}-\mathbf{C}_e)(\mathbf{w}-\mathbf{C}_e)\rangle \tag{3.34}$$

These quantities represent the electron's number density (n_e), bulk velocity ($\mathbf{C}_e$), pressure tensor ($\underline{\underline{\mathsf{P_e}}}$) and the rank-3 tensor form of the heat flow ($\underline{\underline{\underline{\mathsf{q_e}}}}$). The average electron velocity in the lab frame is $\mathbf{C}'_e = \mathbf{C} + \mathbf{C}_e$. The current is related to the difference between the average electron and ion velocities $\mathbf{j} = Zen_i\mathbf{C} - en_e\mathbf{C}'_e$. Note that, if the plasma is quasi-neutral then $\mathbf{C}_e$ is related to the current ($\mathbf{j} = -en_e\mathbf{C}_e$). Furthermore, it is now straightforward to see why moments in terms of $\mathbf{w}$ are equivalent to those in terms of $\mathbf{v}$. Consider:

$$\frac{\partial v_j}{\partial w_k} = \frac{\partial}{\partial w_k}(w_j + C_j) = \delta_{jk} \tag{3.35}$$

δ_{jk} is the Kronecker delta. The number density moment in terms of $\mathbf{v}$ may be expressed in terms of $\mathbf{w}$ in the following way:

$$n_e = \int f \mathsf{d}^3\mathbf{v} = \int_{v_x=0}^{\infty}\int_{v_y=0}^{\infty}\int_{v_z=0}^{\infty} f \mathsf{d}v_x \mathsf{d}v_y \mathsf{d}v_z = \int f \mathsf{d}^3\mathbf{w} \tag{3.36}$$

Therefore it was justified to write the number density moment as in equation (3.31). The same identification may be made for the other moments in equations (3.32) - (3.34); substitution for the electron velocity in the laboratory frame ($\mathbf{C}'_e = \mathbf{C}_e + \mathbf{C}$) will show these moments to be identical to those using $\mathbf{w}$.

The pressure tensor is usually reduced to the scalar isotropic pressure (P_e); it will be shown that, on expanding the distribution function to $\mathbf{f}_1$ only, anisotropic pressure is neglected. The scalar pressure is related to the temperature by the equation of state ($P_e = \frac{2}{3}n_e k_b T_e$). The heat flow is usually expressed as a vector expressing the velocity-averaged flux of energy. Note that the random part of the electron's velocity is denoted by $\mathbf{w}'$ (where: $\mathbf{w}' = \mathbf{w} - \mathbf{C}_e$).

$$P_e = \frac{n_e m_e}{3}\langle w'^2\rangle \qquad \mathbf{q}_e = \frac{n_e m_e}{2}\langle w'^2 \mathbf{w}'\rangle \tag{3.37}$$

The fluid equations are derived from taking moments of the VFP equation. The general equation is given by multiplying equation (2.10) by $m_e \mathbf{ww}\ldots\mathbf{w}$ – where there are n velocity vectors ($\mathbf{w}$) forming a tensor of rank-n – and integrating over velocity space. This yields [20]:

$$\frac{\partial \mathbf{M}_n}{\partial t} + \nabla_{\mathbf{r}} \cdot \mathbf{M}_{n+1} - n[\mathbf{a}\mathbf{M}_{n-1} - \underline{\omega} \times \mathbf{M}_n]_n = \Delta \mathbf{M}_n \tag{3.38}$$

Where $[\cdots]_l$ is the symmetrization of the tensor inside the bracket. To symmetrize a tensor of rank l one must sum all the possible permutations of the indices and divide by $l!$. For example: $[\mathbf{wC}]_2 = (\mathbf{wC} + \mathbf{Cw})/2!$. The general moment is represented by $\mathbf{M}_n$, $\Delta\mathbf{M}_n$ is the change in the fluid quantity $\mathbf{M}_n$ due to collisions. These are defined by the relations:

$$\mathbf{M}_n = n_e m_e \langle \mathbf{ww}\ldots\mathbf{w}\rangle \qquad \Delta\mathbf{M}_n = m_e \int \mathbf{ww}\ldots\mathbf{w}\left(\frac{\partial f}{\partial t}\right)_{coll} \mathsf{d}^3\mathbf{w} \tag{3.39}$$

Equation (3.38) gives rise to the fluid equations when $n = 0$, $n = 1$ and $n = 2$. These are known as the zeroth, first and second moments respectively and give the equations of MHD. As seen in the next section, these moments yield the continuity equation, momentum equation and an equation for the pressure tensor. The following second 'scalar' moment gives the energy equation, which is usually used instead of the equation for the pressure tensor:

$$M_2 = n_e m_e \langle w^2\rangle \tag{3.40}$$

Equation (3.38) shows that the fluid equations cannot be closed by simply considering higher and higher moments. The equation for the general moment $\mathbf{M}_n$ always involves the higher moment $\mathbf{M}_{n+1}$. A closure relation is needed to relate this moment to those lower than it. In the case of MHD this means an equation for the vector heat flow (the third moment) is required as the second moment (energy) equation was the highest equation considered. The heat flow must be expressed in terms of the lower moments, i.e. the pressure (or temperature), bulk flow velocity and number density. In MHD closure is usually achieved by using the heat flow equation (2.30) from classical transport theory – which only works if the distribution function is almost Maxwellian. A VFP treatment does not have the same requirement for closure.

The distribution function is solved for directly, meaning that any moment can be calculated straightforwardly.

The use of the cartesian tensor expansion complicates this discussion. The VFP equation is now expressed in terms of the components f_0 and $\mathbf{f}_1$. The moments of these are related to the velocity-averages of scalar and vector quantities as follows. Consider the velocity dependent scalar quantity $\alpha(w, \mathbf{r}, t)$. Note that α only depends on the speed. The average is given by:

$$\langle \alpha \rangle = \frac{4\pi}{n_e} \int_0^\infty \alpha f_0(w, \mathbf{r}, t) w^2 \mathtt{d}w \tag{3.41}$$

This is the equivalent of equation (3.30) using the expanded form of the distribution function. Now consider the average of the vector quantity $\underline{\alpha}(w, \mathbf{r}, t)$ (where $\underline{\alpha}$ has the following form):

$$\underline{\alpha} = \alpha(w, \mathbf{r}, t) \frac{\mathbf{w}}{w} \tag{3.42}$$

$$\langle \underline{\alpha} \rangle = \frac{4\pi}{3n_e} \int_0^\infty \alpha \mathbf{f}_1(w, \mathbf{r}, t) w^2 \mathtt{d}w \tag{3.43}$$

The averages of higher rank tensors need not be considered. Only the zeroth, first and scalar second moments will be taken. Comparing the moment equations for the VFP equation involving the full distribution function to those when it is expanded in the cartesian tensors will show which physical effects are neglected by truncating this expansion at $\mathbf{f}_1$.

3.4.2 Velocity moments of the new equations

The truncation of the Cartesian tensor expansion after $\mathbf{f}_1$ introduces approximations into the fluid equations derived from the f_0 and $\mathbf{f}_1$ equations. It is sensible to show what these assumptions are before taking the moments of the transformed f_0 and $\mathbf{f}_1$ equations (3.23) & (3.29) as these contain both the effect of this approximation and the effect of the new terms. On comparing the moments of the un-transformed equations (2.22) & (2.23) and the Vlasov part of the un-transformed VFP equation (2.10) the effects of truncating the expansion will be elucidated. First the moments of the un-transformed f_0 and $\mathbf{f}_1$ equations are taken. In this case $\mathbf{v} = \mathbf{w}$ and $\mathbf{C}'_e = \mathbf{C}_e$ – i.e. there is no net ion velocity. Note that the collisional term will not be included, the transformation leaves this term unchanged.

Zeroth Moment: Yields the continuity equation.

$$\frac{\partial \rho_e}{\partial t} + \nabla_{\mathbf{r}} \cdot (\rho_e \mathbf{C}_e) = 0 \tag{3.44}$$

First Moment: Results in the momentum equation.

$$\frac{\partial}{\partial t}(\rho_e \mathbf{C}_e) + \nabla_{\mathbf{r}} P_e + \nabla_{\mathbf{r}} \left(\frac{\rho_e C_e^2}{3} \right) = \rho_e (\mathbf{a} + \mathbf{C}_e \times \underline{\omega}) \tag{3.45}$$

Second Moment: Gives the energy equation.

$$\frac{\partial E}{\partial t} + \nabla_{\mathbf{r}} \cdot \mathbf{q}_T = \rho_e \mathbf{a} \cdot \mathbf{C}_e \tag{3.46}$$

The second moment involves the electrons average energy (E) and the total heat flow ($\mathbf{q}_T$). These are defined as:

$$E = \frac{n_e m_e}{2} \langle v^2 \rangle \qquad \mathbf{q}_T = \frac{n_e m_e}{2} \langle \mathbf{v} v^2 \rangle \tag{3.47}$$

Now consider the corresponding moments of the Vlasov part of the un-transformed VFP equation 2.10. The zeroth and second moments are the same as those above. The first moment is different.

$$\frac{\partial}{\partial t}(\rho_e \mathbf{C}_e) + \nabla_{\mathbf{r}} \cdot \mathsf{P}_e + \nabla_{\mathbf{r}} \cdot (\rho_e \mathbf{C}_e \mathbf{C}_e) = \rho_e (\mathbf{a} + \mathbf{C}_e \times \underline{\omega}) \tag{3.48}$$

This equation may be reconciled with equation (3.45) by identifying the physical effects that are not included when the distribution function is truncated at $\mathbf{f}_1$. The pressure and bulk flow tensors, used above, are given by:

$$P_{eij} = \rho_e \langle w_i' w_j' \rangle = P_e \delta_{ij} + \Pi_{eij} \tag{3.49}$$

$$P_{Bij} = \rho_e C_{ei} C_{ej} = P_B \delta_{ij} + \Pi_{Bij} \tag{3.50}$$

Here the random part of the electron's velocity is given by $\mathbf{w}' = \mathbf{w} - \mathbf{C}_e$ (recall that this is for the un-transformed case where the ion velocity is zero – the transformed case will be dealt with later). P_e and P_B are the scalar pressure and the scalar bulk flow respectively. Π_{eij} and Π_{Bij} are the tensors describing stress and anisotropic bulk flow. These are defined as:

$$P_e = \rho_e \left\langle \frac{w'^2}{3} \right\rangle \qquad \Pi_{eij} = \rho_e \left\langle w'_i w'_j - \frac{w'^2}{3}\delta_{ij} \right\rangle \tag{3.51}$$

$$P_B = \rho_e \left(\frac{C_e^2}{3} \right) \qquad \Pi_{Bij} = \rho_e \left(C_{ei} C_{ej} - \frac{C_e^2}{3}\delta_{ij} \right) \tag{3.52}$$

The effect of approximating the distribution function to be the sum of f_0 and $\mathbf{f}_1$ is the neglect of the anisotropic tensors $\underline{\underline{\Pi}}_e$ and $\underline{\underline{\Pi}}_B$. To describe anisotropic effects it is necessary to include further terms in the cartesian tensor expansion. This is also true of the transformed equations. In this case the bulk flow tensor is complicated by the electron velocity being defined with respect to the ion velocity $\mathbf{C}$.

Now that the effect that making the cartesian tensor expansion has on the moment equations has been elucidated the effects of the new terms may be discussed. The moments of the transformed f_0 and $\mathbf{f}_1$ equations (3.23) and (3.29) are given below in equations (3.53) - (3.55); a comparison of these with equations (3.44) - (3.46) show the new terms introduced by hydrodynamic flows.

Zeroth Moment: Continuity equation.

$$\frac{\partial \rho_e}{\partial t} + \nabla_{\mathbf{r}} \cdot [\rho_e(\mathbf{C}_e + \mathbf{C})] = 0 \tag{3.53}$$

First Moment: Momentum equation.

$$\begin{aligned} \frac{\partial}{\partial t}\left[\rho_e(\mathbf{C}_e + \mathbf{C})\right] + \nabla_{\mathbf{r}} P_e + \nabla_{\mathbf{r}} \left(\frac{\rho_e C_e^2}{3} \right) + \nabla_{\mathbf{r}} \cdot (\rho_e \mathbf{C}\mathbf{C}) + \\ \nabla \cdot (\rho_e \mathbf{C}_e \mathbf{C}) + \frac{2}{3}\left[\mathbf{C}_e \cdot (\nabla_{\mathbf{r}} \mathbf{C}) + \mathbf{C}_e \nabla \cdot \mathbf{C}\right] = \rho_e \left[\mathbf{a} + (\mathbf{C}_e + \mathbf{C}) \times \underline{\omega}\right] \end{aligned} \tag{3.54}$$

Second Moment: Energy equation.

$$\frac{\partial E_I}{\partial t} + \nabla_{\mathbf{r}} \cdot (E_I \mathbf{C}\rangle) + \frac{2E_I}{3} \nabla_{\mathbf{r}} \cdot \mathbf{C} + \nabla_{\mathbf{r}} \cdot \mathbf{q} = \rho_e \left[\left(\mathbf{a} - \frac{D\mathbf{C}}{Dt} \right) \cdot \mathbf{C} \right] \tag{3.55}$$

Where E_I is the kinetic energy in the ion's rest frame, i.e.:

$$E_I = \frac{n_e m_e}{2} \langle w^2 \rangle \tag{3.56}$$

Note that the new terms are all those involving the ion-flow velocity $\mathbf{C}$. A comparison of these moment equations with those derived from the transformed VFP

equation (3.9) shows that the truncation of the Cartesian tensor expansion affects the transformed moment equations in a more complicated way than those not including ion-motion. As with the un-transformed equations, the zeroth and second moments of equation (3.9) are identical to those of the transformed f_0 and $\mathbf{f}_1$ equations. These are given in equations (3.53) and (3.55). The momentum equation derived from (3.9) is different and is given by:

$$\frac{\partial}{\partial t}(\rho_e \mathbf{C}'_e) + \nabla_{\mathbf{r}} \cdot \mathsf{P}_e + \nabla_{\mathbf{r}} \cdot (\rho_e \mathbf{C}'_e \mathbf{C}'_e) = \rho_e(\mathbf{a} + \mathbf{C}'_e \times \underline{\omega}) \tag{3.57}$$

Where $\mathbf{C}'_e = \mathbf{C} + \mathbf{C}_e$. The difference between equations (3.54) and (3.57) results from the neglect of the stress tensor – as in the un-transformed case. In the case where the first moment of the transformed Vlasov equation is taken – resulting in equation (3.57) – the bulk flow tensor appears in the term $\nabla_{\mathbf{r}} \cdot (\rho_e \mathbf{C}'_e \mathbf{C}'_e)$. Comparing this to equation (3.54) shows that the bulk flow terms do not combine as neatly as this when the Cartesian tensor expansion is truncated. This is because certain terms are neglected as in the un-transformed case. The bulk pressure tensor in the transformed system may be expanded as:

$$\begin{aligned} \rho_e \mathbf{C}'_e \mathbf{C}'_e &= n_e m_e \left(\mathbf{C} + \mathbf{C}_e\right)\left(\mathbf{C} + \mathbf{C}_e\right) \\ &= n_e m_e \left(\mathbf{C}_e\mathbf{C}_e + \mathbf{C}_e\mathbf{C} + \mathbf{C}\mathbf{C}_e + \mathbf{C}\mathbf{C}\right) \end{aligned} \tag{3.58}$$

The first tensor relates only to the electrons and so one might expect the truncation of the Cartesian tensor expansion to affect this in the same way as in the case with no ion-motion, i.e.:

$$\nabla_{\mathbf{r}} \cdot (\rho_e \mathbf{C}_e \mathbf{C}_e) = \nabla_{\mathbf{r}} \left(\frac{\rho_e C_e^2}{3} \right) \tag{3.59}$$

This is consistent with the result in equation (3.54). The Cartesian tensor expansion should not effect the last tensor in equation (3.58), i.e. $\rho_e \mathbf{C}\mathbf{C}$, as this term does not involve the electron velocity. The corresponding term is indeed seen in equation (3.54). The remaining discrepancies between the first moment of the transformed $\mathbf{f}_1$ equation (3.54) and the transformed Vlasov equation (3.57) must be a result of terms neglected in the two mixed tensors $\rho_e \mathbf{C}_e \mathbf{C}$ and $\rho_e \mathbf{C}\mathbf{C}_e$. However, it is not clear how the expansion modifies these tensors. Retaining $\underline{\underline{\mathsf{f}_2}}$ in the cartesian tensor expansion would allow the inclusion of the missing anisotropic effects.

$$\frac{\partial f_0}{\partial t} + \underset{①}{\frac{w}{3}\nabla_{\mathbf{r}}\cdot\mathbf{f}_1} + \underset{②}{\mathbf{C}\cdot\nabla_{\mathbf{r}} f_0} - \underset{③}{\frac{w}{3}\frac{\partial f_0}{\partial w}\nabla_{\mathbf{r}}\cdot\mathbf{C}} + \underset{④}{\frac{1}{3w^2}\frac{\partial}{\partial w}\left\{w^2\left[\mathbf{a}+\mathbf{C}\times\underline{\omega}-\underset{⑤}{\frac{\partial\mathbf{C}}{\partial t}-(\mathbf{C}\cdot\nabla_{\mathbf{r}})\mathbf{C}}\right]\cdot\mathbf{f}_1\right\}} = \left(\frac{\partial f_0}{\partial t}\right)_{coll}$$

$$\frac{\partial f_{1j}}{\partial t} + \underset{⑥}{w\frac{\partial f_0}{\partial r_j}} + \left[\underline{\omega}\times\mathbf{f}_1\right]_j + \underset{⑦}{C_k\frac{\partial f_{1j}}{\partial r_k}} - f_{1k}\frac{\partial C_k}{\partial r_j} + \frac{\partial f_0}{\partial w}\left\{a_j + \underset{⑧}{\left[\mathbf{C}\times\underline{\omega}\right]_j} - \underset{⑨}{\frac{\partial C_j}{\partial t} - C_k\frac{\partial C_j}{\partial r_k}}\right\} - \underset{⑩}{\frac{w^2}{3}\left[\frac{\partial C_k}{\partial r_j}\frac{\partial}{\partial w}\left(\frac{f_{1k}}{w}\right) + \frac{\partial C_j}{\partial r_k}\frac{\partial}{\partial w}\left(\frac{f_{1k}}{w}\right) + \frac{\partial C_k}{\partial r_k}\frac{\partial}{\partial w}\left(\frac{f_{1j}}{w}\right)\right]} = \left(\frac{\partial f_{1j}}{\partial t}\right)_{coll}$$

Figure 3.4: The physical meaning of the terms in the transformed f_0 and $\mathbf{f}_1$ equations gleaned by taking moments.

3.4.3 The resulting physical insight into the new terms

The fluid equations (3.53)-(3.55) derived from the transformed f_0 and $\mathbf{f}_1$ equations were quoted without a detailed discussion of their derivation. This was in the interest of brevity. A detailed discussion of the moments of each term in the f_0 and $\mathbf{f}_1$ would have elucidated which term is responsible for describing which physical effect. The terms responsible for important physical effects are outlined in figure 3.4 and are marked 1-10. Term 1 gives the term $\mathbf{C}_e\cdot\nabla_{\mathbf{r}}\rho_e$ in the continuity equation and term 2 gives $\mathbf{C}\cdot\nabla_{\mathbf{r}}\rho_e$. These two terms together give advection of the electron density at the average velocity in the lab frame $\mathbf{C}'_e = \mathbf{C}_e + \mathbf{C}$. Term 3 gives the following term in the energy equation: $P_e\nabla_{\mathbf{r}}\cdot\mathbf{C}$ – i.e. compressional heating. Terms 4 and 5 give the work done by the electric field on the ions, this is proportional to $\mathbf{a}\cdot\mathbf{C}$, the other terms arise as corrections to the E-field. The $\mathbf{C}\times\underline{\omega}$ term is the relativistic correction to the E-field by defining it in the ion's rest frame; $\partial\mathbf{C}/\partial t$ and $(\mathbf{C}\cdot\nabla_{\mathbf{r}})\mathbf{C}$ account for the acceleration of this frame. Similar explanations apply to the terms in the $\mathbf{f}_1$ equation. Terms 8 and 9 apply the same corrections to the electric field as those in the f_0 equation. In the momentum equation these terms give $\rho_e(\mathbf{a}+\mathbf{C}'_e\times\underline{\omega})$, which describe the forces from the (relativistically corrected) electric field and $\mathbf{j}\times\mathbf{B}$. Term 6 describes pressure gradient acceleration (i.e. gives the term $\nabla_{\mathbf{r}}P_e$ in the momentum equation). Terms 7 and 10 contribute to the terms in the momentum equation in $\mathbf{C}_e$ and $\mathbf{C}$ – the bulk flow terms.

3.4.4 Ohm's law with flows

As a final validation of the new equations Ohm's law is derived including the effect of hydrodynamic plasma flow. To aid comparison with the established result – given in equation (2.29) – the derivation of Epperlein is followed [24]. The $\mathbf{f}_1$ equation can be recast to be comparable to that used by Epperlein:

$$w\nabla f_0 + \underline{\omega} \times \mathbf{f}_1 - \frac{\partial f_0}{\partial w}\bar{\mathbf{a}} = -\nu_{ei}\mathbf{f}_1 - \mathbf{T}_C \tag{3.60}$$

As was done by Epperlein, electron inertia has been neglected and the Lorentz approximation has been made. $\mathbf{T}_C$ is a correction introduced by ion motion and $\bar{\mathbf{a}}$ is the electric field including hydrodynamic corrections.

$$T_{Cj} = C_k\frac{\partial f_{1j}}{\partial r_k} - f_{1k}\frac{\partial C_k}{\partial r_j} - \frac{w^2}{3}\left[\frac{\partial C_k}{\partial r_j}\frac{\partial}{\partial w}\left(\frac{f_{1k}}{w}\right) + \frac{\partial C_j}{\partial r_k}\frac{\partial}{\partial w}\left(\frac{f_{1k}}{w}\right) + \frac{\partial C_k}{\partial r_k}\frac{\partial}{\partial w}\left(\frac{f_{1j}}{w}\right)\right] \tag{3.61}$$

$$\bar{\mathbf{a}} = \mathbf{a} - \mathbf{C}\times\underline{\omega} - \frac{\partial \mathbf{C}}{\partial t} - (\mathbf{C}\cdot\nabla)\mathbf{C} \tag{3.62}$$

The isotropic part of the distribution function is assumed to be a Maxwellian:

$$f_0 = f_m = n_e\left(\frac{m_e}{2\pi T_e}\right)^{3/2}\exp\left(-\frac{m_e w^2}{2T_e}\right) \tag{3.63}$$

This must be substituted into equation (3.60). The following relations are required:

$$\frac{\partial f_0}{\partial r_j} = \left(\frac{1}{n_e}\frac{\partial n_e}{\partial r_j} - \frac{3}{2T_e}\frac{\partial T_e}{\partial r_j} + \frac{m_e w^2}{2T_e^2}\frac{\partial T_e}{\partial r_j}\right) f_m \tag{3.64}$$

$$\frac{\partial f_0}{\partial w} = -\frac{m_e w}{T_e} f_m \tag{3.65}$$

Substitution of these results into equation (3.60) yields:

$$-(\mathbf{A}+\mathbf{B})w f_m + \underline{\omega}\times\mathbf{f}_1 = \nu_{ei}\mathbf{f}_1 + \mathbf{T}_C \tag{3.66}$$

Where:

$$\mathbf{A} = \frac{\nabla f_m}{f_m} \qquad \mathbf{B} = -\frac{\bar{\mathbf{a}}}{f_m}\frac{\partial f_m}{\partial w} \tag{3.67}$$

Terms in C^2 and $\mathbf{C}\cdot\mathbf{f}_1$ are now neglected. This is because $\mathbf{C} << \mathbf{w}$ and $|\mathbf{f}_1| << f_m$. In appendix B this derivation is repeated including all terms. Under these assumptions and writing the equations in terms of dimensionless parameters:

$$-(\tilde{\mathbf{A}}+\tilde{\mathbf{B}})W^4F_m + W^3\underline{\Omega}\times\mathbf{F}_1 = \mathbf{F}_1 \tag{3.68}$$

$$\tilde{A}_j = \left(\frac{D_j n_e}{n_e} - \frac{3}{2}\frac{D_j T_e}{T_e} + W^2\frac{D_j T_e}{T_e}\right) \tag{3.69}$$

$$\tilde{B}_j = \epsilon_j - [\underline{\Omega}\times\tilde{\mathbf{C}}]_j - \frac{\partial\tilde{\mathbf{C}}}{\partial\tau} \tag{3.70}$$

The dimensionless parameters are:

$$W=\frac{w}{w_T} \qquad \mathbf{D}=\lambda_T\nabla \qquad \underline{\Omega}=\frac{\underline{\omega}}{\nu_T} \qquad F=\frac{4\pi w_T^3}{n_e}f$$
$$\underline{\epsilon}=\frac{e\mathbf{E}}{m_e w_T\nu_T} \qquad \tilde{\mathbf{C}}=\frac{\mathbf{C}}{w_T} \qquad \frac{\partial}{\partial\tau}=\tau_T\frac{\partial}{\partial t}$$

Now $\mathbf{w}_T$ represents the thermal speed in the $(\mathbf{w},\mathbf{r},t)$ coordinate system; note that $w_T = v_T = (2k_bT_e/m_e)^{1/2}$. Dropping the tildes for brevity (whilst noting that the variables are in dimensionless form from now on) and using the fact that $\underline{\Omega}=(0,0,\Omega)$ the following equations are derived for the components of $\mathbf{F}_1$:

$$F_x = \frac{F_m}{1+W^6\Omega^2}\left[W^7\Omega\left(A_y+B_y\right) - W^4\left(A_x+B_x\right)\right] \tag{3.71}$$

$$F_y = -\frac{F_m}{1+W^6\Omega^2}\left[W^4\left(A_y+B_y\right) + W^7\Omega\left(A_x+B_x\right)\right] \tag{3.72}$$

Taking the first moment of these equations – i.e. $\int w...\mathsf{d}^3\mathbf{w}$ – yields:

$$\underline{\epsilon} - \frac{\partial\mathbf{C}}{\partial\tau} + \mathbf{C}\times\underline{\Omega} = -\frac{\mathbf{D}P_e}{2P_e} + \mathbf{J}\times\underline{\Omega} + \frac{4}{3\sqrt{\pi}}\underline{\underline{\alpha}}^c\cdot\mathbf{J} - \underline{\underline{\beta}}^c\cdot\frac{\mathbf{D}T_e}{2T_e} \tag{3.73}$$

This is as expected. The new terms resulting from ion motion are collected on the left-hand side and act to modify the electric field because of hydrodynamic effects.

3.5 The ion model

The effects of including ion flow on the electron model have been discussed in depth. The question of how to model the ions hydrodynamically remains – $\mathbf{C}$ must be supplied to the new f_0 and $\mathbf{f}_1$ equations. Consider the two-fluid equations, which describe the motion of separate ion and electron fluids.

$$m_i n_i \frac{D_i \mathbf{C}_i}{Dt} = n_i Z e \left(\mathbf{E} + \mathbf{C}_i \times \mathbf{B}\right) - \nabla P_i + \Delta \mathbf{p}_{ie} \tag{3.74}$$

$$m_e n_e \frac{D_e \mathbf{C}_e}{Dt} = 0 = -n_e e \left(\mathbf{E} + \mathbf{C}_e \times \mathbf{B}\right) - \nabla P_e + \Delta \mathbf{p}_{ei} \tag{3.75}$$

$$\frac{D_{i/e}}{Dt} = \frac{\partial}{\partial t} + \mathbf{C}_{i/e} \nabla \cdot$$

The average ion number density is given by n_i, the ion velocity by $\mathbf{C}_i$ and the ion pressure by P_i. $\Delta \mathbf{p}_{\alpha\beta}$ describes the rate of exchange of momentum between species α and species β due to collisions between these species. These changes are related by conservation of momentum ($\Delta \mathbf{p}_{ei} = -\Delta \mathbf{p}_{ie}$). Electron inertia may be neglected as it is much smaller than the ion inertia. Adding equation (3.74) to equation (3.75) yields:

$$\rho_i \frac{D_i \mathbf{C}_i}{Dt} = (Z n_i - n_e) e \mathbf{E} + \mathbf{j} \times \mathbf{B} - \nabla (P_e + P_i) \tag{3.76}$$

$$\mathbf{j} = Z n_i e \mathbf{C}_i - n_e e \mathbf{C}_e$$

Here ρ_i is the ion mass density. Next substitute for $\mathbf{j}$, using Ampere's law:

$$\mathbf{j} = \frac{1}{\mu_0} \nabla \times \mathbf{B} - \epsilon_0 \frac{\partial \mathbf{E}}{\partial t}$$

This yields:

$$\rho \frac{D\mathbf{C}}{Dt} = (Z n_i - n_e) e \mathbf{E} + \left[\frac{1}{\mu_0} (\nabla \times \mathbf{B}) - \epsilon_0 \frac{\partial \mathbf{E}}{\partial t} \right] \times \mathbf{B} - \nabla (P_e + P_i) \tag{3.77}$$

Equation (3.77) is the fluid momentum equation for the plasma. The ion inertia is dominant, so the ion density and velocity are equal to the total plasma density (ρ) and bulk velocity ($\mathbf{C}$). Consider the charge separation electric field term. The time-scale over which electric fields due to charge separation will be important is the plasma

wave period. This is the time-scale over which electrons in the plasma can shield out charge imbalances. IMPACT typically has to resolve time-scales of the order of the electron-ion collision time to get an accurate solution (although one could make the time-step larger than this). The plasmas discussed here typically have a ratio of the plasma frequency to the collision frequency which is large. This is required by the fact that the Debye sphere must contain a large number of electrons. Therefore charge separation effects may be neglected if the simulation time-step is not much smaller than the collision frequency, i.e. is much larger than the plasma period. In this case quasi-neutrality can be assumed, i.e. $Zn_i \approx n_e$; this does not mean that there is no charge separation but because large charge imbalances tend to be neutralised on a short time-scale, there are only tiny charge imbalances. Thus the plasma does contain electric fields, these are given by Ohm's law.

Consider the displacement current term; this can be done by substituting the electric field from Ohm's law into Ampere-Maxwell's law. Letting the electric field vary harmonically in time, i.e.:

$$\mathbf{E} = \mathbf{E}_0 e^{i\omega t} \tag{3.78}$$

Also, assuming that Ohm's law is given by the simplified form:

$$\mathbf{E}_0 = \eta\mathbf{j} - \mathbf{C}\times\mathbf{B} + \frac{\eta}{\nu_{ei}}\frac{\partial\mathbf{j}}{\partial t} + \frac{m_i}{Ze\rho}[\mathbf{j}\times\mathbf{B} - \nabla(P_e + P_i)] \tag{3.79}$$

Here, η is the resistivity of the plasma. Substitution of equation (3.78) into equation (3.79) gives the following equation – which is most revealing when expressed in normalised units (the normalisations are detailed in section 4.2):

$$\tilde{\nabla}\times\tilde{\underline{\omega}} = \frac{\omega_{pe}}{\nu_n}\frac{v_n}{c}\tilde{\mathbf{j}} + \left(\frac{v_n}{c}\right)^2\left(\frac{\omega}{\nu_n}\right)^2\frac{\tilde{\eta}}{\tilde{\nu}}\tilde{\mathbf{j}} + i\left(\frac{v_n}{c}\right)^2\frac{\omega}{\nu_n}\left[\tilde{\eta}\tilde{\mathbf{j}} - \frac{1}{\tilde{n_e}}\tilde{\underline{\omega}}\times(\tilde{\mathbf{j}} - \tilde{n_e}\tilde{\mathbf{C}}) - \frac{1}{2\tilde{n_e}}\tilde{\nabla}(\tilde{P_e} + \tilde{P_i})\right] \tag{3.80}$$

The variables ν_n and v_n are the normalising collision frequency and thermal speed. Assuming that the normalised variables are not very large – this will be borne out by the simulation results presented in chapter 5 – then the following conditions must be satisfied if the displacement current is to be neglected:

$$\frac{\omega_{pe}}{\omega}\frac{c}{v_n} >> 1 \qquad \frac{\omega_{pe}}{\omega}\frac{c}{v_n}\frac{\nu_n}{\omega} >> 1 \tag{3.81}$$

These conditions are generally satisfied – provided phenomena which are slowly

varying with respect to the plasma period (i.e. $\omega << \omega_{pe}$) are being considered and the plasma is highly collisional ($\omega << \nu_n$). The ions are cold, as discussed in section 3.1.3, so the ion temperature is neglected.

The model developed here is effectively a single fluid model. As a consequence of quasi-neutrality the electron and ion densities are related. These densities can be represented by a single fluid density ρ. The neglect of electron inertia means that the ion velocity is equal to the single fluid velocity $\mathbf{C}$. This is accurate to the order of m_e/m_i. Even though the hydrodynamic plasma motion is described by a single velocity $\mathbf{C}$, the average velocities of the electrons and ions need not be equal. This can be seen from the condition imposed on the current by quasi-neutrality, i.e. $\nabla \cdot \mathbf{j} = 0$ but $\mathbf{j} \neq 0$. This means that the electron currents are allowed to circulate, allowing magnetic fields.

The simplified equation of motion for the ions, where the magnetic filed field is perpendicular to gradients, is:

$$\frac{\partial(\rho\mathbf{C})}{\partial t} + \nabla_{\mathbf{r}} \cdot \left[\rho_i \mathbf{C}\mathbf{C} + \left(P_e + \frac{B^2}{2\mu_0}\right)\underline{\underline{\mathrm{I}}}\right] = 0 \tag{3.82}$$

$$\rho = \frac{n_e m_i}{Z} \qquad P_e = (\gamma - 1)\rho_e \epsilon_e$$

Here ϵ_e is the electron's average internal energy per unit mass. The electron density, current, electric field, magnetic field and electron pressure are all provided by IMPACT. The procedure by which the hybrid VFP-hydrodynamic code will be designed is illustrated in figure 3.5. A more complete ion model including charge separation and ion temperature is described in appendix C.

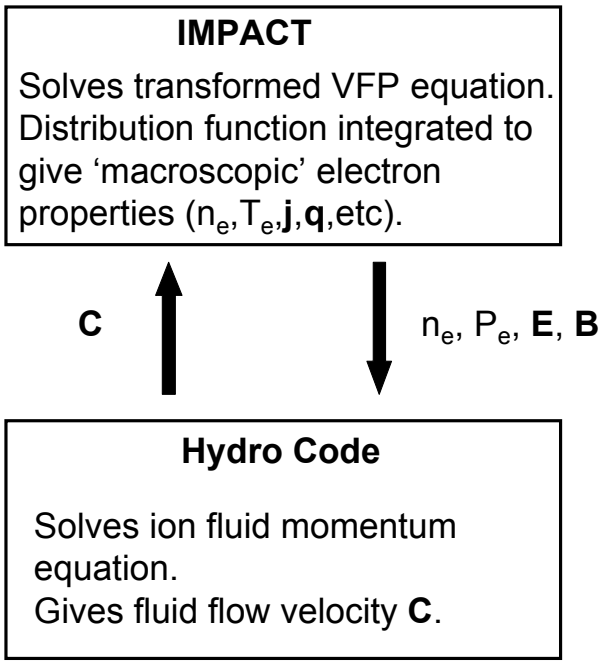

Figure 3.5: An illustration of the coupling procedure between IMPACT and the fluid algorithm. The arrows denote how quantities need to be passed between the codes.

Chapter 4

Numerical solution of the new model

4.1 Background – VFP codes

4.1.1 Explicit versus implicit codes

Non-classical analytical theories are only valid in very specific circumstances (for example in the description of small amplitude waves). To describe more general situations one must resort to solving the VFP equation numerically. In fact many of the simulation results described in section 2.4.3 were obtained using VFP codes. The VFP equation may be solved implicitly or explicitly, to detail the difference between these approaches consider solving the following 1-D partial differential equation:

$$\frac{\partial \alpha}{\partial t} = -\frac{\partial F}{\partial x} \tag{4.1}$$

Incidentally, this equation describes the flux of α (represented by F) in 1-D. In order to solve this equation numerically its finite difference form must be specified. Consider the way that time is discretised. The left hand side may be approximated by Euler's method:

$$\alpha_j^{n+1} = \alpha_j^n - \Delta t \left(\frac{\partial F}{\partial x}\right)_j^{n*} \tag{4.2}$$

The time t^n is defined as that after which n (uniformly spaced) time-steps have occurred, i.e. $t^n = n\Delta t$. The derivative of the flux must be evaluated at the spatial point x_j and at time t^{n*}, where this lies in between times t^n and t^{n+1}. A fully explicit scheme is one where $n*$ is chosen to be the time at which the quantities are known

(t^n), a fully implicit scheme is where t^{n*} is the time to which the solution is being advanced (t^{n+1}). Using an explicit scheme imposes a constraint on how large the time-step can be. Information cannot cross more than a single cell in one time-step, if this occurs the numerical solution is unstable and will produce un-physical results. This condition is known as the Courant-Friedrichs-Lewy (CFL) condition [83]. An implicit scheme on the other-hand is unconditionally stable (although, if a very large time-step is chosen accuracy is compromised). This means that to simulate the same length of time an implicit code generally needs fewer time-steps, so is the advantageous method to use for long-time simulations.

If the spatial derivative in equation (4.2) is evaluated by centre-differencing and the time discretisation is implicit, then the following equation is arrived at:

$$\alpha_j^{n+1} + \frac{\Delta t}{2\Delta x}\left(F_{j+1}^{n+1} - F_{j-1}^{n+1}\right) = \alpha_j^n \tag{4.3}$$

The spatial grid-cell size is Δx. In general F is a function of α. Therefore a matrix can be formed for equations like (4.3) for all the cells in the system. The equation in this case will be tridiagonal as F and so α are required at x_{i-1}, x_i and x_{i+1} in equation (4.3). If the partial differential equation to be solved were more complicated than (4.1), then the matrix would take a more complicated form, but would be likely to be sparse (less non-zero than zero elements). For completeness, the corresponding explicit differencing scheme is:

$$\alpha_j^{n+1} = \alpha_j^n - \frac{\Delta t}{2\Delta x}(F_{j+1}^n - F_{j-1}^n) \tag{4.4}$$

Finally, the solution of an equation such as the one below (the non-linear diffusion equation) will also be illustrative.

$$\frac{\partial \alpha}{\partial t} = \frac{\partial}{\partial x}\left[D(\alpha)\frac{\partial \alpha}{\partial x}\right] \tag{4.5}$$

Here α is a generic physical quantity and D is an arbitrary function of α. Treating this equation implicitly yields:

$$\alpha_j^{n+1} = \alpha_j^n + \Delta t\left[\frac{\partial}{\partial x}\left(D\frac{\partial \alpha}{\partial x}\right)\right]_j^{n+1} \tag{4.6}$$

This presents a problem, both of the unknowns D^{n+1} and α^{n+1} cannot be solved for simultaneously. In this case D may be treated as a non-linear coefficient, i.e.:

$$\alpha_j^{n+1,l+1} = \alpha_j^n + \Delta t \left[\frac{\partial}{\partial x} \left(D^{n+1,l} \frac{\partial \alpha^{n+1,l+1}}{\partial x} \right) \right]_j \tag{4.7}$$

Where $D^{n+1,l}$ is initially D^n. Equation (4.7) may then be solved for $\alpha^{n+1,l+1}$. This can then be used to calculate $D^{n+1,l+1}$, which is then put into equation (4.7) as $D^{n+1,l}$ and the solution is computed again. This procedure is iterated until the difference in $\alpha^{n+1,l+1}$ between two iterations is below a specified tolerance.

4.1.2 The development of implicit VFP codes

The most important implicit codes to discuss here are SPARK and IMPACT. Many other VFP codes (solving the VFP equation and Maxwell's equations) have been developed – the first for simulating LPI being published in 1981 by Bell, Evans & Nicholas [45, 47, 75, 84]. Of all the other codes the work of Kho & Haines in investigating the importance of the Nernst effect in advecting the magnetic field from an ablating plasma should be mentioned [85]. Their code was one-dimensional (in configuration space) and so did not include the self-generation of magnetic fields, but could look at the dynamics of an imposed field. The ions were modelled as a static neutralising background. They found that the rate of Nernst advection was strongly affected by non-locality.

The two-dimensional (in space) VFP code SPARK [86, 87] was developed by Epperlein, Rickard & Bell in 1988. This code used the diffusive approximation. Hydrodynamic ion response was included in 2D as was IB laser absorption. The VFP equation was solved implicitly to allow the authors to study long time-scale effects. Note that the code was not fully implicit; the 'Alternating Direction Implicit' (ADI) method was used. Under this scheme the spatial derivatives are treated fully implicitly and the velocity derivatives fully explicitly for one time step, this is then switched for the next time-step. This code did not include the effects of magnetic fields. The first 2D implicit VFP code to include magnetic fields self-consistently was IMPACT (2002) [22,63]. Here, the affects of electron-electron collisions were neglected in the $\mathbf{f}_1$ equation and those of electron-ion collisions were neglected in the f_0 equation. The ions were treated as a static neutralising background and IB laser heating was modelled via the Langdon operator [43]. The equations were solved on a 2D cartesian spatial grid and the magnetic field was constrained to always be perpendicular to this plane (this code was designed to study transport across the B-field).

The increment to VFP modelling which has already been mentioned and will provide the subject matter for this thesis is the inclusion of hydrodynamic plasma

motion into IMPACT – thus providing the first 2D VFP code with self-consistent magnetic fields, ion motion and the ability to run over long time scales. IMPACT solves the f_0 and $\mathbf{f}_1$ equations by treating the distribution function components and the electric field implicitly. The magnetic field is treated explicitly [22]. Such a choice allows one to use a large time-step. To get an accurate solution the electron-ion collision time of the thermal electrons (or the shortest time-scale of the phenomena of interest) should be resolved. The long-pulse experiments simulated here have time-scales of the order of a few nanoseconds. The problem with using purely explicit differencing to model such experiments is that they require a time-step which is too small. This can be seen by noting that in any distribution there will always be a small number of fast particles in the tail moving with speeds close to the speed of light. The CFL condition then limits the time-step of an explicit code to be less than the speed of light transit time for a grid-cell – this is generally much smaller than an electron-ion collision time (and very much smaller than 1ns). Additionally, a fully implicit treatment of the electric field increased the robustness of the code and ensured that the rate of change of the magnetic field was stable.

4.2 Normalising the new equations

IMPACT uses the following system of normalisations:

$$\begin{aligned}
&\tilde{w} = \frac{w}{w_n} \qquad \tilde{\mathbf{C}} = \frac{\mathbf{C}}{w_n} \qquad \tilde{t} = \frac{t}{\tau_n} \qquad \tilde{\mathbf{r}} = \frac{\mathbf{r}}{\lambda_n} \\
&\frac{\partial}{\partial \tilde{w}} = w_n \frac{\partial}{\partial w} \qquad \frac{\partial}{\partial \tilde{t}} = \tau_n \frac{\partial}{\partial t} \qquad \tilde{\nabla}_{\mathbf{r}} = \lambda_n \nabla_{\mathbf{r}} \\
&\tilde{f}_p = \frac{f_p w_n^3}{n_{e0}} \qquad \tilde{\mathbf{a}} = \frac{\mathbf{a}\tau_n^2}{\lambda_n} \qquad \tilde{\omega} = \omega \tau_n \qquad \tilde{Z} = \frac{Z}{Z_0}
\end{aligned} \tag{4.8}$$

The normalising quantities refer to a reference plasma; such a plasma is homogeneous and in a steady state. The number density of electrons in the reference plasma is n_{e0}. The electron-ion mean free path of thermal electrons (electrons moving with speed w_n) in this plasma is given by λ_n – the corresponding collision time is given by τ_n (as given in equation (2.25) with v replaced by w_n). The ionic charge of the reference plasma is Z_0, when the un-normalised ionic charge of the plasma is being discussed the symbol $\hat{Z}$ will be used. Note that the temperature is normalised (T_n) at twice the 'background' temperature (T_{e0}), these temperatures are defined as:

$$w_n = \left(\frac{2k_bT_{e0}}{m_e}\right)^{1/2} \qquad T_n = 2T_{e0} \tag{4.9}$$

On applying these normalisations to the f_0 and $\mathbf{f}_1$ equations, and canceling common factors, one obtains:

$$\frac{\partial \tilde{f}_0}{\partial \tilde{t}} + \frac{\tilde{w}}{3}\tilde{\nabla}_{\mathbf{r}}\cdot\tilde{\mathbf{f}}_1 + \tilde{\mathbf{C}}\cdot\tilde{\nabla}_{\mathbf{r}}\tilde{f}_0 - \frac{\tilde{w}}{3}\frac{\partial \tilde{f}_0}{\partial \tilde{w}}\tilde{\nabla}_{\mathbf{r}}\cdot\tilde{\mathbf{C}} + \frac{1}{3\tilde{w}^2}\frac{\partial}{\partial \tilde{w}}\left\{\tilde{w}^2\left[\tilde{\mathbf{a}} + \tilde{\mathbf{C}}\times\underline{\tilde{\omega}} - \frac{\partial \tilde{\mathbf{C}}}{\partial \tilde{t}} - (\tilde{\mathbf{C}}\cdot\tilde{\nabla}_{\mathbf{r}})\tilde{\mathbf{C}}\right]\cdot\tilde{\mathbf{f}}_1\right\} = \text{collisional terms} \tag{4.10}$$

$$\frac{\partial \tilde{f}_{1j}}{\partial \tilde{t}} + \tilde{C}_i\frac{\partial \tilde{f}_{1j}}{\partial \tilde{r}_i} + \tilde{w}\frac{\partial \tilde{f}_0}{\partial \tilde{r}_j} + \epsilon_{jik}\tilde{\omega}_i\tilde{f}_{1k} + \frac{\partial \tilde{f}_0}{\partial \tilde{w}}\left(\tilde{a}_j + \epsilon_{jik}\tilde{C}_i\tilde{\omega}_k - \frac{\partial \tilde{C}_j}{\partial \tilde{t}} - \tilde{C}_i\frac{\partial \tilde{C}_j}{\partial \tilde{r}_i}\right) - \tilde{f}_{1i}\frac{\partial \tilde{C}_i}{\partial \tilde{r}_j} - \frac{\tilde{w}^2}{3}\left[\frac{\partial \tilde{C}_i}{\partial \tilde{r}_j}\frac{\partial}{\partial \tilde{w}}\left(\frac{\tilde{f}_{1i}}{\tilde{w}}\right) + \frac{\partial \tilde{C}_j}{\partial \tilde{r}_i}\frac{\partial}{\partial \tilde{w}}\left(\frac{\tilde{f}_{1i}}{\tilde{w}}\right) + \frac{\partial \tilde{C}_i}{\partial \tilde{r}_i}\frac{\partial}{\partial \tilde{w}}\left(\frac{\tilde{f}_{1j}}{\tilde{w}}\right)\right] = \text{collisional terms} \tag{4.11}$$

Note that for the remainder of this chapter normalised quantities will be used – the tildes are dropped for brevity. When any variables which are not normalised are introduced this will be clearly stated.

4.3 The finite difference equations

In this section the considerations involved in the numerical implementation of the equations will be discussed. It is first necessary to talk about the numerical scheme used in IMPACT without ion motion – this will show where the code requires augmentation.

4.3.1 The numerics of IMPACT

IMPACT solves the following normalised forms of thef_0 and $\mathbf{f}_1$ equations:

$$\frac{\partial f_0}{\partial t} + \frac{w}{3}\nabla_{\mathbf{r}}\cdot\mathbf{f}_1 - \frac{1}{3w^2}\frac{\partial}{\partial w}\left(w^2\mathbf{a}\cdot\mathbf{f}_1\right) = C_{ee0} + H \tag{4.12}$$

$$\frac{\partial \mathbf{f}_1}{\partial t} + w\nabla f_0 - \mathbf{E}\frac{\partial f_0}{\partial w} - \underline{\omega}\times\mathbf{f}_1 = -\frac{\hat{Z}^2 n_i}{w^3}\mathbf{f}_1 \tag{4.13}$$

Where C_{ee0} is the normalised electron-electron collision operator and is given by:

$$C_{ee0} = \frac{1}{\hat{Z}w^2}\frac{\partial}{\partial w}\left[C(f_0)f_0 + D(f_0)\frac{\partial f_0}{\partial w}\right] \tag{4.14}$$

$$C(w,\mathbf{r},t) = 4\pi\int_0^w f_0(u,\mathbf{r},t)u^2\mathsf{d}u \tag{4.15}$$

$$D(w,\mathbf{r},t) = \frac{4\pi}{w}\int_0^w u^2\left[\int_u^\infty f_0(y,\mathbf{r},t)y\mathsf{d}y\right]\mathsf{d}u \tag{4.16}$$

H is responsible for laser heating (discussed in section 4.3.5). This laser heating term is present only in the f_0 equation as this equation determines the energy of a region of plasma. The finite-differencing scheme employed by IMPACT, to solve the f_0 and $\mathbf{f}_1$ equations, is:

$$\frac{f_0^{n+1,l+1}-f_0^n}{\Delta t} + \frac{w}{3}\nabla\cdot\mathbf{f}_1^{n+1,l+1} - \frac{1}{3w^2}\frac{\partial}{\partial w}\left(w^2\mathbf{E}^{n+1}\cdot\mathbf{f}_1^{n+1,l}\right) = [C_{ee0}+H]^{n+1} \tag{4.17}$$

$$\frac{\mathbf{f}_1^{n+1,l+1}-\mathbf{f}_1^n}{\Delta t} + w\nabla f_0^{n+1,l+1} - \mathbf{E}^{n+1}\frac{\partial f_0^{n+1,l}}{\partial w} - \underline{\omega}^n\times\mathbf{f}_1^{n+1,l+1} = -\frac{\hat{Z}^2 n_i}{w^3}\mathbf{f}_1^{n+1,l+1} \tag{4.18}$$

$$\nabla\times\mathbf{E}^{n+1} = -\left(\frac{\underline{\omega}^{n+1}-\underline{\omega}^n}{\Delta t}\right) \tag{4.19}$$

From these equations it is clear that the electric field is treated implicitly and f_0 is a lagged non-linear coefficient (note that l denotes the time-step within an iteration). The computational domain is two-dimensional in configuration space and one-dimensional in velocity space – a point on this grid is represented by (x_i, y_j, w_k). The z-direction is an ignorable coordinate meaning that there are no gradients of any physical variables in this direction. f_{1z} may also be ignored – if the it is initially zero, and there are no gradients in the z-direction, it is always zero. Note that this is only true if the magnetic field only has a z-component. Making $\mathbf{f}_1^{n+1,l+1}$ the subject of equation (4.18) yields:

$$(f_{1r}^b)_{ijk}^{n+1,l+1} = \left\{ \chi_k^n \sum_{q=x,y} (\delta_{rq} + \epsilon_{rzq}\omega^n \tau_k') \left[-w_k (\nabla_q)_k^{n+1,l+1} + E_q^{n+1} \left(\frac{\partial f_0}{\partial w} \right)_k^{n+1,l} + \frac{(f_{1q})_k^n}{\Delta t} \right] \right\}_{ij}^b \tag{4.20}$$

$$\chi_{ijk}^{b,n} = \frac{\tau_k'}{1 + (\omega_{ij}^{b,n} \tau_k')^2} \qquad \tau_k' = \left[\frac{1}{\Delta t} + \frac{1}{\tau_{ei}(w_k)} \right] \tag{4.21}$$

Here f_{1r}^b is the r-component of $\mathbf{f}_1$ on the boundary b of the spatial grid-cell. $\tau_{ei}(w_k) = w_k^3/\hat{Z}^2 n_i$ is the electron-ion scattering time for an electron traveling at speed w_k; δ_{qr} is the Kronecker delta and ϵ_{qrz} is the Levi-Civita symbol. The current-constraint is also used.

$$\mathbf{j}^{n+1,l+1} = -\frac{4\pi}{3} \int_0^\infty \mathbf{f}_1^{n+1,l+1} w^3 \mathbf{d}w = \left(\frac{c}{\omega_{pe}\lambda_n} \right)^2 \nabla \times \underline{\omega}^n \tag{4.22}$$

This ensures that the current produced by the code is consistent with Ampere's law (ignoring the displacement current). ω_{pe} is the plasma frequency of the reference plasma. In finite-difference form equation (4.22) becomes:

$$\left[(\nabla \times \underline{\omega})_r^b \right]_{ij}^n = \epsilon_{rqz} (\nabla_q \omega_z)_{ij}^{b,n} = -4\pi \left(\frac{\omega_{pe}\lambda_n}{c} \right)^2 \sum_{k=1}^{nv} (f_{1r}^b)_{ijk}^{n+1} v_k^3 \Delta v_k \tag{4.23}$$

Where $\underline{\omega} = (0, 0, \omega_z)$ has been used. The next step is to eliminate f_{1r}^b from equations (4.17) and (4.23). This is a complicated procedure and in the interests of brevity will not be outlined; the result are the equations which form the matrix solved by IMPACT.

$$G_{p,q,s}(x_i, y_j, w_k) f_0\left(x_{i+p}, y_{j+q}, w_{k+s}, t^{n+1}\right) + H_{r,b,m,n}(x_i, y_j, w_k) E_r^b\left(x_{i+l}, y_{j+m}, t^{n+1}\right) = C(x_i, y_j, w_k) \tag{4.24}$$

$$M_{c,r,u}(r, b, x_i, y_j) f_0\left(x_{i+c}, y_{j+d}, w_u, t^{n+1}\right) + N_g(r, b, x_i, y_j) E_g^b\left(x_i, y_j, t^{n+1}\right) = D(r, b, x_i, y_j) \tag{4.25}$$

Note that summation is implied over repeated indices. Equation (4.24) corre-

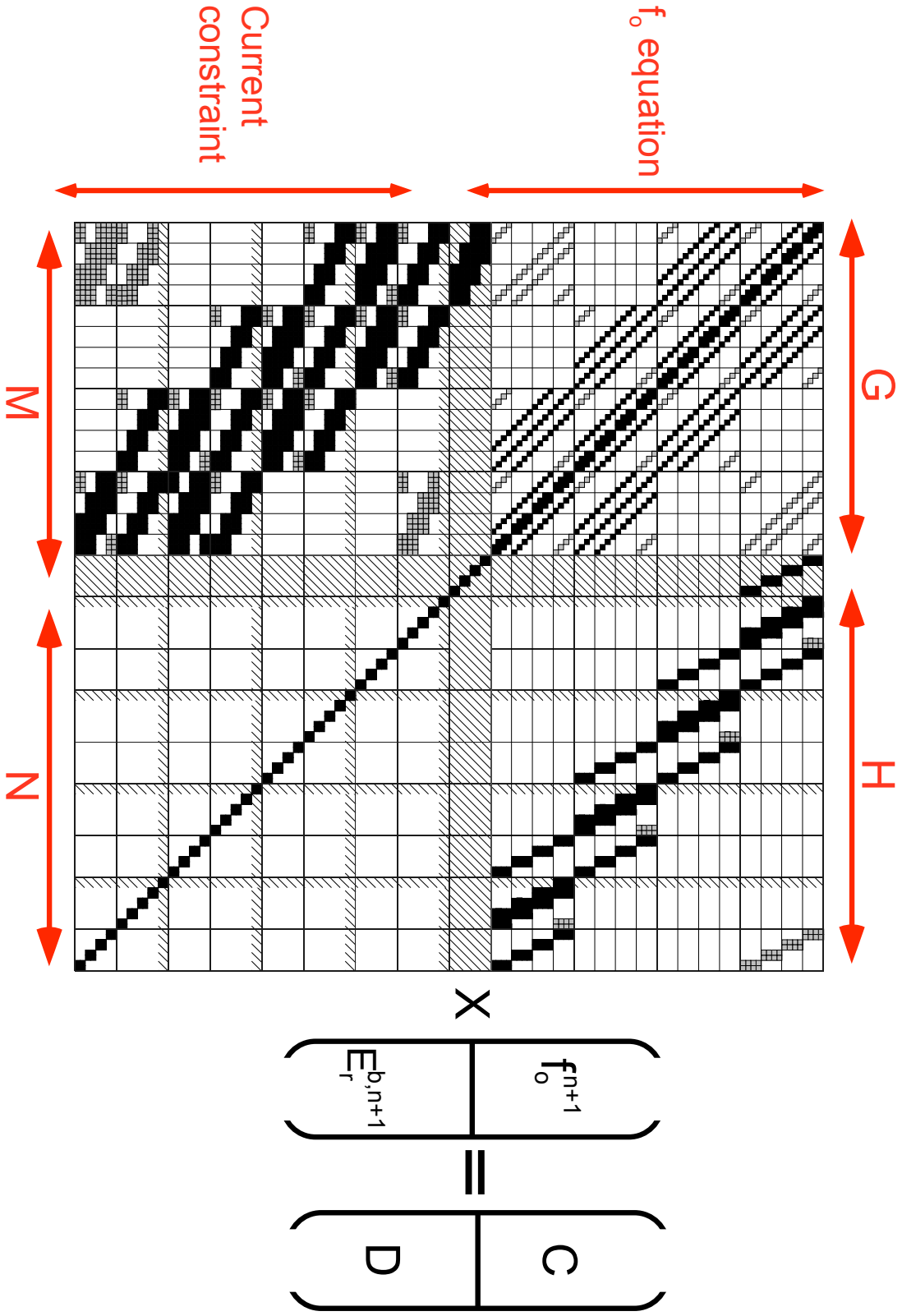

Figure 4.1: A diagram showing the matrix equation solved by IMPACT.

sponds to the finite-difference approximation of the f_0 and $\mathbf{f}_1$ equations and (4.25) to the current constraint. G, H, M and N are the coefficients pre-multiplying f_0 and $\mathbf{E}$ in these equations. The labels p, q, s, m, n, c, d are all finite difference offsets running over the following ranges:

$$c, d, p, q, s = \{-1, 0, 1\} \qquad m, n = \{-1, 0\} \tag{4.26}$$

The indices r, b and g refer to which component is being discussed. The index u affects integration over velocity.

$$r, b, g = \{x, y\} \qquad u = \{1, \ldots, nv\} \tag{4.27}$$

The matrix equation is illustrated for a $4 \times 4 \times 4$ grid ($nx \times ny \times nw$) in figure 4.1. The matrix elements which are shaded are those that are non-zero. The matrix is rather complex, fortunately the constant vector containing C and D is all that needs to be modified to include hydrodynamic ion-motion. This is a consequence of the choice to treat the new terms explicitly (as justified in the next section). This matrix is solved by the stabilised biconjugate gradient method [88]. The details of this method are not important here, however one should note that this method solves the matrix iteratively to a specified tolerance. So there are two tolerances to specify, one for the non-linear iteration in equation (4.17) and the other for the matrix solver.

Some features of the matrix should be noted. Each quadrant highlighted in figure 4.1 is labeled with the part of equation (4.17) or (4.23) to which it corresponds. Figure 4.2 shows a simplified version of the matrix. The top diagram corresponds to the top part of the full matrix in figure 4.1; the bottom diagram in figure 4.2 corresponds to the top part of the current constraint. Each row of the matrix corresponds to one of the nd equations given in equations (4.24) and (4.25) – note that $nd = nc + 2[2(nx \times ny) + nx + ny]$ and $nc = nx \times ny \times nw$ (nc corresponds to the number of cell-centres, the additional term is a result of the fact that the electric field array has ghost cells outside the domain, as well as two components and being defined on two sets of boundaries). Each row of the matrix is represented pictorially by the smallest shaded square in figure 4.2, this is highlighted by the red line in the figure. The most coarse cells represent the x-coordinate, then the y-coordinate and w-coordinate are represented by finer divisions. As an example consider the black shaded square in the top-left of figure 4.2; this corresponds to coordinates $(ix = 1, iy = 2, iw = 2)$. For the electric field and the current the matrix also divided into sections representing these quantities on the x cell-boundaries ($\mathbf{E}^x, \mathbf{j}^x$) and the y cell-boundaries ($\mathbf{E}^y, \mathbf{j}^y$).

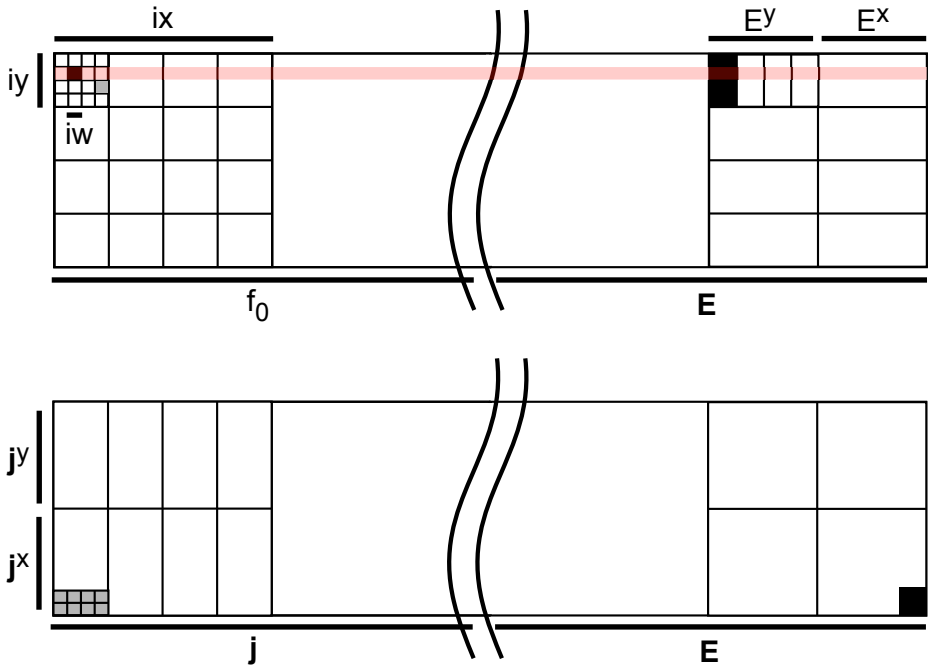

Figure 4.2: A simplified explanation of the matrix.

The black shaded areas are always present, the grey are only present for periodic boundary conditions.

4.3.2 The f_0 equation

It has been shown where the new terms must be inserted into the matrix equation, now these terms must be implemented numerically. On simple rearrangement, the new f_0 equation (3.23) is given by:

$$\frac{\partial f_0}{\partial t} + \frac{w}{3}\nabla_{\mathbf{r}} \cdot \mathbf{f}_1 + \frac{1}{3w^2}\left(w^2 \mathbf{a} \cdot \mathbf{f}_1\right) + \mathbf{C} \cdot \nabla_{\mathbf{r}} f_0 - \frac{w}{3}\frac{\partial f_0}{\partial w}\nabla_{\mathbf{r}} \cdot \mathbf{C} + \frac{1}{3w^2}\frac{\partial}{\partial w}\left\{w^2\left[\mathbf{C} \times \underline{\omega} - \frac{\partial \mathbf{C}}{\partial t} - (\mathbf{C} \cdot \nabla_{\mathbf{r}})\mathbf{C}\right] \cdot \mathbf{f}_1\right\} = \left(\frac{\partial f_0}{\partial t}\right)_{coll} \tag{4.28}$$

Here the old terms have been separated from the new terms. As the new terms are treated explicitly they do not modify the form of the matrix. Note that it is possible to treat the new terms in this way as they are expected to evolve on the hydrodynamic time-scale, which is much longer than the electron-ion collision time, negating any CFL considerations. Note that this assumes that the hydrodynamic

motion is sonic or sub-sonic: in this case the ratio of the hydrodynamic speed to the thermal speed is at most $c_s/v_T = (m_e/m_i)^{1/2}$ (c_s is the ion sound speed). The finite-difference approximations to the the new terms are taken in the most straightforward way possible.

For brevity, define:

$$\mathbf{a}' = \mathbf{C} \times \underline{\omega} - \frac{\partial \mathbf{C}}{\partial t} - (\mathbf{C}.\nabla_{\mathbf{r}})\mathbf{C} \tag{4.29}$$

The finite difference forms of each of the new terms are:

$$[\mathbf{C} \cdot \nabla_{\mathbf{r}} f_0]^n_{ijk} = (C_x)^n_{ij} \left[\frac{(f_0)_{i+1} - (f_0)_{i-1}}{\Delta x_{i+1/2} + \Delta x_{i-1/2}}\right]^n_{jk} + (C_y)^n_{ij} \left[\frac{(f_0)_{j+1} - (f_0)_{j-1}}{\Delta y_{j+1/2} + \Delta y_{j-1/2}}\right]^n_{ik} \tag{4.30}$$

$$\left[\frac{w}{3}\frac{\partial f_0}{\partial w}\nabla_{\mathbf{r}} \cdot \mathbf{C}\right]^n_{ijk} = \frac{w_k}{3}\left[\frac{(f_0)_{k+1} - (f_0)_{k-1}}{\Delta w_{k+1/2} + \Delta w_{k-1/2}}\right]^n_{ij} \times \left\{\left[\frac{C_{x,i+1} - C_{x,i-1}}{\Delta x_{i+1/2} + \Delta x_{i-1/2}}\right]_{jk} + \left[\frac{C_{y,j+1} - C_{y,j-1}}{\Delta y_{j+1/2} + \Delta y_{j-1/2}}\right]^n_{ik}\right\} \tag{4.31}$$

$$\left[\frac{1}{3w^2}\frac{\partial}{\partial w}\left(w^2 \mathbf{a}' \cdot \mathbf{f}_1\right)\right]^n_{ijk} = \frac{(a'_x)^n_{ij}}{3(w^n_k)^2}\left[\frac{w^2_{k+1/2}(f_{1x})_{k+1} - w^2_{k-1/2}(f_{1x})_k}{\Delta w_k}\right]^n_{ij} + \frac{(a'_y)^n_{ij}}{3(w^n_k)^2}\left[\frac{w^2_{k+1/2}(f_{1y})_{k+1} - w^2_{k-1/2}(f_{1y})_k}{\Delta w_k}\right]^n_{ij} \tag{4.32}$$

It is important to note that as a result of using the simplest differencing schemes possible the above are not conservative in mass or energy. However exact conservation is not necessary; the code need only be conservative to a specified level of accuracy. The discrepancy in the conservation is expected to be dependent on the Courant number – how many cells the hydrodynamic motion is expected to move across in a single time-step. This should be small as the hydrodynamic motion is expected to be slow (provided it is sub-sonic). Conservation will be discussed in more detail when testing the algorithm.

Note that the differencing of the advective term in equation (4.30) would be unconditionally unstable if this term were solved in isolation; however, the coupling this term to IMPACT has a stabilising effect. This mitigates the instability in the simula-

tion results presented in this chapter and in chapters 5-7; they show no evidence of a hydrodynamic instability. This is thought to be because the hydrodynamics varies very slowly in every case, in order to simulate shocks a better scheme would be required. This differencing scheme has the advantage of being accurate to second-order.

4.3.3 The $\mathbf{f}_1$ equation

The new $\mathbf{f}_1$ equation is given by:

$$\frac{\partial f_{1j}}{\partial t} + w\frac{\partial f_0}{\partial r_j} + \frac{\partial f_0}{\partial w}a_j + [\omega \times \mathbf{f}_1]_j + \frac{\partial f_0}{\partial w}[\mathbf{C} \times \omega]_j - \frac{\partial f_0}{\partial w}\frac{\partial C_j}{\partial t} + C_k\frac{\partial f_{1j}}{\partial r_k} - f_{1k}\frac{\partial C_k}{\partial r_j} - \frac{\partial f_0}{\partial w}C_k\frac{\partial C_j}{\partial r_k} - \frac{w^2}{3}\left[\frac{\partial C_k}{\partial r_j}\frac{\partial}{\partial w}\left(\frac{f_{1k}}{w}\right) + \frac{\partial C_j}{\partial r_k}\frac{\partial}{\partial w}\left(\frac{f_{1k}}{w}\right) + \frac{\partial C_k}{\partial r_k}\frac{\partial}{\partial w}\left(\frac{f_{1j}}{w}\right)\right] = \left(\frac{\partial f_{1j}}{\partial t}\right)_{coll} \tag{4.33}$$

Again, the most simple finite difference approximations are used:

$$\begin{aligned}(f_{1x,i+1/2})^{n+1}_{jk} = (f_{1x,i+1/2})^n_{jk} &+ \Delta t(a'_x)^n_{ij}\left[\frac{(f_0)_{k+1}-(f_0)_{k-1}}{\Delta w_{k+1/2}+\Delta w_{k-1/2}}\right]^n_{i+1/2,j} - \Delta t[(\mathbf{C}\cdot\nabla_{\mathbf{r}})f_{1r}]^n_{i+1/2,jk} \\ &+\Delta t(f_{1x})^n_{i+1/2,jk}\left[\frac{C_{x.i+1}-C_{x,i}}{\Delta x_i}\right]^n_j + \Delta t(f_{1y})^n_{i+1/2,jk}\left[\frac{C_{y,j+1/2}-C_{y,j-1/2}}{\Delta y_{j+1/2}+\Delta y_{j-1/2}}\right]^n_{i+1/2} \\ &+\frac{\Delta t w_k^2}{3}\left[\frac{C_{x,i+1}-C_{x,i}}{\Delta x_i}\right]^n_j\left[\frac{f_{1x}/w_{k+1}-f_{1x}/w_{k-1}}{\Delta w_{k+1/2}+\Delta w_{k-1/2}}\right]^n_{i+1/2,j} \\ &+\frac{\Delta t w_k^2}{3}\left[\frac{C_{y,i+1}-C_{y,i}}{\Delta x_i}\right]^n_j\left[\frac{f_{1y}/w_{k+1}-f_{1y}/w_{k-1}}{\Delta w_{k+1/2}+\Delta w_{k-1/2}}\right]^n_{i+1/2,j} \\ &+\frac{\Delta t w_k^2}{3}\left[\frac{C_{x,i+1}-C_{x,i}}{\Delta x_i}\right]^n_j\left[\frac{f_{1x}/w_{k+1}-f_{1x}/w_{k-1}}{\Delta w_{k+1/2}+\Delta w_{k-1/2}}\right]^n_{i+1/2,j} \\ &+\frac{\Delta t w_k^2}{3}\left[\frac{C_{x,j+1/2}-C_{x,j-1/2}}{\Delta y_{j+1/2}+\Delta y_{j-1/2}}\right]^n_{i+1/2}\left[\frac{f_{1y}/w_{k+1}-f_{1y}/w_{k-1}}{\Delta w_{k+1/2}+\Delta w_{k-1/2}}\right]^n_{i+1/2,j}\end{aligned}$$

$$+\frac{\Delta t w_k^2}{3}\left[\frac{C_{x,i+1}-C_{x,i}}{\Delta x_i}\right]_j^n\left[\frac{f_{1x}/w_{k+1}-f_{1x}/w_{k-1}}{\Delta w_{k+1/2}+\Delta w_{k-1/2}}\right]_{i+1/2,j}^n$$
$$+\frac{\Delta t w_k^2}{3}\left[\frac{C_{y,j+1/2}-C_{y,j-1/2}}{\Delta y_{j+1/2}+\Delta y_{j-1/2}}\right]_{i+1/2}^n\left[\frac{f_{1x}/w_{k+1}-f_{1x}/w_{k-1}}{\Delta w_{k+1/2}+\Delta w_{k-1/2}}\right]_{i+1/2,j}^n \tag{4.34}$$

Note that the convective derivative is differenced using a centred method – as in the f_0 equation. The above differencing scheme is certainly not conservative in momentum. Once again the errors will be small in the low Courant number limit.

4.3.4 The ion model

Finally consider the finite difference approximation to the ion's equation of motion (3.82). On rearrangement (employing the continuity equation), the x-component of this equation is expressed in normalised form as:

$$n_e\frac{\partial C_x}{\partial t}=-n_eC_x\frac{\partial C_x}{\partial x}-n_eC_y\frac{\partial C_x}{\partial y}-\frac{\partial}{\partial x}\left(a_1P_e+\frac{a_2B^2}{2}\right) \tag{4.35}$$

A similar equation holds for the y-momentum. Note that the non-conservative form of this equation is used; this is consistent with the corrections to the f_0 and $\mathbf{f}_1$ equations not being differenced conservatively. The dimensionless constants a_1 and a_2 are given by:

$$a_1=\frac{\hat{Z}m_e}{m_i}\qquad a_2=\frac{\hat{Z}m_e}{m_i}\left(\frac{\nu_{ei}}{\omega_{pe}}\frac{c}{w_n}\right)^2 \tag{4.36}$$

The flow velocity will be updated in two stages. Firstly the effects of thermal and magnetic pressure are accounted for:

$$(C_x^*)_{i,j}^n=(C_x)_{i,j}^n-\Delta t\left[\frac{(P_T)_{i+1}-(P_T)_{i-1}}{\Delta x_{i+1/2}+\Delta x_{i-1/2}}\right]_j^n \tag{4.37}$$

Where P_T is the 'total' pressure – including magnetic pressure. Next the plasma is advected with the bulk flow velocity:

$$(C_x)_{i,j}^{n+1}=(C_x)_{i,j}^{n*}-\Delta t\left[(C_x)_i\frac{(C_x)_{i+1}-(C_x)_{i-1}}{\Delta x_{i+1/2}+\Delta x_{i-1/2}}\right]_j^{n*}-\Delta t\left[(C_y)_j\frac{(C_x)_{j+1}-(C_x)_{j-1}}{\Delta y_{j+1/2}+\Delta y_{j-1/2}}\right]_i^{n*} \tag{4.38}$$

This simple finite difference scheme is based on a centre-differencing scheme and

as a result will fail in the presence of large density and velocity gradients – for example if shocks occur in the simulation. A more robust model would be needed in this case. Such a scheme is described in appendix D.

4.3.5 The laser – inverse bremsstrahlung and Maxwellian heating

Inverse bremsstrahlung heating is the most important method of laser absorption at the intensities that will be simulated with the new code – as discussed in section 2.1. In IMPACT this is treated using the Langdon operator [43, 89]. In normalised units this is given by:

$$\left(\frac{\partial f_0}{\partial t}\right)_{IB} = \frac{Z^2 n_i}{w^2}\frac{\partial}{\partial w}\left(\frac{v_{osc}^2 g(w)}{6w}\frac{\partial f_0}{\partial w}\right) \tag{4.39}$$

The (normalised) electron's quiver velocity in the laser field is given by v_{osc}^2, this and the function $g(w)$ are given by:

$$v_{osc}^2 = \frac{0.091}{\alpha}\left(\frac{I\lambda_0^2}{10^{15}\mathrm{Wcm}^{-2}\mu\mathrm{m}^2}\right)\left(\frac{T_{e0}}{keV}\right)^{-1} \tag{4.40}$$

$$g(w) = \left[1 + \left(\frac{Z^2 n_i}{\omega_0 w^3}\right)^2\right]^{-1} \tag{4.41}$$

The variables on the right-hand side of equation (4.40) are not in normalised units. The quantity α takes the value of $1/2$ if the laser light is circularly polarised or 1 if it is linearly polarised. The laser intensity is given by I and its wavelength by λ_0. ω_0 is the normalised laser frequency, i.e.:

$$\omega_0 = \frac{0.6(T_{e0}/eV)^{3/2}}{(\lambda_0/\mu\mathrm{m})(n_i/10^{21}\mathrm{cm}^{-3})Z_0^2 \mathsf{ln}\Lambda_{ei}} \tag{4.42}$$

It is possible to calculate the rate at which the plasma heats up due to inverse bremsstrahlung. Taking the second moment of equation (4.39) yields:

$$\frac{\partial}{\partial t}(n_e T_e)_{IB} = \frac{4\pi Z^2 n_i v_{osc}^2 f_0|_{w=0}}{9} \tag{4.43}$$

Langdon showed that IB heating causes the isotropic part of the distribution function f_0 to tend to a Langdon distribution ($f_0 \propto e^{-v^5}$) [43]. IMPACT also has the ability to heat the plasma but have f_0 remain Maxwellian – this is useful to

disentangle the effects that IB and non-locality have on distorting the distribution function. The operator used in the f_0 equation to give this 'Maxwellian heating' (MH) is [89]:

$$\left(\frac{\partial f_0}{\partial t}\right)_{MH} = \frac{1}{\hat{Z}w^2}\frac{\partial}{\partial w}\left(D_0 w^2 \frac{\partial f_0}{\partial w}\right) \tag{4.44}$$

D_0 is the arbitrary constant which determines the heating rate. The form of this operator is explained in appendix E. Taking the energy moment of equation (4.44) yields an expression for the rate of increase in energy density due to Maxwellian heating.

$$\left(\frac{\partial T_e}{\partial t}\right)_{MH} = \frac{D_0}{\hat{Z}} \tag{4.45}$$

Note that the rate of Maxwellian heating is constant – compared to IB whose rate depends on the f_0 at $w = 0$ which decreases with increasing temperature. Note that this is easily understood by considering the case where f_0 is a Maxwellian: $f_M|_{w=0} \propto T_e^{-3/2}$.

4.4 Testing the code

To test the code the simplest linear solution involving ion-hydrodynamics and B-fields will be simulated: adiabatic magnetosonic waves. This will prove to be surprisingly difficult. The problem arises because IMPACT is not a magnetohydrodynamics solver and as such is not designed to work well in the regime of adiabatic hydrodynamic waves – it is designed to study thermal conduction. To understand how to run the code in the adiabatic regime a discussion of MHD in the presence of thermal conduction and Ohmic heating is required – i.e. resistive MHD. At the outset it is important to note that this test is adequate enough to trust the results presented in the remaining chapters, but that additional tests would be useful. The magnetosonic wave tests the effects the new terms 2, 3, 7, 8 and 9 (in figure 3.4) on linear wave propagation. The non-linear effects of these terms and their effects on transport are not tested. Testing such effects is left as further work. Note that the transport and IB have been tested in IMPACT without hydrodynamics.

Consider the equations of resistive MHD – in un-normalised units and in the one-dimensional geometry shown below:

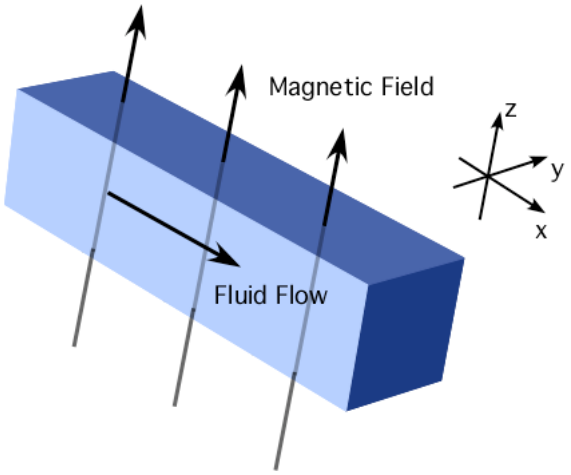

Figure 4.3: A diagram of the 1D MHD system considered here.

$$\frac{\partial \rho}{\partial t} + \frac{\partial}{\partial x}(\rho C) = 0 \tag{4.46}$$

$$\frac{\partial (\rho C)}{\partial t} + \frac{\partial}{\partial x}\left(\rho C^2 + P_e + \frac{B^2}{2\mu_0}\right) = 0 \tag{4.47}$$

$$\frac{\partial (\rho \epsilon_e)}{\partial t} + \frac{\partial}{\partial x}(\rho \epsilon_e C) + P_e \frac{\partial C}{\partial x} + \frac{\partial}{\partial x}\left(\kappa_\perp \frac{\partial (k_b T)}{\partial x}\right) - \alpha_\perp j^2 = 0 \tag{4.48}$$

$$\frac{\partial B}{\partial t} + \frac{\partial}{\partial x}(BC) = 0 \tag{4.49}$$

$$P_e = (\gamma - 1)\rho \epsilon_e \tag{4.50}$$

The variable ϵ_e is the electron's internal energy per unit mass. In the equation of state the gas constant (γ) is set to 5/3. To examine the propagation of small amplitude waves the MHD equations given above must be linearised. The physical variables (B,C,ρ,ϵ_e,T) are given by a background value α_0 plus a small amplitude harmonic perturbation (with amplitude α_{1A}).

$$\alpha(x,t) = \alpha_0 + \alpha_{1A} e^{i(kx - \omega t)} \qquad \text{Where:} \quad \alpha_{1A} << \alpha_0$$

On treating the physical variables in this way, the following dispersion relation is derived (in normalised units):

$$\frac{\omega^3}{k^3} = \left(\frac{\gamma a_1 P_0}{\rho_0} + \frac{a_2 B_0^2}{\rho_0}\right)\frac{\omega}{k} - i\beta k\left(\frac{\omega^2}{k^2} - \frac{a_1 P_0}{\rho_0} - \frac{a_2 B_0^2}{\rho_0}\right) \tag{4.51}$$

$$k\beta = \frac{4\pi(\gamma-1)\kappa_{\|} m_i}{\rho_0^{1/2}\lambda_p a_2^{1/2} B_0^3} \tag{4.52}$$

C_m is the normalised magnetosonic speed and is given by:

$$C_m^2 = \frac{a_1 \gamma P_0}{\rho_0} + a_2 \frac{B_0^2}{\rho_0} \tag{4.53}$$

For simplicity, the adiabatic limit will be simulated. The condition for this to be so is that the second term on the right-hand side of equation (4.51) – which is responsible for damping the wave – is negligible, i.e.:

$$\frac{k\beta}{C_m} = \frac{4\pi(\gamma-1)\kappa_{\perp} m_i}{\rho_0^{1/2}\lambda_p a_2^{1/2} B_0^3 C_m} << 1 \tag{4.54}$$

To make this term small there must be a large background magnetic field and a long wavelength perturbation (λ_p). To get undamped propagation this parameter is set to be to be of order of 10^{-3}. This is achieved with the following set of physical parameters:

$$\rho_0 = 1 \quad P_0 = 1 \quad B_0 = 10 \quad \omega_{pe}/\nu_{ei} = 40 \quad c/v_t = 50 \tag{4.55}$$

There is further significance to this choice of parameters. This becomes clear on consideration of the (normalised) internal energy equation.

$$\rho\left(\frac{\partial \epsilon_e}{\partial t} + C\frac{\partial \epsilon_e}{\partial x}\right) + P\frac{\partial C}{\partial x} + \frac{\partial}{\partial x}\left(\kappa\frac{\partial T}{\partial x}\right) - \alpha_{\perp}\left|\nabla \times \mathbf{B}\right|^2\left(\frac{c/v_t}{\omega_{pe}/\nu_{ei}}\right)^2 = 0 \tag{4.56}$$

The test runs will be over a spatial scale of $1000\lambda_{ei}$ and a time-scale of $5000\tau_{ei}$; in this time the waves will be made to cycle once through the system. This is only possible if the magnetosonic speed is sufficiently high. This is the case for the parameters chosen in equation (4.55). It will simplify the analysis considerably if the effects of Ohmic heating can be ignored – these are described by the final term in the energy equation. This term is proportional to precisely the term which was to be greater than unity in order to get the waves to move at a measurable velocity. To be able to neglect non-linear Ohmic heating effects we would want this term to be

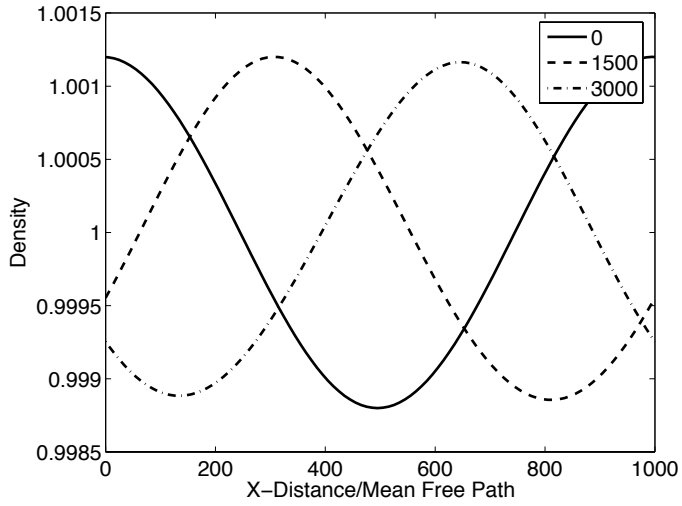

Figure 4.4: Magnetosonic waves are simulated correctly with the new code. Shown here are three 'snapshots' of the wave's density profile (the wave is moving from left to right). The numbers in the legend refer to the time (normalised to τ_n) at which these 'snapshots' were taken.

small. Fortunately IMPACT has the facility to 'turn off' Ohmic heating – doing this prevents non-linear heating effects becoming important whilst allowing the waves to propagate a measurable distance.

4.5 Test results – the propagation of a magnetosonic wave

Figure 4.4 shows that that the new code does indeed simulate magnetosonic waves correctly. The speed of such waves is given by the equation for the normalised magnetosonic speed. The plasma conditions used gave a speed of 0.21, which agreed with the value measured from the simulation to within 2%. The wave did not lose a significant amount of amplitude as it propagated for $3000\tau_n$, thus the ion hydrodynamics scheme is not too diffusive.

4.5.1 Measuring the speed by taking the Fourier transform

The wave's speed may be measured more accurately by using more data than two snap-shots. Consider the (spatial) Fourier Transform of a single-frequency travelling wave (with frequency ω and wavevector k_1).

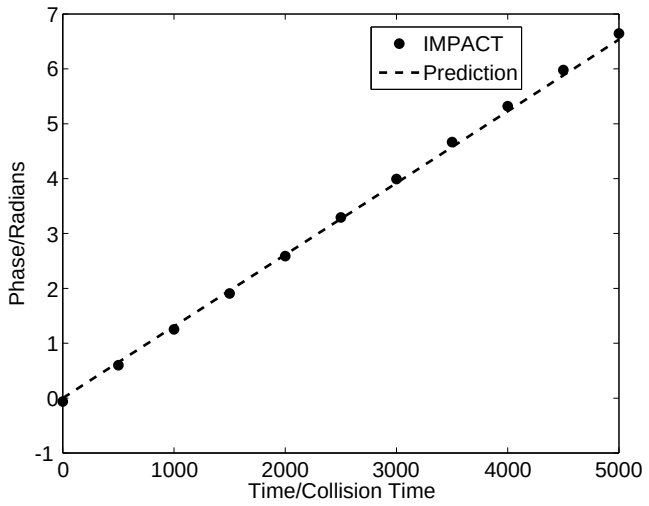

Figure 4.5: The phase of the wave gives the expected propagation speed (dashed line).

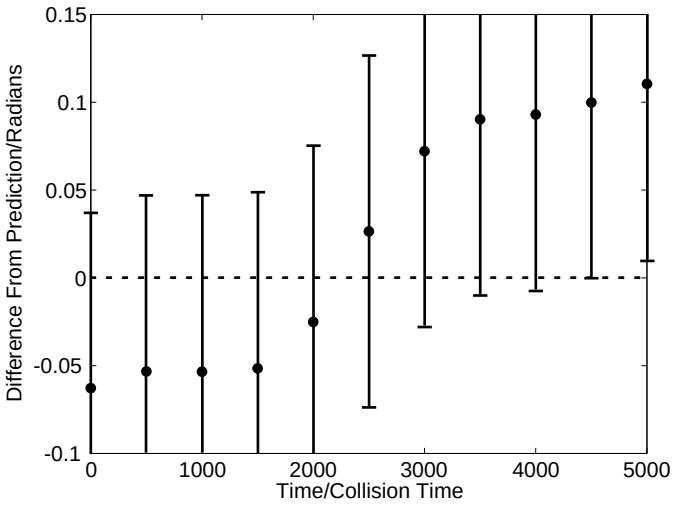

Figure 4.6: The difference between the measured and predicted phases. The error bars express the numerical error – agreement is good to within these limits.

$$f(x,t) = Ae^{i(k_1 x - \omega t)} \tag{4.57}$$

$$\hat{F}[f] = \frac{A}{\sqrt{2\pi}} e^{-ik_1 c_m t} \int_{-\infty}^{\infty} e^{i(k_1 - k)x} dx \tag{4.58}$$

$$\hat{F}[f] = \frac{A}{\sqrt{2\pi}} e^{-ik_1 c_m t} \delta(k_1 - k) \tag{4.59}$$

Where A is a constant. Notice that the result of the Fourier Transform is complex. The magnitude and phase of this complex function are:

$$R = \frac{A}{\sqrt{2\pi}} \delta(k_1 - k) \qquad \theta = -k_1 c_m t \tag{4.60}$$

The changing phase of the wave with time (figure 4.5) shows that the measured speed is in very good agreement with the magnetosonic speed over the duration of the simulation. Figure 4.6 shows the error in the phase produced by IMPACT. The error bars express the fact that one can only measure the position of the wave to $\pm\Delta x$. The systematic cycling of the error may be explained by noting how the sign of the error changes after 2000 collision times. This corresponds to the crest of the wave passing the centre of the simulation domain at which the point the method used to measure the position of the crest flipped from the left boundary to the right – thus changing the sign of the error.

4.5.2 The conservation properties of the new code

Earlier in this chapter it was discussed that the new code is not conservative. Figures 4.7 and 4.8 show that the new code does not perform much worse than IMPACT without ion motion. The density, momentum and energy changes over 5000 collision times were very small (0.001%, 0.12% and 0.1% respectively).

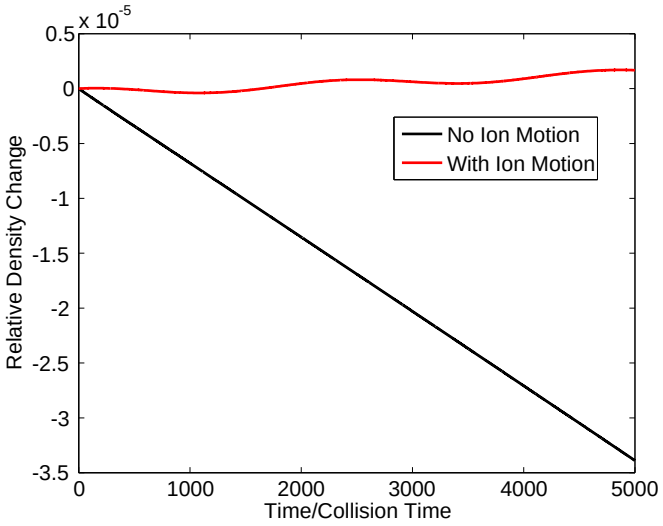

Figure 4.7: The relative density change with and without the effects of hydrodynamic ion motion.

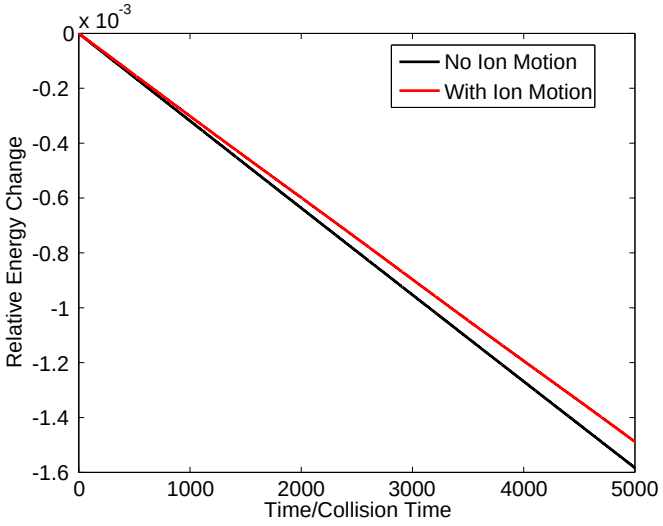

Figure 4.8: The relative energy change with and without the effects of hydrodynamic ion motion.

Chapter 5

Non-local transport in a magnetic field

In this chapter the first fully kinetic simulations of the coupling between non-local transport and the dynamical evolution of the magnetic field including hydrodynamic plasma motion will be discussed. As discussed in the introduction kinetic simulations have addressed spontaneous generation of B-fields including non-local effects [59, 63]. Others have considered how B-fields affect non-locality or how non-local effects modify B-field dynamics [52, 85] but have not elucidated how these phenomena evolve when coupled together. It will be shown that an applied magnetic field – which is initially sufficient to localize transport – is eventually expelled from a laser-heated region, leading to a re-emergence of non-local transport here. The question of the cause of non-classicality will be addressed, i.e. the effects of inverse bremsstrahlung heating on the distribution function will be decoupled from those of non-local transport.

Figure 5.1 shows a schematic of the experiment conducted by Froula *et al* which was described in section 2.4.1 [12]. Recall that several such long-pulse laser-gas jet interactions have been studied [12, 56]; first with the aim of directly measuring non-local heat flow and then to suppress it with a large externally applied magnetic field. The addition of hydrodynamic ion-motion to IMPACT gives a powerful tool for studying these effects. The experiment of Froula *et al* will be simulated. As such it is now essential to briefly summarise the experiment and its results.

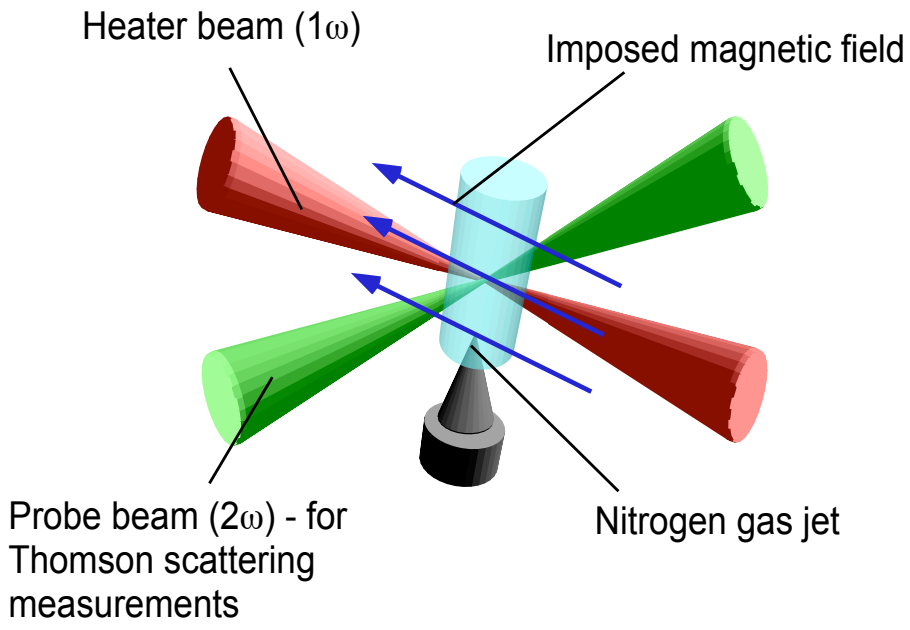

Figure 5.1: Froula's experiment investigating the suppression of non-local heat flow.

5.1 The experimental setup of Froula *et al* & their results

The laser had a wavelength of $\lambda = 1.054\mu$m and delivered 100J over a pulse duration of 1ns (giving an on-target intensity of 10^{15}Wcm^{-2}). This was shone into a nitrogen gas jet which had an initial temperature of 20eV and created a plasma with an electron number density of 1.5×10^{19}cm^{-3}. A 4T or 12T initially uniform magnetic field could be applied parallel to the heater beam. The temperature profile was measured at various times by Thomson scattering using a frequency doubled beam perpendicular to the main beam. In figure 5.2 these profiles are shown after 1.35ns for the field-free case and the 12T case. The profile for the field-free case clearly has pre-heat ahead of the main heat front while the magnetized case does not. The pre-heat is postulated to be the result of non-local heat flow – this hypothesis will be tested. The magnetic field profile was not measured but was thought to be frozen in to the plasma, the inclusion of hydrodynamic plasma motion in the model will allow this hypothesis to be tested.

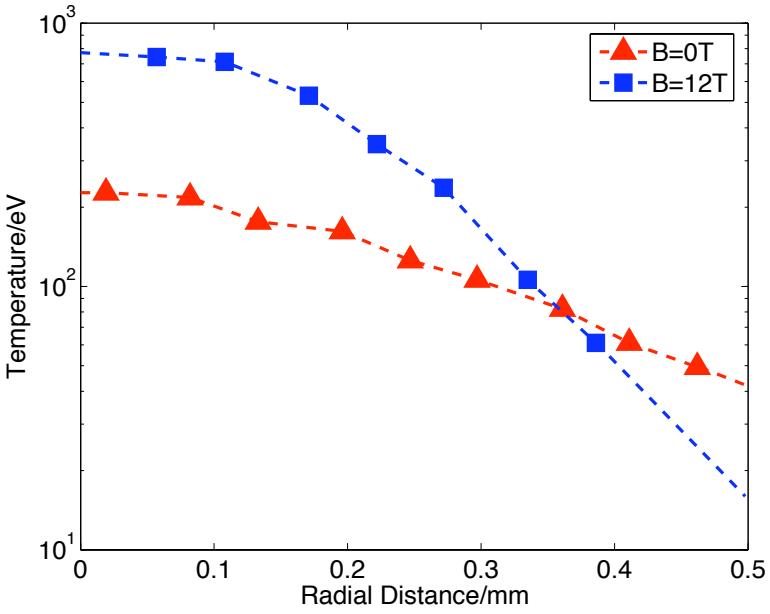

Figure 5.2: Electron temperature profiles in the long-pulse laser-gas jet experiment undertaken by Froula *et al.* The red profile is in the case where no external magnetic field was applied; the blue profile is with a 12T field

5.2 Simulation considerations

Figure 5.3 shows the geometry of the simulations. The magnetic field is in the z-direction while the current, electric field, density gradient and bulk flow velocity are in the (x, y) plane, i.e. the cross-field transport will be studied. This is equivalent to taking a slice through the laser perpendicular to its direction of propagation; giving a circular heating region in 2-D. With z being the ignorable coordinate the simulations are of a cylindrical laser beam aligned with the z-axis. This holds true if the laser is sufficiently defocussed; that is, if it has a long depth of focus compared to the gas jet diameter. This is illustrated in figure 5.4. Consider the propagation of a laser beam; as it is focussed the power per unit area in the beam – the intensity – increases as the area decreases. The depth of focus (also known as the confocal parameter) is a measure of the distance over which the intensity of the beam is approximately constant. This is shown as the parameter b in figure 5.4. The minimum radius of the beam is known as the beam waist (w_o). The distance along the direction of propagation of the laser beam – the z-axis in the diagram – at which the laser intensity in the centre of the spot falls by a factor two is known as the Rayleigh length (z_o). The depth of focus is given by $2z_o$. In Froula's experiment the beam waist was 75μm and the wavelength was 1.054μm meaning that the depth of focus was 30mm. This is

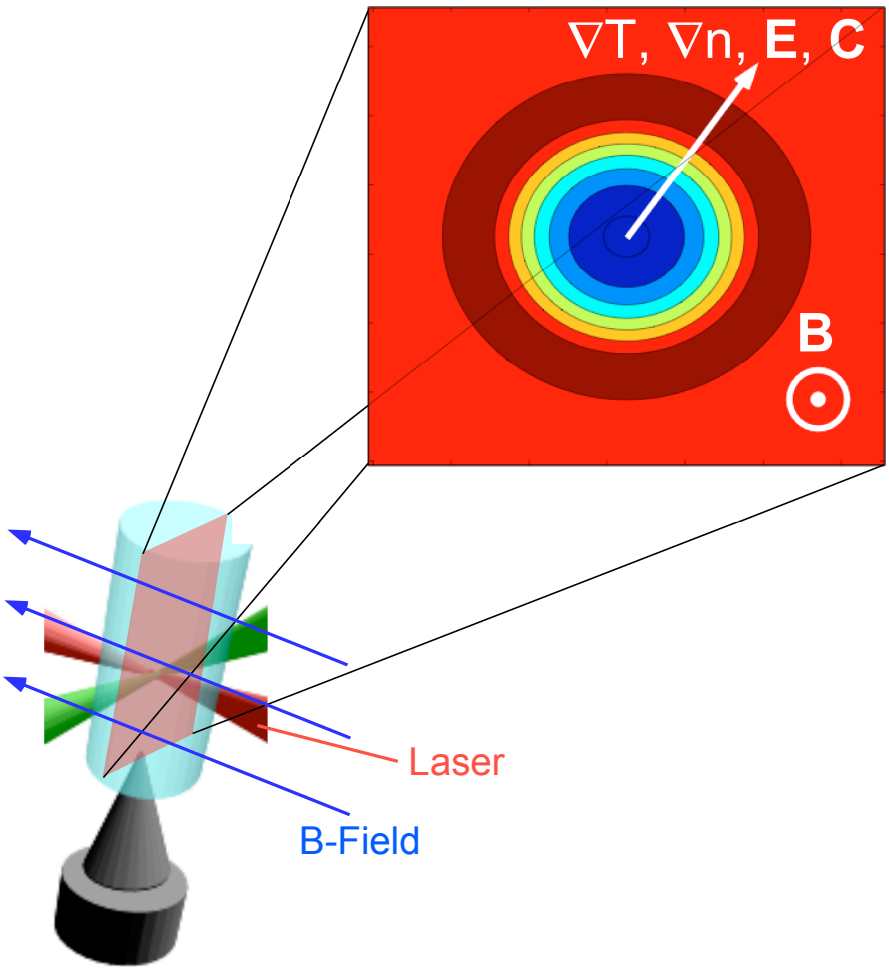

Figure 5.3: The simulation geometry used in the modelling of Froula's experiment. The magnetic field is perpendicular to the flows, gradients and electric field.

indeed much larger than the gas jet's diameter (1.5mm) so gradients of the physical variables in the z-direction are negligible compared to in the x and y-directions; 2D modelling in this situation is justified. Ideally the plasma would be modelled in plane-polar coordinates, however IMPACT uses cartesian coordinates – modifying this will involve directly changing the matrix coefficients discussed in section 4.3.1 and is left as future work.

The fact that an (x, y) grid is used to simulate a problem whose symmetry is naturally cylindrical forces the use of a rather complicated grid. Figure 5.5 shows this grid. In the very centre of the grid there are nine cells of the same size. From these the cells get larger, in a geometric progression, moving along the x or y axis from the centre. The ratio of the lengths of the sides of the corner grid-cells to those

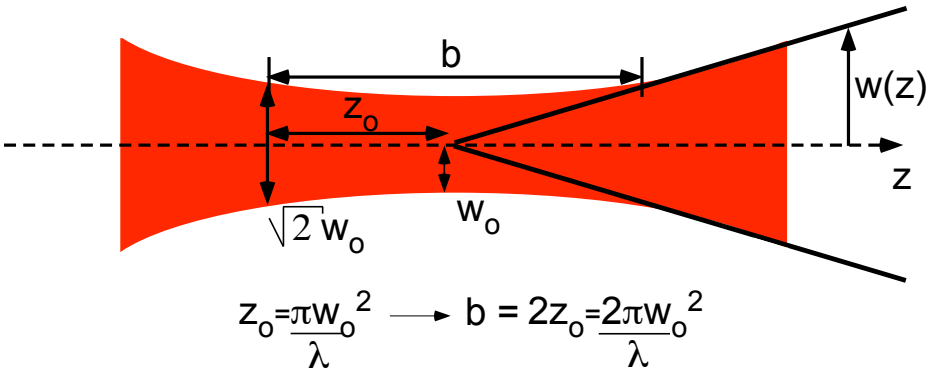

Figure 5.4: An illustration of the depth of focus.

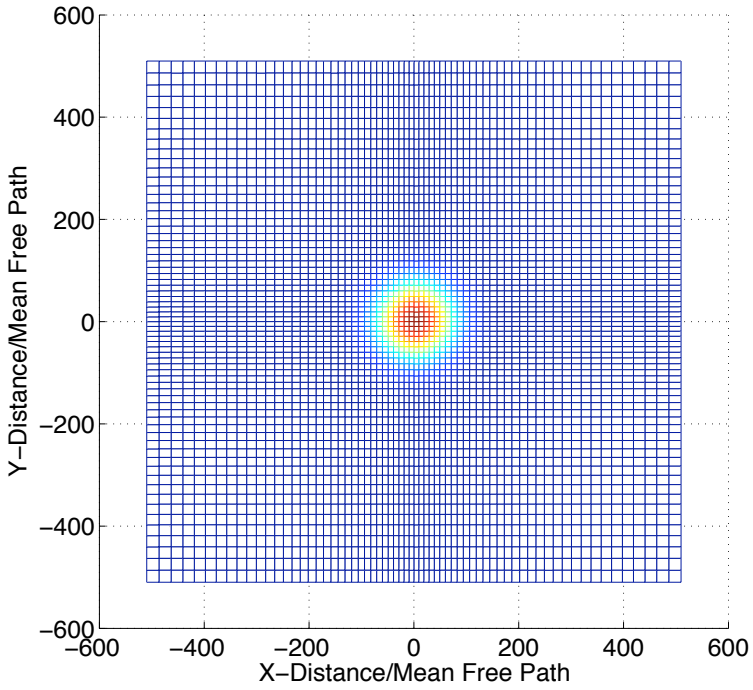

Figure 5.5: The computational grid used in the simulations described in this chapter. The laser heated region is shown – in the centre of this are the nine uniform grid cells.

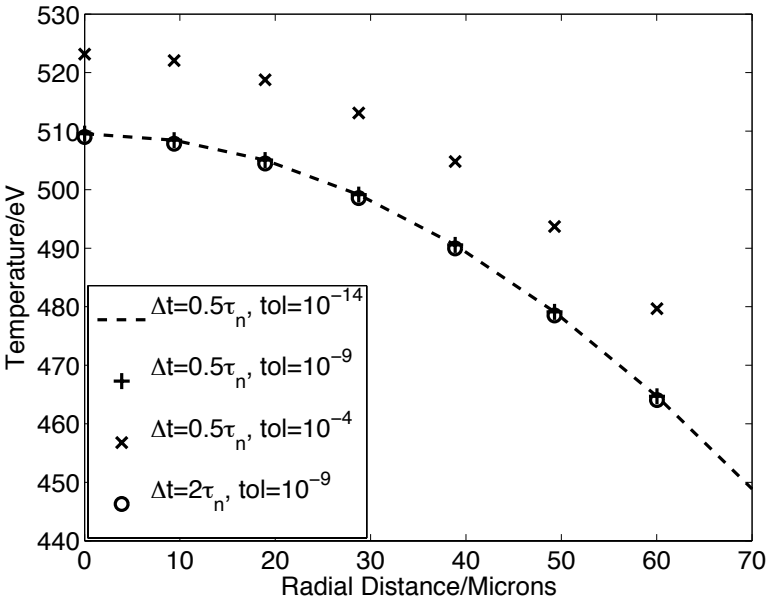

Figure 5.6: The temperature profiles from one-dimensional simulations of Froula's experiment after $5000\tau_n$. 'tol' refers to the accuracy in the non-linear iterations and matrix solver.

at the centre are set to be 2.5:1. The finer gridding in the centre allows adequate resolution of the laser spot. The coarser cells around the edge of the grid form a large buffer zone to ameliorate the problem of the hot electrons (which are highly mobile) reaching the edge of the simulation domain. Note that periodic boundary conditions are used in space (open were used in velocity space). Using this grid only 65 grid-cells may be used to simulate a region 6000 thermal mean free paths (for the 20eV background electrons)square, despite the fact that the laser spot has a radius of only 450 mean free paths (at the initial temperature of the gas jet – 20eV – the thermal mean free path is 0.167μm). The simulation domain is 1mm in length.

In order to properly resolve the distribution function as the plasma gets hotter the velocity space grid must go out to 30 times the thermal speed at 20eV. In order to resolve the distribution function well at low velocities and achieve a large enough grid size a geometric grid is required here too. 45 velocity-space grid-cells give adequate resolution. The ratio of the sizes of the first to last cells is 12:1. The simulation duration is 885ps. This corresponds to 14,000 thermal electron ion-collision times (again for the 20eV background particles). For the sake of accuracy a time-step of two collision times is chosen - requiring simulation for 7000 time-steps. The accuracy of the solution is also determined by the tolerance of the non-linear iterations and matrix solver. These are set to be 1×10^{-9} allowing an accurate solution in a reasonable

amount of computational time. These tolerances may seem low when compared to the numerical accuracy of double precision numbers – 1×10^{-16}. In figure 5.6 the consequences of using such relatively low tolerances and a large time-step are shown. The resulting temperature profiles from four one-dimensional simulations after $5000\tau_n$ show that there is very little difference between simulations using a time-step of $0.5\tau_{ei}$ and tolerances of 1×10^{-14} and those using $2\tau_{ei}$ and 1×10^{-9}. Dropping the tolerance to 1×10^{-4} is unacceptably deleterious to the accuracy of the solution.

The diffusive approximation – $f = f_0 + \mathbf{f}_1 \cdot \hat{\mathbf{v}}$ is valid for this simulation. The maximum value of the ratio $|f_1/f_0|$ is 0.1 between 0-4 times the local thermal speed in the spot's centre for a 12T applied field after 440ps. In the 12T case the temperature gradients are greatest and so the largest $\mathbf{f}_1$ develops. Finally, the laser heating profile and the magnetic field need to be considered. A Gaussian profile is imposed for the laser intensity with an e-folding half-width of 75μm:

$$\frac{\partial \tilde{T}_e}{\partial \tilde{t}} = \left(\frac{\partial \tilde{T}_e}{\partial \tilde{t}} \right)_{MAG} \exp\left[-\frac{(\tilde{x}^2 + \tilde{y}^2)}{\tilde{\lambda}^2} \right] \tag{5.1}$$

Here, λ is the width of the heating spot. The magnitude of the heating profile for inverse bremsstrahlung and Maxwellian heating are as given in the previous chapter, i.e.:

$$\left(\frac{\partial \tilde{T}_e}{\partial \tilde{t}} \right)_{IB} = \frac{4}{9\sqrt{\pi}} \frac{\tilde{Z}^2 \tilde{n}_i \tilde{v}_{osc}^2}{\tilde{n}_e \left(2\tilde{T}_e \right)^{3/2}} \qquad \left(\frac{\partial \tilde{T}_e}{\partial \tilde{t}} \right)_{MH} = \frac{D_0}{\hat{Z}} \tag{5.2}$$

The heating rate for the Maxwellian heating simulations is set to be equal to the rate of inverse bremsstrahlung. Thus D_0 is chosen to be:

$$D_0 = \frac{4\hat{Z}\tilde{Z}^2 \tilde{n}_i \tilde{v}_{osc}^2}{9\sqrt{\pi}\tilde{n}_e \left(2\tilde{T}_e \right)^{3/2}} \tag{5.3}$$

The light is circularly polarised and deposits 100J of energy in 1ns – the wavelength is set as 1.054μm. The heating profile is chosen so that the laser intensity rises linearly from zero to its maximum value in 180ps, is constant for 525ps and then linearly decreases for the remaining 180ps. This emulates the real situation in experiments – the laser is not 'switched on' instantly. Four different magnetic fields are externally imposed - 0T,2T,4T and 12T.

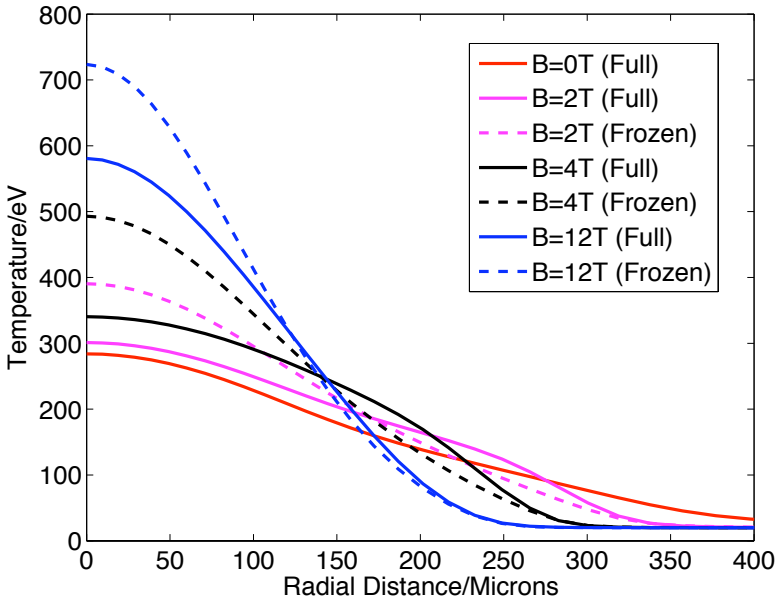

Figure 5.7: Plasma temperature profiles after laser heating for 440ps with imposed magnetic fields at 0T, 2T, 4T and 12T. The solid lines – labelled 'full' – use the full equation for the magnetic field. Those labelled 'frozen' – the dashed lines – assume that the magnetic field is frozen to the plasma.

5.3 Simulation results

Figure 5.7 gives the radial temperature profiles after 440ps. In the field-free case there is the expected non-local pre-heat of the plasma due to the low collisionality of the hot electrons [12,45]. The peak plasma temperature in this case is 284eV. At this temperature the mean free path of an electron moving at twice the thermal speed is $244\mu m$ – larger than the laser spot size – non-local behaviour is expected. Recall that the heat is carried by those electrons moving with speeds between two to three times the thermal speed. In the 12T case the pre-heat is suppressed. The maximum temperature in this case is 581eV, giving a mean free path for electrons moving at twice the thermal speed of 1.24mm; however, the Larmor radius of these electrons is $26\mu m$ in the centre of the spot – where the plasma is hottest and the magnetic field strength least. The fact that the larmor radius is less than the mean free path means the consequent reduction in the mobility of the electrons should go some way towards localising the heat transport; exactly how local the transport is in this and the other cases will be discussed in section 5.5.

The increased levels of pre-heat when the applied magnetic field strength is reduced from 12T – to 4T and then to 2T – suggest that non-local effects are becoming

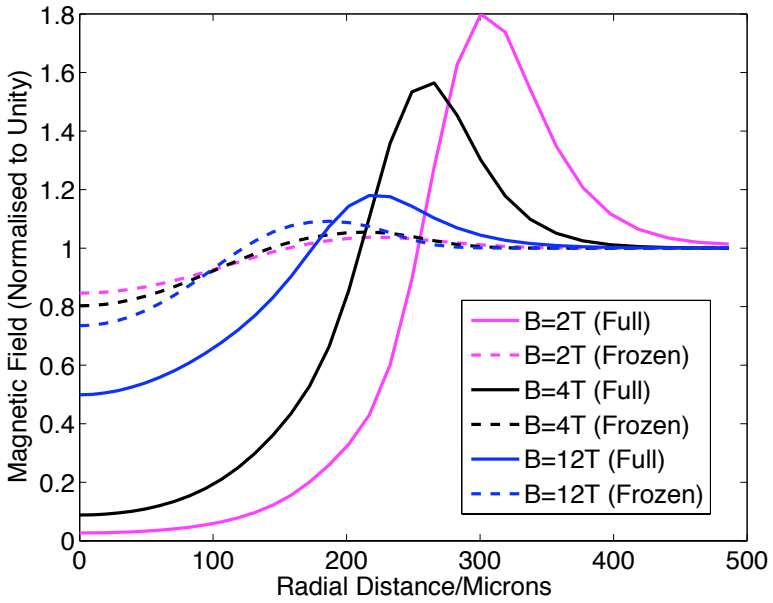

Figure 5.8: Magnetic Field profiles after 440ps. The solid lines are for the simulations where the full magnetic field calculation has been carried out, the dashed lines for those where only frozen-in flow has been used.

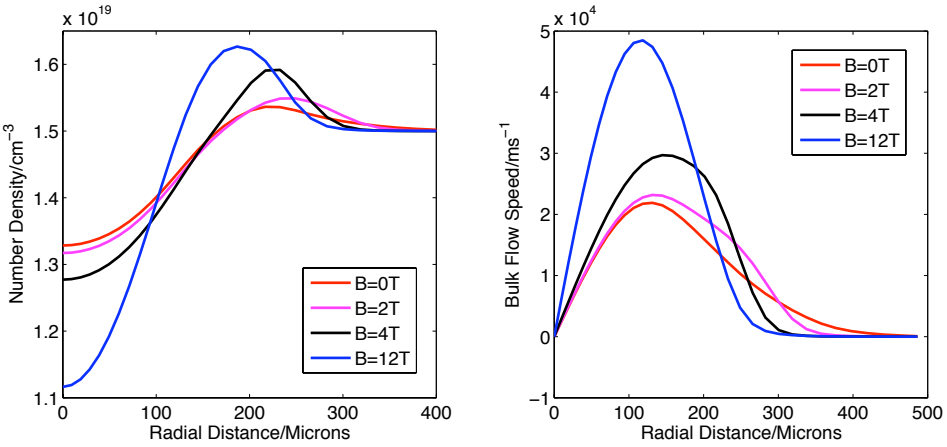

Figure 5.9: The electron density (left) and radial flow velocity (right) for each applied magnetic field after 440ps.

more important as the B-field strength is decreased. The 'kinks' in the temperature profiles for 2T and 4T (between $200\mu m$ and $300\mu m$ from the centre of the spot) indicate that transport barriers are formed in these simulations. This is confirmed by the magnetic field profiles – shown by the solid lines in figure 5.8. In the 2T and 4T cases the magnetic field is largely cavitated in the laser heated region and 'piles up' several hundred microns away from the centre of the spot, in the next section this will be shown to be the result of Nernst advection of the field [13]. This accumulated field forms the transport barrier – the consequent reduction in the electron's mobility slows heat transport here. The profiles of the important hydrodynamic parameters – the density and radial bulk flow velocity – after 440ps are shown in figure 5.9. As the applied magnetic field strength increases the more heat is 'bottled up' in the central laser heated region by the reduction in the electron's mobility. This means that an increased amount of hydrodynamic flow at a higher flow velocity takes place as the applied field is increased. Note that plots of the current density and heat flow will be shown in sections 5.4 and 5.5.

The new terms in the augmented code are not conservative with regards to number density or energy. However the change in these two variables is expected to be insignificant for a simulation which is adequately resolved spatially and temporally. The time evolution of the total number density has been examined in a typical simulation (B=12T) for the old code and the version with hydrodynamics in order to compare them – the results are shown in figure 5.10. The new code does indeed numerically gain mass, but only by 0.5% at the worst. The simulation using Maxwellian heating is also included (see section 4.3.5). The plasmas simulated are being heated so energy is not conserved. The effects of the new terms on energy gain in the system may be examined by comparing to IMPACT without hydrodynamics – energy input is comparable in the new code when using IB heating and MH. The results are not identical for these two heating mechanisms as the precise rate of energy input depends on T_e and n_e and these evolve differently in the two situations. The change in the modulus of the total momentum after 440ps is only 0.01% of the maximum momentum (also after 440ps).

5.4 Magnetic field advection

Figure 5.11 shows the azimuthal component of the current (j_θ) after 440ps for a 12T imposed B-field. The radial current is initially zero but may grow up at late times (after 440ps) due to an instability. This instability is discussed in section 5.7.1. Before

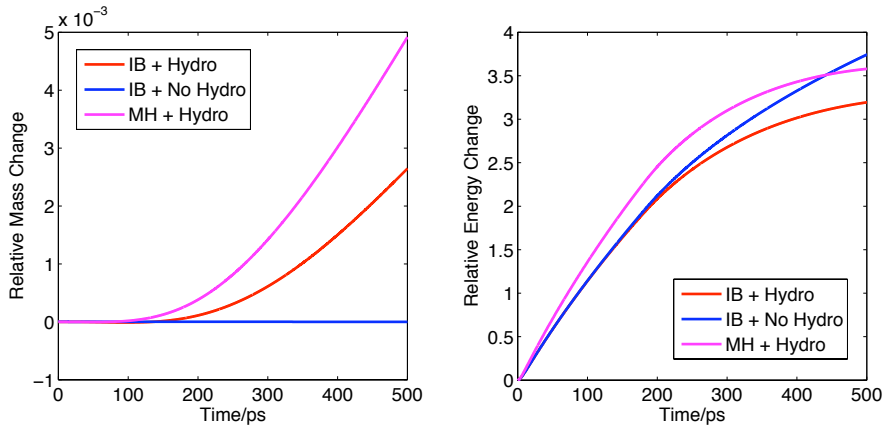

Figure 5.10: Time evolution of the relative change in the total mass (left) and the total energy (right) of the system. The plots are for IMPACT with and without hydrodynamic ions and also compare the effects of Maxwellian heating to inverse bremsstrahlung.

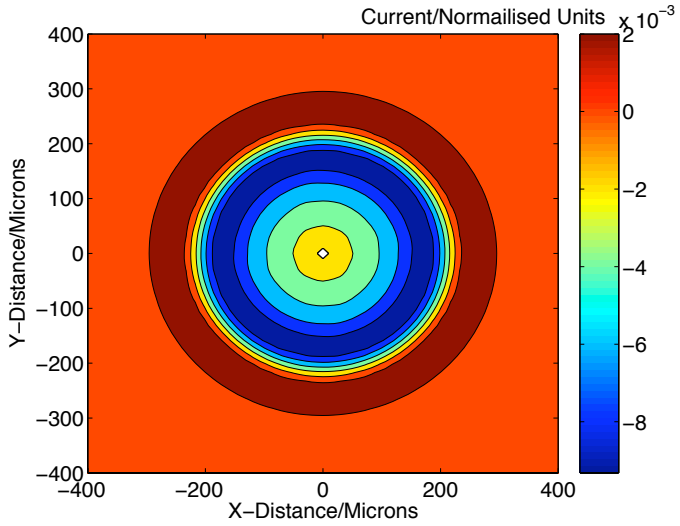

Figure 5.11: The current density in the azimuthal direction (j_θ) for a 12T imposed field after 440ps.

the onset of this instability the following equation holds:

$$\frac{\partial B}{\partial r} = -\mu_0 j_\theta \tag{5.4}$$

Therefore,the radial gradient in the B-field is supported by the azimuthal current. This current is consistent with that shown in figure 5.11.

In section 2.3.2 an equation for the rate of change of the magnetic field was derived from the classical Ohm's law [33, 34]. In the geometry considered here, i.e. where the gradients of the physical variables are perpendicular to the magnetic field and the system displays cylindrical symmetry along an axis parallel to this field, this equation becomes:

$$\frac{\partial B}{\partial t} + \nabla \cdot \left[\left(\mathbf{C} + \mathbf{v}_N \right) B \right] = \nabla \cdot \left(\frac{\eta_\perp}{\mu_0} \nabla B \right) \tag{5.5}$$

$$\eta_\perp = \frac{\alpha_\perp}{n_e^2 e^2} - \frac{\beta_\wedge^2 T_e}{e^2 \kappa_\perp} \tag{5.6}$$

It should be noted that in order for this equation to hold the system must be uniform in the z-direction. The divergence term on the left describes frozen-in flow and the Nernst effect [90, 91]. The term on the right hand side is resistive diffusion. Resistive diffusion may be neglected, this is justified by the fact that the magnetic Reynolds number is of the order of 10^6 (this is calculated at the point of maximum hydrodynamic flow). $\mathbf{C}$ is the plasma flow velocity and $\mathbf{v}_N$ is the Nernst velocity and describes advection of the magnetic field by the Nernst effect. The Nernst velocity is proportional to the heat flow and is given by [33, 52]:

$$\mathbf{v}_N = \frac{\beta_\wedge}{e \kappa_\perp B} \mathbf{q}_e \approx \frac{\mathbf{q}_e}{5/2 n_e T_e} \tag{5.7}$$

Here $\beta_\wedge$ and $\kappa_\perp$ are the thermoelectric coefficient perpendicular to the B-field and temperature gradient and the thermal conductivity perpendicular to the B-field and parallel to the cross-field component of the temperature gradient. The second (simpler) form has been derived making the assumption that the electron-ion collision frequency is proportional to v^{-2} [33]. This assumption works well for the plasma conditions simulated here.

The dashed lines in figure 5.8 show the magnetic field profiles if frozen-in flow is the only advection mechanism. This profile is calculated by noticing the similarity between the continuity equation and the magnetic induction equation, taking their

ratio and exploiting the 1-D symmetry of the problem (which is valid up to 440ps – see section 5.7.1).

$$\frac{\partial n_e}{\partial t} + \frac{\partial}{\partial r}\left[n_e C\right] = 0 \qquad \frac{\partial B}{\partial t} + \frac{\partial}{\partial r}\left[BC\right] = 0 \tag{5.8}$$

$$\frac{\partial}{\partial t}\left(\frac{B}{n_e}\right) + C\frac{\partial}{\partial r}\left(\frac{B}{n_e}\right) = 0 \tag{5.9}$$

Equation (5.9) shows that the ratio B/n_e is constant in a given fluid element. In the simulations this ratio is initially uniform everywhere, thus it must remain so – enabling calculation of the magnetic field given the density profile. Figure 5.8 shows that frozen-in flow leads to much less cavitation of the magnetic field from the laser heated region in all cases. The Nernst effect is particularly dominant for 2T and 4T. This variation of the relative importance of the Nernst effect and frozen-in flow is described by the 'Nernst number' (analogous to the magnetic Reynolds number):

$$R_N = \frac{v_N}{C} = \frac{1900}{Z\mathsf{ln}\Lambda_{ei}} \frac{T_e(\mathrm{keV})^{3/2}}{n_e(n_c)} \frac{\partial T_e(\mathrm{keV})}{\partial r(\mu\mathrm{m})} \frac{\beta_\wedge^c}{\omega\tau_B} \tag{5.10}$$

Here the temperatures are measured in keV, the distances in microns and the electron number density in terms of the critical density for 1.054μm light ($n_c = 10^{27}\mathrm{m}^{-3}$). The scaling in equation (5.10) shows that frozen-in flow should become dominant as the magnetic field is increased. Physically, this is due to the suppression of the heat flow by the magnetic field. In the 2T, 4T and 12T cases the values for R_N (at the point where the heat flow is largest and at $t = 440$ps) are 8, 3 and 0.3 respectively. If only frozen-in flow is included in the calculation at 2T and 4T the transport barriers are absent and the peak temperatures are over-estimated – these features could in principle be measured, giving an experimental verification of the dominance of the Nernst term. The conditions in this experiment are similar to those in the gas-fill of an ICF hohlraum. Taking typical values of: the density to be 0.025 times the critical density for 0.33μm light; the temperature to be 5keV and to change by 1keV over 500μm and the magnetic field to be 1T [7]; then R_N is of order one. Hence the Nernst effect is expected to be at least as important as frozen-in flow in causing the advection of magnetic fields generated at the hohlraum wall.

5.4.1 The Ettinghausen effect

The radial heat flow in the geometry of the simulations is given by:

$$q_r = \frac{-n_e T_e \tau_B}{m_e} \kappa_\perp^c \frac{\partial T_e}{\partial r} - \beta_\wedge^c \frac{j_\theta T_e}{e} \tag{5.11}$$

In deriving equation (5.10) the Ettinghausen term (the second term on the right-hand side) has been neglected. To justify this consider an 'Ettinghausen number' given by the ratio of the first and second terms on the right-hand side of equation (5.11) [92].

$$R_E = \left(\frac{n_e T_e \tau_B}{m_e} \frac{\partial T_e}{\partial r} \kappa_\perp^c \right) \left(\beta_\wedge^c \frac{j_\theta T_e}{e} \right)^{-1} \tag{5.12}$$

The ratio of this number to the Nernst number yields something which is easy to calculate:

$$\frac{R_E}{R_N} = \frac{\tilde{n}_e \tilde{C}}{\tilde{j}_\theta} \frac{\kappa_\perp^c}{(\beta_\wedge^c)^2} \omega \tau_B \tag{5.13}$$

The neglect of the Ettinghausen term should be worst for the B=12T case. A more magnetized plasma has a larger azimuthal current but a smaller radial heat flow. R_E is of the order of 1, 200 and 3000 in the 12T, 4T and 2T cases. Note that as the Ettinghausen number, defined in this way, becomes larger the relative importance of the Ettinghausen term decreases. Thus for large magnetic fields (>12T) the Ettinghausen term should be included in a calculation of the Nernst number. It is always included in the simulations.

5.4.2 The Nernst effect and the break-down of classical transport

The time evolution of the magnetic field and the degree of non-locality are strongly coupled to one another. The effect of the break-down in Braginskii transport has been shown to significantly affect the magnitude of Nernst advection [85]. Comparison of the rate of advection of the magnetic field at 250ps (when the 2T and 4T fields have cavitated by about 50% from the central region) as predicted by Braginskii transport with that produced by the VFP code shows that the VFP result is markedly reduced below that predicted classically. This is shown in figure 5.12. In the 2T case it is found to be five times smaller than predicted, for a 4T imposed field it is 1.3 times reduced on the laser axis. Thus the degree of non-locality controls the rate of B-field advection, which in turn controls the B-field strength and so the importance of non-locality. The classical prediction was made by inserting the current and temperature

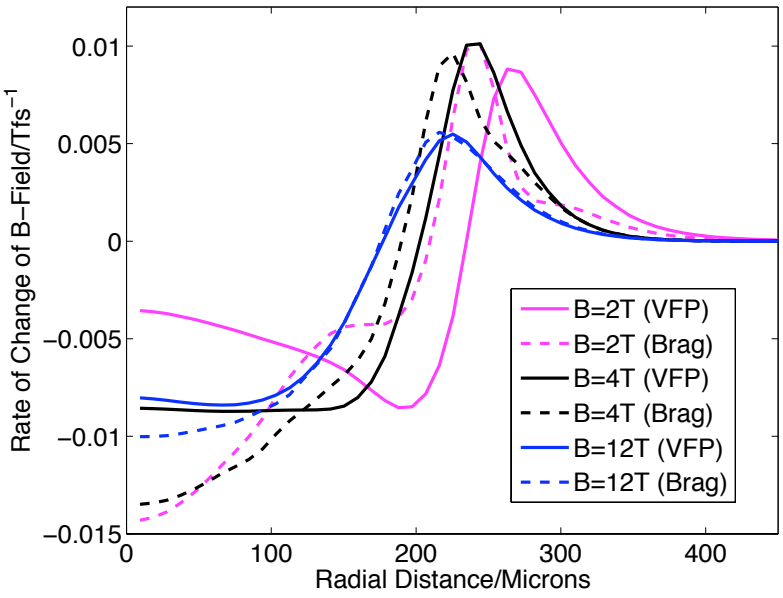

Figure 5.12: The rate of change of the magnetic field after 250ps as calculated from the curl of the electric field. The solid lines show the prediction of the VFP code, the dashed those of classical transport.

profiles from the VFP code at 250ps into the classical form of Ohm's law, i.e. equation (2.29). A similar method will be used to predict the classical heat flow using equation (2.30) in the next section.

5.5 Departures from classical transport

It is now appropriate to examine the applicability of Braginskii's theory to the simulations discussed thus far. Figure 5.13 shows the radial heat flow for each magnetic field and those calculated from classical transport theory. The radial heat flow is classical in the 12T case – the agreement with Braginskii's transport theory gets progressively worse as the imposed magnetic field strength decreases. Figure 5.14 shows the azimuthal (Righi-Leduc) heat flows from the simulations compared to those expected classically. Note that in the field-free case the heat-flow has no θ-component. Again, as the magnetic field strength increases the agreement with Braginskii improves. In the 12T case there is a discrepancy away from classical in the laser-heated region (from the spot's centre to 75μm) and well away from it (more than 250μm from the spot centre). An examination of the distribution function reveals that this is due to the combined effects of inverse bremsstrahlung heating causing the distribution to

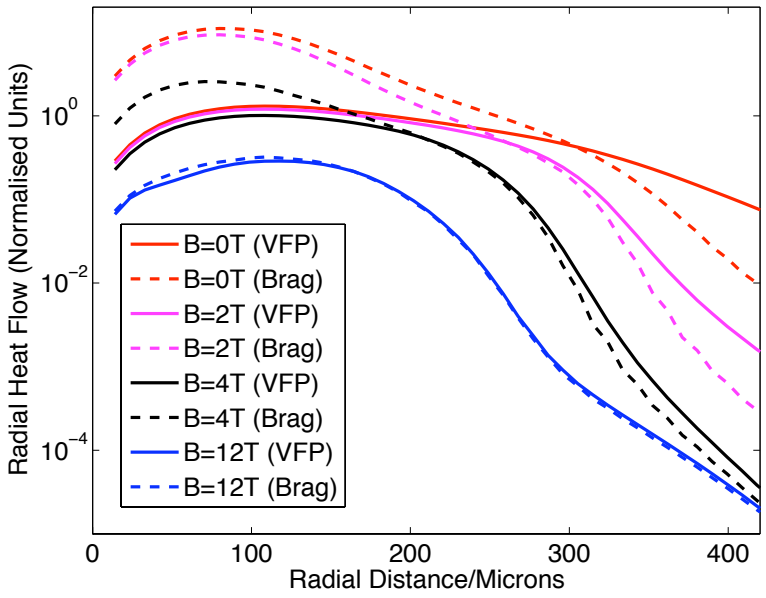

Figure 5.13: Spatial profile of the radial heat flow (normalised to the free-streaming limit for the background 20eV plasma) after 440ps at each of the applied B-fields. The solid lines are those calculated by those VFP code, the dashed are from classical transport theory.

tend to a super-Gaussian ($f \propto e^{(-v/v_T)^5}$) and the rise of non-local transport due to the expulsion of some the magnetic field from the centre. The increased importance of non-locality in the central region means that hot electrons from this region can pre-heat the plasma far away (more than 250 μm from the centre). Although the azimuthal heat flow is not important in the situation considered here it can play an important role when there is not such a high degree of symmetry.

Figure 5.15 shows the time evolution of the deviation of the radial heat flow away from Braginskii for each imposed magnetic field. This is calculated using the formula $\Delta q_r = (q_r - q_r^B)/q_r^B$ (q_r is the maximum radial heat flow from the VFP code and q_r^B is the maximum as predicted by Braginskii). The discrepancy from classical theory decreases as the imposed magnetic field is increased; this is as expected. More surprisingly, the general trend is for the agreement to be poor initially, improve and then deteriorate with time. The agreement at early times is poor in all cases. Up to 20ps the transport should still be 'local' – the maximum mean free path here is 1.7μm. The break-down of Braginskii theory comes from the IB heating. After 200ps (for an imposed field of 4T) non-local transport becomes important. In the field-free and 2T cases classical transport theory never works well although they do exhibit the same qualitative behaviour in their agreement with Braginskii as with the 4T field. The general pattern is for IB heating being important early on, non-locality later on;

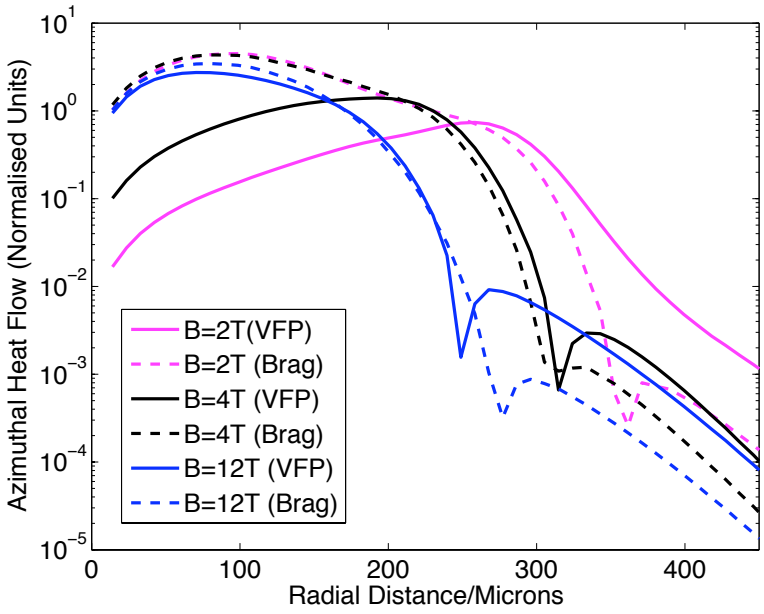

Figure 5.14: The radial profile of the azimuthal heat flow (normalised as in figure 5.13). The solid lines are those calculated by the VFP code, the dashed are those predicted by classical transport theory.

this is elucidated in section 5.6.3. Although the 12T case behaves more classically up to 440ps it will later be shown that by 885ps non-locality has re-emerged due to the magnetic field being cavitated to 1T in the central region.

The importance of the coupling between magnetic field cavitation and non-locality is illustrated by figures 5.16 and 5.17. Here this coupling has been removed by forcing the magnetic field to advect by frozen-in flow. In this case the advection velocity depends on the bulk flow velocity, which is takes longer to be strongly affected by the degree of non-locality – as a result of the slower response time of the ions. Figures 5.16 and 5.17 show that non-locality plays a much smaller role at 440ps in this case as the magnetic field has not cavitated at all strongly from the laser heated region.

5.6 The distortion parameter

It has already been mentioned that classical transport can break-down in long-pulse laser-plasma interactions because of non-locality but also because of the distortion of the distribution function due to IB heating. The difference between the distribution function and a Maxwellian distribution can be quantified in order to determine which of these effects is causing the deviation from classical transport. The distortion

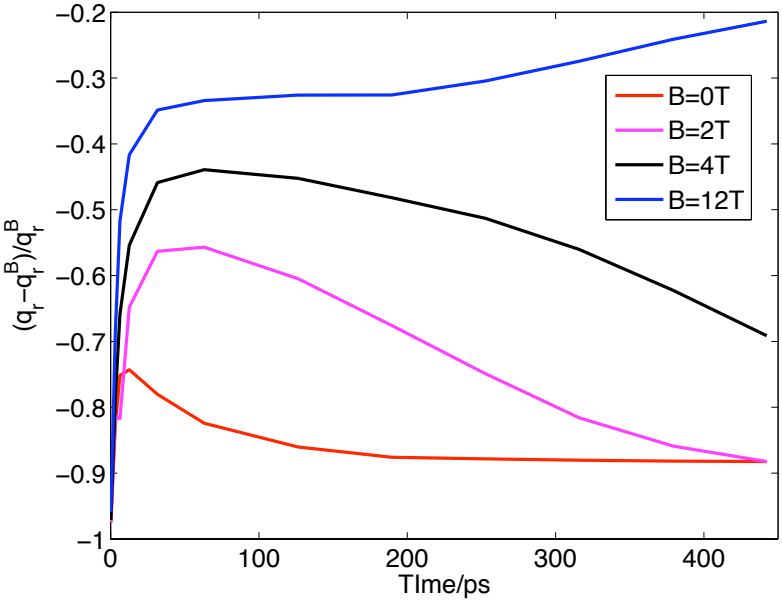

Figure 5.15: Time evolution of the relative discrepancy of the radial heat flow from Braginskii.

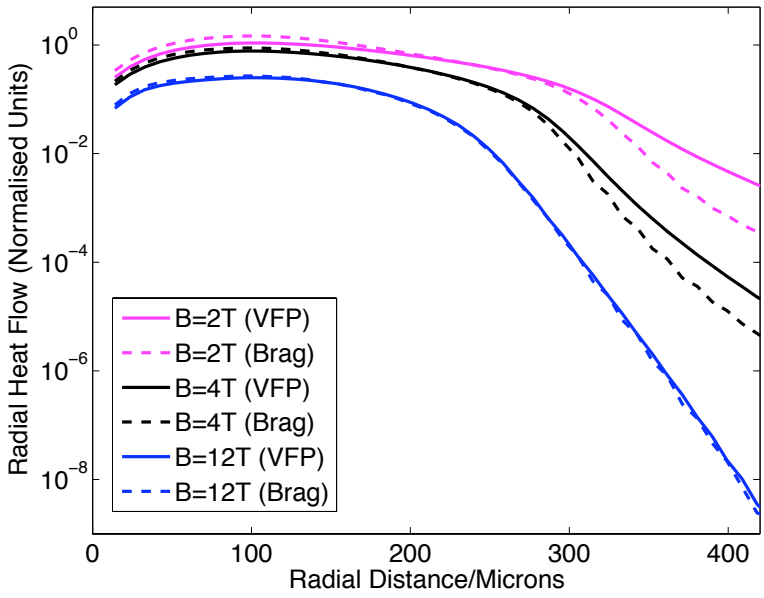

Figure 5.16: Spatial profile of the radial heat flow when frozen-in flow advects the B-field.

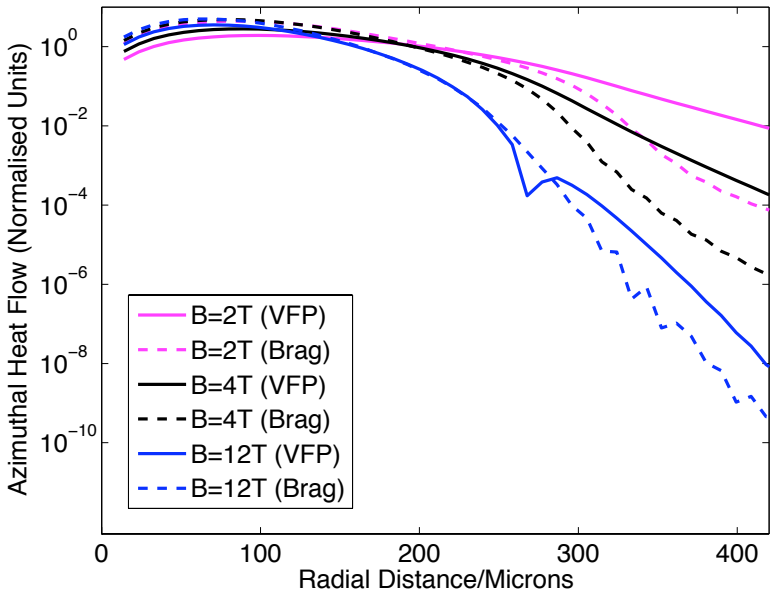

Figure 5.17: The radial profile of the azimuthal heat flow when frozen-in flow advects the B-field.

parameter is defined as:

$$\Delta = \frac{\langle \tilde{w}^{-2} \rangle}{\langle \tilde{w}^{-2} \rangle_M} \tag{5.14}$$

Where:

$$\langle \tilde{w}^m \rangle = \int_0^\infty \tilde{f}_0 \tilde{w}^{m+2} \mathrm{d}\tilde{w} \qquad \langle \tilde{w}^m \rangle_M = \int_0^\infty \tilde{f}_m \tilde{w}^{m+2} \mathrm{d}\tilde{w}$$

The variables in the above equations are all in normalised form – although this need not be the case for a dimensionless ratio such as Δ. The w^{-2} moment was chosen for simplicity, a generalised form of the distortion parameter is described in appendix F. The normalised Maxwellian (f_m) is the equivalent Maxwellian distribution with the same temperature and density as the plasma at that point, i.e.:

$$\tilde{f}_m = \frac{\tilde{n}_e}{\left(2\pi \tilde{T}_e\right)^{3/2}} e^{-\tilde{w}^2/2\tilde{T}_e} \tag{5.15}$$

Calculating the integral for a Maxwellian yields:

$$\langle \tilde{w}^{-2} \rangle_M = \frac{\tilde{n}_e}{4\pi \tilde{T}_e} \tag{5.16}$$

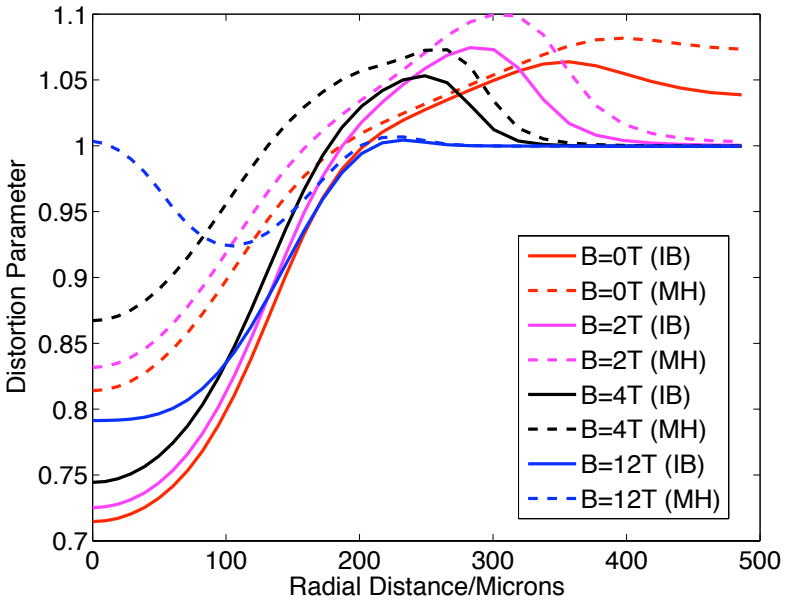

Figure 5.18: The distortion parameter calculated after 440ps for each magnetic field using both inverse bremsstrahlung (IB) and Maxwellian heating (MH).

The integral of f_0 must be calculated numerically, this is computed using Simpson's 1/3 rule – where the integral is represented by the sum $I = \frac{1}{3}\Delta x\,(f_0 + 4f_1 + 2f_2 + 4f_3 + \ldots)$. The distortion parameter calculated using this method is shown in figure 5.18.

5.6.1 The distortion from non-local transport

Figure 5.18 shows that the distortion parameter can be greater than or less than unity in different regions of the plasma. In the next two sections it will be shown that the sign of $(\Delta - 1)$ can be used to determine the mechanism by which the distribution function is distorted, i.e. it allows the distinction of regions where IB is dominant from those where non-locality is most important. To do this it is first necessary to calculate the distortion parameter analytically using a simple model of non-local transport.

A non-locally heated region is one with an excess of hot electrons in the tail of the distribution above that expected for a Maxwellian. This may be modelled by supposing that a 'non-local distribution' can be represented by a two-temperature Maxwellian – with the 'cold' distribution representing the bulk plasma and the 'hot' particles arising from the non-local pre-heat. The distribution function in this case is given by:

$$\tilde{f}_0 = \tilde{f}_{mc} + \tilde{f}_{mh} = \frac{\tilde{n}_{ec}}{\left(2\pi\tilde{T}_{ec}\right)^{3/2}} e^{-\tilde{w}^2/2\tilde{T}_{ec}} + \frac{\tilde{n}_{eh}}{\left(2\pi\tilde{T}_{eh}\right)^{3/2}} e^{-\tilde{w}^2/2\tilde{T}_{eh}} \tag{5.17}$$

Here $\tilde{n}_{ec}$ and $\tilde{T}_{ec}$ are the number density and temperature of the 'colds'; similarly $\tilde{n}_{eh}$ and $\tilde{T}_{eh}$ are those for the 'hots'. This formulation allows analytical calculation of the moments in equation (5.14), yielding the following expression for Δ:

$$\Delta = \frac{4\pi\tilde{T}_e}{\tilde{n}_e}\left(\frac{\tilde{n}_{ec}}{4\pi\tilde{T}_{ec}} + \frac{\tilde{n}_{eh}}{4\pi\tilde{T}_{eh}}\right) \tag{5.18}$$

$\tilde{n}_{ec}\,\tilde{T}_{ec}$ and $\tilde{n}_{eh}\,\tilde{T}_{eh}$ can be related to $\tilde{n}_e\,\tilde{T}_e$.

$$\tilde{n}_e = \tilde{n}_{ec} + \tilde{n}_{eh} \qquad \tilde{T}_e = \tilde{T}_{ec}\left(1 + \frac{\tilde{T}_{eh}}{\tilde{T}_{ec}}\frac{\tilde{n}_{eh}}{\tilde{n}_{ec}}\right)\left(1 + \frac{\tilde{n}_{eh}}{\tilde{n}_{ec}}\right)^{-1}$$

Substituting these results into equation (5.18) and making the assumption that the number density of 'hots' is much less than the number density of 'colds' – neglecting terms of the order of $(\tilde{n}_{eh}/\tilde{n}_{ec})^2$ and higher – yields:

$$\Delta = 1 + \frac{\tilde{n}_{eh}}{\tilde{n}_{ec}}\left(\tilde{T}_{eh} - \tilde{T}_{ec}\right)^2 \tag{5.19}$$

This gives a distortion parameter that is always greater than one. The appropriateness of this model is examined in figure 5.19. This shows a comparison of the isotropic part of the distribution function to a two-temperature Maxwellian and a single temperature Maxwellian (using least squares fitting) after 440ps with B=0T. Far from the laser heated region there should be some pre-heat from hot electrons – thus the two temperature fit shown in figure 5.19 is made 590μm from the spot centre; this is well in front of the main heat front. The two-temperature distribution fits the data much better in the tail of the distribution – where the non-local electrons are important. The number densities and temperatures from the 'cold' and 'hot' distributions can be extracted from the fit.

$$\begin{aligned} n_{ec} &= 0.95 n_{e0} & T_{ec} &= 1.04 T_{e0} \\ n_{eh} &= 2.90 \times 10^{-4} n_{e0} & T_{eh} &= 5.98 T_{e0} \end{aligned}$$

Note that n_{e0} is the background electron number density and T_{e0} is the background electron temperature. The assumption that the number of hot electrons is small

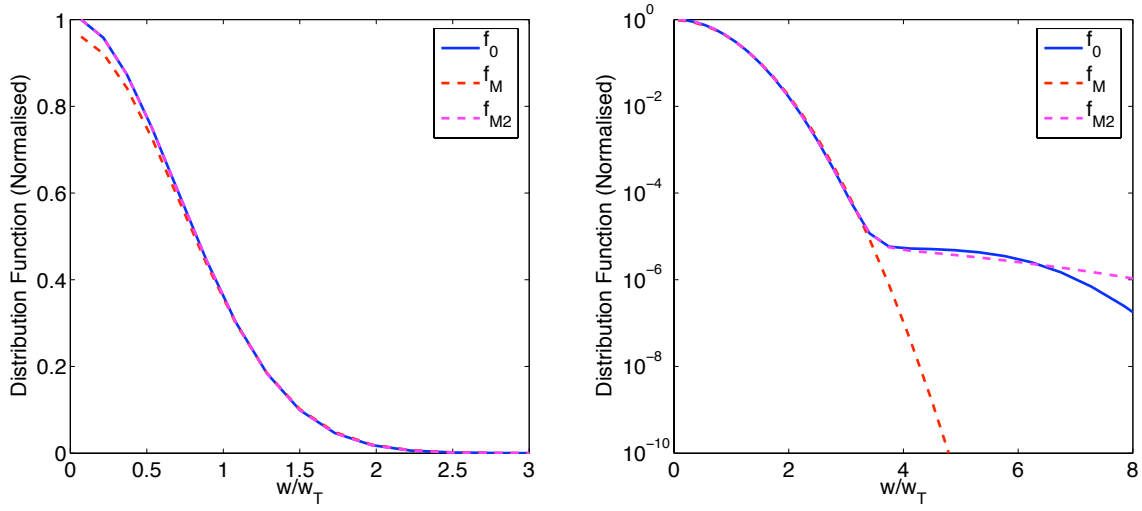

Figure 5.19: A comparison between the isotropic part of the distribution function (f_0), the best fitting Maxwellian (f_M) and two-temperature Maxwellian (f_{M2}). The left-hand plot indicates the fit to the body of the distribution, the right-hand plot emphasises the tails. The velocity is localised to the local thermal speed (which may be different from the background thermal speed) and the distributions are normalised such that $f_0(w=0)=1$.

is borne out. From these parameters the distortion parameter is estimated to be 1.01. Figure 5.18 shows that this is a reasonable estimate well outside the laser heated region, where non-locality is expected to pre-heat the plasma. The residuals ($r = \sum |f_0 - f_{0fit}|^2$) for the single temperature and two-temperature fits are 1×10^{-4} and 6×10^{-13}; the agreement, as quantified in this way, is ten times better using the two-temperature Maxwellian.

5.6.2 The distortion from inverse bremsstrahlung

The effect of inverse bremsstrahlung heating on the distortion parameter will now be determined. IB heating results in distribution functions which tend to a Langdon distribution. When electron-electron collisions are accounted for it is necessary to work with the more general distribution where m is not 5 (a super-Gaussian distribution). This was discussed in section 2.4.5. The normalised form of the super-Gaussian distribution is:

$$\tilde{f}_0^{SG} = C(m)\frac{\tilde{n}_e}{(2\tilde{T}_e)^{3/2}} e^{\left(-\tilde{w}/\alpha_e(2\tilde{T}_e)^{1/2}\right)^m} \tag{5.20}$$

Here $\alpha_e = [3\Gamma(3/m)/2\Gamma(5/m)]^{1/2}$ and $C(m) = m/4\pi\alpha_e^3\Gamma(3/m)$. Substituting equation (5.20) into equation (5.14) yields the following result for the distortion pa-

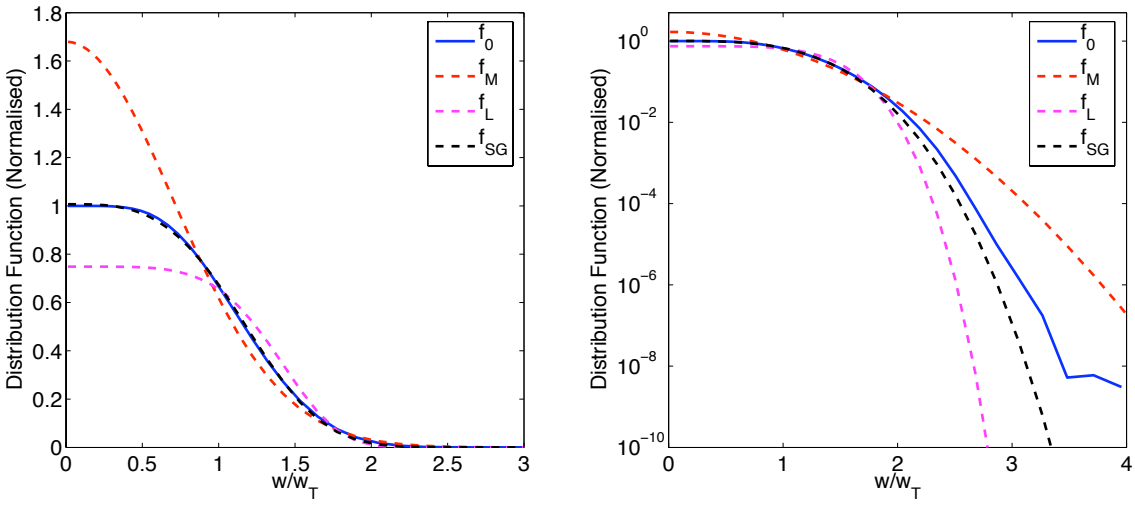

Figure 5.20: A comparison of the distribution function f_0 to the best fitting Maxwellian f_M, Langdon f_L and super-Gaussian distribution f_{SG} emphasising the body (left) and the tail (right). The velocity and distributions are normalised in the same way as in figure 5.19.

rameter:

$$\Delta_{SG} = \frac{\Gamma\left(5/m\right)\Gamma\left(1/m\right)}{3\Gamma\left(3/m\right)^2} \tag{5.21}$$

In fact in the idealised case of IB heating with no electron-electron collisions or thermal transport the distribution tends towards a super-Gaussian with $m = 5$ (Langdon). In this case equation (5.21) yields the following result in terms of gamma functions:

$$\Delta_{m=5} = \frac{\Gamma\left(1/5\right)}{3\Gamma\left(3/5\right)^2} = 0.69 \tag{5.22}$$

Figure 5.18 shows that Δ never gets as low as this, implying that the distribution function has $2 < m < 5$. The distribution function from the simulation, at the spots centre, is compared with the best fitting Langdon and super-Gaussian distributions in figure 5.20 (for an applied B-field of 12T and after 440ps). The $m = 5$ does not fit the data well; an $m = 3.4$ is best – with a residual of 5×10^{-10}. Such a distribution gives a Δ of 0.77. The super-Gaussian fit is good for the bulk of the distribution – out to eight times the thermal speed – but fails in the tail. This means that the such a fit may not be able to predict transport quantities which rely on high moments of the distribution function [78]. This will be dealt with further in chapter 6.

Now the utility of the distortion parameter becomes clear. For a non-locally pre-heated distribution function it will be greater than unity; for distortions from

IB heating it will be less than unity. This allows the identification of the spatial extent of the non-classicality caused by each of these effects. This simple explanation of the distortion parameter is complicated when one notes that a deficiency of hot electrons, which occurs in a non-locally cooling region (i.e. the region from which the hot electrons are flowing), also leads to a value of the distortion parameter which is less than unity. The distortion parameters for the simulations using Maxwellian heating illustrate this in figure 5.18. Comparing the distortion when using IB with that using Maxwellian heating, shows that non-locality has an effect even in the most magnetised (12T) case. However the distortion due to IB heating is in this case much larger. In the 0T case non-locality causes most of the distortion in the central region. The 2T and 4T cases lie somewhere between these limiting cases, i.e. both IB heating and the deficit of hot electrons distort the distribution function in the central region. The relative importance of IB heating increases with the applied magnetic field strength. Non-local pre-heat is the mechanism responsible for the distortion outside this central region and is suppressed as the strength of the externally magnetic field is increased.

5.6.3 Time evolution of the distortion parameter

The time evolution of the distortion parameter for a 4T imposed magnetic field is shown in figure 5.21. The dashed lines in this figure show the evolution of the distortion when Maxwellian heating is used. This shows the increased importance of non-locality with time which has already been discussed. The solid lines show that when inverse bremsstrahlung is used there is much more distortion of the distribution function in the laser heated region. In this case the rate of this distortion in the centre saturates after 190ps.

5.7 The behaviour of the system after 440ps

5.7.1 A Nernst driven instability

The time limit of 440ps on the simulations in this chapter was due to the growth of an instability – computational constraints allowed the simulation of the system up to 885ps on a single processor. In figure 5.22 the temperature, magnetic field and heat flow profiles are shown for the circular heating pattern with a 12T imposed field after 885ps. The magnetic field shows a small departure from circular symmetry and this leads to a much larger asymmetry observed in the radial heat flow. The instability

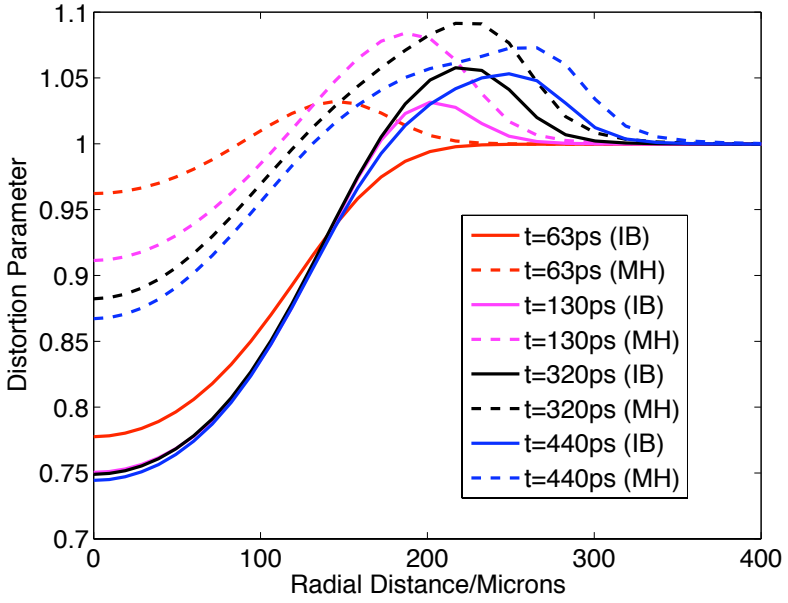

Figure 5.21: The time evolution of the distortion parameter for an imposed field of 4T.

is not dependent on the inclusion of ion motion and gets more severe as the imposed magnetic field increases.

Is this instability physical? A typical signature of a numerical instability is that its wavelength tends to be equal to the grid cell size. This does not appear to be the case in the results shown in figure 5.22. One numerical cause of this instability may be the attempt to resolve a circular laser spot on a square grid. In order to rule this possibility out a planar Gaussian heating profile has been simulated with an imposed sinusoidal heating perturbation with an amplitude of 1% of the laser and a wavelength one-quarter of the system size. In this simulation a uniform grid may be used, spanning a $6000\lambda_n$ by $4000\lambda_n$ system with a grid of dimensions 65×55. The velocity space gridding was the same as the simulations already described in this chapter. The results of these simulations are shown in figure 5.23. They show clearly that the system is inherently unstable.

For the circular heating profile the instability is less severe. In this case the fact that the heat fronts are spread over cylindrical surfaces means that any perturbations in the temperature profile will be stretched as the heat front expands and so their amplitude will decrease. Another difference between the circular and linear simulations is that in the latter case a one in one hundred perturbation is made to the temperature – in the former case the perturbation is due to numerical noise. This noise is enhanced by the non-uniform grid used in the circular simulations; thus the

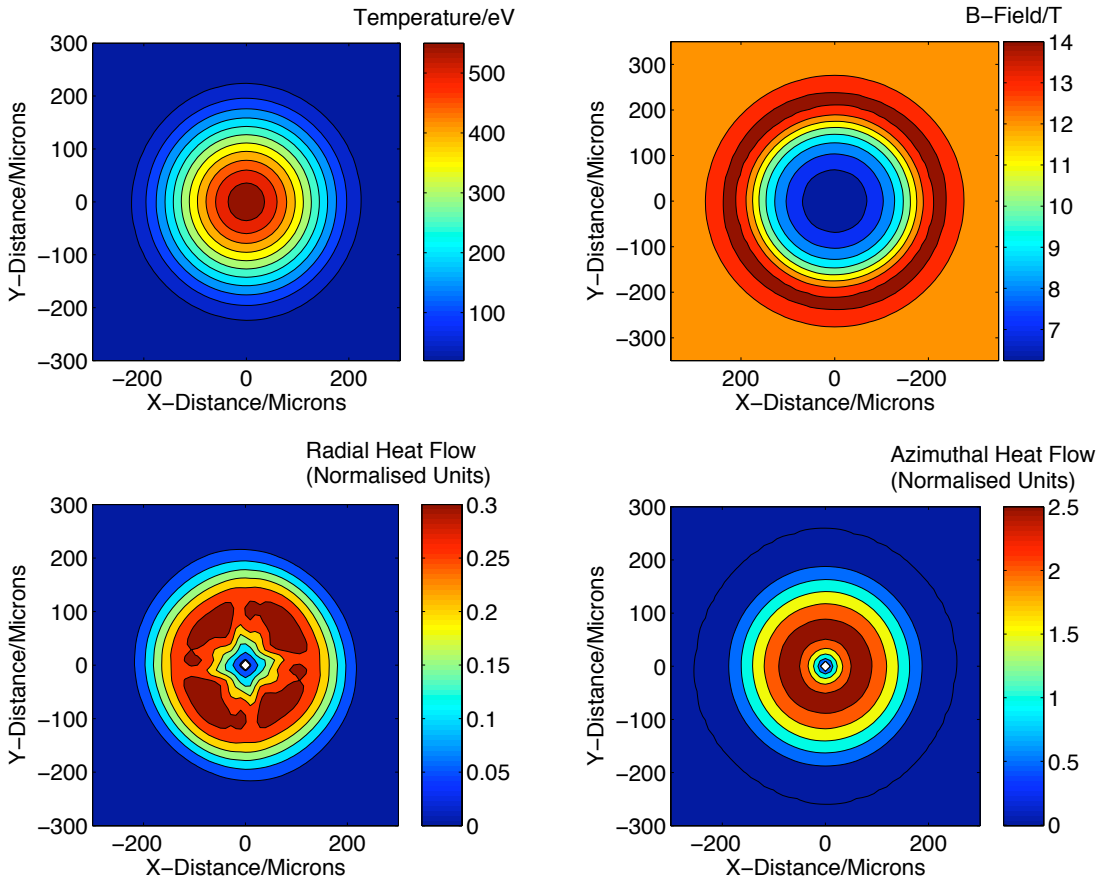

Figure 5.22: Profiles after 885ps in B=12T circular heating run. Top left: temperature. Top right: magnetic field. Bottom left: radial heat flow. Bottom right: azimuthal heat flow.

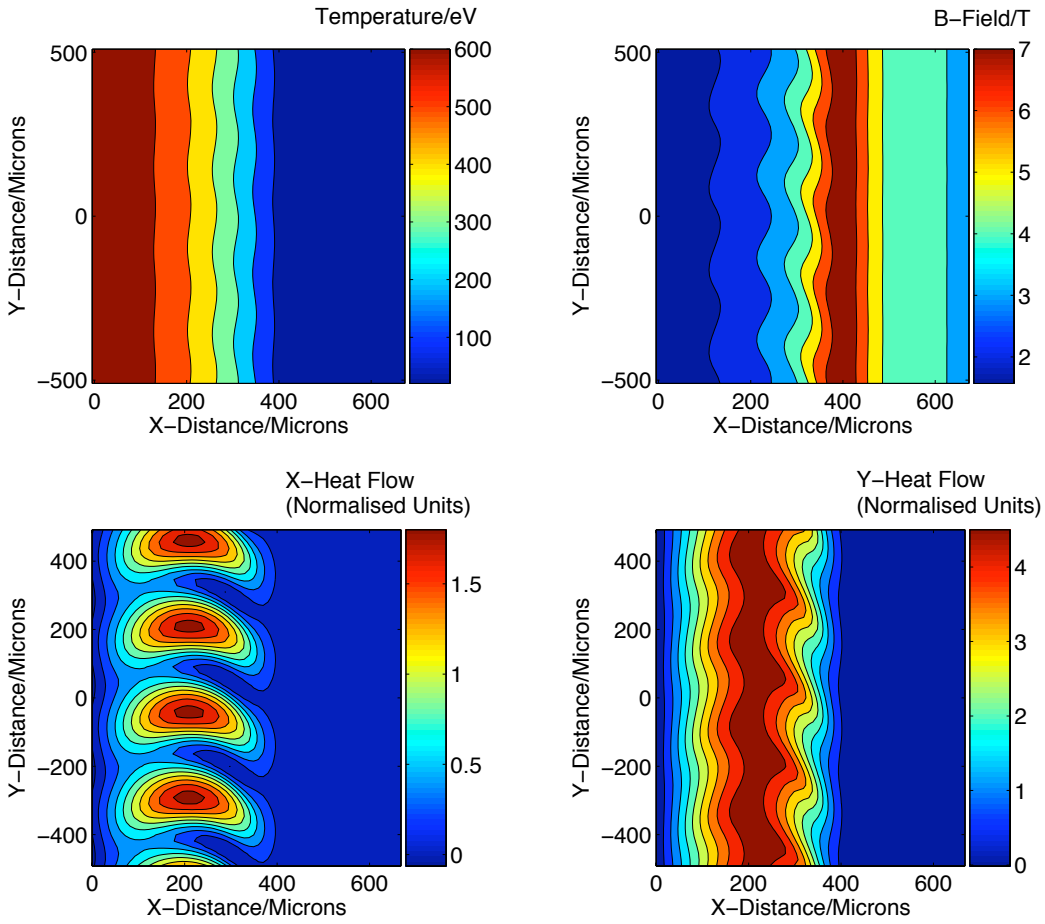

Figure 5.23: Profiles after 885ps in B=4T linear heating run. Top left: temperature. Top right: magnetic field. Bottom left: x-component of the heat flow. Bottom right: y-component of the heat flow.

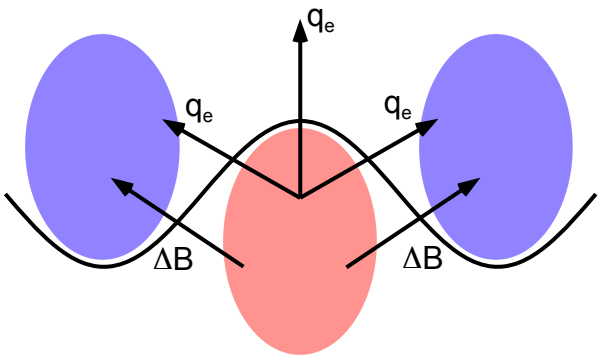

Figure 5.24: An illustration of a proposed qualitative mechanism for the Nernst instability.

onset of the instability may be controlled by the enlargement of the cells experienced by the expanding heat front. Determining the onset of this instability in an experimental situation will require a knowledge of the inhomogeneities inherent in such an experiment.

As the Nernst effect is dominant in advecting the B-field it is reasonable to suppose that it is the cause of the instability. In fact a similar Nernst-driven instability has already been discussed with no background magnetic field [93]. Determining the mechanism of the instability is left as further work. Figure 5.24 gives one possible qualitative explanation. A perturbed temperature profile is represented by the sinusoidal contour, the red region is 'hot' and the blues are 'cold'. A uniform background magnetic field is applied. The directions of the expected heat flows are shown; as is the compression or rarefaction of the B-field – ΔB is the change in B and the magnetic field is always in the z-direction, which is out of the page in the figure. The magnetic field is expected to be advected out of the hot region by the Nernst effect, causing it to build up in the 'cold' regions. This will limit transport in these regions. If the plasma is being heated it is then plausible to imagine that this might cause 'fingers' of hot plasma to flow between the 'cold' regions. The Nernst effect amplifies the perturbation to the B-field [90, 91].

5.7.2 Nernst cooling of the central region

On the condition that the instability described in the previous section is not a numerical effect – the reasons for believing this have been discussed – the simulations discussed in this chapter may be extended to 885ps. The central (maximum) temperature is plotted against time in figure 5.25. The temperatures in each case seem

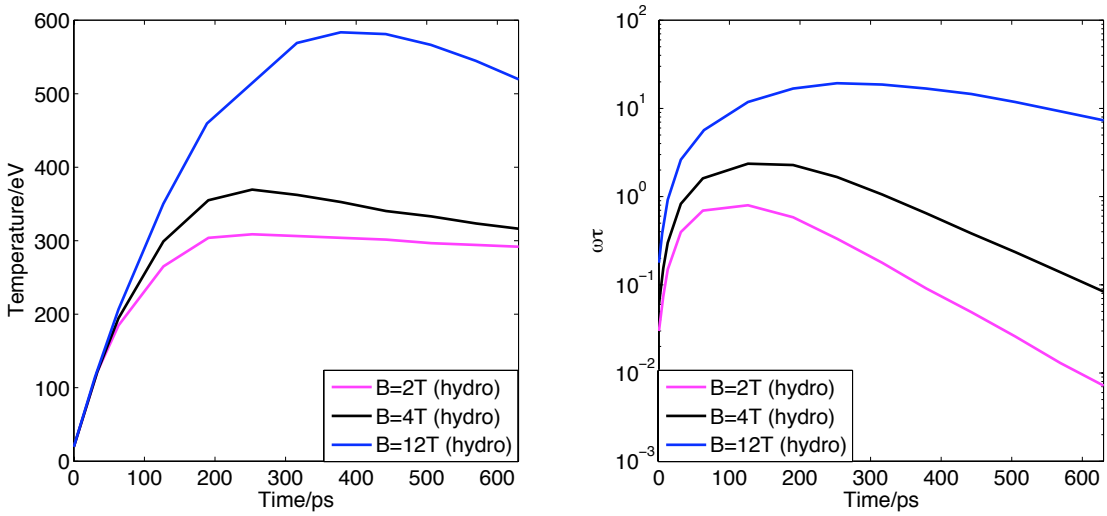

Figure 5.25: The time evolution of the central (maximum) temperature (left) and Hall parameter (right) for B-fields of 2T, 4T and 12T.

to saturate, the maximum temperature being higher as the imposed magnetic field strength is increased. The maximum temperature in the centre of the spot depends upon the balance of heating and thermal conduction. The rate of heating decreases as the temperature increases. Equation (4.43) shows that this rate is proportional to $T_e^{-3/2}$. This explains the saturation. The rate of thermal conduction decreases as the imposed field increases thus the saturated temperature gets larger with increasing B-field. The central temperature decreases between $t = 400$ps and $t = 700$ps in the 2T, 4T and 12T cases; this is despite the fact that the laser heats the plasma with its maximum intensity.

The mechanism for this decrease can be determined by considering the Hall parameter:

$$\omega\tau = \frac{eB}{m_e}\frac{1}{YZ^2 n_i \ln\Lambda_{ei}}\left(\frac{2T_e}{m_e}\right)^{3/2} = \alpha\frac{B}{n_e}T_e^{3/2} \qquad \alpha = \frac{2^{3/2}e}{YZm_e^{5/2}\ln\Lambda_{ei}} \tag{5.23}$$

As previously discussed, if frozen-in flow were the dominant mechanism of magnetic field advection then B/n_e would be a constant. In this case $\omega\tau \propto T_e^{3/2}$. If this were true it would be impossible for $\omega\tau$ to decrease and so the central region could not cool while the laser were still on at full power. The importance of the Nernst effect, for all the values of the applied field simulated, means that the magnetic field cavitates from the central region faster than the density does. As a result B/n_e decreases

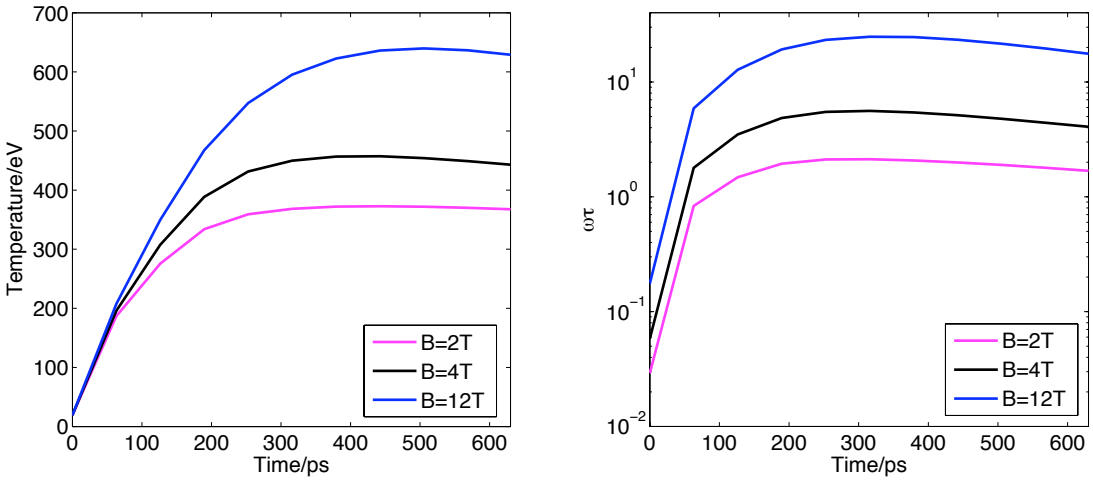

Figure 5.26: The time evolution of the central (maximum) temperature (left) and Hall parameter (right) when only frozen-in flow is responsible for the advection of the B-field.

and so does $\omega\tau$ which causes the central temperature to decrease. Of course there is electron density dependence in the Coulomb logarithm which has been suppressed. This dependence is weak and would have a much smaller effect. The time evolution of the central temperature and Hall parameter when frozen-in flow advects the B-field are shown in figure 5.26. The temperature does indeed decrease much less rapidly than when the Nernst effect is included.

5.8 Summary

Magnetic field cavitation and the re-emergence of non-local transport

In the presence of magnetic fields large enough to significantly reduce the mobility of the hot electrons (12T) it was shown that the cross-field transport of heat could still deviate from classical – this was manifested most readily in the azimuthal component of this transport. Not all of this deviation was due to non-locality, IB heating also distorted the distribution function away from Maxwellian. Further deviation away from Braginskii heat transport occurred as the externally applied B-field was reduced from 12T to 4T, then to 2T. This was due to the increasing importance of non-local effects. In the field-free case Braginskii gave a radial heat flow which was two orders of magnitude too large. The situation was complicated by the fact that the Nernst effect lead to much more advection of the magnetic field than that predicted by frozen-in flow alone (previous modelling used ideal MHD [12]). For externally applied B-fields of 2T and 4T the magnetic field at the centre was completely cavitated after

440ps; in the 12T case it was reduced to 1T after 885ps. The relative importance of frozen-in flow and the Nernst effect was quantified by the 'Nernst number' which was defined to be the ratio of the Nernst velocity to the hydrodynamic flow velocity. This showed that the importance of the Nernst effect decreased with increasing magnetic field strength; it was 8, 5 and 0.3 in the 2T, 4T and 12T cases respectively. Nernst advection lead to the accumulation of the B-field away from the laser-heated region. This then formed a transport barrier.

Non-locality and Nernst advection were shown to be closely coupled to one another. Nernst advection lead to cavitation of the imposed magnetic field from the laser heated region, and thus an increase in the importance of non-local transport. On the other hand the degree of non-locality determined the rate of Nernst advection and so affected the amount of B-field cavitation – the rate of Nernst was found to be up to five times reduced by non-locality. As a result of Nernst causing depletion of the B-field classical theory only approximated the transport well in the 12T case after 440ps; even in this case the field was low enough at 1ns (1T) for the re-emergence of non-locality.

Decoupling non-classical IB effects from non-local transport

A parameter was defined (the 'distortion parameter') which was used to distinguish regions of the plasma where IB was the most important from those where non-locality was dominant. Additionally IMPACT has the ability to heat the plasma without distorting f_0. This has allowed the definitive demonstration that although non-locality is suppressed by a large magnetic field, the distribution function can still be heavily distorted by IB. If a 12T field was applied the distribution tended towards a super-Gaussian distribution with $m = 3.4$.

A Nernst driven instability & Nernst cooling

Previous simulations of laser heating using an azimuthally symmetric laser heating profile have been one dimensional [12]. This would seem to be justified. It has been shown that strong laser heating of a plasma where the Nernst effect is important for B-field advection is an inherently unstable situation. The higher the magnetic field the more unstable the system is. The instability breaks the azimuthal symmetry of the system, necessitating a two-dimensional treatment.

On using late time data from the simulations, another interesting effect is apparent. The systems where an external B-field was imposed began to cool after 300ps,

even though the laser was still supplying its full power to the plasma. This was a result of the importance of the Nernst effect. The temperature gradient, and so the maximum temperature, which the plasma could support was dependent on the magnetic field strength. The larger the B-field, the greater the reduction in the thermal conductivity and so the higher the peak temperature. The rapid decrease in the magnetic field as a result of Nernst advection lead to a large decrease in the Hall parameter. This reduced the temperature which could be supported in the centre; this region subsequently cooled.

Chapter 6

Transport theory for a super-Gaussian distribution

In the previous chapter the effects of magnetic fields on the break-down of classical transport were elucidated in the context the interaction of a long-pulse laser beam with a nitrogen gas jet. It was shown that magnetic fields can suppress non-locality. However, the distortion of the distribution function caused by IB heating is not necessarily suppressed; as was shown with the aid of the distortion parameter. This effect has been considered theoretically and experimentally in the context of laser-plasmas, but the effects of B-fields have not been considered [73, 74, 77, 94]. Numerical work has been done considering IB heating and magnetic fields by Kho & Haines, but no transport theory was derived [85]. Here a transport theory for a plasma being heated by IB in the presence of magnetic fields will be derived. Similar work has also been done with regards to the theory of turbulence in plasmas [72, 95], which can lead to the same distorted distribution as IB heating. In this case magnetic fields were included and the transport derivation of Braginskii followed [23]. In this chapter a different approach will be taken. The derivation of Epperlein will be followed [24]. This involves a direct numerical solution for the transport coefficients instead of the use of polynomial expansions and so is more accurate; additionally, the method of Braginskii produces the wrong asymptotic behavior for some coefficients. We give results which are much more amenable to transport calculations by giving rational polynomial fits to the coefficients. These fits allow the transport in MHD codes to be corrected to account for the new effects. Additionally, the new transport coefficients will be validated by IMPACT. The new theory will then be applied to Froula's experiment. Non-locality modifies the effect that IB has on transport as was shown be Epperlein & Short [96]. Therefore, comparisons to the new theory will be made when

non-locality is not important, i.e. early on in the simulations of Froula's experiment and for the largest applied field (12T).

6.1 Deriving the transport theory

In order to derive useful expressions for transport the method used by Epperlein is followed [24] – as was done when deriving the expression for Ohm's law including hydrodynamic flows in section 3.4.4. Again, it is necessary to start from a reduced form of the $\mathbf{f}_1$ equation (2.23).

$$-v\nabla f_0 + \underline{\omega} \times \mathbf{f}_1 + \frac{e}{m_e}\mathbf{E}\frac{\partial f_0}{\partial v} = \frac{\mathbf{f}_1}{\tau_{ei}} \tag{6.1}$$

Where τ_{ei} is the electron-ion collision time for electrons moving with speed v. The variables are expressed in the following dimensionless forms:

$$W = \frac{w}{w_T} \qquad \mathbf{D} = \lambda_T \nabla \qquad \underline{\Omega} = \frac{\underline{\omega}}{\nu_T} \qquad F = \frac{4\pi w_T^3}{n_e} f$$
$$\underline{\epsilon} = \frac{e\mathbf{E}}{m_e w_T \nu_T} \qquad \mathbf{J} = \frac{\mathbf{j}}{n_e e w_T} \qquad \mathbf{Q} = \frac{\mathbf{q}}{n_e m_e w_T^3}$$

Substitution of the super-Gaussian distribution – given by equation (5.20) – into equation (6.1) and expressing the variables in dimensionless form yields the following expressions for the components of $\mathbf{F}_1$:

$$F_x = \frac{F_0}{1+\Omega^2 W^6}\Bigg\{ -W^4\left[\frac{D_x n_e}{n_e} - \frac{3}{2}\frac{D_x T_e}{T_e} + \frac{m}{2}\left(\frac{W}{\alpha_e}\right)^m \frac{D_x T_e}{T_e}\right] + W^7\Omega\left[\frac{D_y n_e}{n_e} - \frac{3}{2}\frac{D_y T_e}{T_e} + \frac{m}{2}\left(\frac{W}{\alpha_e}\right)^m \frac{D_y T_e}{T_e}\right] - \frac{m\epsilon_x}{\alpha_e^m}W^{m+2} + \frac{m\Omega\epsilon_y}{\alpha_e^m}W^{m+5}\Bigg\} \tag{6.2}$$

$$F_y = \frac{F_0}{1+\Omega^2 W^6}\Bigg\{ -W^4\left[\frac{D_y n_e}{n_e} - \frac{3}{2}\frac{D_y T_e}{T_e} + \frac{m}{2}\left(\frac{W}{\alpha_e}\right)^m \frac{D_y T_e}{T_e}\right] - W^7\Omega\left[\frac{D_x n_e}{n_e} - \frac{3}{2}\frac{D_x T_e}{T_e} - \frac{m}{2}\left(\frac{W}{\alpha_e}\right)^m \frac{D_x T_e}{T_e}\right] - \frac{m\epsilon_y}{\alpha_e^m}W^{m+2} + \frac{m\Omega\epsilon_x}{\alpha_e^m}W^{m+5}\Bigg\} \tag{6.3}$$

Ohm's law and the heat flow equation may then be derived by taking the third and fifth moments respectively, i.e. multiplying by W^3 and W^5 and integrating over

velocity. Taking these integrals results in equations for the current and the heat flow.

$$\mathbf{J} = -\frac{1}{3}\int_0^\infty \mathbf{F}_1 W^3 \mathtt{d}W \qquad \mathbf{Q} = \frac{1}{6}\int_0^\infty \mathbf{F}_1 W^5 \mathtt{d}W + \frac{5}{4}\mathbf{J} \tag{6.4}$$

On rearranging these moment equations the resulting transport equations are:

$$\underline{\epsilon} = -\underline{\underline{\gamma}}^c \cdot \frac{\mathbf{D}P_e}{2P_e} + \mathbf{J} \times \underline{\Omega} + \frac{4}{3\sqrt{\pi}}\underline{\underline{\alpha}}^c \cdot \mathbf{J} - \underline{\underline{\beta}}^c \cdot \frac{\mathbf{D}T_e}{2T_e} \tag{6.5}$$

$$\mathbf{Q} = -\frac{3\sqrt{\pi}}{8}\underline{\underline{\kappa}}^c \cdot \frac{\mathbf{D}T_e}{2T_e} - \underline{\underline{\psi}}^c \cdot \frac{\mathbf{J}}{2} - \frac{3\sqrt{\pi}}{8}\underline{\underline{\phi}}^c \cdot \frac{\mathbf{D}P_e}{2P_e} \tag{6.6}$$

The forms of the transport coefficients are explicitly given in appendix G. Note that similar transport coefficients were expressed using a different approach by Dum [95]. Two important points should be noted. Firstly, if the distribution function is non-Maxwellian then Onsager symmetry breaks down [97]. In this case the transport coefficients appearing in the terms proportional to the temperature gradient are different in equations (6.5) and (6.6). In classical transport theory – when the distribution is Maxwellian – they are the same and denoted by $\underline{\underline{\beta}}$. There is also the need to introduce two completely new transport coefficients ($\underline{\underline{\gamma}}$ and $\underline{\underline{\phi}}$). These result in the heat flow being dependent on the pressure (and so number density) gradient and in a more complicated dependence of the electric field on the pressure gradient. The new coefficients are expressed in dimensionless form according to: $\underline{\underline{\gamma}} = \underline{\underline{\gamma}}^c$ and $\underline{\underline{\phi}} = T_e\tau_B\underline{\underline{\phi}}^c/m_e$. These transport coefficients introduce new effects, such as heat flowing up density gradients in the absence of temperature gradients, which have not been discussed before.

Equations (6.5) and (6.6) are more usefully expressed in a 'dimensional' form:

$$en_e\mathbf{E} = -\underline{\underline{\gamma}} \cdot \nabla P_e + \mathbf{j} \times \mathbf{B} - \frac{\underline{\underline{\alpha}} \cdot \mathbf{j}}{n_e e} - n_e\underline{\underline{\beta}} \cdot \nabla T_e \tag{6.7}$$

$$\mathbf{q}_e = -\underline{\underline{\kappa}} \cdot \nabla T_e - \underline{\underline{\psi}} \cdot \mathbf{j}\frac{T_e}{e} - \underline{\underline{\phi}} \cdot \nabla P_e \tag{6.8}$$

6.1.1 The transport coefficients for a Langdon distribution

The plots of the transport coefficients against $\omega\tau_B$ in figures 6.1 and 6.2 show several important features. Firstly, note that all the 'old' coefficients ($\underline{\underline{\alpha}}^c$, $\underline{\underline{\beta}}^c$ and $\underline{\underline{\kappa}}^c$) mostly have the same functional dependence on Hall parameter as those for a Maxwellian in the high and low $\omega\tau_B$ cases. However the coefficients can differ by large numerical

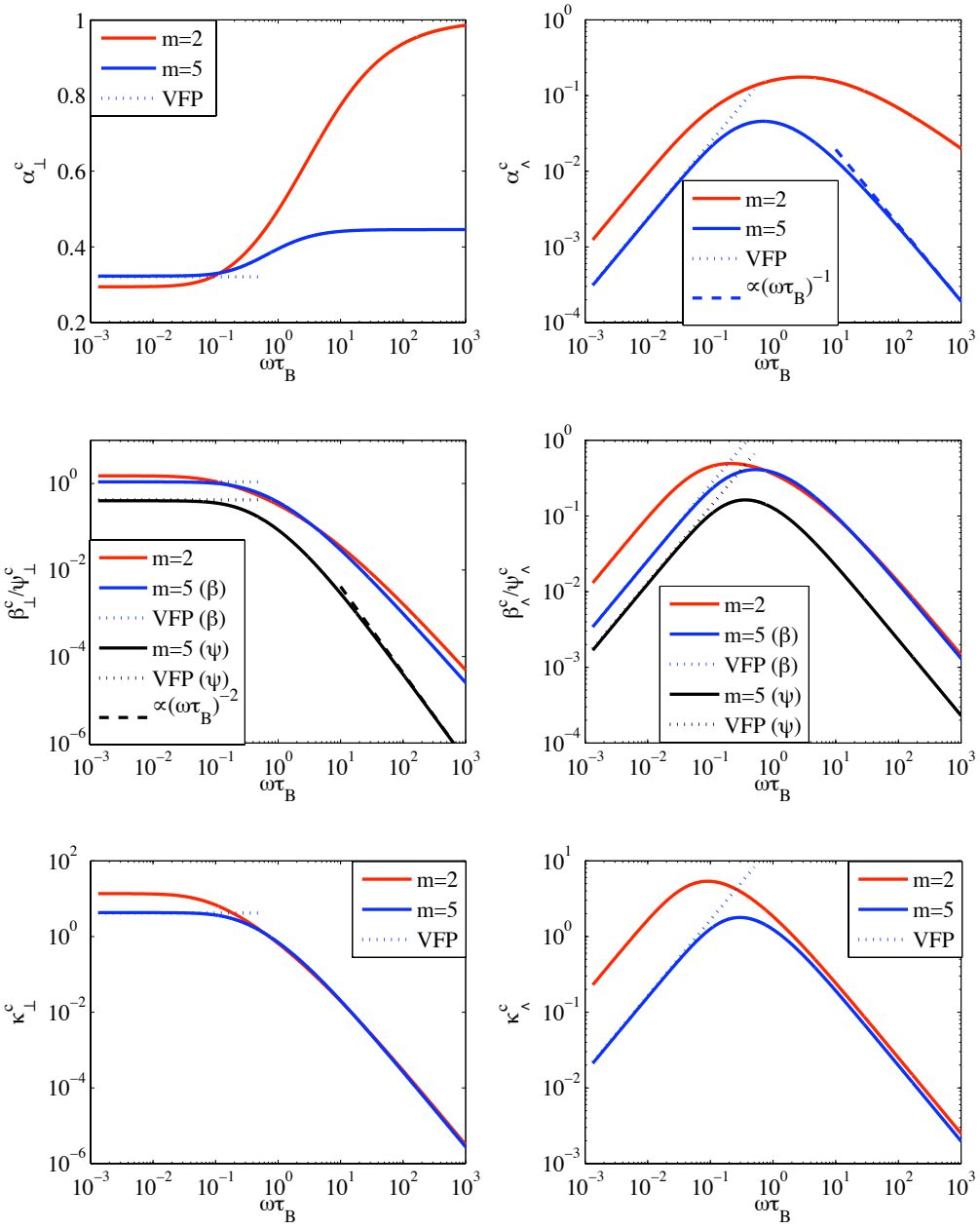

Figure 6.1: The 'old' transport coefficients for a Maxwellian and a Langdon distribution. The asymptotic fits of Braginskii are shown by the dashed lines.

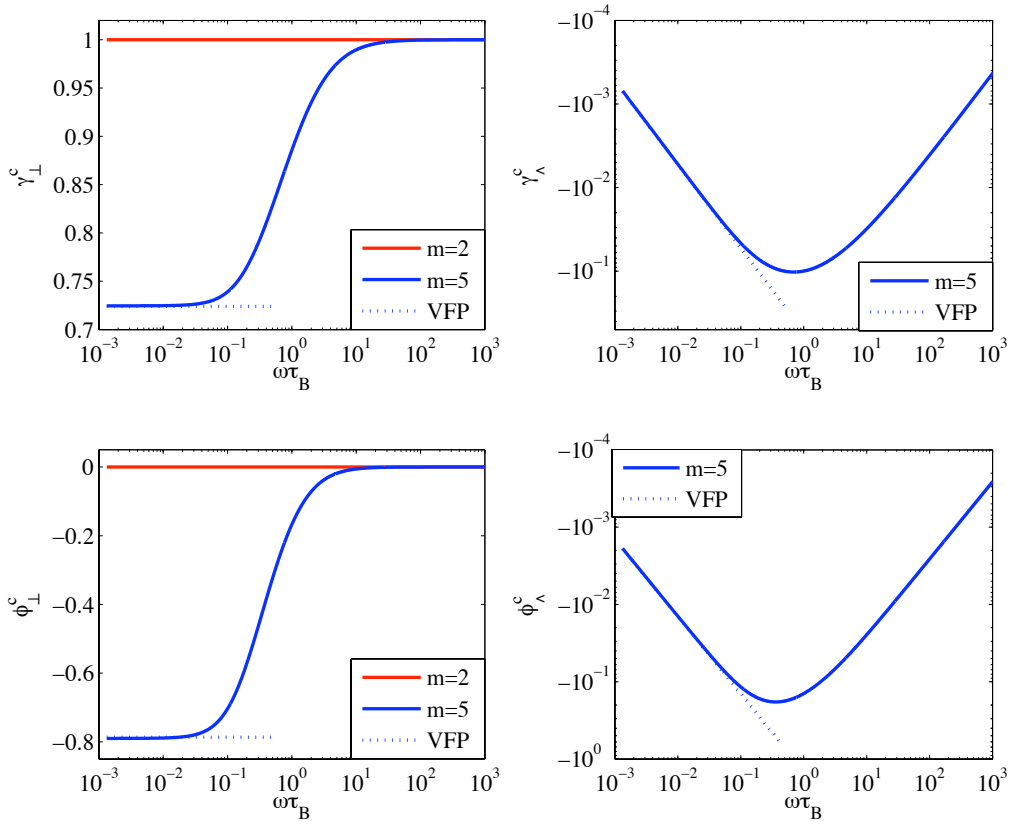

Figure 6.2: The newly introduced transport coefficients for a Maxwellian and a Langdon distribution.

factors (up to an order of magnitude). The functional forms of $\alpha^c_\wedge$ and $\psi^c_\perp$ are different in the limit of high B-field. The forms of $\kappa^c_\perp$ and $\kappa^c_\wedge$ show the interesting result that the Langdon distribution does not dramatically affect the heat flow if the Hall parameter is sufficiently large ($\omega\tau_B > 1$). The break down in Onsager symmetry is clearly shown. For a Maxwellian $\underline{\underline{\beta}}$ and $\underline{\underline{\psi}}$ are identical, for a Langdon distribution they diverge widely from one-another.

The new transport coefficients are plotted in figure 6.2. The components $\gamma^c_\perp$ and $\phi^c_\perp$ have the same general variation with Hall parameter, as do $\gamma^c_\wedge$ and $\phi^c_\wedge$. The former – the 'perpendicular' components – are identical to the Maxwellian values in the limit of high $\omega\tau_B$. The difference at low Hall parameter is particularly interesting in the case of $\phi^c_\perp$. This can lead to heat flowing up density gradients in the absence of temperature gradients. The 'cross' components ($\gamma^c_\wedge$ and $\phi^c_\wedge$) yield the interesting result that heat flows and electric fields generated by a density gradient are not parallel to this gradient.

It may be shown that the dependence of all of the transport coefficients on $\omega\tau_B$, in the limit of high Hall parameter, are identical to those of Epperlein and Haines except for $\alpha^c_\wedge$ and $\psi^c_\perp$; these agree with Braginskii's scaling laws ($\alpha^c_\wedge \propto (\omega\tau_B)^{-1}$ and $\psi^c_\perp \propto (\omega\tau_B)^{-2}$) [23]. Epperlein & Haines's scalings for these are: $\alpha^c_\wedge \propto (\omega\tau_B)^{-2/3}$ and $\beta^c_\perp \propto (\omega\tau_B)^{-5/3}$. The asymptotic scalings for the remaining transport coefficients as $\omega\tau_B$ tends to infinity are: $\beta^c_\perp \propto (\omega\tau_B)^{-5/3}, \beta^c_\wedge \propto (\omega\tau_B)^{-1}, \kappa^c_\perp \propto (\omega\tau_B)^{-2}, \kappa^c_\wedge \propto (\omega\tau_B)^{-1}$. It is interesting to note that $\beta^c_\perp$ for the Langdon distribution follows the dependency of Epperlein & Haines, while the corresponding thermoelectric term in the heat flow equation $\psi^c_\perp$ follows Braginskii. This is explained further in appendix G.

Finally, the dotted lines labeled 'VFP' in figures 6.1 and 6.2 are the values of the transport coefficients, for low B-fields, as calculated using the VFP code IMPACTA; this was developed by A. G. R. Thomas. This new version of IMPACT allows the distribution function to be clamped as an arbitrary function; in this case a Langdon distribution. The agreement between the code and the analytical theory is very good – the disagreement is never larger than 4%.

6.1.2 Polynomial fits to the new transport coefficients

As an aid to performing transport calculations using the new theory, rational polynomials have been fitted to the transport coefficients. The forms of these polynomials closely follow those used by Epperlein & Haines [24] and are as follows:

$\alpha_\perp^c$:	$\alpha_0 = 0.0311$	$\alpha_1 = 0.0618$	$a_0 = 0.251$	$a_1 = 0.609$	$a_2 = 0.445$
$\alpha_\wedge^c$:	$\alpha'_0 = 0.145$	$\alpha'_1 = 0.190$	$a'_0 = 0.602$	$a'_1 = 1.68$	$a'_2 = 4.28$
$\beta_\perp^c$:	$\beta_0 = 54.7$	$\beta_1 = 2.53$	$b_0 = 76.7$	$b_1 = 159$	$b_2 = 48.6$
$\beta_\wedge^c$:	$\beta'_0 = 0.743$	$\beta'_1 = 1.29$	$b'_0 = 0.281$	$b'_1 = 0.893$	$b'_2 = 3.30$
$\psi_\perp^c$:	$\delta_0 = 0.455$	$\delta_1 = 0.408$	$d_0 = 1.10$	$d_1 = 2.76$	$d_2 = 5.32$
$\psi_\wedge^c$:	$\delta'_0 = 0.0137$	$\delta'_1 = 0.233$	$d'_0 = 0.0110$	$d'_1 = 0.163$	$d'_2 = 0.754$
$\kappa_\perp^c$:	$\kappa_0 = 2.02$	$\kappa_1 = 2.72$	$k_0 = 0.458$	$k_1 = 1.35$	$k_2 = 4.00$
$\kappa_\wedge^c$:	$\kappa'_0 = 0.124$	$\kappa'_1 = 1.99$	$k'_0 = 0.00788$	$k'_1 = 0.112$	$k'_2 = 0.578$
$\gamma_\perp^c$:	$\gamma_0 = 0.0689$	$\gamma_1 = 0.139$	$c_0 = 0.248$	$c_1 = 0.608$	N/A
$\gamma_\wedge^c$:	$\gamma'_0 = 0.326$	$\gamma'_1 = 0.426$	$c'_0 = 0.602$	$c'_1 = 1.68$	$c'_2 = 4.28$
$\phi_\perp^c$:	$\phi_0 = 0.902$	$\phi_1 = 0.809$	$p_0 = 1.101$	$p_1 = 2.76$	$p_2 = 5.32$
$\phi_\wedge^c$:	$\phi'_0 = 0.0153$	$\phi'_1 = 0.261$	$p'_0 = 0.0109$	$p'_1 = 0.163$	$p'_2 = 0.754$

Table 6.1: Tabulated constants for the rational polynomial fits to the transport coefficients.

$$\alpha_\perp^c = a_2 - \frac{\alpha_1\omega\tau_B + \alpha_0}{\omega\tau_B^2 + a_1\omega\tau_B + a_0} \qquad \alpha_\wedge^c = \frac{\omega\tau_B(\alpha'_1\omega\tau_B + \alpha'_0)}{\omega\tau_B^3 + a'_2\omega\tau_B^2 + a'_1\omega\tau_B + a'_0} \tag{6.9}$$

$$\beta_\perp^c = \frac{\beta_1\omega\tau_B + \beta_0}{(\omega\tau_B^3 + b_2\omega\tau_B^2 + b_1\omega\tau_B + b_0)^{8/9}} \qquad \beta_\wedge^c = \frac{\omega\tau_B(\beta'_1\omega\tau_B + \beta'_0)}{\omega\tau_B^3 + b'_2\omega\tau_B^2 + b'_1\omega\tau_B + b'_0} \tag{6.10}$$

$$\psi_\perp^c = \frac{\delta_1\omega\tau_B + \delta_0}{\omega\tau_B^3 + d_2\omega\tau_B^2 + d_1\omega\tau_B + d_0} \qquad \psi_\wedge^c = \frac{\omega\tau_B(\delta'_1\omega\tau_B + \delta'_0)}{\omega\tau_B^3 + d'_2\omega\tau_B^2 + d'_1\omega\tau_B + d'_0} \tag{6.11}$$

$$\kappa_\perp^c = \frac{\kappa_1\omega\tau_B + \kappa_0}{\omega\tau_B^3 + k_2\omega\tau_B^2 + k_1\omega\tau_B + k_0} \qquad \kappa_\wedge^c = \frac{\omega\tau_B(\kappa'_1\omega\tau_B + \kappa'_0)}{\omega\tau_B^3 + k'_2\omega\tau_B^2 + k'_1\omega\tau_B + k'_0} \tag{6.12}$$

$$\gamma_\perp^c = 1 - \frac{\gamma_1\omega\tau_B + \gamma_0}{\omega\tau_B^2 + c_1\omega\tau_B + c_0} \qquad \gamma_\wedge^c = -\frac{\omega\tau_B(\gamma'_1\omega\tau_B + \gamma'_0)}{\omega\tau_B^3 + c'_2\omega\tau_B^2 + c'_1\omega\tau_B + c'_0} \tag{6.13}$$

$$\phi_\perp^c = -\frac{\phi_1\omega\tau_B + \phi_0}{\omega\tau_B^3 + p_2\omega\tau_B^2 + p_1\omega\tau_B + p_0} \qquad \phi_\wedge^c = -\frac{\omega\tau_B(\phi'_1\omega\tau_B + \phi'_0)}{\omega\tau_B^3 + p'_2\omega\tau_B^2 + p'_1\omega\tau_B + p'_0} \tag{6.14}$$

Using the constants in table 6.1 these polynomials fit the transport coefficients with a maximum error of 3%. Note that the fits are achieved by minimizing the difference between the logarithm (to base 10) of the fit and the relevant transport coefficient.

6.2 Kinetic simulations

6.2.1 The effect of IB on the heat flow

In order to determine if the theory derived thus far is of significance to current long-pulse LPI experiments the recent experiment conducted by Froula *et al* [12] will be

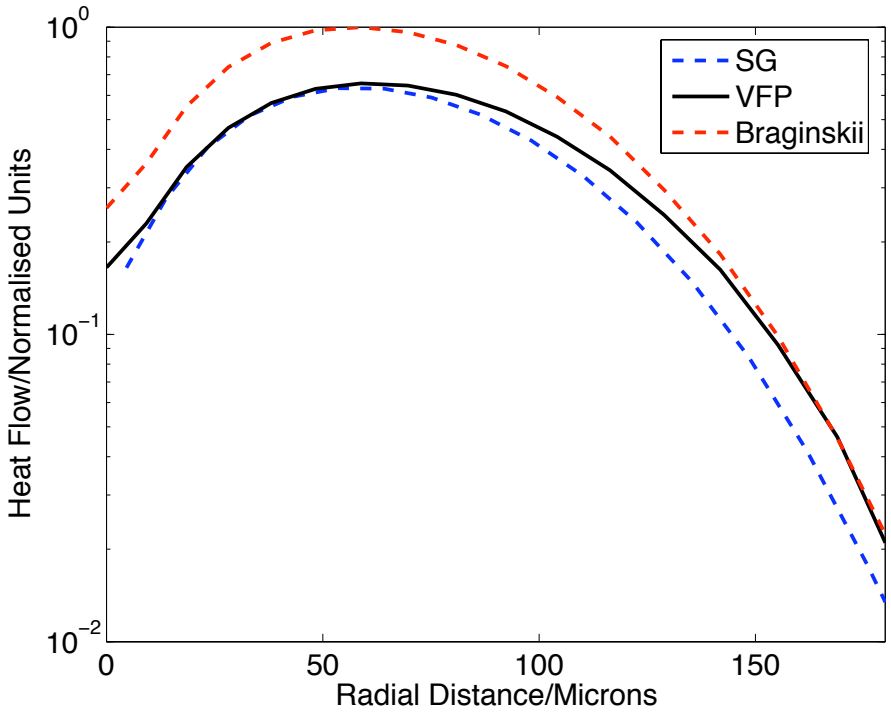

Figure 6.3: A comparison between the azimuthal heat flows from the VFP code, from classical transport theory and from the new theory derived here with the best fitting m at the centre (labeled 'SG').

considered. This experiment was discussed in depth in the previous chapter. The discrepancy between the radial heat flow as produced by the VFP code compared to that predicted by Braginskii decreased as the imposed magnetic field was increased; as the magnetic field strength got larger non-locality was increasingly suppressed. In the case of the largest magnetic field (12T) non-locality should not be important at early times, yet the transport still disagreed markedly from Braginskii's theory. Therefore, the breakdown of Braginskii early on, with a large imposed field, is expected to be almost entirely caused by the inverse bremsstrahlung heating. The heat-flow for the 12T imposed field at $t = 63$ps will be considered in detail here. At this moment the largest electron-ion mean-free path, for electrons moving at twice the thermal speed, is 144μm but the largest Larmor radius is 8μm; meaning that the B-field ensures that non-locality should not yet be very important (recall that the temperature scale-length was of the order of 100μm).

Figure 6.3 shows that the new theory predicts the azimuthal heat flow (after 63ps for B=12T) much better than classical transport theory. The azimuthal heat flow has been chosen for this comparison as it is more sensitive to the distortion of the

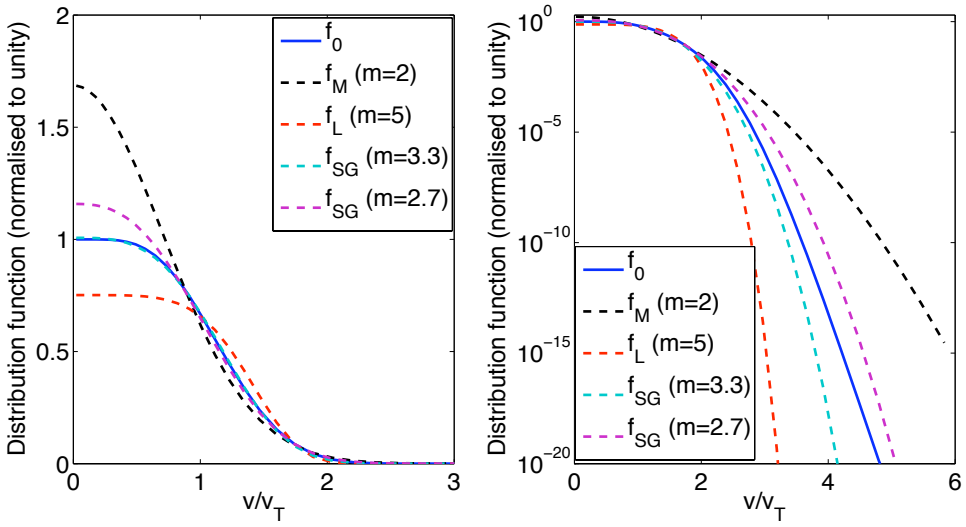

Figure 6.4: A comparison of the distribution function f_0 to the best fitting Maxwellian f_M, Langdon f_L and super-Gaussian distribution f_{SG} after 63ps (for a 12T imposed B-field). The left plot emphasises the body of the distribution and the right the tail. The velocity is normalised to the local thermal velocity and the distributions are normalised such that $f_0(w=0)=1$.

distribution away from Maxwellian than the radial heat flow (as shown in figure 6.1). The curve labeled 'SG' is the heat flow predicted from the new theory with a value of $m = 3.3$. This is the best fitting super-Gaussian at the centre of the laser spot at that time; this predicts q_θ close to the spot much better than classical theory (which is out by a factor of two). The classical theory can be seen to work well away from the laser spot, where the distribution is Maxwellian. Using the transport coefficients with $2 \leq m \leq 3.3$ will allow a smooth transition in the heat flow between these two extremes. Note that in order to apply this new theory as a 'fix' in an MHD code, which could then be used to simulate Froula's experiment, a way of determining m from the macroscopic plasma properties is required. Such a formula was given in equation (2.67). Determining how effective this formula is in predicting m in the presence of magnetic fields and transport is left as further work; as is fitting the transport coefficients with both free parameters $\omega\tau$ and m.

6.2.2 How good a fit is the super-Gaussian distribution?

The relevance of the transport theory derived so far depends crucially on a super-Gaussian distribution being a good fit to f_0. It has been shown that although IB heating causes the distribution to tend towards a super-Gaussian, the reduced colli-

sionality of the hot electrons ($\lambda_{ei} \propto v^4$) can lead to f_0 developing a 'Maxwellian tail' (as discussed by Brunner & Valeo [78]). In this section it will be shown that although the Maxwellian tail is indeed present, the error in the super-Gaussian fit to f_0 leads to a small error in the transport quantities (<5% in this case). f_0 from the simulation is compared with the best fitting Langdon and super-Gaussian distributions in figure 6.4. The Langdon distribution does not fit the data well; an m of 3.3 is best – with a least-squares residual of 1×10^{-8} (compared to 7×10^{-6} and 3×10^{-5} for the Langdon and Maxwellian respectively). The data used to get this fit was taken from the centre of the laser spot after 63ps with an imposed field of 12T. The super-Gaussian fit is good for the bulk of the distribution – out to 2.5 times the thermal speed – but fails in the tail, just as predicted by Brunner & Valeo [78].

If truncating the integrals used to calculate the transport quantities in equations (6.5) and (6.6) at a velocity of 2.5 times the thermal speed does not introduce an unacceptable amount of error then the transport theory derived is entirely applicable to the early stages of Froula's experiment. Consider truncating such an integral at a critical speed w_c:

$$\langle W^n \rangle_{approx} = \int_0^{w_c} \frac{F_0 W^{n+2}}{1 + \Omega^2 W^6} \mathrm{d}W \tag{6.15}$$

If the magnetic field is zero this can be expressed in terms of the lower incomplete gamma-function:

$$\langle W^n \rangle_{approx} = \frac{4\pi C \alpha_e^{n+3}}{m} \Gamma_{inc} \left(\frac{n+3}{m}, w_c^m \right) \tag{6.16}$$

The error in the moment – from truncating the integral – can be expressed as:

$$\delta = \frac{\langle W^n \rangle - \langle W^n \rangle_{approx}}{\langle W^n \rangle} = 1 - \frac{\Gamma_{inc} \left(\frac{n+3}{m}, w_c^m \right)}{\Gamma \left(\frac{n+3}{m} \right)} \tag{6.17}$$

The error is worst for higher n. The highest moment in the calculation of the transport coefficients is the $n = 12$ moment. Figure 6.4 also shows a super-Gaussian distribution with $m = 2.7$; this distribution always weights the tail more than f_0 from the code does (out to the point where numerical error in f_0 obscures the low electron densities in the far tail) and so overestimates any error made by truncation. On calculating the error from equation (6.17) for a super-Gaussian with $m = 2.7$ we find that the error introduced by truncating the distribution at $w_c = 2.5$ is less than 5%.

Here it should be noted that the effects of f_2 have been neglected in the determi-

nation of m. It was shown by Mora & Yahi that higher order terms in the expansion of the distribution function may modify m [73]. The ratio of the mean free path to the scale-length (λ_T/L) in the simulations was very small (its minimum value after 63ps was 1/25). The relative importance of f_2 compared to f_0 in calculating the transport goes as $(\lambda_T/L)^2$ – for the portion of the distribution which dominates the calculation of the relevant velocity moments; for velocities less than $2.5v_T$ – and so its effects on the transport should be small. However, it should be included in a calculation of the rate of IB heating. This may affect the value of m for the best-fitting super-Gaussian, but not the transport theory (provided the laser is circularly polarised – otherwise anisotropic effects must be included).

6.2.3 Distinguishing IB from non-locality

The super-Gaussian fits in figure 6.4 were considered only in the case of the 12T B-field because this is the applied B-field at which non-locality is not significant. When no magnetic field is applied the effects of non-locality on transport are much more important than those of IB heating; this is reflected in the much larger discrepancy between Braginskii transport and IMPACT in the $B = 0$T case – as shown in figure 5.15. The large degree of suppression of non-locality in Froula's experiment is shown by repeating the simulations with a heating operator which heats f_0 as a Maxwellian. This removes the distortion of f_0 by IB but not non-locality. In this case f_0 remains close to a Maxwellian for the first 63ps of the interaction; the best-fitting super-Gaussian distribution has $m = 2.02$ after 63ps. This means that the system is behaving according to Braginskii's transport theory and non-locality is not important. This demonstrates that IB heating is responsible for distorting the distribution at early times for a large imposed B-field.

Non-local transport can distort f_0 away from a super-Gaussian by leading to an enhancement in the distribution's energetic tail. In this case transport may not be well described by the theory expounded here. Addressing this issue, the method by which the transport theory was derived here could be applied when the distribution is not Maxwellian due to non-locality. For example one could apply this approach to the non-locally pre-heated region by re-deriving the theory for a two-temperature Maxwellian fit to f_0.

6.3 Summary

A transport theory has been derived for a super-Gaussian distribution in the presence of magnetic fields. This theory is significantly different from the classical theory of transport (where the distribution is assumed to be close to Maxwellian) in that the existing transport coefficients are modified and new ones must be introduced. Using VFP simulations it has been shown that a super-Gaussian is a good fit to the isotropic part of the distribution function in a recent long-pulse LPI experiment (early in time and for large imposed B-fields); the new transport theory is applicable in this case. Furthermore, any instabilities dependent on the transport (Tidman-Shanny for example [98]) will also be affected by the change in the transport coefficients.

The new theory places a second bound on the transport coefficients – as well as highlighting some new effects which become important when the distribution is non-Maxwellian, the breaking of Onsager symmetry for example. The limiting case on f_0 under the influence of strong laser heating is a Langdon distribution. On the other hand, the equilibrium distribution is Maxwellian; we have shown that the intermediate case is sometimes described well by a super-Gaussian. Note that in the more general case a Maxwellian tail on the distribution should be accounted for. In either case, the transport coefficients are expected to lie between the extremes of the Maxwellian and the Langdon; deriving the second bounding solution is therefore essential. An interesting result produced in deriving this bounding solution is that the transport coefficients $\alpha^c_\wedge$ and $\psi^c_\perp$ follow the Braginskii scalings in the high Hall parameter limit, not those of Epperlein & Haines. These scalings are therefore appropriate when IB heating is significant (after being shown to be incorrect in the Maxwellian case [25]).

Chapter 7

Non-classical magnetic field generation

So far it has been demonstrated that Braginskii's theory fails to describe transport when non-locality or IB are important. This leads to a discrepancy in the rate of magnetic field advection as predicted by the classical theory which is particularly bad if non-locality is crucial to determining the heat flow and the advection is dominated by the Nernst effect. The advection velocity is in this case proportional to the heat flow, which can be different from Braginskii's theory by up to a factor of 100. In order to further show the crucial importance of modelling long-pulse LPI kinetically, the generation of B-fields by the commonly considered thermoelectric mechanism will now be shown to be dependent on non-locality.

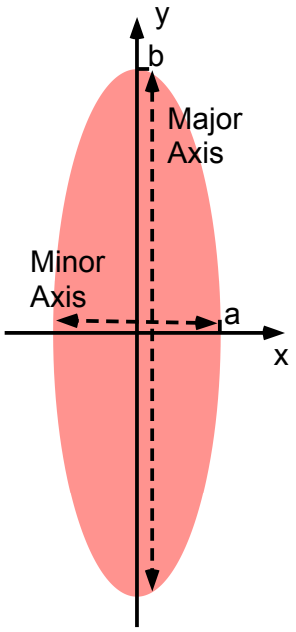

Figure 7.1: The elliptical heating profile

The non-local generation of B-fields has been discussed previously [63], but has yet to be applied to experimentally relevant situations. To investigate how the breakdown of classical transport affects B-field generation the experimental setup of Froula *et al* is not useful. Classical and non-local theories predict that a circular spot such as the one studied in chapter 5 will not generate B-fields. The symmetry of this situation must be relaxed. This will be done by investigating an elliptical laser spot. Thermoelectric magnetic field generation would be expected to produce B-fields in this case – the addition of hydrodynamic ion-motion to IMPACT will allow it to be definitively shown that the field from the elliptical spot is not due to this mechanism. The limitation of

this investigation is that the effects of $\underline{\underline{\mathsf{f}}}_2$ are not considered. It has been shown that anisotropic pressure (which is the result of a non-zero $\underline{\underline{\mathsf{f}}}_2$) can generate B-fields larger than those seen in this chapter [38]. However, for the long scale-lengths studied here ($> 4000\lambda_n$) the approximation that the pressure is isotropic is a good one. However, the non-local mechanism is affected by $\underline{\underline{\mathsf{f}}}_2$ [99] and so this should really be accounted for. This is left as further work.

7.1 The elliptical spot

The elliptical heating profile is given by:

$$\frac{\partial \tilde{T}_e}{\partial \tilde{t}} = \left(\frac{\partial \tilde{T}_e}{\partial \tilde{t}}\right)_{MAG} \mathsf{exp}\left[-\left(\frac{\tilde{x}^2}{\tilde{a}^2} + \frac{\tilde{y}^2}{\tilde{b}^2}\right)\frac{1}{\tilde{\lambda}^2}\right] \tag{7.1}$$

Figure 7.1 illustrates this. The plasma conditions are the same as those simulated in the last chapter. As for the laser parameters: v_{osc} doubles, but the area of the spot has also changed. The ellipse is chosen with $a = 3$ and $b = 1$ so its area ($\pi ab/4$) is three times larger than in the previous case – meaning the laser delivers 600J in 1ns. A non-uniform grid is again required in order to resolve the laser spot adequately and give enough buffer space for the non-local electrons to propagate as far as is possible without hitting the boundary. The spatial gridding is such that 75 grid-cells span a distance of 3500 electron-ion mean free paths (for the 20eV background plasma) in the x-direction, 55 span 2000 λ_n in the y-direction. The ratio of smallest to largest spatial cell is chosen to be 3:1. The velocity grid and temporal resolution are the same as those used in chapter 5. The background plasma temperature is 20eV and again, a fully ionised nitrogen plasma is simulated. In order to achieve better resolution of the laser spot reflective boundary conditions are used, allowing the simulation of one-quarter of the spot only. Note that there is no initial magnetic field and the plasma density is uniform initially.

7.1.1 Self-generated magnetic fields

The evolution of the magnetic field generated by the elliptical spot (in the z-direction) is shown in figure 7.2. The peak field generated under these conditions after 885ps is 1.36T. The peak magnetisation is reached at 440ps and is 0.63; a consideration of the transport coefficients in figure 2.5 shows that such a magnetisation will affect them all. It is important to determine that this magnetic field is not caused by numerical errors

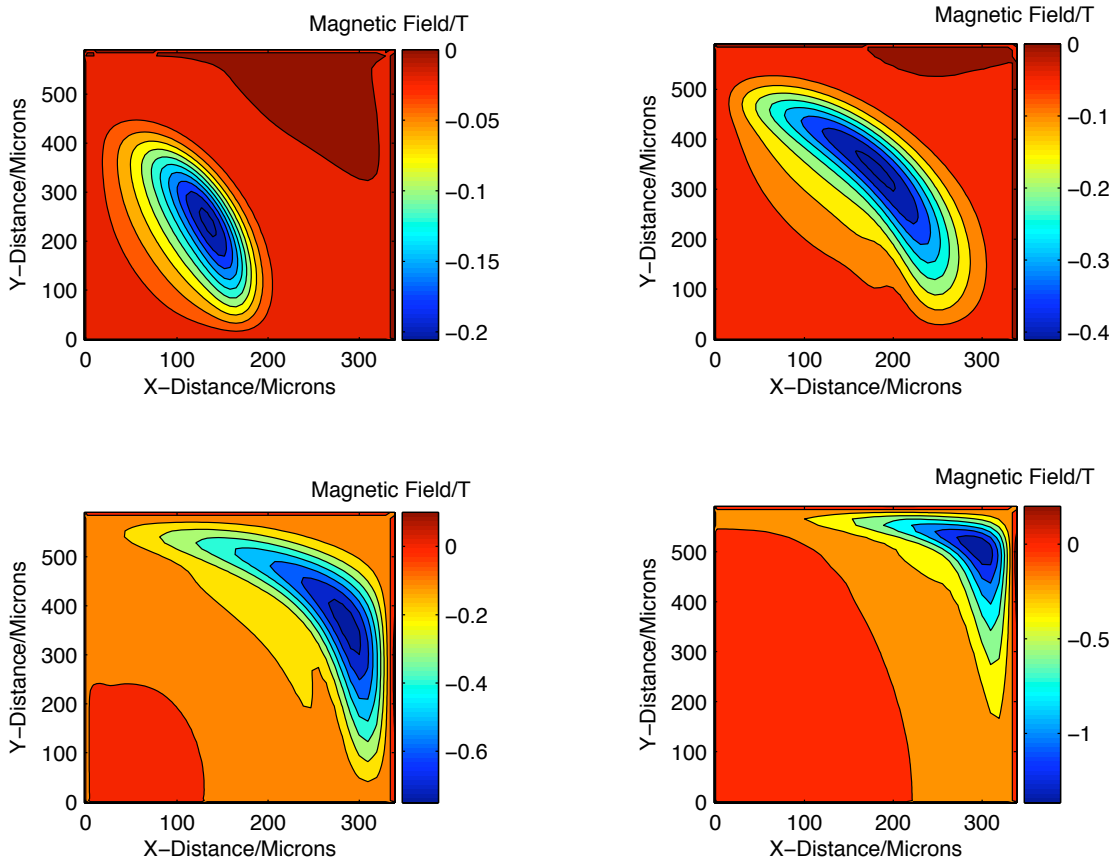

Figure 7.2: Magnetic field generated by the elliptical spot. These snapshots are taken after: top left – 63.2ps, top right – 190ps, bottom left – 442ps, bottom right – 885ps.

and to quantify any such errors. In order to do this the spatial and velocity grids were altered. The fields are well resolved spatially, the resolution in velocity space will shown to be crucial to the generated fields (they will be shown to be generated by a non-local mechanism which is very sensitive to velocity-gridding [71]). When the number of velocity grid cells is increased from 45 to 75 the maximum variation in the field is found to be only 0.02%.

7.1.2 The thermoelectric mechanism

On the relaxation of the cylindrical symmetry of the system, but retention of the constraint that the magnetic field is perpendicular to the gradients of the physical variables, classical Ohm's law gives the following equation for the evolution of the z-component of the magnetic field (the other two components are always zero):

$$\frac{\partial B}{\partial t} + \nabla \cdot \left[\left(\mathbf{C} + \mathbf{v}_N \right) B \right] - \nabla \cdot \left(\frac{\eta_\perp}{\mu_0} \nabla B \right) = \frac{1}{e n_e} \left\{ \left[\nabla T_e + \frac{1}{n_e} \nabla \left(\frac{B^2}{2\mu_0} \right) \right] \times \nabla n_e \right\}_z + \frac{1}{e} \left\{ \nabla \left(\frac{B^2}{2\mu_0} \right) \times \nabla \alpha_1 + \nabla \beta_1 \times \nabla T_e \right\}_z \tag{7.2}$$

where

$$\alpha_1 = \frac{1}{n_e \omega_e \tau_e} \left(\alpha_\wedge^c - \frac{\beta_\wedge^c \beta_\perp^c}{\kappa_\perp^c} \right) \tag{7.3}$$

$$\beta_1 = \beta_\perp^c + \frac{\beta_\wedge^c \kappa_\wedge^c}{\kappa_\perp^c} \tag{7.4}$$

The terms on the left-hand side of equation (7.2) are the advection (frozen-in flow, Nernst effect) and resistive diffusion terms. Those on the right-hand side are responsible for magnetic field generation. Equation (7.2) may be simplified by neglecting resistive diffusion and some generation effects. The first generation term can be re-written as:

$$\frac{1}{e n_e} \left[\nabla T_e + \frac{1}{n_e} \nabla \left(\frac{B^2}{2\mu_0} \right) \right] = \frac{1}{e n_e^2} \nabla \left(P_e + \frac{B^2}{2\mu_0} \right) = \frac{1}{e n_e^2} \nabla \left[P_e \left(1 + \frac{1}{2\beta} \right) \right] \tag{7.5}$$

In the limit where $\beta >> 1$ the magnetic pressure may be neglected. The minimum

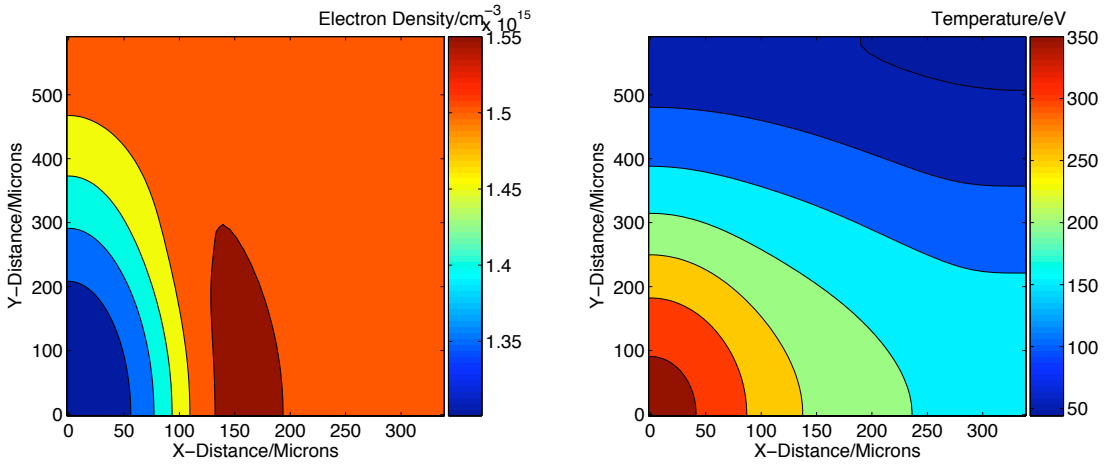

Figure 7.3: The electron number density (left) and temperature (right) after heating with the elliptical laser profile for 440ps.

value β may take is where the B-field is maximum – this is 590μm from the spot's centre. Here β is 600 after 885ps, thus the magnetic pressure is indeed negligible. In this case this term becomes that on the right-hand side of equation (7.7). The term in α_1 is the collisional correction to the Hall term. It can be shown that for $Z = 7$ the maximum value of this correction is 6%, therefore it is neglected [33] . The term in β_1 can be written:

$$\nabla\beta_1 \times \frac{\nabla T_e}{e} = \frac{d\beta_1}{d\omega\tau}\nabla(\omega\tau) \times \frac{\nabla T_e}{e} \tag{7.6}$$

It has been shown that β_1 is very weakly dependent on $\omega\tau$ – varying by 4% over four orders of magnitude of $\omega\tau$ [33]. When this term is compared to the '$\nabla n_e \times \nabla T_e$' term, for the conditions considered here, it is found to be a factor of 10^6 smaller. Therefore the equation for the evolution of the magnetic field becomes:

$$\frac{\partial B}{\partial t} + \nabla \cdot [(\mathbf{C} + \mathbf{v}_N)\, B] = \frac{1}{en_e}\left[\nabla T_e \times \nabla n_e\right]_z \tag{7.7}$$

The generation mechanism which survives this series of assumptions is the thermoelectric mechanism. The shape of the B-field generated by this may be understood by figure 7.3. The gradients of the temperature and density profiles are no longer parallel; the density profile, which has been driven out by hydrodynamic expansion from the laser-heated region, exhibits variation in the azimuthal direction. The polarity of field that this mechanism would generate is given in figure 7.4. Here a plot of the rate of change of the magnetisation with time is plotted, this mechanism should produce the observed quadrupole; note that the non-local mechanism (discussed in

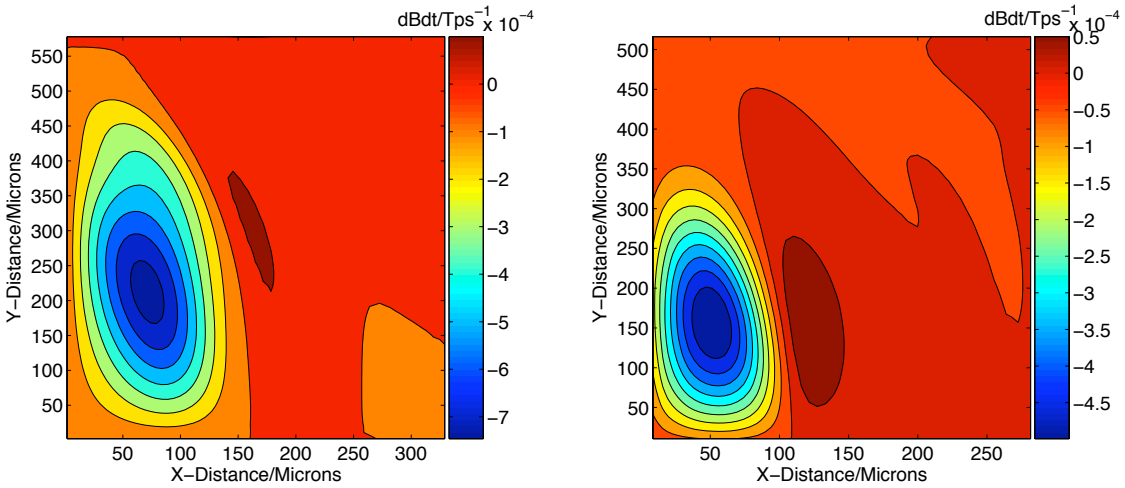

Figure 7.4: The theoretically predicted rate of change of the B-field caused by the thermoelectric mechanism (left) and the non-local mechanism (right) after 440ps.

section 2.4.4) gives the same polarity and so this cannot be used to determine which is dominant.

So far the discussion of the role of the thermoelectric mechanism in generating the B-field has been qualitative, its quantitative importance may be understood by comparing simulations of the elliptical spot with and without hydrodynamic plasma response. In figure 7.5 the difference between the maximum values of the magnetic field generated with and without hydrodynamic ion motion is plotted against time. The effect of hydrodynamics is seen to get stronger with time – the thermoelectric mechanism plays more of a role at later times. Figure 7.6 shows a two-dimensional snapshot of the difference between these simulations. The difference in the magnetic fields in both figures is less than 5% of the field strength generated. It is clear that the thermoelectric mechanism is not the dominant process even though it predicts the correct field polarity. Another mechanism must be responsible for the magnetic field generation. This is postulated to be the non-local mechanism. In addition, the fact that the magnetic field produced by the elliptical spot is the same regardless of whether ion-motion is included shows that the advection of the generated B-field is dominated by the Nernst effect. This will not behave classically. The work in the previous chapter clearly demonstrates that a magnetic field of 1.36T is not enough to localise the transport.

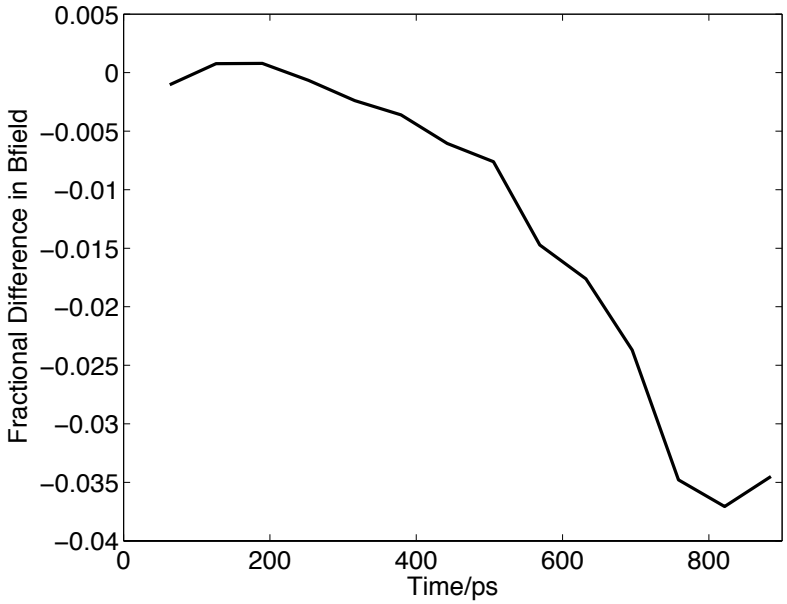

Figure 7.5: The fractional difference between the maximum value of the modulus of the generated B-field with and without hydrodynamic ion motion.

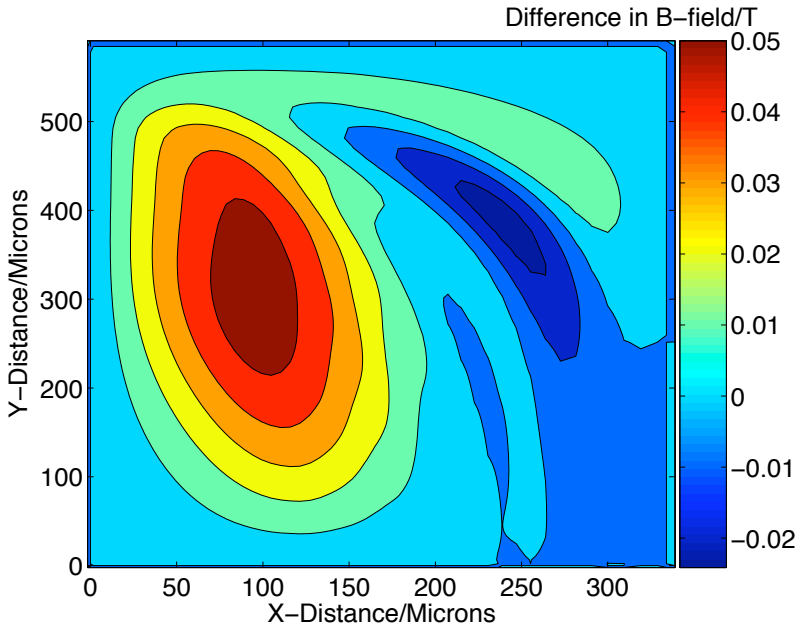

Figure 7.6: The difference in magnetic fields generated by the elliptical spot with and without the inclusion of hydrodynamic ion motion at 440ps.

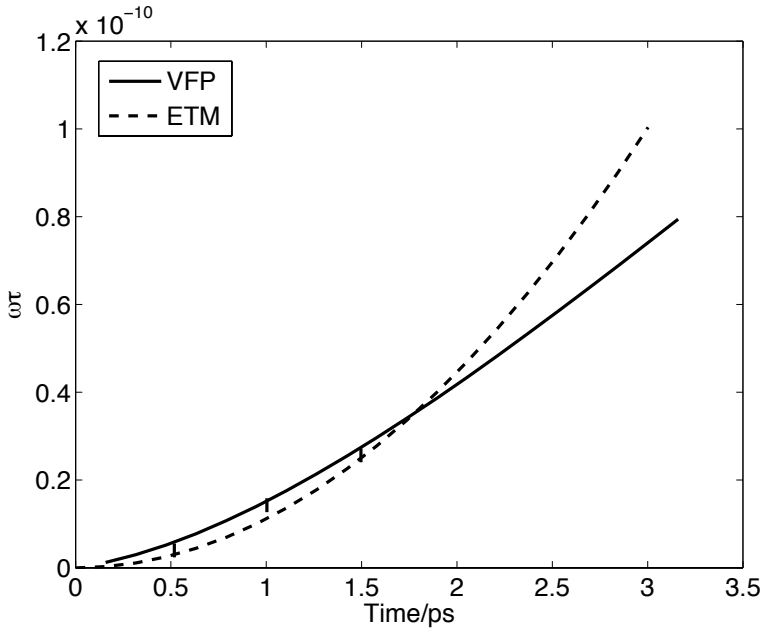

Figure 7.7: The maximum value of the Hall parameter generated by the elliptical hot spot (solid line) compared to the early time model (dashed line).

7.1.3 The non-local mechanism

In section 2.4.4 the generation of magnetic fields in the non-classical regime was discussed. The analytical theory presented here will now be used to provide further evidence that the B-field generated by the elliptical spot is due to a non-local mechanism. The early time model shows that a magnetic field can be generated without density gradients according to the following equation:

$$\underline{\tilde{\omega}}\bar{\tau} = -\frac{1}{2}\left(\frac{\tilde{t}}{\bar{\tau}_{ei}}\right)^2 \frac{\tilde{\nabla}\tilde{T}_e}{\tilde{T}_e} \times \left[154\frac{\tilde{\nabla}(\tilde{\nabla}^2\tilde{T}_e)}{\tilde{T}_e} + 620\frac{|\nabla\tilde{T}_e|^2}{\tilde{T}_e{}^2}\right]\frac{\bar{\lambda}_{ei}^4}{6\pi\sqrt{2}} \tag{7.8}$$

This model only works if the plasma's temperature is approximately constant over the time considered – this is why it is only valid for early times. To ascertain whether such a mechanism could be responsible for the magnetic field generated in the case of the elliptical laser spot, the B-field from a slowly cooling elliptical hot spot was compared to the early-time model (ETM). The difference between the maximum temperature of the cooling hot spot and the background had to be chosen to be small in order to retard the rate of cooling sufficiently – the maximum temperature was therefore set to be 20.2eV (the elliptical laser spot will reach this temperature after only 70fs). Figure 7.7 shows a comparison of the magnetic field generated by this hot spot with the ETM. The agreement is good until 2ps – beyond this the early

time assumption breaks down. The error bars in this figure are an expression of the fact that the magnetic field generated in the simulation is crucially dependent on the velocity space gridding. The B-field from the ETM is derived from the equation:

$$\frac{\partial \underline{\tilde{\omega}}}{\partial \tilde{t}} = \frac{\tilde{\nabla}\left(\tilde{n}_e \langle \tilde{w}^5 \rangle\right) \times \tilde{\nabla}\left(\tilde{n}_e \langle \tilde{w}^3 \rangle\right)}{6\left(\tilde{n}_e \langle \tilde{w}^3 \rangle\right)^2} \tag{7.9}$$

The dependence of this field on high moments of the distribution function (e.g. $\langle \tilde{w}^5 \rangle$) requires the resolution of very small changes to the tail of the distribution function. If this is not resolved well enough numerical errors will swamp the very small early time field. The numerical field had a different polarity from that generated by non-locality (an octupole compared to the quadrupole); this made numerical errors easy to distinguish. To minimise the error a finely resolved velocity grid was used – 170 cells divided up a domain that was bounded at seven times the thermal speed of the background plasma. The relative size of the numerical error (as compared to the early-time B-field) decreased with time, this is reflected in the error bars in figure 7.7. Electron-electron collisions were included in the simulations but had no effect on such a short time-scale; although the ETM does not include these collisions but the agreement was still good. The ETM cannot be applied to the fields shown in figure 7.2, the heating is too rapid. However, the slowly cooling system studied here gives a very early time snapshot of the rapidly heating system valid over a very short time window and so the results support the suggestion that the B-field generated by an elliptical laser spot is due to the non-local mechanism described. For conclusive proof a non-local model which works over long time-scales and for strong heating is required, to develop such a model would be very difficult.

7.2 Summary

The effect of non-locality on B-field generation under experimentally realisable conditions was studied. To do this the circular symmetry of the simulations in chapter 5 was relaxed. It was shown that this makes magnetic field generation possible. An elliptical laser-spot was considered (with an aspect ratio of 3:1). If the laser delivered 600J in 1ns this was found to generate a maximum B-field of 1.36T. One might naively expect the field to be generated by the classical thermoelectric mechanism. This was shown not to be the case. A non-classical mechanism derived from a generalised non-local Ohm's law was postulated to be responsible. This was tested by comparing a slowly cooling elliptical hotspot, under the same conditions as the heated

case, to the non-local early time model. These were found to be in good agreement if the velocity-space grid resolution was sufficiently high. However, the non-local model should be developed to include the effect of $\underline{\underline{\mathsf{f}}}_2$.

Chapter 8

Conclusions

8.1 Summary of results

In order to study the recent experiment of Froula *et al* the first 2D VFP code with self-consistent B-fields and the ability to run over nanosecond time-scales was upgraded to include ion-motion. This allowed the definitive demonstration that in the interaction of a long-pulse laser with a gas-jet plasma under the influence of an (initially uniform) externally applied B-field the Nernst effect dominated the magnetic field dynamics; frozen-in flow was the only advection mechanism previously considered in this interaction. The fact that the Nernst advection velocity is proportional to the heat flow then lead to a strong coupling between the magnetic field advection and the degree of non-locality. The B-field and so the Nernst velocity determined the importance of non-locality, which directly affected the heat flow which determined the Nernst velocity. The rapid advection of the imposed B-field, which was initially sufficiently strong to suppress non-locality, lead to the re-emergence of non-local transport after a relatively short time – 500ps into the simulation of Froula's experiment, whose duration was longer than 2ns. The dominance of the Nernst effect could be demonstrated experimentally in such experiments as those of Froula *et al* by measuring a cooling of the plasma in the central region while the laser is still heating the plasma. This is a result of the enhanced magnetic field advection leading to a decrease in the central Hall parameter and so enhancing heat transport out of this region. As well as dominating advection, it was determined that, for conditions similar to Froula's experiment, a non-local mechanism was likely responsible for magnetic field generation.

The break-down of classical theory in Froula's experiment has been discussed here and previously in terms of non-locality [12]. However IB heating can also cause this to

happen. Both non-locality and IB cause the distribution function to be distorted away from Maxwellian; this causes the break-down of the classical theory. The distortion of the distribution has been quantified using the 'distortion parameter'. This parameter allowed the discrimination of regions of the plasma where IB heating was the dominant cause of the distortion from those where non-locality was responsible. It was found that both effects were significant unless the magnetic field was very large; for the imposed field of 12T IB heating was dominant early in time – later on magnetic field cavitation lead to the re-emergence of non-locality. To quantify the effect of IB heating on transport a transport theory was developed for a super-Gaussian distribution (the analytical solution for the distribution function with strong IB heating). In this case the new theory explained the early-time heat flow for B=12T better than the classical theory. IB heating was found to affect thermal transport less than non-locality; the heat flow was different by a factor of two as a result of IB compared to two orders of magnitude for the B=0T case where non-locality was dominant.

8.2 Conclusions

The importance of both non-local transport and B-fields in ICF hohlraums were separately discussed in the introduction to this thesis. The possible coupling between these effects elucidated in chapter 5 means that extra care must be taken when modelling the transport in such a situation. The enhanced dynamics of the magnetic field given by Nernst advection, above that expected from frozen-in flow, can lead to the unexpected breakdown of Braginskii's transport theory (if the B-field is expelled from the region of plasma being examined). Although the results presented here only definitively demonstrate that the Nernst effect is important near the laser entrance hole of a hohlraum, it was possible to estimate (using the Nernst number) that it should be included in any simulation throughout the gas-fill. Both non-locality and Nernst effect must be included in hohlraum modelling.

The question of how strong a B-field is required to re-localise transport has not only been answered for the conditions simulated here, but the need to extend the question has been discussed for the first time. It has been shown that even very strong fields can be rapidly advected away from the laser heated region mitigating the re-localisation there. The importance of non-locality in a given LPI needs to be considered as dynamically varying with time. Furthermore, the Nernst effect has some important consequences other than its effect on non-locality. The fact that it may lead to an instability has ramifications for any situation where there are strong

heat flows in the presence of a large B-field. This effect is included in classical theory, but should be modified by non-locality (as non-locality significantly affects the rate of Nernst advection). In recent experiments examining magnetic reconnection in the high energy-density regime an instability has been observed [80]. Investigating if this could be driven by Nernst is left as further work.

Furthermore it must be noted that although B-fields suppress non-locality, they do not prevent the distortion of the distribution function by IB heating. Determining the effect of IB on transport in the presence of B-fields is important in long-pulse LPI – where this is the main heating mechanism. The modification by IB to the transport coefficients predicted in this thesis should have important consequences such as changing the Nernst velocity and the rate of instabilities (Tidman-Shanny).

The ability of classical theory to predict the rate of magnetic field generation under typical experimental conditions has been called into question. Non-locality has been shown to significantly modify the generation rate [63]. Non-locality significantly affects '$\nabla n_e \times \nabla T_e$' field generation – this is the main mechanism in long-pulse laser-solid interactions (and so in hohlraums). Therefore a kinetic treatment of long-pulse LPI is required to correctly determine the heat flow, magnetic field advection and magnetic field generation; all of these are crucial to accurate modeling of the laser-plasma interaction.

Finally, the new version of IMPACT with hydrodynamic ions should be applied to many more aspects of ICF simulation. The results presented in this thesis lead us to conclude that to study the generation and advection of magnetic fields during direct drive implosions one should employ a kinetic treatment. The new version of IMPACT would provide an excellent tool for determining whether kinetic effects modified the implosion velocity in this situation. Similarly the new code could provide insight into the generation of B-fields in the interaction of a laser with the wall of a hohlraum. An alternative application of the work presented here has recently been suggested (by Froula *et al*). The interaction of a de-focussed laser with a gas jet could be used to create density channels by expulsion of the plasma from the laser-heated region; the long-pulse beam would then be followed by a short pulse beam which would accelerate electrons by the method of wakefield acceleration [100]. The density channel acts as a waveguide and allows the accelerated electrons to acquire more energy. An applied B-field parallel to the laser could be used to taylor the shape of these channels (which is advantageous). To conclude, the applications of the new code are much more diverse than those presented in this thesis and there is much interesting work still to be done using it.

Appendix A

Polynomial fits to the transport coefficients

In section 2.3.1 it was stated that the most convenient way to calculate the classical transport coefficients is to use the polynomial fits of Epperlein & Haines [33]. These are given below:

$$\begin{aligned}
\alpha_{\parallel}^{c} &= \alpha_0 \quad \alpha_{\perp}^{c} = 1 - \frac{\alpha_1'\omega\tau_B + \alpha_0'}{(\omega\tau_B)^2 + a_1'\omega\tau_B + a_0'} \quad \alpha_{\wedge}^{c} = \frac{\omega\tau_B(\alpha_1''\omega\tau_B + \alpha_0'')}{[(\omega\tau_B)^3 + a_2''(\omega\tau_B)^2 + a_1''\omega\tau_B + a_0'']^{8/9}} \\
\beta_{\parallel}^{c} &= \beta_0 \quad \beta_{\perp}^{c} = \frac{\beta_1'\omega\tau_B + \beta_0'}{[(\omega\tau_B)^3 + b_2'(\omega\tau_B)^2 + b_1'\omega\tau_B + b_0']^{8/9}} \quad \beta_{\wedge}^{c} = \frac{\omega\tau_B(\beta_1''\omega\tau_B + \beta_0'')}{(\omega\tau_B)^3 + b_2''(\omega\tau_B)^2 + b_1''\omega\tau_B + b_0''} \\
\kappa_{\parallel}^{c} &= \gamma_0 \quad \kappa_{\perp}^{c} = \frac{\gamma_1'\omega\tau_B + \gamma_0'}{(\omega\tau_B)^3 + c_2'(\omega\tau_B)^2 + c_1'\omega\tau_B + c_0'} \quad \kappa_{\wedge}^{c} = \frac{\omega\tau_B(\gamma_1''\omega\tau_B + \gamma_0'')}{(\omega\tau_B)^3 + c_2''(\omega\tau_B)^2 + c_1''\omega\tau_B + c_0''}
\end{aligned} \tag{A.1}$$

The values of the constants depend on Z and were tabulated by Epperlein & Haines [25]. Since the plasmas of interest in this thesis had an ionic charge of 7, the constants are given for this value.

α_0	0.3454	α'_0	1.82	α'_1	3.12	α''_0	794	α''_1	2.53
a'_0	2.79	a'_1	6.26	a''_0	3250	a''_1	11700	a''_2	793
β_0	1.218	β'_0	1730	β'_1	6.33	β''_0	2.92	β''_1	1.5
b'_0	3530	b'_1	11300	b''_0	0.629	b''_1	3.33	b''_2	7.68
γ_0	8.685	γ'_0	8.84	γ'_1	3.49	γ''_0	0.268	γ''_1	2.5
c'_0	1.02	c'_1	5.19	c''_0	0.00461	c''_1	0.0465	c''_2	0.539

Appendix B

A more general Ohm's law with flows

In section 3.4.4 a form of Ohm's law including the effects of hydrodynamic ion flow was derived. In this derivation terms of $O(C^2)$ or $O(C_i f_{1j})$ were neglected. Here these terms have been included. Previously it was shown that Ohm's law could be derived from the following equations:

$$-(\tilde{\mathbf{A}} + \tilde{\mathbf{B}})W^4 F_m + W^3 \underline{\Omega} \times \mathbf{F}_1 = \mathbf{F}_1 \tag{B.1}$$

$$\tilde{A}_j = \left(\frac{D_j n_e}{n_e} - \frac{3}{2}\frac{D_j T_e}{T_e} + W^2 \frac{D_j T_e}{T_e} \right) \tag{B.2}$$

$$\tilde{B}_j = 2\left(\epsilon_j - [\underline{\mathbf{\Omega}} \times \mathbf{C}]_j - \frac{\partial \tilde{\mathbf{C}}}{\partial \tau} \right) \tag{B.3}$$

As usual the tildes denote normalised units – these will be dropped for brevity – the magnetic field is in the z-direction. Retaining all the terms in equations (B.1) - (B.3), the following expressions may then be derived for the normalised components of $\mathbf{f}_1$:

$$F_x = \frac{F_m}{1 + W^6\Omega^2}\left[W^7 \Omega \left(A_y + B_y \right) + \gamma \Omega W^6 T_{cy} - W^4 \left(A_x + B_x \right) + \gamma W^3 T_{cx} \right] \tag{B.4}$$

$$F_y = -\frac{F_m}{1 + W^6\Omega^2}\left[W^4 \left(A_y + B_y \right) + \gamma \Omega W^6 T_{cx} + W^7 \Omega \left(A_x + B_x \right) + \gamma W^3 T_{cy} \right] \tag{B.5}$$

where $\gamma = 4w_T^3/\pi n_e \nu_T$. Ohm's law is obtained from the first moment of equations (B.4) and (B.5). This yields:

$$\underline{\epsilon} - \frac{\partial \mathbf{C}}{\partial \tau} - \mathbf{C} \cdot \nabla \mathbf{C} + \mathbf{C} \times \underline{\Omega} = -\frac{\mathbf{D}P_e}{2P_e} + \mathbf{J} \times \underline{\Omega} + \frac{4}{3\sqrt{\pi}} \underline{\underline{\alpha}}^c \cdot \mathbf{J} - \underline{\underline{\beta}}^c \cdot \frac{\mathbf{D}T_e}{2T_e} + \underline{\underline{\delta}}^c \cdot \hat{\mathbf{e}} \quad \text{(B.6)}$$

The differences are that: on the left-hand side the convective derivative is now included; on the right-hand side a new transport coefficient ($\underline{\underline{\delta}}^c$) has been introduced. This is given by:

$$\underline{\underline{\delta}}^c = \frac{\gamma}{8\pi} \begin{pmatrix} M_x^4 & \Omega M_y^7 \\ \Omega M_x^7 & M_y^4 \end{pmatrix} \qquad M_j^n = \int \frac{w^n T_{cj} F_m}{1 + \Omega^2 w^6} \mathsf{d}^3\mathbf{w} \qquad \hat{\mathbf{e}} = \begin{pmatrix} 1 \\ 1 \end{pmatrix} \qquad \text{(B.7)}$$

The moments M_j^n must be calculated numerically as they are moments of complicated combinations of F_m and $\mathbf{F}_1$. This was ignored previously as these terms are expected to be small.

Appendix C

Improving the ion fluid model

C.1 The relaxation of $T_i = 0$

It is possible to relax the assumption that the ions are cold. In order to do this the ion's energy equation must be solved for the ion pressure P_i.

$$\frac{\partial \rho E_i}{\partial t} + \nabla \cdot (\rho_i E_i \mathbf{C} + P_i \mathbf{C}) = \Delta E_{ie} \tag{C.1}$$

E_i is the total energy of the ion fluid and given by the sum of the ion fluids kinetic energy and it's internal energy ϵ_i. The internal energy is given by the equation of state.

$$E_i = \frac{1}{2}\rho C^2 + \epsilon_i \qquad P_i = (\gamma - 1)\rho\epsilon_i \tag{C.2}$$

γ is the same as in an ideal gas ($\gamma = 5/3$). The term ΔE_{ie} expresses the energy exchange between the ions and the electrons. The way in which this term is treated is the main challenge to including the ion pressure in the model.

C.2 A two-species model

In order to describe higher frequency phenomena resulting from charge separation or Maxwell's displacement current it would not only be necessary to solve the full equation for the fluid momentum – but also to introduce a two species description. The ion continuity equation would need to be solved for the ion density:

$$\frac{\partial n_i}{\partial t} + \nabla \cdot (n_i \mathbf{C}) = 0 \tag{C.3}$$

As stated previously, when considering high frequency phenomena, the displacement current needs to be included in the Ampere-Maxwell equation. The ion momentum equation which must be solved is then equation (3.77).

Appendix D

The simulation of shocks

The finite difference scheme used in the ion-model will become unstable when the gradients of the physical variables become too steep – for example when a shock starts to form. In this case a more robust hydrodynamics algorithm will be required [101, 102]. To simulate this the fluid scheme must be upgraded to make use of second order Van Leer advection [103]. The shock scale-length cannot be resolved without the inclusion of ion kinetics. An artificially high viscosity must be included in order to dissipate the strength of the shock such that it is spread over several grid cells.

D.1 The artificial viscosity

The addition of viscosity modifies the ion's momentum and internal energy equations in the following way [101, 104]:

$$\frac{\partial (\rho \mathbf{C})}{\partial t} + \nabla \cdot (\rho \mathbf{C}\mathbf{C}) = \nabla (P_T + q) \tag{D.1}$$

$$\frac{\partial (\rho \epsilon_i)}{\partial t} + \nabla \cdot (\rho \epsilon_i \mathbf{C}) = - (P_T + q) \nabla \cdot \mathbf{C} \tag{D.2}$$

To a first approximation ion temperature has been neglected – to correctly model shocks this assumption must be relaxed and both of the above equations solved. The artificial viscosity – required on the cell boundaries – is generally given by:

$$\begin{aligned} q_{i+1/2,j} =& \alpha\rho_{i+1/2,j}(x_{i+1}-x_i)^2[(C_x)_{i,j}-(C_x)_{i+1,j}]^2+ \\ & \beta\rho_{i+1/2,j}(x_{i+1}-x_i)^2(C_m)_{i+1/2,j}[(C_x)_{i,j}-(C_x)_{i+1,j}] \qquad \text{(D.3)} \\ q_{i,j+1/2} =& \alpha\rho_{i,j+1/2}(y_{j+1}-y_j)^2[(C_y)_{i,j}-(C_y)_{i,j+1}]^2+ \\ & \beta\rho_{i,j+1/2}(y_{j+1}-y_j)^2(C_m)_{i,j+1/2}[(C_y)_{i,j}-(C_y)_{i,j+1}] \qquad \text{(D.4)} \end{aligned}$$

Where C_m is the magnetosonic speed. The first term in each equation is known as the non-linear term and the second as the linear term; the coefficients α and β determine the amount of each used and need to be set arbitrarily to suit the problem simulated.

The inclusion of q in the ion's momentum and energy equations acts to smear out any discontinuities in these quantities caused by the shock. The same must be done for the electrons. In equations D.1 and D.2 the artificial viscosity acts on the terms responsible for the acceleration due to pressure gradients and compressional heating. This can be achieved by adding q into the terms in the f_0 and $\mathbf{f}_1$ equations responsible for these effects. In the f_0 equation the artificial viscosity term must be added to the compressional heating term – equation (D.2) shows that the effect of viscosity is simply to augment this term. Compressional heating is given by the second moment of the following term:

$$T_{CH} = \frac{w}{3}\frac{\partial f_0}{\partial w}\nabla_{\mathbf{r}}\cdot\mathbf{C} \Longrightarrow \int T_{CH} m_e w^2 \mathsf{d}^3\mathbf{w} = P_e \nabla_{\mathbf{r}}\cdot\mathbf{C} \qquad \text{(D.5)}$$

Augmenting this term to include artificial viscosity is simply a matter of replacing it with:

$$T_{CH} = \left(1+\frac{q}{P_e}\right)\frac{w}{3}\frac{\partial f_0}{\partial w}\nabla_{\mathbf{r}}\cdot\mathbf{C} \Longrightarrow \int T_{CH} m_e w^2 \mathsf{d}^3\mathbf{w} = (P_e+q)\nabla_{\mathbf{r}}\cdot\mathbf{C} \qquad \text{(D.6)}$$

The term in the $\mathbf{f}_1$ equation that is responsible for pressure-gradient acceleration should be replaced by:

$$T_{pg} = w\nabla_{\mathbf{r}}\left[f_0\left(1+\frac{q}{P_e}\right)\right] \Longrightarrow \int T_{pg} m_e w \mathsf{d}^3\mathbf{w} = \nabla_{\mathbf{r}}(P_e+q) \qquad \text{(D.7)}$$

D.2 Second-order Van Leer advection

The form of Van Leer's algorithm described here was originally proposed by Youngs and best described by Town [103]. This technique will be described in one-dimension for the sake of simplicity; it can readily be extended to two-dimensions. In the second-order Van Leer advection scheme, the flow velocity is approximated by:

$$C_x = (C_x)^n_{i+1/2} + \left(\frac{\partial C_x}{\partial x}\right)^n_{i+1/2} x \tag{D.8}$$

The finite difference approximation to the derivative of C_x in the above equation uses the simplest method possible:

$$\left(\frac{\partial C_x}{\partial x}\right)^n_{i+1/2} \Longrightarrow \frac{(C_x)^n_{i+1} - (C_x)^n_i}{x_{i+1} + x_i}$$

This gives the following equation for the momentum transfer across the cell boundary at $x_{i+1/2}$:

$$\begin{aligned} V\rho^{n+1}_i (C_x)^{n+1}_i = &- \left((C_x)^n_i + \frac{1}{2}(1-\eta)\,\bar{D}_{i+1/2}\right) A_{i+1/2}\Delta M^n_{i+1/2} + \\ &\left((C_x)^n_{i-1} - \frac{1}{2}(1-\eta)\,\bar{D}_{i+1/2}\right)(1 - A_{i+1/2})\Delta M^n_{i+1/2} \end{aligned} \tag{D.9}$$

V is the volume of the cell, $\Delta M_{i+1/2}$ is the amount of mass transferred across the cell face. The variable A expresses the direction of the flow at the cell faces.

$$\begin{aligned} A_{i+1/2} &= 1 \quad \text{if fluid flows into cell i across face } i + 1/2 \\ &= 0 \quad \text{if fluid flows out of cell i across face } i + 1/2 \end{aligned}$$

η and $D_{i+1/2}$ are given by:

$$\eta = \frac{(C_x)^n_{i+1/2}\Delta t}{x_{i+1} - x_i} \qquad D_{i+1/2} = (C_x)^n_{i+1} - (C_x)^n_i \tag{D.10}$$

The Van Leer algorithm, as given so far, would suffer from spurious oscillations in the solution. This is prevented by employing a non-linear cut-off [103]. This technique detects when such oscillation begins and damps it out by reverting to a lower-order accurate scheme (donor-cell advection) – the large numerical diffusion inherent in this method provides the required dissipation. Using this non-linear cut-off means that $\bar{D}$

must be employed in equation D.9 instead of D.

$$\bar{D}_{i+1/2} = S\left[Min\left(\mid D_{i+1/2} \mid, 2 \mid (C_x)_i^n - (C_x)_{i-1}^n \mid\right)\right] \tag{D.11}$$

Where

$$S = \begin{cases} Sign\left[(C_x)_{i+1}^n - (C_x)_i^n\right] & : \quad Sign\left[(C_x)_{i+1}^n - (C_x)_i^n\right] = Sign\left[(C_x)_i^n - (C_x)_{i-1}^n\right] \\ 0 & : \quad Sign\left[(C_x)_{i+1}^n - (C_x)_i^n\right] \neq Sign\left[(C_x)_i^n - (C_x)_{i-1}^n\right] \end{cases} \tag{D.12}$$

The operators *Sign* and *Min* return the sign and the minimum value of the bracketed quantities respectively. The cut-off is activated in two situations: (1) when the signs of the gradients of the fluid quantity at each cell edge are different, this indicates a spurious oscillation may be occurring with wavelength equal to the mesh length; (2) if the modulus of the gradient at one cell edge is larger than twice the modulus of the gradient at the other, this indicates a shocked region – it is in these regions that spurious oscillations usually appear. The Van Leer scheme is much more complicated than the simple centred-difference scheme currently employed.

Appendix E

The Maxwellian heating operator

As seen in section 4.3.5 the Maxwellian heating operator is (in normalised units):

$$\left(\frac{\partial \tilde{f}_0}{\partial \tilde{t}}\right)_{MH} = \frac{1}{\hat{Z}^2 \tilde{w}^2} \frac{\partial}{\partial \tilde{w}} \left(D_0 \tilde{w}^2 \frac{\partial \tilde{f}_0}{\partial \tilde{w}} \right) \tag{E.1}$$

The form of this heating term can be understood by noting that Maxwellian heating is implemented by augmenting the Rosenbluth 'D' coefficient in the Fokker-Planck collision operator – introduced in the f_0 equation (2.22). This is modified by the addition of a term proportional to w^2, i.e. [89]:

$$\bar{D}(w) = D(w) + D_0 w^2 \tag{E.2}$$

The reasoning behind this is made clear by a consideration of the effect of the heating term given above on f_0 (in un-normalised units):

$$\left(\frac{\partial f_0}{\partial t}\right)_{MH} = \frac{m_e Y_e e D_0}{w^2} \frac{\partial}{\partial w} \left(w^2 \frac{\partial f_0}{\partial w} \right) \tag{E.3}$$

The solution to this equation is of the form:

$$f_0 \propto \left(\frac{n_e}{v_T^{3/2}}\right) e^{(-w^2/v_T^2)} \qquad v_T(t) = \sqrt{1 + \frac{4 m_e Y_{ee} D_0}{v_{T0}^2}} \tag{E.4}$$

Thus the solution to the form of the heating operator given in equation (E.1) is always a Maxwellian.

Appendix F

The generalised distortion parameter

Is it possible to use a different moment in the distortion parameter? To answer this consider the general case (Δ_G):

$$\Delta_G = \frac{\langle w^m \rangle}{\langle w^m \rangle_M} \tag{F.1}$$

Analytical progress may be made by evaluating the denominator.

$$\langle w^m \rangle_M = \int_0^\infty f_m w^{2+m} \mathsf{d}w = A \int_0^\infty e^{-aw^2} w^{2+m} \mathsf{d}w \tag{F.2}$$

Where the constants have been subsumed into A and a for brevity. This integration yields:

$$\langle w^m \rangle_M = \frac{A}{2} a^{-(m+3)/2} \Gamma\left(\frac{3+m}{2}\right) \tag{F.3}$$

In figure F.1 the gamma function is plotted against it's argument. If n is zero or a negative integer then $\Gamma(n)$ is discontinuous. This limits the choice of m in equation (F.2). Aesthetically one might want m to be an integer – although there is no mathematical reason why it should be. The simplest integral to evaluate is that where $m = -2$ as this causes the velocity to disappear from the integral while allowing the velocity moment to converge. The choice of m determines which velocity is weighted the most in the integral used to calculate Δ_G. Using a larger m will produce a result which is more sensitive to distortion of the distribution in the tail than in the body. Therefore Δ_G may be tuned to study distortion of different parts

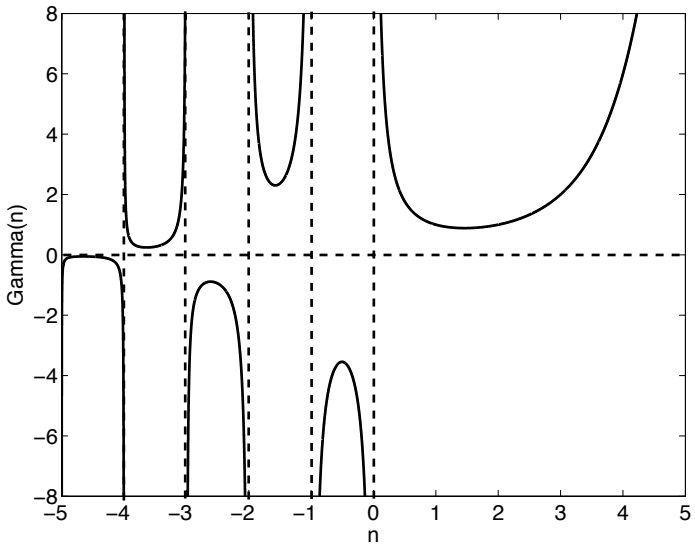

Figure F.1: The gamma function - the vertical dashed lines denote discontinuities.

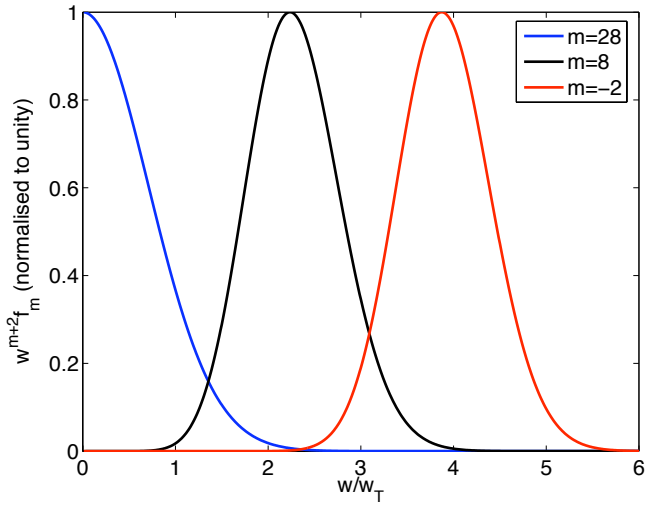

Figure F.2: The effect of taking higher moments in the distortion parameter is to weight the tail of the distribution more strongly.

of the distribution. This is illustrated in figure F.2; here the effect of increasing m on the integrand in equation Δ_G is illustrated for a Maxwellian distribution.

Appendix G

Super-Gaussian transport coefficients

The components of the transport coefficients are in given terms of the following integral:

$$\langle W^n \rangle = \int_0^\infty \frac{F_0 W^{n+2}}{1+\Omega^2 W^6} \mathsf{d}W \tag{G.1}$$

The components of the 'old' transport coefficients $(\underline{\underline{\alpha}}, \underline{\underline{\beta}}, \underline{\underline{\kappa}})$ when f_0 is a super-Gaussian are:

$$\alpha_\perp^c = \frac{9\sqrt{\pi}}{4\delta\Delta\langle W^{m+3}\rangle} \tag{G.2}$$

$$\alpha_\wedge^c = \frac{3\sqrt{\pi}\Omega}{4}\left(\frac{3\langle\langle W_{m+3}^{m+6}\rangle\rangle}{\delta\Delta\langle W^{m+3}\rangle} - 1\right) \tag{G.3}$$

$$\beta_\perp^c = \frac{1}{\Delta}\left[\langle\langle W_{m+3}^{m+5}\rangle\rangle + \Omega^2\langle\langle W_{m+3}^{m+6}\rangle\rangle\langle\langle W_{m+3}^{m+8}\rangle\rangle - \frac{5}{\delta}\langle\langle W_{m+3}^{5}\rangle\rangle - \frac{5\Omega^2}{\delta}\langle\langle W_{m+3}^{m+6}\rangle\rangle\langle\langle W_{m+3}^{8}\rangle\rangle\right] \tag{G.4}$$

$$\beta_{\wedge}^{c} = \frac{\Omega}{\Delta}\left[\langle\langle W_{m+3}^{m+8}\rangle\rangle - \langle\langle W_{m+3}^{m+6}\rangle\rangle\langle\langle W_{m+3}^{m+5}\rangle\rangle + \frac{5}{\delta}\langle\langle W_{m+3}^{m+6}\rangle\rangle\langle\langle W_{m+3}^{5}\rangle\rangle - \frac{5}{\delta}\langle\langle W_{m+3}^{8}\rangle\rangle\right] \tag{G.5}$$

$$\begin{aligned}\kappa_{\perp}^{c} = \frac{8}{9\sqrt{\pi}}\Bigg[&\frac{\delta}{2}\langle W^{m+7}\rangle - \frac{5}{2}\langle W^{7}\rangle + \frac{\Omega^2\langle W^{m+8}\rangle}{2\Delta}\left(\delta\langle\langle W_{m+3}^{m+8}\rangle\rangle - \delta\langle\langle W_{m+3}^{m+6}\rangle\rangle\langle\langle W_{m+3}^{m+5}\rangle\rangle\right)\\ &+\frac{\Omega^2\langle W^{m+8}\rangle}{2\Delta}\left(5\langle\langle W_{m+3}^{m+6}\rangle\rangle\langle\langle W_{m+3}^{5}\rangle\rangle - 5\langle\langle W_{m+3}^{8}\rangle\rangle\right)\\ &-\frac{\langle W^{m+5}\rangle}{2\Delta}\left(\delta\langle\langle W_{m+3}^{m+5}\rangle\rangle + \Omega^2\delta\langle\langle W_{m+3}^{m+6}\rangle\rangle\langle\langle W_{m+3}^{m+8}\rangle\rangle\right)\\ &+\frac{\langle W^{m+5}\rangle}{2\Delta}\left(5\langle\langle W_{m+3}^{5}\rangle\rangle + 5\Omega^2\langle\langle W_{m+3}^{m+6}\rangle\rangle\langle\langle W_{m+3}^{8}\rangle\rangle\right)\Bigg]\end{aligned} \tag{G.6}$$

$$\begin{aligned}\kappa_{\wedge}^{c} = \frac{8\Omega}{9\sqrt{\pi}}\Bigg[&\frac{\delta}{2}\langle W^{m+10}\rangle - \frac{5}{2}\langle W^{10}\rangle - \frac{\langle W^{m+8}\rangle}{2\Delta}\left(\delta\langle\langle W_{m+3}^{m+5}\rangle\rangle + \delta\Omega^2\langle\langle W_{m+3}^{m+6}\rangle\rangle\langle\langle W_{m+3}^{m+8}\rangle\rangle\right)\\ &+\frac{\langle W^{m+8}\rangle}{2\Delta}\left(5\Omega^2\langle\langle W_{m+3}^{m+6}\rangle\rangle\langle\langle W_{m+3}^{8}\rangle\rangle + 5\langle\langle W_{m+3}^{5}\rangle\rangle\right)\\ &-\frac{\langle W^{m+5}\rangle}{2\Delta}\left(\delta\langle\langle W_{m+3}^{m+8}\rangle\rangle - \delta\langle\langle W_{m+3}^{m+6}\rangle\rangle\langle\langle W_{m+3}^{m+5}\rangle\rangle\right)\\ &+\frac{\langle W^{m+5}\rangle}{2\Delta}\left(5\langle\langle W_{m+3}^{8}\rangle\rangle - 5\langle\langle W_{m+3}^{m+6}\rangle\rangle\langle\langle W_{m+3}^{5}\rangle\rangle\right)\Bigg]\end{aligned} \tag{G.7}$$

The following variables used in these equations are defined as:

$$\delta = \frac{2^{m/2}m}{\alpha_e^m} \qquad \langle\langle W_q^p\rangle\rangle = \frac{\langle W^p\rangle}{\langle W^q\rangle} \qquad \Delta = 1 + \Omega^2\langle\langle W_{m+3}^{m+6}\rangle\rangle^2 \tag{G.8}$$

The 'new' transport coefficients are given by:

$$\psi_{\perp}^{c} = \frac{1}{\Delta}(\langle\langle W_{m+3}^{m+5}\rangle + \Omega^2\langle\langle W_{m+3}^{m+8}\rangle\rangle\langle\langle W_{m+3}^{m+6}\rangle\rangle) - \frac{5}{2} \tag{G.9}$$

$$\psi_{\wedge}^{c} = \frac{\Omega}{\Delta}(\langle\langle W_{m+3}^{m+8}\rangle\rangle - \langle\langle W_{m+3}^{m+5}\rangle\rangle\langle\langle W_{m+3}^{m+6}\rangle\rangle) \tag{G.10}$$

$$\gamma_{\perp}^{c} = \frac{2}{\delta\Delta}(\langle\langle W_{m+3}^{5}\rangle\rangle + \Omega^2\langle\langle W_{m+3}^{m+6}\rangle\rangle\langle\langle W_{m+3}^{8}\rangle\rangle) \tag{G.11}$$

$$\gamma_{\wedge}^{c} = \frac{2\Omega}{\delta\Delta}(\langle\langle W_{m+3}^{8}\rangle\rangle - \langle\langle W_{m+3}^{m+6}\rangle\rangle\langle\langle W_{m+3}^{5}\rangle\rangle) \tag{G.12}$$

$$\phi_{\perp}^{c} = \frac{\sqrt{\pi}}{4}\Big[\langle W^{7}\rangle + \frac{\Omega^{2}\langle W^{m+8}\rangle}{\Delta}\left(\langle\langle W_{m+3}^{8}\rangle\rangle - \langle\langle W_{m+3}^{m+6}\rangle\rangle\langle\langle W_{m+3}^{5}\rangle\rangle\right) - \frac{\langle W^{m+5}\rangle}{\Delta}\left(\langle\langle W_{m+3}^{5}\rangle\rangle + \Omega^{2}\langle\langle W_{m+3}^{m+6}\rangle\rangle\langle\langle W_{m+3}^{8}\rangle\rangle\right)\Big] \tag{G.13}$$

$$\phi_{\wedge}^{c} = \frac{\sqrt{\pi}\Omega}{4}\Big[\langle W^{10}\rangle - \frac{\langle W^{m+8}\rangle}{\Delta}\left(\langle\langle W_{m+3}^{5}\rangle\rangle + \Omega^{2}\langle\langle W_{m+3}^{m+6}\rangle\rangle\langle\langle W_{m+3}^{8}\rangle\rangle\right) + \frac{\langle W^{m+5}\rangle}{\Delta}\left(\langle\langle W_{m+3}^{m+6}\rangle\rangle\langle\langle W_{m+3}^{5}\rangle\rangle - \langle\langle W_{m+3}^{8}\rangle\rangle\right)\Big] \tag{G.14}$$

By numerically evaluating the integrals in the expressions for the transport coefficients (using Simpson's one-third rule) plots such as those in figures 6.1 and 6.2 may be produced.

The high and low Hall parameter asymptotes of the transport coefficients may be derived by considering the following integral at $\omega\tau$ approaches zero and infinity:

$$\langle W^{n}\rangle = \int_{0}^{\infty} \frac{F_{0}W^{n+2}}{1+\Omega^{2}W^{6}}\mathsf{d}W \tag{G.15}$$

The case where $\Omega = 0$ can be evaluated straightforwardly; in this case the integral is represented by a gamma function. The high Hall parameter limit is more difficult to find. As shown by Epperlein & Haines, the first term in the denominator may not be neglected for all values of n if $\omega\tau$ is very large [25]. This is because the lower limit of the integral is zero – no matter how large Ω is there will be some W for which $\Omega^{2}W^{6}$ is not large. It is necessary to split up the integral as follows:

$$\begin{aligned}\frac{\langle W^{n}\rangle}{\Phi} = {} & \frac{1}{2\alpha_{e}'^{6}\Omega^{2}}\Gamma\left(\frac{n-3}{m}\right) \\ & - \frac{m}{2}(\alpha_{e}'^{3}\Omega)^{-(3+n)/3}\int_{0}^{(\alpha_{e}'^{3}\Omega)^{m/3(m+6)}} \mathsf{d}x\frac{x^{n-4}}{1+x^{6}}\left[1-\left(\frac{x}{\alpha_{e}'\Omega^{1/3}}\right)^{m}+\ldots\right] \\ & - \frac{1}{2\alpha_{e}'^{12}\Omega^{4}}\int_{(\alpha_{e}'^{3}\Omega)^{-2m/(m+6)}}^{\infty} \mathsf{d}x\mathsf{e}^{-x}x^{(n-m-9)/m}\left[1-\left(\frac{1}{\alpha_{e}'^{3}\Omega x^{3/m}}\right)^{2}+\ldots\right]\end{aligned} \tag{G.16}$$

Where $\Phi = 8\pi\alpha_{e}'^{3}C(m)/m$. The integrals above may be determined using the same standard integrals as in Epperlein & Haines [25]. The integrals used to determine the anomalous transport coefficients ($\alpha_{\wedge}^{c}$,$\psi_{\perp}^{c}$), for $m = 5$, are then given by:

$$\frac{\langle W^8 \rangle}{\Phi} = \frac{1}{2\alpha_e'^3\Omega^2} - \frac{5\pi}{6}\frac{1}{(\alpha_e'^3\Omega)^{11/3}} + \dots \tag{G.17}$$

$$\frac{\langle W^{11} \rangle}{\Phi} = \frac{1}{2\alpha_e'^6\Omega^2}\Gamma\left(\frac{8}{5}\right) - \frac{1}{2\alpha_e'^{12}\Omega^4}\Gamma\left(\frac{2}{5}\right) + \dots \tag{G.18}$$

$$\frac{\langle W^{13} \rangle}{\Phi} = \frac{1}{2\alpha_e'^6\Omega^2} - \frac{1}{2\alpha_e'^{12}\Omega^4}\Gamma\left(\frac{4}{5}\right) + \dots \tag{G.19}$$

The reason for the recovery of Braginskii's asymptotes for a Langdon distribution and the difference between those of $\beta_\perp^c$ and $\psi_\perp^c$ may now be understood. Braginskii's asymptotes are correct if the second term in the series for the relevant integrals is proportional to Ω^{-4}. This is not the case for the $n = 8$ integral. The term in $\Omega^{-11/3}$ comes from the first integral in equation (G.16) which is a result the contribution of the low velocity electrons to the integral – as the moment gets higher this eventually becomes neglidgible. In the Maxwellian case this term is important for $\alpha_\wedge^c$ and $\beta_\perp^c$ and so in these cases the Braginskii asymptotes are incorrect. When f_0 is a Langdon distribution the integrals which are important for calculating $\alpha_\wedge^c$ and $\psi_\perp^c$ (as $\omega\tau$ gets very large) are those with $n = 11$ and $n = 13$, so the Braginskii scalings are correct. However, the $n = 8$ moment is important for $\beta_\perp^c$ and so the Epperlein and Haines scalings should be used for this coefficient.

Bibliography

[1] WEC, *World Energy Assessment (United Nations Development Programme)* (2000).

[2] S. Atzeni and J. Meyer-Ter-Vehn, *The Physics of Inertial Fusion*, Oxford University Press (2004).

[3] T. J. M. Boyd and J. J. Sanderson, *The Physics of Plasmas*, Cambridge University Press (2003).

[4] M. G. Haines, *Review of inertial confinement fusion*, Astrophysics and Space Science **256**, 125 (1998).

[5] J. Sanz and R. Bettti, *Analytical model of the ablative Rayleigh-Taylor instability in the deceleration phase*, Physics of Plasmas **12** (2005).

[6] M. D. Rosen, *The physics issues that determine inertial confinement fusion target gain and driver requirements: A tutorial*, Physics of Plasmas **6**, 1690 (1999), Part 2.

[7] J. D. Lindl, P. Amendt, R. L. Berger, S. G. Glendinning, S. H. Glenzer, S. W. Haan, R. L. Kauffman, O. L. Landen, and L. J. Suter, *The physics basis for ignition using indirect-drive targets on the National Ignition Facility*, Physics of Plasmas **11**, 339 (2004).

[8] T. W. L. Sanford, R. E. Olson, R. L. Bowers, G. A. Chandler, M. S. Derzon, D. E. Hebron, R. J. Leeper, R. C. Mock, T. J. Nash, D. L. Peterson, L. E. Ruggles, W. W. Simpson, K. W. Struve, and R. A. Vesey, *Z pinch-generated x rays demonstrate potential for indirect-drive ICF experiments*, Physical Review Letters **83**, 5511 (1999).

[9] M. G. Haines, T. W. L. Sanford, and V. P. Smirnov, *Wire-array z-pinch: a powerful x-ray source for ICF*, Plasma Physics and Controlled Fusion **47**, B1 (2005), Sp. Iss. SI Suppl. 12B.

[10] S. Nakai, *Design Study and Technology Assessment on Inertial Fusion Energy Power Plant*, First Research Coordination Meeting of the Coordinated Research Programme on "Elements of Power Plant Design for Inertial Fusion Energy" (2001).

[11] S. H. Glenzer, W. E. Alley, K. G. Estabrook, J. S. De Groot, M. G. Haines, J. H. Hammer, J. P. Jadaud, B. J. MacGowan, J. D. Moody, W. Rozmus, L. J. Suter, T. L. Weiland, and E. A. Williams, *Thomson scattering from laser plasmas*, Physics of Plasmas **6**, 2117 (1999), Part 2.

[12] D. H. Froula, J. S. Ross, B. B. Pollock, P. Davis, A. N. James, L. Divol, M. J. Edwards, A. A. Offenberger, D. Price, R. P. J. Town, G. R. Tynan, and S. H. Glenzer, *Quenching of the nonlocal electron heat transport by large external magnetic fields in a laser-produced plasma measured with imaging thomson scattering*, Physical Review Letters **98** (2007).

[13] C. P. Ridgers, R. J. Kingham, and A. G. R. Thomas, *Magnetic cavitation and the reemergence of nonlocal transport in laser plasmas*, Physical Review Letters **1** (2008).

[14] D. W. Forslund, J. M. Kindel, and K. Lee, *Theory of Hot-Electron Spectra at High Laser Intensity*, Physical Review Letters **39**, 284 (1977).

[15] P. Gibbon, *Short Pulse Laser Interactions with Matter*, Imperial College Press (2005).

[16] R. Liboff, *Kinetic Theory. Classical, Quantum and Relativistic Descriptions*, Springer (1998).

[17] J. Tonge, M. Tzoufras, F. S. Tsung, W. B. Mori, C. Ren, M. Marti, and L. Silva, *Fast Ignition with Ultra-High Intensity Lasers*, 49th Annual Meeting of the Division of Plasma Physics (2007).

[18] M. N. Rosenbluth, M. MacDonald, and D. L. Judd, *Fokker-Planck Equation for an Inverse-Square Force*, The Physical Review **107**, 1 (1957).

[19] M. Haines, *Laser-Plasma Interactions 4*, Proceedings of the Scottish Universities Summer School (1979).

[20] I. Shkarofsky, T. Johnston, and M. Bachyinski, *The Particle Kinetics of Plasmas*, Addison-Wesley (1966).

[21] T. W. Johnston, *Cartesian Tensor Scalar Product and Spherical Harmonic Expansion in Boltzmann's Equation*, Physical Review **120**, 1103 (1960).

[22] R. J. Kingham and A. R. Bell, *An implicit Vlasov-Fokker-Planck code to model non-local electron transport in 2-D with magnetic fields*, Journal of Computational Physics **194**, 1 (2004).

[23] S. Braginskii, *Transport Processes in a Plasma*, Reviews of Plasma Physics **1**, 205 (1966).

[24] E. M. Epperlein, *The Accuracy of Braginskii Transport-Coefficients for a Lorentz Plasma*, Journal of Physics D-Applied Physics **17**, 1823 (1984).

[25] E. M. Epperlein and M. G. Haines, *Plasma Transport-Coefficients in a Magnetic-Field by Direct Numerical-Solution of the Fokker-Planck Equation*, Physics of Fluids **29**, 1029 (1986).

[26] I. P. Shkarofsky, I. B. Berstein, and B. B. Robinson, *Condensed Presentation of Transport Coefficients in a Fully Ionized Plasma*, Physics of Fluids **6**, 8 (1963).

[27] J. A. Stamper, Papadopo.K, R. N. Sudan, S. O. Dean, E. A. McLean, and J. M. Dawson, *Spontaneous Magnetic Fields in Laser-Produced Plasmas*, Physical Review Letters **26**, 1012 (1971).

[28] J. A. Stamper and B. H. Ripin, *Faraday-Rotation Measurements of Megagauss Magnetic-Fields in Laser-Produced Plasmas*, Physical Review Letters **34**, 138 (1975).

[29] M. G. Drouet and R. Bolton, *Distribution of Self-Generated Current in Laser-Produced Plasmas*, Physical Review Letters **36**, 591 (1976).

[30] D. G. Colombant and N. K. Winsor, *Thermal-Force Terms and Self-Generated Magnetic-Fields in Laser-Produced Plasmas*, Physical Review Letters **38**, 697 (1977).

[31] A. Raven, O. Willi, and P. T. Rumsby, *Megagauss Magnetic-Field Profiles in Laser-Produced Plasmas*, Physical Review Letters **41**, 554 (1978).

[32] M. Borghesi, A. J. MacKinnon, A. R. Bell, R. Gaillard, and O. Willi, *Megagauss magnetic field generation and plasma jet formation on solid targets irradiated by an ultraintense picosecond laser pulse*, Physical Review Letters **81**, 112 (1998).

[33] M. G. Haines, *Heat-Flux Effects in Ohms Law*, Plasma Physics and Controlled Fusion **28**, 1705 (1986).

[34] M. G. Haines, *Magnetic-Field Generation in Laser Fusion and Hot-Electron Transport*, Canadian Journal of Physics **64**, 912 (1986).

[35] J. R. Davies, A. R. Bell, M. G. Haines, and S. M. Guerin, *Short-pulse high-intensity laser-generated fast electron transport into thick solid targets*, Physical Review E **56**, 7193 (1997).

[36] J. J. Thomson, C. E. Max, and K. Estabrook, *Magnetic-Fields Due to Resonance-Absorption of Laser Light*, Physical Review Letters **35**, 663 (1975).

[37] J. A. Stamper and D. A. Tidman, *Magnetic-Field Generation Due to Radiation Pressure in a Laser-Produced Plasma*, Physics of Fluids **16**, 2024 (1973).

[38] B. Dubroca, M. Tchong, P. Charrier, V. T. Tikhonchuk, and J. P. Morreeuw, *Magnetic field generation in plasmas due to anisotropic laser heating*, Physics of Plasmas **11**, 3830 (2004).

[39] M. G. Haines, *Generation of an axial magnetic field from photon spin*, Physical Review Letters **8713** (2001).

[40] M. Tatarakis, K. Krushelnick, Z. Najmudin, E. L. Clark, M. Salvati, M. I. K. Santala, A. E. Dangor, V. Malka, D. Neely, R. Allott, and C. Danson, *Measurements of the Inverse Faraday effect in high power laser produced plasmas*, CLF Annual Report 1998/1999 pg. 16–17 (1999).

[41] D. R. Gray, J. D. Kilkenny, M. S. White, P. Blyth, and D. Hull, *Observation of Severe Heat-Flux Limitation and Ion-Acoustic Turbulence in a Laser-Heated Plasma*, Physical Review Letters **39**, 1270 (1977).

[42] A. R. Bell, *Electron-Energy Transport in Ion Waves and Its Relevance to Laser-Produced Plasmas*, Physics of Fluids **26**, 279 (1983).

[43] A. B. Langdon, *Non-Linear Inverse Bremsstrahlung and Heated-Electron Distributions*, Physical Review Letters **44**, 575 (1980).

[44] A. P. L. Robinson, A. R. Bell, and R. J. Kingham, *Fast electron transport and ionization in a target irradiated by a high power laser*, Plasma Physics and Controlled Fusion **48**, 1063 (2006).

[45] A. R. Bell, R. G. Evans, and D. J. Nicholas, *Electron Energy-Transport in Steep Temperature-Gradients in Laser-Produced Plasmas*, Physical Review Letters **46**, 243 (1981).

[46] D. Shvarts, J. Delettrez, R. L. McCrory, and C. P. Verdon, *Self-Consistent Reduction of the Spitzer-Harm Electron Thermal Heat-Flux in Steep Temperature-Gradients in Laser-Produced Plasmas*, Physical Review Letters **47**, 247 (1981).

[47] J. P. Matte and J. Virmont, *Electron Heat-Transport Down Steep Temperature-Gradients*, Physical Review Letters **49**, 1936 (1982).

[48] J. F. Luciani, P. Mora, and J. Virmont, *Nonlocal Heat-Transport Due to Steep Temperature-Gradients*, Physical Review Letters **51**, 1664 (1983).

[49] J. R. Albritton, E. A. Williams, I. B. Bernstein, and K. P. Swartz, *Nonlocal Electron Heat-Transport by Not Quite Maxwell-Boltzmann Distributions*, Physical Review Letters **57**, 1887 (1986).

[50] E. M. Epperlein, *Kinetic-Theory of Laser Filamentation in Plasmas*, Physical Review Letters **65**, 2145 (1990).

[51] R. C. Malone, R. L. McCrory, and R. L. Morse, *Indications of Strongly Flux-Limited Electron Thermal Conduction in Laser-Target Experiments*, Physical Review Letters **34**, 721 (1975).

[52] J. F. Luciani, P. Mora, and A. Bendib, *Magnetic-Field and Nonlocal Transport in Laser-Created Plasmas*, Physical Review Letters **55**, 2421 (1985).

[53] E. M. Epperlein and R. W. Short, *A Practical Nonlocal Model for Electron Heat-Transport in Laser Plasmas*, Physics of Fluids B-Plasma Physics **3**, 3092 (1991).

[54] G. P. Schurtz, P. D. Nicolai, and M. Busquet, *A nonlocal electron conduction model for multidimensional radiation hydrodynamics codes*, Physics of Plasmas **7**, 4238 (2000).

[55] P. Nicolai, M. Vandenboomgaerde, B. Canaud, and F. Chaigneau, *Effects of self-generated magnetic fields and nonlocal electron transport in laser produced plasmas*, Physics of Plasmas **7**, 4250 (2000).

[56] G. Gregori, S. H. Glenzer, J. Knight, C. Niemann, D. Price, D. H. Froula, M. J. Edwards, R. P. J. Town, A. Brantov, W. Rozmus, and V. Y. Bychenkov, *Effect of nonlocal transport on heat-wave propagation*, Physical Review Letters **92** (2004).

[57] D. G. Colombant, W. M. Manheimer, and M. Busquet, *Test of models for electron transport in laser produced plasmas*, Physics of Plasmas **12** (2005).

[58] P. Nicolai, J. L. Feugeas, and G. Schurtz, *A model for the nonlocal transport and the associated distribution function deformation in magnetized laser-plasmas*, Journal De Physique Iv **133**, 159 (2006).

[59] G. Schurtz, S. Gary, S. Hulin, C. Chenais-Popovics, J. C. Gauthier, F. Thais, J. Breil, F. Durut, J. L. Feugeas, P. H. Maire, P. Nicolai, O. Peyrusse, C. Reverdin, G. Soullie, V. Tikhonchuk, B. Villette, and C. Fourment, *Revisiting nonlocal electron-energy transport in inertial-fusion conditions (vol 98, pg 095002, 2007)*, Physical Review Letters **98** (2007).

[60] J. R. Albritton, *Laser-Absorption and Heat-Transport by Non-Maxwell-Boltzmann Electron Distributions*, Physical Review Letters **50**, 2078 (1983).

[61] E. M. Epperlein, *Kinetic Simulations of Laser Filamentation in Plasmas*, Physics of Fluids B-Plasma Physics **3**, 3082 (1991).

[62] T. H. Kho and M. G. Haines, *Nonlinear Electron-Transport in Magnetized Laser Plasmas*, Physics of Fluids **29**, 2665 (1986).

[63] R. J. Kingham and A. R. Bell, *Nonlocal magnetic-field generation in plasmas without density gradients*, Physical Review Letters **88** (2002).

[64] A. V. Brantov, V. Y. Bychenkov, W. Rozmus, C. E. Capjack, and R. Sydora, *Linear theory of nonlocal transport in a magnetized plasma*, Physics of Plasmas **10**, 4633 (2003).

[65] T. Kho and D. J. Bond, *Application of a Moment Method to Calculation of Heat-Flow in a Plasma with a Fokker-Planck Collision Term*, Journal of Physics D-Applied Physics **14**, L117 (1981).

[66] H. Grad, *On the kinetic theory of rarefied gases*, Communications on Pure and Applied Mathematics **2**, 331 (1949).

[67] M. S. White, J. D. Kilkenny, and A. E. Dangor, *Measurement of Thermal-Conductivity in a Laser-Heated Plasma*, Physical Review Letters **35**, 524 (1975).

[68] D. R. Gray and J. D. Kilkenny, *Measurement of Ion-Acoustic Turbulence and Reduced Thermal-Conductivity Caused by a Large Temperature-Gradient in a Laser Heated Plasma*, Plasma Physics and Controlled Fusion **22**, 81 (1980).

[69] A. Dyson, A. E. Dangor, A. K. L. Dymokebradshaw, and R. G. Evans, *Measurements of the Heat-Flux, Inverse Bremsstrahlung Absorption and Equilibration in an under-Dense Laser Heated Plasma*, Plasma Physics and Controlled Fusion **30**, 1259 (1988).

[70] J. Hawreliak, D. M. Chambers, S. H. Glenzer, A. Gouveia, R. J. Kingham, R. S. Marjoribanks, P. A. Pinto, O. Renner, P. Soundhauss, S. Topping, E. Wolfrum, P. E. Young, and J. S. Wark, *Thomson scattering measurements of heat flow in a laser-produced plasma*, Journal of Physics B-Atomic Molecular and Optical Physics **37**, 1541 (2004).

[71] R. Kingham and A. Bell, *Analytical Models of Non-Local Magnetic Field Generation in Laser-Plasmas*, Unpublished (2007).

[72] C. T. Dum, *Anomalous Heating by Ion Sound Turbulence*, Physics of Fluids **21**, 945 (1978).

[73] P. Mora and H. Yahi, *Thermal Heat-Flux Reduction in Laser-Produced Plasmas*, Physical Review A **26**, 2259 (1982).

[74] J. P. Matte, M. Lamoureux, C. Moller, R. Y. Yin, J. Delettrez, J. Virmont, and T. W. Johnston, *Non-Maxwellian Electron Distributions and Continuum X-Ray-Emission in Inverse Bremsstrahlung Heated Plasmas*, Plasma Physics and Controlled Fusion **30**, 1665 (1988).

[75] J. P. Matte, T. W. Johnston, J. Delettrez, and R. L. McCrory, *Electron Heat-Flow with Inverse Bremsstrahlung and Ion Motion*, Physical Review Letters **53**, 1461 (1984).

[76] F. A. Bibi and J. P. Matte, *Influence of the electron distribution function shape on nonlocal electron heat transport in laser-heated plasmas*, Physical Review E **66** (2002), Part 2.

[77] F. A. Bibi and J. P. Matte, *Nonlocal electron heat transport and electron-ion energy transfer in the presence of strong collisional heating*, Laser and Particle Beams **22**, 103 (2004).

[78] S. Brunner and E. Valeo, *Simulations of electron transport in laser hot spots*, Physics of Plasmas **9**, 923 (2002).

[79] C. K. Li, F. H. Seguin, J. A. Frenje, J. R. Rygg, R. D. Petrasso, R. P. J. Town, P. A. Amendt, S. P. Hatchett, O. L. Landen, A. J. Mackinnon, P. K. Patel, V. A. Smalyuk, T. C. Sangster, and J. P. Knauer, *Measuring E and B fields in laser-produced plasmas with monoenergetic proton radiography*, Physical Review Letters **97** (2006).

[80] C. K. Li, F. H. Seguin, J. A. Frenje, J. R. Rygg, R. D. Petrasso, R. P. J. Town, O. L. Landen, J. P. Knauer, and V. A. Smalyuk, *Observation of megagauss-field topology changes due to magnetic reconnection in laser-produced plasmas*, Physical Review Letters **99** (2007).

[81] P. M. Nilson, L. Willingale, M. C. Kaluza, C. Kamperidis, S. Minardi, M. S. Wei, P. Fernandes, M. Notley, S. Bandyopadhyay, M. Sherlock, R. J. Kingham, M. Tatarakis, Z. Najmudin, W. Rozmus, R. G. Evans, M. G. Haines, A. E. Dangor, and K. Krushelnick, *Magnetic reconnection and plasma dynamics in two-beam laser-solid interactions*, Physical Review Letters **97** (2006).

[82] C. K. Li, F. H. Seguin, J. A. Frenje, J. R. Rygg, R. D. Petrasso, R. P. J. Town, P. A. Amendt, S. P. Hatchett, O. L. Landen, A. J. Mackinnon, P. K. Patel, M. Tabak, J. P. Knauer, T. C. Sangster, and V. A. Smalyuk, *Observation of the decay dynamics and instabilities of megagauss field structures in laser-produced plasmas*, Physical Review Letters **99** (2007).

[83] J. D. Hoffman, *Numerical Methods for Engineers and Scientists*, Marcel Dekker (2001).

[84] R. P. J. Town, A. R. Bell, and S. J. Rose, *Fokker-Planck Calculations with Ionization Dynamics of Short-Pulse Laser-Solid Interactions*, Physical Review Letters **74**, 924 (1995).

[85] T. H. Kho and M. G. Haines, *Nonlinear Kinetic Transport of Electrons and Magnetic-Field in Laser-Produced Plasmas*, Physical Review Letters **55**, 825 (1985).

[86] E. M. Epperlein, G. J. Rickard, and A. R. Bell, *A Code for the Solution of the Vlasov-Fokker-Planck Equation in 1-D or 2-D*, Computer Physics Communications **52**, 7 (1988).

[87] E. M. Epperlein, G. J. Rickard, and A. R. Bell, *Two-Dimensional Nonlocal Electron-Transport in Laser-Produced Plasmas*, Physical Review Letters **61**, 2453 (1988).

[88] H. A. Van der Vorst, *Bi-CGSTAB: a fast and smoothly converging variant of the Bi-CG for the solution of nonsymmetric linear systems*, SIAM Journal on Scientific Computing **13**, 631 (1992).

[89] R. J. Kingham, *Magnetic Fields in Gas-Filled Hohlraums*, LLNL Technical Report Subcontact B529387 (2004).

[90] A. Nishiguchi, T. Yabe, M. G. Haines, M. Psimopoulos, and H. Takewaki, *Convective Amplification of Magnetic-Fields in Laser-Produced Plasmas by the Nernst Effect*, Physical Review Letters **53**, 262 (1984).

[91] A. Nishiguchi, T. Yabe, and M. G. Haines, *Nernst Effect in Laser-Produced Plasmas*, Physics of Fluids **28**, 3683 (1985).

[92] J. P. Chittenden and M. G. Haines, *Nernst and Ettinghausen Effects in the Dense Z-Pinch - Their Impact Upon Equilibria and Runaway Electrons*, Journal of Physics D-Applied Physics **26**, 1048 (1993).

[93] J. H. Brownell, *Magnetic-Field Generation in Implosions due to Nernst Refridgeration*, Comments on Plasma Physics and Controlled Fusion **4**, 131 (1979).

[94] J. M. Liu, J. S. Degroot, J. P. Matte, T. W. Johnston, and R. P. Drake, *Electron Heat-Transport with Non-Maxwellian Distributions*, Physics of Plasmas **1**, 3570 (1994).

[95] C. T. Dum, *Anomalous Electron-Transport Equations for Ion Sound and Related Turbulent Spectra*, Physics of Fluids **21**, 956 (1978).

[96] E. M. Epperlein, *Fokker-Planck Modeling of Electron-Transport in Laser-Produced Plasmas*, Laser and Particle Beams **12**, 257 (1994).

[97] L. Onsager, *Reciprocal Relations in Irreversible Processes I*, Physical Review **37**, 405 (1931).

[98] D. A. Tidman and R. A. Shanny, *Field-Generating Thermal Instability in Laser-Heated Plasmas*, Physics of Fluids **17**, 1207 (1974).

[99] A. G. R. Thomas, *Private communication* (2008).

[100] T. Tajima and J. M. Dawson, *Laser Electron-Accelerator*, Physical Review Letters **43**, 267 (1979).

[101] R. A. Gentry, R. E. Martin, and B. J. Daly, *An Eulerian Differencing Method for Unsteady Compressible Flow Problems*, Journal of Computational Physics **1**, 87 (1966).

[102] P. Woodward and P. Colella, *The Numerical-Simulation of Two-Dimensional Fluid-Flow with Strong Shocks*, Journal of Computational Physics **54**, 115 (1984).

[103] R. P. J. Town, *3-D Hydrodynamical Simulation of Laser Driven Implosions*, PhD Thesis (1990).

[104] J. Von Neumann and R. D. Richtmyer, *A Method for the Numerical Calculation of Shocks*, Journal of Applied Physics **21**, 232 (1949).